Université Fédérale

Toulouse Midi-Pyrénées

THÈSE

En vue de l'obtention du

DOCTORAT DE L'UNIVERSITÉ DE TOULOUSE

Délivré par :

Institut Supérieur de l'Aéronautique et de l'Espace

Présentée et soutenue par :
Sovanna THAI

le jeudi 25 novembre 2021

Titre :

Advanced anti-windup flight control algorithms for fast time-varying aerospace systems
Algorithmes de contrôle en vol avancés avec compensation anti-windup pour des systèmes aérospatiaux variant rapidement dans le temps

---

École doctorale et discipline ou spécialité :

EDSYS : Automatique

Unité de recherche :

Équipe d'accueil ISAE-ONERA ACDC

Directeur(s) de Thèse :

M. Clément ROOS (directeur de thèse)
M. Spilios THEODOULIS (co-directeur de thèse)

Jury :

M. Marco LOVERA Professeur École polytechnique de Milan - Président
M. Samir BENNANI Ingénieur de recherche ESA-ESTEC- Examinateur
M. Jean-Marc BIANNIC Directeur de recherche ONERA Toulouse - Examinateur
M. Clément ROOS Maître de recherche ONERA Toulouse - Directeur de thèse
M. Jean-Sébastien SCHWARTZ Ingénieur DGA Techniques terrestres Bourges - Examinateur
M. Olivier SENAME Professeur GIPSA-lab INP Grenoble - Rapporteur
M. Spilios THEODOULIS Ingénieur de recherche ISL St-Louis - Co-directeur de thèse
M. Matthew TURNER Professeur Université de Southampton - Rapporteur

Acknowledgements

First and foremost, I am deeply grateful to my thesis advisors, Clément Roos and Spilios Theodoulis, as well as Jean-Marc Biannic. Clément, Jean-Marc, it was a real pleasure to study and work under your guidance, starting from your lectures and labs on robust control. It was particularly exciting to see part of my thesis be so closely related to your own projects, to see my contributions be integrated in your tools, and to benefit from the improvements and refinements. Spilios, thank you for your attention, your open-mindedness, and your sound advice, which truly helped me delimit the scope of my thesis. Most of all, I thank all three of you for always having my best interests at heart, and for your unfailing kindness in all our discussions, which allowed me to move forward serenely throughout these three years.

I would like to thank Pr. Olivier Sename and Pr. Matthew Turner for accepting to review this thesis manuscript, and for their relevant and kind comments. I also thank Pr. Marco Lovera for presiding the jury, and Dr. Samir Bennani and Jean-Sébastien Schwartz for their interest in this work and for the enriching and insightful discussions.

I am also thankful to Christelle Cumer, head of the AEI research unit at ONERA Toulouse, and Sébastien Changey, head of the GNC group at ISL, for welcoming me in their respective teams, and for their availability.

Special thanks are due to my officemates at the studiously lively "Bureau des doctorants". Cédric, Edouard, Pauline, Gustav, thank you for the advice, the help, and for your inspiring dedication to your own theses. Milo, Sofiane, Waly, William, our delightful discussions on a great variety of topics (humanities, physics, pure maths, highly specific pop culture, the thesis paperwork, to list a few) never failed to entertain and was something to look forward to. Thanks as well to the coffeemates: Sébastien, Valentin, Oktay, Paul, Lucien, Quentin, Arthur, Félix, Clément, Matthias, Damien, Iban, Iryna, Julio, Franca, Guido, Hedwin. Thank you Carsten, Guillaume, Mario, and Philippe, for keeping tabs on us from the other side of the corridor or from upstairs, and thank you Thomas for introducing me to the game of go. I am also thankful to the people who made my short stays at ISL enjoyable: Emmanuel, Gian, Guillaume, Michael, Nadège, Valentin.

To my friends, thank you for cheering for me. To my family, thank you for your endorsement and your support, particularly during this final stretch.

To Raquel, thank you for your unwavering support despite the distance, your uplifting trust, your patience, and for being a primary source of motivation in all aspects of life.

Résumé

Dans le secteur aérospatial, la conception de contrôleurs pour des systèmes évoluant sur un domaine de vol étendu constitue un défi majeur. La dépendance non-linéaire de la dynamique de ces systèmes à des paramètres variant dans le temps, les saturations des actionneurs, et les incertitudes de modélisation comptent parmi les sources de difficulté les plus importantes. Les exigences croissantes en terme de performance et les contraintes de coût associées aux applications industrielles modernes rendent la tâche d'autant plus ardue pour l'ingénieur automaticien, qui doit alors le plus souvent recourir à un processus itératif coûteux. Il existe donc un réel besoin de développer des algorithmes et des outils avancés pour traiter les non-linéarités et les incertitudes, et qui soient applicables à des systèmes aérospatiaux réalistes. Les travaux de thèse s'inscrivent dans ce contexte. L'objectif est de mettre en place une méthodologie pour la conception de lois de contrôle pour des systèmes incertains à paramètres variants, et avec saturation des actionneurs. Pour ce faire, l'idée est d'exploiter et de combiner de manière pertinente le séquencement de gain, la théorie de la commande robuste $\mathcal{H}_\infty$, la synthèse anti-windup, et les méthodes d'analyse de robustesse (μ-analyse et analyse IQC) durant la phase de design. Dans cette optique, la μ-analyse probabiliste fait l'objet de contributions théoriques et algorithmiques qui permettent de mieux répondre aux besoins industriels par rapport à la μ-analyse classique. Le développement de la méthodologie générale s'appuie sur l'étude d'une application aéronautique spécifique, à savoir un concept innovant de projectile guidé gyrostabilisé, caractérisé par de fortes non-linéarités et des couplages dynamiques importants. L'étude de ce système va de la modélisation en boucle ouverte jusqu'aux simulations de Monte Carlo non-linéaires en boucle fermée, illustrant la méthodologie proposée dans un cadre applicatif réaliste.

Abstract

In the aerospace field, a major challenge related to the development of flight control algorithms consists in designing controllers for systems required to operate over a large flight envelope. The challenges stem from multiple factors, among which parameter-dependent nonlinearities, actuator saturations, and model uncertainties feature prominently. Beyond these technical aspects, the task of the control engineer is further complicated by industrial trends. Indeed, applications grow increasingly complex, while being subject to stringent requirements and cost constraints. Hence, control engineers must often resort to a costly iterative process involving controller tuning and simulations. Thus, there is a need for advanced algorithms and tools able to address the aforementioned nonlinearities and uncertainties in an efficient manner, while being applicable to realistic aerospace systems. The thesis takes place in this context. It aims at setting up a methodology for the control design of parameter-varying systems subject to actuator saturations and uncertainties. This is done by integrating elements of gain scheduling, robust $\mathcal{H}_\infty$ control theory, anti-windup synthesis, and robustness μ/IQC-analysis techniques in a cohesive way in the design process. With this goal in mind, theoretical and algorithmic contributions to probabilistic μ-analysis are proposed, bringing μ-analysis closer to industrial needs. Further motivating this work, a specific aeronautic application is considered, namely a novel guided dual-spin projectile concept, steered by four independently actuated canards. This class of systems is characterised by highly nonlinear and coupled dynamics, making control design challenging. The system is studied starting from the open-loop flight dynamics modelling, to nonlinear Monte Carlo closed-loop simulations for autopilot performance evaluation, allowing to illustrate the proposed control design methodology in a realistic context.

Contents

List of Figures

List of Tables

Publications

Journal papers

Thai, S., Theodoulis, S., Roos, C., and Biannic, J.-M. (2022). "Design of a gain scheduled autopilot with anti-windup compensation for a guided projectile". In: *Journal of Guidance, Control, and Dynamics*. Submitted.

Conference papers

Thai, S., Roos, C., and Biannic, J.-M. (2019a). "Probabilistic μ-analysis for stability and H_∞ performance verification". In: *2019 American Control Conference (ACC)*. IEEE.

Thai, S., Theodoulis, S., Roos, C., and Biannic, J.-M. (2019b). "Robust design for the roll-channel autopilot of a canard-guided dual-spin projectile". In: *IFAC-PapersOnLine* 52.12, pp. 232–237.

Thai, S., Theodoulis, S., Roos, C., and Biannic, J.-M. (2021). "An interpolated model recovery anti-windup for a canard-guided projectile subject to uncertainties". In: *2021 European Control Conference (ECC)*. IEEE.

Thai, S., Theodoulis, S., Roos, C., Biannic, J.-M., and Proff, M. (2020). "Gain-scheduled autopilot design with anti-windup compensator for a dual-spin canard-guided projectile". In: *2020 IEEE Conference on Control Technology and Applications (CCTA)*. IEEE.

Chapter 1

Introduction

Contents

1.1 Context of the thesis

In the aerospace field, a major challenge related to the development of flight control algorithms consists in designing controllers for systems required to operate over a large flight envelope. The difficulties related to this task stem from multiple factors. First, most aerospace systems such as aircraft, missiles, or space launchers, feature parameter-dependent nonlinear dynamics. In response, controller design should take parameter variations into account to achieve satisfactory closed-loop dynamics under all operating conditions. Another frequent source of nonlinearity is actuator saturations. These constraints on the control signals may stem both from mechanical limitations, and from aerodynamic model validity considerations. If left unchecked, saturations can lead to severe performance loss, or even flight instability. Finally, most control design methods rely on a model of the system to control. Since differences between the real physical system and its mathematical model are unavoidable in practice, there is a need to assess robustness against model uncertainties and neglected dynamics.

Beyond these technical aspects, the task of the control engineer is further complicated by industrial trends. Indeed, applications grow increasingly complex, while being subject to stringent requirements and cost constraints. Hence, control engineers must resort to a costly iterative process involving controller tuning and simulations. A solution to lighten this process is to develop advanced algorithms and tools directly addressing the aforementioned nonlinearities and uncertainties, and to integrate them in the design methodology.

1.2 Dealing with parameter variations

A well-known and widely used approach to design controllers taking into account parameter-dependency is the gain scheduling method (see [Leith and Leithead, 2000] and [Rugh and Shamma, 2000] for surveys on the topic). In its most standard form, it consists in performing a Jacobian linearisation of the system at its equilibrium points. The resulting linearised systems are used as the basis to design linear controllers. These controllers are finally interpolated to cover the whole operating domain. Gain scheduling is conceptually simple, and allows the use of the most familiar methods from linear control theory. This includes more advanced methods from robust control theory, such as structured $\mathcal{H}_\infty$ synthesis based on nonsmooth optimisation [Apkarian and Noll, 2006]. All this contributes to the appeal of gain scheduling. On the other hand, it generally provides no guarantee of stability and performance between design points.

An alternative addressing this issue is to use LPV (Linear Parameter-Varying) synthesis, initiated after LPV systems were formally defined in [Shamma and Athans, 1991]. The starting point to this family of methods is either a polytopic model [Apkarian et al., 1995], or an LFT (Linear Fractional Transformation) model [Apkarian and Gahinet, 1995] of the system to control. For a polytopic model, quadratic Lyapunov functions are used to determine sufficient conditions for stability or performance. In the case of an LFT model, sufficient conditions derive from the small gain theorem, applied after using appropriate scaling matrices to reduce conservatism. In both cases, the synthesis problem amounts to solving a linear matrix inequality (LMI) problem, for which solvers are broadly available. In addition, the use of parameter-dependent Lyapunov functions allow to take into account bounds on the rate of variations of the parameters [Wu, 2001; Wu and Dong, 2006]. LPV methods have been used on multiple applications [Hoffmann and Werner, 2014], and the LPVTools software suite is dedicated to their implementation [Hjartarson et al., 2015], attesting to the the ongoing interest and growing maturity of the topic. However, although these methods are able to guarantee global stability and performance, the preliminary modelling step can be quite involved, and the results are potentially conservative. In the case where an LPV model is not available, the more general class of quasi-LPV models may be adequate, but this comes with additional difficulties, such as the appearance of hidden coupling terms.

1.3 Dealing with actuator saturations

Saturations are present in all physical systems, and can cause severe degradation of the system performance. A first strategy to avoid this scenario is to design a controller that will not reach the saturation levels, at the cost of potentially lower performance. Another strategy is to allow saturations to occur, while modifying the closed-loop dynamics to mitigate their detrimental effects. This second approach usually involves a two-step procedure. In a first step, a linear baseline controller is designed and validated as if saturations were absent from the system. The second step addresses saturations by addition of a so-called anti-windup compensator, which only becomes active when saturations occur. For this reason, nominal performance is unaffected as long as saturations are not reached.

Early works on saturated systems and anti-windup design focused on PID controllers [Lozier,

1956; Åström and Rundqwist, 1989]. The topic gained in impetus with the work of [Kothare et al., 1994], where a unifying framework was formulated, encompassing many previously proposed compensation schemes, and inspired by the standard form from robust control theory. Modern anti-windup theory, as described for instance in [Galeani et al., 2009; Tarbouriech et al., 2011; Zaccarian and Teel, 2011], identifies two families of methods for anti-windup design: Direct Linear Anti-Windup (DLAW), and Model Recovery Anti-Windup (MRAW). The DLAW approach relies on Lyapunov stability theory and modified sector conditions from [Gomes da Silva and Tarbouriech, 2005] to express the anti-windup design problem as a bilinear matrix inequality (BMI) problem. With some additional assumptions on the anti-windup dynamics, the problem becomes convex, and its resolution yields the state-space matrices for an anti-windup compensator. The MRAW approach embeds the plant dynamics into the anti-windup dynamics to track the mismatch with respect to the unconstrained model. The anti-windup output signal then aims to minimise this mismatch in an attempt to recover the unconstrained response.

1.4 Dealing with uncertainties

Robustness analysis is a necessary part of the design process to ensure that closed-loop behaviour remains satisfactory in a sufficiently large neighbourhood of the nominal configuration. The industrial standard for evaluating robustness is the Monte Carlo approach [Helton et al., 2006; Landau and Binder, 2014]. The idea is to perform time-domain simulations on a large number of uncertainty samples, and to do a statistical analysis of the results. While relatively easy to implement, this approach suffers from several drawbacks. Due to the random nature of the samples, worst-case configurations may be missed, and only soft bounds on the system performance are obtained. Moreover, a large number of samples is needed to guarantee the accuracy and confidence level of the statistical result. As the computational effort to run a time-domain simulation can be significant, this makes the validation process costly.

On the other hand, deterministic methods aim to guarantee the detection of worst-cases. In the case of a linear system subject to LTI (Linear Time Invariant) uncertainties, a measure of robustness is provided by the structured singular value μ, which was introduced by [Doyle, 1982]. In fact, the associated μ-analysis framework proves quite flexible, and is able to evaluate the robustness of other criteria beyond stability, such as $\mathcal{H}_\infty$ worst-case performance [Fan and Tits, 1992], or worst-case margins [Lescher and Roos, 2011]. While the computation of the structured singular value was established to be NP-hard in [Braatz et al., 1994], a lot of research has been done to develop algorithms providing tight bounds [Roos and Biannic, 2015; Lesprier et al., 2015], so that μ-analysis is now recognised as a mature tool by the control community. However, it still has some shortcomings which prevent it from becoming an industrial standard. Most notably, no measure of the likelihood of the detected worst-cases is provided. This can lead to an undesirable outcome where controllers are invalidated on the basis of unrealistic or conservative scenarios.

In the presence of nonlinearities, such as actuator saturations, robustness analysis can be conducted using integral quadratic constraints (IQC). This framework, which was introduced by [Megretski and Rantzer, 1997], involves the search for a multiplier simultaneously describing the uncertainties and nonlinearities and satisfying an infinity of frequency-domain inequalities (FDI). Using the Kalman-Yakubovich-Popov (KYP) lemma allows to replace the infinite set of FDI by

an equivalent LMI. The numerous works on IQC theory provide multipliers for a wide variety of uncertainties and nonlinearities (see e.g. [Veenman et al., 2016; Fetzer and Scherer, 2017]), making it a flexible approach. However, conservatism and computational complexity remain recurring issues.

1.5 Overview of the contributions

It is clear from the above that all of the described topics gave rise to dedicated research, with a lot of development still ongoing in each of them. However, from the perspective of the control engineer, these are all parts of the same control design problem. When integrating some of the above advanced methods in the design, care should be taken that each step (modelling, controller and anti-windup synthesis, robustness analysis, simulations) interacts smoothly with the others, so as to facilitate iterations.

This thesis takes place in this context. It aims at setting up a generic methodology for the preliminary control design of a parameter-varying aerospace system subject to actuator saturations and uncertainties by exploiting some of the previously reviewed methods. Further motivating this study, a specific aeronautic application is considered, namely a novel guided dual-spin projectile concept, steered by four independently actuated canards. This class of systems is characterised by highly nonlinear and coupled dynamics, making control design challenging.

It is worth emphasising that literature on control theory applied to guided projectiles remains scarce. Several ad hoc open-loop algorithms based on trajectory tracking or impact point prediction [Fresconi, 2011] have been investigated for a wealth of steering mechanisms, but these approaches fail to handle aerodynamic uncertainties in a satisfying manner. Regarding the dual-spin configuration, the first full nonlinear model was published in [Costello and Peterson, 2000] for an unguided projectile, while early results on the control of such systems based on trajectory tracking can be found in [Gagnon and Lauzon, 2007; Gagnon and Lauzon, 2008]. Recent ISL studies [Theodoulis et al., 2015; Sève et al., 2017b; Sève et al., 2017a] developed linearisation algorithms specific to dual-spin projectiles, as well as efficient gain scheduled autopilots based on local $\mathcal{H}_\infty$ syntheses for canards acting in pairs. In line with these developments, the present study uses a slightly different steering mechanism where all three axes of the projectile are aerodynamically controlled using the canards, and extends the existing work in several ways:

- the gain scheduling methodology is revisited to involve less tedious tuning, both for the roll channel and for the pitch/yaw channels;

- theoretical contributions to probabilistic μ-analysis are proposed, allowing for a more in-depth local robustness analysis, and bringing μ-analysis closer to industrial needs;

- anti-windup compensators to address canard saturations are proposed for the first time, accompanied with IQC analysis to evaluate robustness against aerodynamic uncertainties, and simulations.

1.6 Thesis outline

The manuscript is organised as follows:

- Chapter 2 sets up the model of the projectile airframe that will be used to tackle the control problems. To do so, a nonlinear model stemming from flight mechanics is first developed. This model is subsequently linearised and decomposed into an LPV system for the roll channel, and a quasi-LPV system for the pitch/yaw channels. Finally, the linearised models are complemented with actuator and sensor models, and with model uncertainties, in anticipation of closed-loop robustness analysis.

- The obtained models are used in Chapter 3 to design a baseline autopilot, which does not take saturations into account. Local controllers are computed using structured $\mathcal{H}_\infty$ synthesis under a mixed-sensitivity approach. Several measures of robustness are then evaluated at the design points. In particular, a probabilistic extension to μ-analysis is used to evaluate the probability of $\mathcal{H}_\infty$ performance and margins, for a given probability distribution of the aerodynamic uncertainties. It is shown that this approach can greatly contribute to reducing the conservatism of standard μ-analysis, and complements Monte Carlo methods nicely. The autopilot for the roll channel was presented in [Thai et al., 2019b], while early results on probabilistic μ-analysis were presented in [Thai et al., 2019a].

- Chapter 4 deals with anti-windup design, and starts with reminders of theoretical elements related to the study of saturated systems. This includes stability and performance analysis using quadratic Lyapunov functions and sector conditions, anti-windup synthesis using the DLAW and MRAW frameworks, and robustness analysis using IQCs. The anti-windup design step for the pitch/yaw channels of the guided projectile is then presented, where three different methods are considered for local syntheses. The resulting augmented closed-loops are then evaluated and compared through time-domain simulations and IQC analysis. These contributions were presented in [Thai et al., 2020] and [Thai et al., 2021].

- In Chapter 5, complete guided flight scenarios are simulated to evaluate the control design. These scenarios include trajectories affected by a wind disturbance, perturbed launch conditions, or aerodynamic uncertainties. Simulations with deactivated saturations are first conducted both to validate the baseline autopilot and to identify the conditions under which saturation levels are reached. The improvements brought by the proposed anti-windup compensators are then evaluated on the scenarios where saturations occur.

- Finally, Chapter 6 summarises the main contributions of the thesis, and perspectives for further work are discussed.

References

Apkarian, P. and Gahinet, P. (1995). “A convex characterization of gain-scheduled H_∞ controllers”. In: *IEEE Transactions on Automatic Control* 40.5, pp. 853–864.

Apkarian, P. and Noll, D. (2006). “Nonsmooth H_∞ Synthesis”. In: *IEEE Transactions on Automatic Control* 51.1, pp. 71–86.

Apkarian, P., Gahinet, P., and Becker, G. (1995). "Self-scheduled H_∞ control of linear parameter-varying systems: a design example". In: *Automatica* 31.9, pp. 1251–1261.

Åström, K. J. and Rundqwist, L. (1989). "Integrator windup and how to avoid it". In: *1989 American Control Conference*. IEEE.

Braatz, R. P., Young, P. M., Doyle, J. C., and Morari, M. (1994). "Computational complexity of μ calculation". In: *IEEE Transactions on Automatic Control* 39.5, pp. 1000–1002.

Costello, M. and Peterson, A. (2000). "Linear theory of a dual-spin projectile in atmospheric flight". In: *Journal of Guidance, Control, and Dynamics* 23.5, pp. 789–797.

Doyle, J. (1982). "Analysis of feedback systems with structured uncertainties". In: *IEE Proceedings D Control Theory and Applications* 129.6, p. 242.

Fan, M. K. H. and Tits, A. L. (1992). "A measure of worst-case H_∞ performance and of largest acceptable uncertainty". In: *Systems & Control Letters* 18.6, pp. 409–421.

Fetzer, M. and Scherer, C. W. (2017). "Full-block multipliers for repeated, slope-restricted scalar nonlinearities". In: *International Journal of Robust and Nonlinear Control* 27.17, pp. 3376–3411.

Fresconi, F. (2011). "Guidance and control of a projectile with reduced sensor and actuator requirements". In: *Journal of Guidance, Control, and Dynamics* 34.6, pp. 1757–1766.

Gagnon, E. and Lauzon, M. (2007). "Maneuverability analysis of the conventional 155 mm gunnery projectile". In: *AIAA Guidance, Navigation and Control Conference and Exhibit*. American Institute of Aeronautics and Astronautics.

Gagnon, E. and Lauzon, M. (2008). "Course correction fuze concept analysis for in-service 155 mm spin-stabilized gunnery projectiles". In: *AIAA Guidance, Navigation and Control Conference and Exhibit*. American Institute of Aeronautics and Astronautics.

Galeani, S., Tarbouriech, S., Turner, M., and Zaccarian, L. (2009). "A Tutorial on Modern Anti-windup Design". In: *European Journal of Control* 15.3-4, pp. 418–440.

Gomes da Silva, J. M. and Tarbouriech, S. (2005). "Antiwindup design with guaranteed regions of stability: an LMI-based approach". In: *IEEE Transactions on Automatic Control* 50.1, pp. 106–111.

Helton, J. C., Johnson, J. D., Sallaberry, C. J., and Storlie, C. B. (2006). "Survey of sampling-based methods for uncertainty and sensitivity analysis". In: *Reliability Engineering & System Safety* 91.10-11, pp. 1175–1209.

Hjartarson, A., Seiler, P., and Packard, A. (2015). "LPVTools: A Toolbox for Modeling, Analysis, and Synthesis of Parameter Varying Control Systems". In: *IFAC-PapersOnLine* 48.26, pp. 139–145.

Hoffmann, C. and Werner, H. (2014). "A survey of linear parameter-varying control applications validated by experiments or high-fidelity simulations". In: *IEEE Transactions on Control Systems Technology* 23.2, pp. 416–433.

Kothare, M. V., Campo, P. J., Morari, M., and Nett, C. N. (1994). "A unified framework for the study of anti-windup designs". In: *Automatica* 30.12, pp. 1869–1883.

Landau, D. P. and Binder, K. (2014). *A guide to Monte Carlo simulations in statistical physics*. Cambridge university press.

Leith, D. J. and Leithead, W. E. (2000). "Survey of gain-scheduling analysis and design". In: *International Journal of Control* 73.11, pp. 1001–1025.

Lescher, F. and Roos, C. (2011). "Robust stability of time-delay systems with structured uncertainties: a μ-analysis based algorithm". In: *50th IEEE Conference on Decision and Control and European Control Conference*. IEEE.

Lesprier, J., Roos, C., and Biannic, J.-M. (2015). "Improved μ upper bound computation using the μ-sensitivities". In: *IFAC-PapersOnLine* 48.14, pp. 215–220.

Lozier, J. (1956). "A steady state approach to the theory of saturable servo systems". In: *IRE Transactions on Automatic Control* 1.1, pp. 19–39.

Megretski, A. and Rantzer, A. (1997). "System analysis via integral quadratic constraints". In: *IEEE Transactions on Automatic Control* 42.6, pp. 819–830.

Roos, C. and Biannic, J.-M. (2015). "A detailed comparative analysis of all practical algorithms to compute lower bounds on the structured singular value". In: *Control Engineering Practice* 44, pp. 219–230.

Rugh, W. J. and Shamma, J. S. (2000). "Research on gain scheduling". In: *Automatica* 36.10, pp. 1401–1425.

Sève, F., Theodoulis, S., Wernert, P., Zasadzinski, M., and Boutayeb, M. (2017a). "Flight dynamics modeling of dual-spin guided projectiles". In: *IEEE Transactions on Aerospace and Electronic Systems* 53.4, pp. 1625–1641.

Sève, F., Theodoulis, S., Wernert, P., Zasadzinski, M., and Boutayeb, M. (2017b). "Gain-scheduled H_∞ loop-shaping autopilot design for spin-stabilized canard-guided projectiles". In: *AerospaceLab Journal* Issue 13, December 2017, ISSN: 2107–6596.

Shamma, J. S. and Athans, M. (1991). "Guaranteed properties of gain scheduled control for linear parameter-varying plants". In: *Automatica* 27.3, pp. 559–564.

Tarbouriech, S., Garcia, G., Gomes da Silva, J. M., and Queinnec, I. (2011). *Stability and stabilization of linear systems with saturating actuators*. Springer London.

Thai, S., Roos, C., and Biannic, J.-M. (2019a). "Probabilistic μ-analysis for stability and H_∞ performance verification". In: *2019 American Control Conference (ACC)*. IEEE.

Thai, S., Theodoulis, S., Roos, C., and Biannic, J.-M. (2019b). "Robust design for the roll-channel autopilot of a canard-guided dual-spin projectile". In: *IFAC-PapersOnLine* 52.12, pp. 232–237.

Thai, S., Theodoulis, S., Roos, C., and Biannic, J.-M. (2021). "An interpolated model recovery anti-windup for a canard-guided projectile subject to uncertainties". In: *2021 European Control Conference (ECC)*. IEEE.

Thai, S., Theodoulis, S., Roos, C., Biannic, J.-M., and Proff, M. (2020). "Gain-scheduled autopilot design with anti-windup compensator for a dual-spin canard-guided projectile". In: *2020 IEEE Conference on Control Technology and Applications (CCTA)*. IEEE.

Theodoulis, S., Sève, F., and Wernert, P. (2015). "Robust gain-scheduled autopilot design for spin-stabilized projectiles with a course-correction fuze". In: *Aerospace Science and Technology* 42, pp. 477–489.

Veenman, J., Scherer, C. W., and Köroğlu, H. (2016). "Robust stability and performance analysis based on integral quadratic constraints". In: *European Journal of Control* 31, pp. 1–32.

Wu, F. (2001). “A generalized LPV system analysis and control synthesis framework”. In: *International Journal of Control* 74.7, pp. 745–759.

Wu, F. and Dong, K. (2006). “Gain-scheduling control of LFT systems using parameter-dependent Lyapunov functions”. In: *Automatica* 42.1, pp. 39–50.

Zaccarian, L. and Teel, A. R. (2011). *Modern Anti-windup Synthesis: Control Augmentation for Actuator Saturation*. Princeton University Press.

Chapter 2

Modelling of a 7-degree of freedom guided projectile

Contents

2.1 Introduction

Standard ballistic projectiles suffer from a lack of accuracy, due to various factors such as incorrect launch conditions or wind perturbations. As a consequence, multiple rounds must typically be fired to intercept a single target. This leads to significant risks of collateral damage, high deployment and operational costs, and logistical concerns. Guided projectiles aim to overcome these limitations. Among the numerous guided projectile concepts, that of a course

correction fuse (CCF) decoupled from the body and equipped with canards is particularly attractive, as it can then be used to retrofit older projectiles. This economic solution leads to a dual-spin guided projectile with seven degrees of freedom (7DoF), whose precision and performance are then highly dependent on the embedded hardware and flight control algorithms. In turn, the development of flight control algorithms relies on a mathematical model of the system to control. This model must be a sufficiently accurate description of the behaviour of the system, while also being compatible with control design methods.

This chapter sets up a model of the projectile open-loop that will be used to undertake the design of a gain scheduled controller. It is organised as follows. Section 2.2 introduces the studied guided projectile concept. Section 2.3 starts by defining the reference frames and coordinate systems that will be used to describe the airframe behaviour. A nonlinear model using first principles from flight mechanics is then derived. This model is used as a ballistic trajectory simulator, which is useful to plot the evolution of state variables or efforts, or to establish the flight envelope of the projectile. In Section 2.4, a linearisation process is applied to obtain models that can be used for the design of a gain scheduled autopilot. Finally, the linearised airframe models are completed with actuator and sensor models described in Section 2.5, and with model uncertainties described in Section 2.6, providing the basis for both controller synthesis and robustness analysis.

2.2 Presentation of the guided projectile concept

The guided projectile concept studied in this thesis is a dual-spin projectile consisting of a standard 155 mm ammunition retrofitted with a roll-decoupled fuse. The body, or aft part, contains the explosive payload. The fuse, or forward part, is equipped with four canards, as shown in Figure 2.1, which are independently actuated. The fuse also embeds GNC hardware and software.

This concept has numerous advantages over other steering mechanisms proposed in the literature on guided projectiles. Unlike impulse jet thrusters [Jitpraphai and Costello, 2001; Burchett et al., 2002; Davis et al., 2009; Hahn et al., 2009] or inertial loads [Frost and Costello, 2006; Rogers and Costello, 2009; Cooper and Costello, 2011], aerodynamic surfaces provide a correction which can be modelled in continuous time as aerodynamic effects. Moreover, the resulting guided projectile shows some similarities to missiles, whose associated control problem has been extensively studied [Wise, 1990; Shamma and Cloutier, 1993; Wise and Roy, 1998; Biannic and Apkarian, 1999; Pellanda et al., 2002; Mracek and Ridgely, 2005; White et al., 2007]. Additional benefits of the dual-spin configuration, as opposed to fin-stabilised projectiles, are the capability to retrofit existing unguided shells, thus greatly reducing development costs, and a greater range due to the lack of stabilising surfaces [Theodoulis and Wernert, 2017].

The flight scenario of the studied projectile can be broken into several phases, depicted in Figure 2.2. In the first one, electronic components are switched on. This is done after launch to avoid possible hardware degradations due to the harsh initial conditions. Then roll control is initiated to stabilise the fuse, which at this point has a large spin velocity caused by the mechanical bearing between the two parts of the projectile. Finally, the projectile enters its guided phase, during which additional efforts on the pitch and yaw axes are generated by the

canards to alter its trajectory. The CCF concept considered here differs from [Theodoulis et al., 2013] and [Sève et al., 2017a], where a coaxial motor dedicated to roll control is included. Instead, all three axes are aerodynamically controlled using the canards.

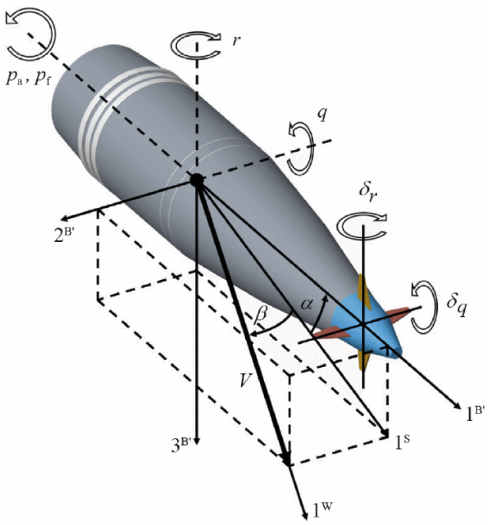

Figure 2.1: 155 mm projectile with a course correction fuse equipped with canards

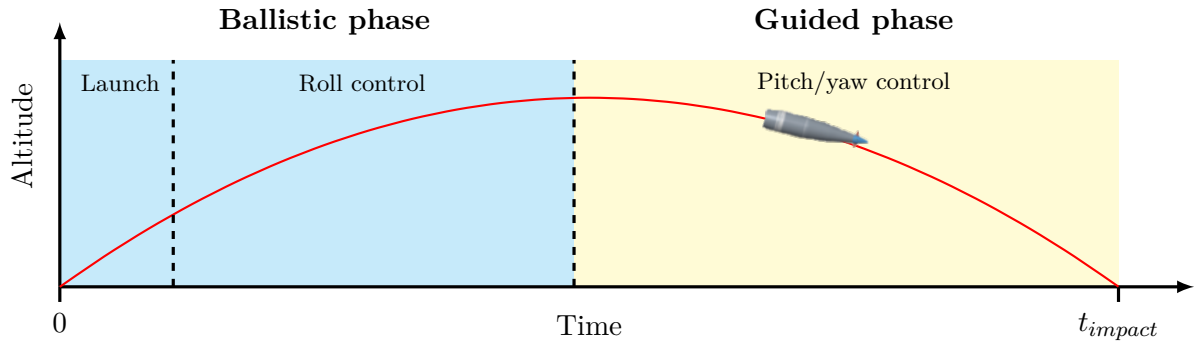

Figure 2.2: Standard flight scenario of a canard-guided dual-spin projectile

2.3 Nonlinear modelling using flight mechanics

2.3.1 Reference frames and coordinate systems

A preliminary step to the development of the equations of motion is to define a set of reference frames and coordinate systems. As emphasised in [Zipfel, 2007], the two notions are distinct yet frequently taken to be the same. A reference frame can be viewed as a fictitious body, and it is entirely defined by an origin point together with three orthonormal base vectors. Reference frames are used to establish symbolic equations which are valid independently of the choice of coordinate systems in the context of tensor-based flight dynamics. On the other hand, coordinate systems allow to express these symbolic equations numerically. While an infinity of coordinate systems can be associated with a reference frame R, a natural choice, called the preferred coordinate system and denoted $]^R$, is to use the orthonormal vectors of the frame as a basis. The following frames are defined:

- The Earth frame E has its origin at the projectile launch point. It is considered to be inertial, given the distances and durations brought into play in the studied system, and is thus used to apply Newton's and Euler's laws of motions. A flat-Earth assumption is adopted, so that the three basis vectors $(\boldsymbol{e}_1, \boldsymbol{e}_2, \boldsymbol{e}_3)$ point respectively towards the North, the East, and downward. The coordinate system associated to these vectors is called the local-level (also North-East-Down) coordinate system, and noted $]^L$.

- The body frame B follows the movements of the projectile. Its origin is located at the centre of mass of the projectile. Its three basis vectors $(\boldsymbol{b}_1, \boldsymbol{b}_2, \boldsymbol{b}_3)$ are associated respectively to the longitudinal, lateral, and normal axes of the projectile, with $\boldsymbol{b}_1$ pointing forward. The vector $\boldsymbol{b}_2$ is perpendicular to $\boldsymbol{b}_1$, horizontal before launch, i.e. contained in the plane defined by the vectors $(\boldsymbol{e}_1, \boldsymbol{e}_2)$, and pointing to the right when looking at the projectile from behind. The vector $\boldsymbol{b}_3$ completes the orthonormal frame according to the right-hand rule and points down. Finally, the vectors $\boldsymbol{b}_2$ and $\boldsymbol{b}_3$ spin along with the projectile body.

- The body-fixed-roll (BFR) frame B' follows the movements of the projectile save for its rolling motion. Its origin is located at the centre of mass of the projectile and its first basis vector $\boldsymbol{b}'_1$ is equal to $\boldsymbol{b}_1$. Before launch, the vector $\boldsymbol{b}'_2$ coincides with $\boldsymbol{b}_2$, but unlike the latter, $\boldsymbol{b}'_2$ remains horizontal and pointing to the right for the whole flight. The vector $\boldsymbol{b}'_3$ completes the orthonormal frame according to the right-hand rule. The BFR is introduced because the coordinate system $]^B$ associated to the body frame is ill-suited for simulation of a dual-spin projectile. Indeed, expressing the equations of motion in $]^B$ leads to dynamics that are dependent on the body roll angle. Due to its fast variations, simulating the system would then require very small integration steps, thus lengthening simulation time and introducing numerical errors. The use of the coordinate system $]^{B'}$ overcomes this issue [Wernert et al., 2010].

- The atmospheric frame A has its origin located at an arbitrary point in the air. As the associated preferred coordinate system $]^A$ will not be used, the orthonormal vectors are of no relevance. This frame is nevertheless useful because it allows to define variables (airspeed and aerodynamic angles) that are tied to the aerodynamic forces and moments applied on the projectile.

When studying the motion of an object, it is useful to be able to go from one coordinate system to another. This is achieved by means of rotation matrices. As is standard in aerospace applications, we favour the yaw, pitch, and roll angles to describe these rotations. Thus the rotation matrix to go from $]^L$ to $]^B$ is given by:

$$
\begin{aligned}
[\boldsymbol{T}]^{BL} &= \begin{bmatrix} 1 & 0 & 0 \\ 0 & \cos\phi_a & \sin\phi_a \\ 0 & -\sin\phi_a & \cos\phi_a \end{bmatrix} \begin{bmatrix} \cos\theta & 0 & -\sin\theta \\ 0 & 1 & 0 \\ \sin\theta & 0 & \cos\theta \end{bmatrix} \begin{bmatrix} \cos\psi & \sin\psi & 0 \\ -\sin\psi & \cos\psi & 0 \\ 0 & 0 & 1 \end{bmatrix} \\
&= \begin{bmatrix} \cos\psi\cos\theta & \sin\psi\cos\theta & -\sin\theta \\ \cos\psi\sin\theta\sin\phi_a - \sin\psi\cos\phi_a & \sin\psi\sin\theta\sin\phi_a + \cos\psi\cos\phi_a & \cos\theta\sin\phi_a \\ \cos\psi\sin\theta\cos\phi_a + \sin\psi\sin\phi_a & \sin\psi\sin\theta\cos\phi_a - \cos\psi\sin\phi_a & \cos\theta\cos\phi_a \end{bmatrix}
\end{aligned}
\tag{2.1}
$$

with (ϕ_a, θ, ψ) the roll, pitch, and yaw angles of the projectile body. Note that due to the dual-spin configuration, the body roll angle ϕ_a is distinct from the fuse roll angle, noted ϕ_f. More generally, the subscripts $\bullet_a$ and $\bullet_f$ will be used to denote the aft and forward parts respectively.

The frame B' shares its pitch and yaw angles with B but has zero roll angle. Hence the rotation matrix from $]^L$ to $]^{B'}$ reduces to:

$$[\boldsymbol{T}]^{B'L} = \begin{bmatrix} \cos\psi\cos\theta & \sin\psi\cos\theta & -\sin\theta \\ -\sin\psi & \cos\psi & 0 \\ \cos\psi\sin\theta & \sin\psi\sin\theta & \cos\theta \end{bmatrix} \tag{2.2}$$

2.3.2 Nonlinear dynamic and kinematic equations

The 7DoF airframe model is described by its translational and attitude dynamic equations, given respectively by Newton's and Euler's laws of motions. These are expressed in the coordinate system $]^{B'}$ as:

$$m\left[\frac{d\boldsymbol{v}_B^E}{dt}\right]^{B'} + m\left[\boldsymbol{\Omega}^{B'E}\right]^{B'}\left[\boldsymbol{v}_B^E\right]^{B'} = [\boldsymbol{f}_B]^{B'} \tag{2.3}$$

$$\left[\boldsymbol{I}_B^B\right]^{B'}\left[\frac{d\boldsymbol{\omega}_{aug}^{BE}}{dt}\right]^{B'} + \left[\boldsymbol{\Omega}_{aug}^{B'E}\right]^{B'}\left[\boldsymbol{I}_B^B\right]^{B'}\left[\boldsymbol{\omega}_{aug}^{BE}\right]^{B'} = [\boldsymbol{m}_B]^{B'} \tag{2.4}$$

where:

- $\left[\boldsymbol{v}_B^E\right]^{B'} = [u\ v\ w]^T$ is the linear velocity of the projectile centre of mass with respect to the Earth and expressed in $]^{B'}$,
- $\left[\boldsymbol{\omega}_{aug}^{BE}\right]^{B'} = [p_f\ p_a\ q\ r]^T$ is the angular velocity of the projectile body and fuse with respect to the Earth, expressed in $]^{B'}$,
- $\left[\boldsymbol{\Omega}^{B'E}\right]^{B'}$ is the angular velocity tensor, which is a skew-symmetric matrix used to write the cross product $\left[\boldsymbol{\omega}^{B'E}\right]^{B'} \times \left[\boldsymbol{v}_B^E\right]^{B'}$ as the equivalent matrix multiplication $\left[\boldsymbol{\Omega}^{B'E}\right]^{B'}\left[\boldsymbol{v}_B^E\right]^{B'}$, and $\left[\boldsymbol{\Omega}_{aug}^{B'E}\right]^{B'}$ is an augmented version adapted to the additional degree of freedom brought by the decoupling of the fuse,
- $[\boldsymbol{f}_B]^{B'} = [X\ Y\ Z]^T$ and $[\boldsymbol{m}_B]^{B'} = [L_f\ L_a\ M\ N]^T$ are the external forces and moments applied to the projectile,
- m is the mass of the projectile, and $\left[\boldsymbol{I}_B^B\right]^{B'} = \mathrm{diag}(I_{xf}, I_{xa}, I_t, I_t)$ is the moment of inertia, which is diagonal due to the projectile geometry.

Noting $\left[\boldsymbol{\omega}^{B'E}\right]^{B'} = [p'\ q'\ r']^T$, we have by definition of the BFR that $q' = q$ and $r' = r$. Kinematic relations allow to show that (see e.g. [Wernert et al., 2010]):

$$p' = -r\tan\theta \tag{2.5}$$

and consequently, the angular velocity tensors are given by:

$$\left[\boldsymbol{\Omega}^{B'E}\right]^{B'} = \begin{bmatrix} 0 & -r & q \\ r & 0 & r\tan\theta \\ -q & -r\tan\theta & 0 \end{bmatrix} \text{ and } \left[\boldsymbol{\Omega}_{aug}^{B'E}\right]^{B'} = \begin{bmatrix} 0 & 0 & -r & q \\ 0 & 0 & -r & q \\ 0 & r & 0 & r\tan\theta \\ 0 & -q & -r\tan\theta & 0 \end{bmatrix} \tag{2.6}$$

Expanding Equations (2.3) and (2.4) using the coordinates then leads to:

$$\begin{bmatrix} \dot{u} \\ \dot{v} \\ \dot{w} \end{bmatrix} = \frac{1}{m}\begin{bmatrix} X \\ Y \\ Z \end{bmatrix} - \begin{bmatrix} 0 & -r & q \\ r & 0 & r\tan\theta \\ -q & -r\tan\theta & 0 \end{bmatrix}\begin{bmatrix} u \\ v \\ w \end{bmatrix} \tag{2.7}$$

$$\begin{bmatrix} \dot{p}_f \\ \dot{p}_a \\ \dot{q} \\ \dot{r} \end{bmatrix} = \begin{bmatrix} L_f/I_{xf} \\ L_a/I_{xa} \\ M/I_t \\ N/I_t \end{bmatrix} + \begin{bmatrix} 0 \\ 0 \\ -(I_{xa}{I_t}^{-1}p_a + r\tan\theta)r \\ (I_{xa}{I_t}^{-1}p_a + r\tan\theta)q \end{bmatrix} \tag{2.8}$$

Complementing these equations are the translational and attitude kinematic equations, which describe the linear and angular positions $[x_e\ y_e\ z_e]^T$ and $[\phi_f\ \phi_a\ \theta\ \psi]^T$ with respect to the inertial Earth frame [Zipfel, 2007]. The translational kinematic equation is a mere change of coordinate system from $]^{B'}$ to $]^L$, thus involving the transpose of the rotation matrix $[\boldsymbol{T}]^{B'L}$:

$$\begin{bmatrix} \dot{x}_e \\ \dot{y}_e \\ \dot{z}_e \end{bmatrix} = \begin{bmatrix} \cos\psi\cos\theta & -\sin\psi & \cos\psi\sin\theta \\ \sin\psi\cos\theta & \cos\psi & \sin\psi\sin\theta \\ -\sin\theta & 0 & \cos\theta \end{bmatrix}\begin{bmatrix} u \\ v \\ w \end{bmatrix} \tag{2.9}$$

Finally, the attitude kinematic equation expresses the relationship between the Euler angles and the angular rate vector:

$$\begin{bmatrix} p_f \\ p_a \\ q \\ r \end{bmatrix} = \begin{bmatrix} 1 & 0 & 0 & -\sin\theta \\ 0 & 1 & 0 & -\sin\theta \\ 0 & 0 & 1 & 0 \\ 0 & 0 & 0 & \cos\theta \end{bmatrix}\begin{bmatrix} \dot{\phi}_f \\ \dot{\phi}_a \\ \dot{\theta} \\ \dot{\psi} \end{bmatrix} \tag{2.10}$$

After inversion, we obtain:

$$\begin{bmatrix} \dot{\phi}_f \\ \dot{\phi}_a \\ \dot{\theta} \\ \dot{\psi} \end{bmatrix} = \begin{bmatrix} 1 & 0 & 0 & \tan\theta \\ 0 & 1 & 0 & \tan\theta \\ 0 & 0 & 1 & 0 \\ 0 & 0 & 0 & 1/\cos\theta \end{bmatrix}\begin{bmatrix} p_f \\ p_a \\ q \\ r \end{bmatrix} \tag{2.11}$$

Remark 1. *The singularity at $\theta = \pm 90\,\text{deg}$ does not need to be treated since the corresponding configuration does not occur in practice for a projectile. Thus the use of quaternions is not necessary for this system.*

The benefits of using the BFR, which were already mentioned in Section 2.3.1, appear through

the absence of the body roll angle ϕ_a in the right-hand side of Equations (2.7), (2.8), (2.9), and (2.11).

2.3.3 Aerodynamic variables

The most important efforts applied on the projectile are aerodynamic in nature. That is, they are caused by the motion of the projectile relative to the atmosphere. For this reason, aerodynamic variables are more useful than the linear velocities, both as state variables and to describe the forces and moments. Noting $\left[\boldsymbol{v}_B^A\right]^{B'} = [u_A\ v_A\ w_A]^T$ the velocity of the projectile with respect to the atmosphere expressed in $]^{B'}$, and $\left[\boldsymbol{v}_A^E\right]^{B'} = [u_W\ v_W\ w_W]^T$ the wind, we have: $\left[\boldsymbol{v}_B^A\right]^{B'} = \left[\boldsymbol{v}_B^E\right]^{B'} - \left[\boldsymbol{v}_A^E\right]^{B'}$, i.e.

$$\left[\boldsymbol{v}_B^A\right]^{B'} = \begin{bmatrix} u_A \\ v_A \\ w_A \end{bmatrix} = \begin{bmatrix} u - u_W \\ v - v_W \\ w - w_W \end{bmatrix} \tag{2.12}$$

We then define:

- the airspeed V, which is the norm of $\left[\boldsymbol{v}_B^A\right]^{B'}$:

$$V = \sqrt{u_A^2 + v_A^2 + w_A^2} \tag{2.13}$$

- the angle of attack (AoA) α, angle of sideslip (AoS) β, and angle of incidence (AoI) α':

$$\alpha = \arctan\left(\frac{w_A}{u_A}\right) \tag{2.14}$$

$$\beta = \arcsin\left(\frac{v_A}{V}\right) \tag{2.15}$$

$$\alpha' = \arccos\left(\frac{u_A}{V}\right) = \arccos(\cos\alpha\cos\beta) \tag{2.16}$$

The geometric interpretation of the aerodynamic angles is given in Figure 2.3. These relationships can be inverted to obtain expressions of the velocities:

$$u_A = V\cos\alpha\cos\beta \tag{2.17}$$

$$v_A = V\sin\beta \tag{2.18}$$

$$w_A = V\sin\alpha\cos\beta \tag{2.19}$$

Differentiation of Equations (2.13)-(2.15) yields nonlinear dynamic equations of the aerody-

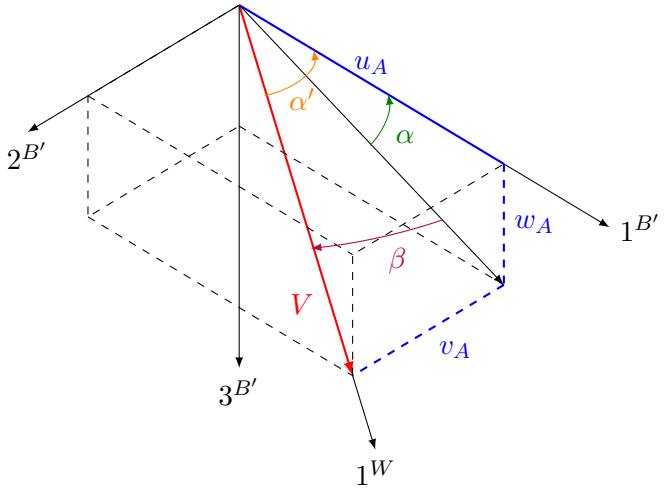

Figure 2.3: Geometric interpretation of the aerodynamic variables

namic variables:

$$\dot{V} = \frac{u_A \dot{u}_A + v_A \dot{v}_A + w_A \dot{w}_A}{V} \tag{2.20}$$

$$\dot{\alpha} = \frac{u_A \dot{w}_A - w_A \dot{u}_A}{u_A^2 + w_A^2} \tag{2.21}$$

$$\dot{\beta} = \frac{-u_A v_A \dot{u}_A + (u_A^2 + w_A^2)\dot{v}_A - v_A w_A \dot{w}_A}{V^2 \sqrt{u_A^2 + w_A^2}} \tag{2.22}$$

For simplicity, we assume that there is no wind, so that $u_A = u$, $v_A = v$, and $w_A = w$. By substituting the expressions of $(\dot{u}, \dot{v}, \dot{w})$ from Equation (2.7), and the expressions of (u, v, w) from Equations (2.17)-(2.19), Equations (2.20)-(2.22) expand to:

$$\begin{bmatrix} \dot{V} \\ \dot{\alpha} \\ \dot{\beta} \end{bmatrix} = \begin{bmatrix} 0 \\ q + r(\cos\alpha \tan\theta - \sin\alpha)\tan\beta \\ -r(\cos\alpha + \sin\alpha \tan\theta) \end{bmatrix} + \frac{1}{mV} \begin{bmatrix} V\cos\alpha\cos\beta & V\sin\beta & V\sin\alpha\cos\beta \\ -\sin\alpha/\cos\beta & 0 & \cos\alpha/\cos\beta \\ -\cos\alpha\sin\beta & \cos\beta & -\sin\alpha\sin\beta \end{bmatrix} \begin{bmatrix} X \\ Y \\ Z \end{bmatrix} \tag{2.23}$$

2.3.4 Definition of the forces and moments

The modelling of the forces and moments is based on aeroballistics theory as presented in [McCoy, 1999]. They involve aerodynamic coefficients whose values are taken from [Wernert, 2005].

Forces

The external forces include body, Magnus, control, and gravitational terms:

$$\begin{bmatrix} X \\ Y \\ Z \end{bmatrix} = \begin{bmatrix} X_B \\ Y_B \\ Z_B \end{bmatrix} + \begin{bmatrix} X_M \\ Y_M \\ Z_M \end{bmatrix} + \begin{bmatrix} X_C \\ Y_C \\ Z_C \end{bmatrix} + \begin{bmatrix} X_G \\ Y_G \\ Z_G \end{bmatrix} \tag{2.24}$$

Damping terms due to friction with the air also exist but are neglected here.

The body axial and normal forces are given by:

$$\begin{bmatrix} X_B \\ Y_B \\ Z_B \end{bmatrix} = \overline{q}S \begin{bmatrix} -C_A(\mathcal{M}, \alpha') \\ -C_{N\alpha}(\mathcal{M}, \alpha')\beta \\ -C_{N\alpha}(\mathcal{M}, \alpha')\alpha \end{bmatrix} \tag{2.25}$$

They correspond to projections of the drag and lift forces on the body axes, drag and lift making use of wind axes instead. The aerodynamic coefficients C_A and $C_{N\alpha}$ depend in a nonlinear manner on the Mach number $\mathcal{M}$ and AoI α'. The Mach number is defined as $\mathcal{M} = \frac{V}{a(h)}$, with $a(h)$ the speed of sound, which depends on the altitude $h = -z_e$. Other variables appearing are the dynamic pressure $\overline{q} = \frac{1}{2}\rho(h)V^2$, with $\rho(h)$ the air density, and the reference area S of the projectile. The description of the altitude-dependency of the speed of sound and the air density is detailed in standard atmosphere models, such as the International Standard Atmosphere model [ISO2533, 1975].

The Magnus force is caused by the spinning motion of the body moving through air, which results in difference in pressure on opposite sides of the body. Its expression is given by:

$$\begin{bmatrix} X_M \\ Y_M \\ Z_M \end{bmatrix} = \overline{q}S\left(\frac{p_a d}{2V}\right) \begin{bmatrix} 0 \\ C_{Yp\alpha}(\mathcal{M})\alpha \\ -C_{Yp\alpha}(\mathcal{M})\beta \end{bmatrix} \tag{2.26}$$

with d being the projectile calibre.

The force generated by the canard deflection angles is expressed as:

$$\begin{bmatrix} X_C \\ Y_C \\ Z_C \end{bmatrix} = \overline{q}S \begin{bmatrix} 0 \\ -C_{N\delta}(\mathcal{M})\delta_r \\ -C_{N\delta}(\mathcal{M})\delta_q \end{bmatrix} \tag{2.27}$$

The control variables (δ_q, δ_r) are virtual control signals depending on the roll angle of the fuse ϕ_f and the real canard deflection angles $(\delta_1, \delta_2, \delta_3, \delta_4)$ through the relations [Siouris, 2004]:

$$\begin{bmatrix} \delta_q \\ \delta_r \end{bmatrix} = \begin{bmatrix} \cos\phi_f & -\sin\phi_f \\ \sin\phi_f & \cos\phi_f \end{bmatrix} \begin{bmatrix} 0 & \frac{1}{2} & 0 & -\frac{1}{2} \\ \frac{1}{2} & 0 & -\frac{1}{2} & 0 \end{bmatrix} \begin{bmatrix} \delta_1 \\ \delta_2 \\ \delta_3 \\ \delta_4 \end{bmatrix} \tag{2.28}$$

As for the gravity term, it is simply given by $mg\boldsymbol{e}_3$, which yields when expressed in $]^{B'}$:

$$\begin{bmatrix} X_G \\ Y_G \\ Z_G \end{bmatrix} = mg \begin{bmatrix} -\sin\theta \\ 0 \\ \cos\theta \end{bmatrix} \tag{2.29}$$

with g the altitude-dependent gravitational acceleration.

Finally, the total forces acting on the projectile are expressed as:

$$\begin{bmatrix} X \\ Y \\ Z \end{bmatrix} = \overline{q}S\left(\begin{bmatrix} -C_A(\mathcal{M},\alpha') \\ -C_{N\alpha}(\mathcal{M},\alpha')\beta \\ -C_{N\alpha}(\mathcal{M},\alpha')\alpha \end{bmatrix} + \frac{p_a d}{2V} \begin{bmatrix} 0 \\ C_{Yp\alpha}(\mathcal{M})\alpha \\ -C_{Yp\alpha}(\mathcal{M})\beta \end{bmatrix} + \begin{bmatrix} 0 \\ -C_{N\delta}(\mathcal{M})\delta_r \\ -C_{N\delta}(\mathcal{M})\delta_q \end{bmatrix} \right) + mg \begin{bmatrix} -\sin\theta \\ 0 \\ \cos\theta \end{bmatrix} \tag{2.30}$$

Moments

The external moments consist of body pitching, Magnus, damping, control, and friction terms:

$$\begin{bmatrix} L_f \\ L_a \\ M \\ N \end{bmatrix} = \begin{bmatrix} L_{f,B} \\ L_{a,B} \\ M_B \\ N_B \end{bmatrix} + \begin{bmatrix} L_{f,M} \\ L_{a,M} \\ M_M \\ N_M \end{bmatrix} + \begin{bmatrix} L_{f,D} \\ L_{a,D} \\ M_D \\ N_D \end{bmatrix} + \begin{bmatrix} L_{f,C} \\ L_{a,C} \\ M_C \\ N_C \end{bmatrix} + \begin{bmatrix} L_{f,F} \\ L_{a,F} \\ M_F \\ N_F \end{bmatrix} \tag{2.31}$$

The body pitching moment (also called overturning moment or static moment) is associated to the body axial and normal forces. These forces act through the centre of pressure, which is distinct from the centre of gravity and located towards the front of the projectile for the studied configuration. The body pitching moment produces a destabilising effect, which is counteracted by the spinning motion of the projectile ensuring gyroscopic stability. The generated moment is given by:

$$\begin{bmatrix} L_{f,B} \\ L_{a,B} \\ M_B \\ N_B \end{bmatrix} = \overline{q}Sd \begin{bmatrix} 0 \\ 0 \\ C_{m\alpha}(\mathcal{M},\alpha')\alpha \\ -C_{m\alpha}(\mathcal{M},\alpha')\beta \end{bmatrix} \tag{2.32}$$

Likewise, the Magnus force acts through a point distinct from the centre of gravity, located towards the rear of the projectile, inducing the Magnus moment:

$$\begin{bmatrix} L_{f,M} \\ L_{a,M} \\ M_M \\ N_M \end{bmatrix} = \overline{q}Sd\left(\frac{p_a d}{2V}\right) \begin{bmatrix} 0 \\ 0 \\ C_{np\alpha}(\mathcal{M})\beta \\ C_{np\alpha}(\mathcal{M})\alpha \end{bmatrix} \tag{2.33}$$

The damping term is provoked by friction with the air, and tends to decrease the rotation motion of the projectile. It is given by:

$$\begin{bmatrix} L_{f,D} \\ L_{a,D} \\ M_D \\ N_D \end{bmatrix} = \overline{q}Sd\left(\frac{d}{2V}\right) \begin{bmatrix} 0 \\ C_{lp}(\mathcal{M})p_a \\ C_{mq}(\mathcal{M})q \\ C_{mq}(\mathcal{M})r \end{bmatrix} \tag{2.34}$$

The control moment term is expressed as follows:

$$\begin{bmatrix} L_{f,C} \\ L_{a,C} \\ M_C \\ N_C \end{bmatrix} = \overline{q}Sd \begin{bmatrix} 0 \\ -C_{l\delta}(\mathcal{M})\delta_p \\ C_{m\delta}(\mathcal{M})\delta_q \\ -C_{m\delta}(\mathcal{M})\delta_r \end{bmatrix} \tag{2.35}$$

where δ_p is another virtual control signal, related to the real canard deflection angles through [Siouris, 2004]:

$$\delta_p = \frac{\delta_1 + \delta_2 + \delta_3 + \delta_4}{4} \tag{2.36}$$

Equation (2.36) can be combined with Equation (2.28) to obtain a relationship between the three virtual control signals $(\delta_p, \delta_q, \delta_r)$ and the real deflection angles $(\delta_1, \delta_2, \delta_3, \delta_4)$:

$$\begin{bmatrix} \delta_p \\ \delta_q \\ \delta_r \end{bmatrix} = T_{VR}(\phi_f) \begin{bmatrix} \delta_1 \\ \delta_2 \\ \delta_3 \\ \delta_4 \end{bmatrix} = \begin{bmatrix} 1 & 0 & 0 \\ 0 & \cos\phi_f & -\sin\phi_f \\ 0 & \sin\phi_f & \cos\phi_f \end{bmatrix} \begin{bmatrix} \frac{1}{4} & \frac{1}{4} & \frac{1}{4} & \frac{1}{4} \\ 0 & \frac{1}{2} & 0 & -\frac{1}{2} \\ \frac{1}{2} & 0 & -\frac{1}{2} & 0 \end{bmatrix} \begin{bmatrix} \delta_1 \\ \delta_2 \\ \delta_3 \\ \delta_4 \end{bmatrix} \tag{2.37}$$

The mechanical friction term between the forward and aft part is given by:

$$\begin{bmatrix} L_{f,F} \\ L_{a,F} \\ M_F \\ N_F \end{bmatrix} = \begin{bmatrix} L_{f-a} \\ -L_{f-a} \\ 0 \\ 0 \end{bmatrix} \tag{2.38}$$

where

$$L_{f-a} = \overline{q}SC_A(\mathcal{M}, \alpha')\,\mathrm{sign}(p_a - p_f)(K_s + K_v|p_a - p_f|) \tag{2.39}$$

with K_s and K_v static and viscous friction coefficients.

Finally, the total moments acting on the projectile are expressed as:

$$\begin{bmatrix} L_f \\ L_a \\ M \\ N \end{bmatrix} = \overline{q}Sd \left(\begin{bmatrix} 0 \\ 0 \\ C_{m\alpha}(\mathcal{M}, \alpha')\alpha \\ -C_{m\alpha}(\mathcal{M}, \alpha')\beta \end{bmatrix} + \frac{p_a d}{2V} \begin{bmatrix} 0 \\ 0 \\ C_{np\alpha}(\mathcal{M})\beta \\ C_{np\alpha}(\mathcal{M})\alpha \end{bmatrix} + \frac{d}{2V} \begin{bmatrix} 0 \\ C_{lp}(\mathcal{M})p_a \\ C_{mq}(\mathcal{M})q \\ C_{mq}(\mathcal{M})r \end{bmatrix} + \begin{bmatrix} 0 \\ -C_{l\delta}(\mathcal{M})\delta_p \\ C_{m\delta}(\mathcal{M})\delta_q \\ -C_{m\delta}(\mathcal{M})\delta_r \end{bmatrix} \right) + \begin{bmatrix} L_{f-a} \\ -L_{f-a} \\ 0 \\ 0 \end{bmatrix} \tag{2.40}$$

2.3.5 Simulation of ballistic trajectories with the nonlinear model

The 7DoF airframe model given by the dynamic and kinematic equations together with the description of the forces and moments allows to build an open-loop simulator of the projectile in Matlab/Simulink, whose general structure is shown in Figure 2.4. Ballistic simulations can then

be conducted by specifying initial launch conditions. Such a simulator is useful to study the behaviour of the projectile during its flight. It can also be used to establish the flight envelope of the projectile, or to compute the coordinates of ballistic impact points. Due to the nature of the system, the set of possible initial conditions is constrained in multiple ways:

- the initial linear velocity u_0 can take four different values, corresponding to the number of gunpowder bags used for launch,
- the initial spin rate $p_{a,0}$ is obtained by a direct relation with u_0 due to the twist of the barrel,
- the launch elevation angle θ_0 lies in the interval $[16\,\text{deg}, 62\,\text{deg}]$.

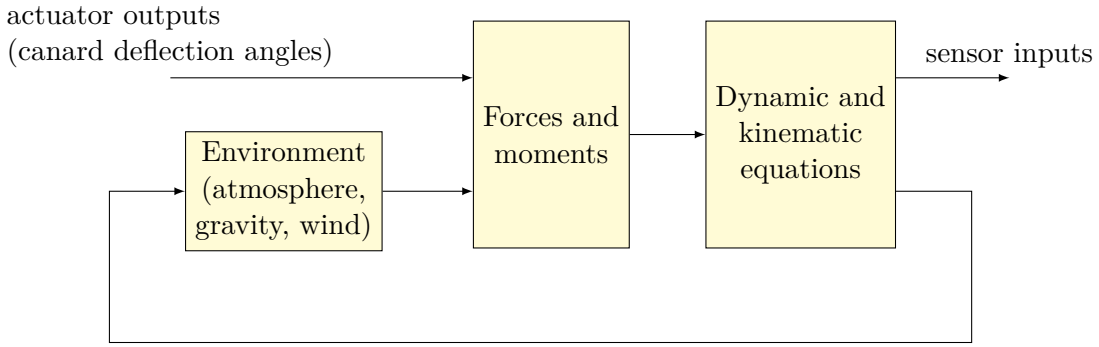

Figure 2.4: Structure of the open-loop 7DoF airframe simulator

Figures 2.5 to 2.9 show the evolution of some of the state variables for a typical long-range ballistic trajectory, with initial conditions $u_0 = 939$ m/s, $p_{a,0} = 1903$ rad/s ≈ 300 Hz, $\theta_0 = 42\,\text{deg}$, and $\psi_0 = 0\,\text{deg}$, and assuming no wind. Figures 2.10 and 2.11 show the forces and moments along the trajectory.

It can be seen on Figure 2.5 that the projectile is significantly deviated to the right during the flight (see also Figure 2.6 for a top view with equally scaled axes). This lateral deviation is characteristic of spin-stabilised projectile. It is caused by the negative values taken by the AoS β during the trajectory, as seen on Figure 2.9, generating the lateral force Y_B, which Figure 2.10 confirms to be the main acting force on the lateral axis. Meanwhile, the axial and gravitational terms X_B and X_G are the driving forces along the longitudinal axis, and the force along the normal axis Z is almost entirely due to the gravitational term Z_G.

Regarding the moments shown in Figure 2.11, the damping term L_{aD} is the driving one along the longitudinal axis, and causes the body spin rate p_a to decrease along the trajectory, as shown in Figure 2.8. The effect of the friction term L_{f-a} is also clearly seen through the sharp increase of both the fuse spin rate p_f and the fuse roll angle ϕ_f shown in Figure 2.7. The pitch and yaw moments M_{PY} and N_{PY} are major contributing terms on their respective axes, but the lateral axis is also characterised by a significant contribution from the Magnus term M_M.

The influence of the initial elevation angle θ_0 is illustrated by Figure 2.12, where the evolution of the aerodynamic variables are plotted for two trajectories with $\theta_0 = 42\,\text{deg}$ (in blue) and $\theta_0 = 62\,\text{deg}$ (in orange). It is observed that higher elevation angles introduce fast oscillations on the state variables α and β.

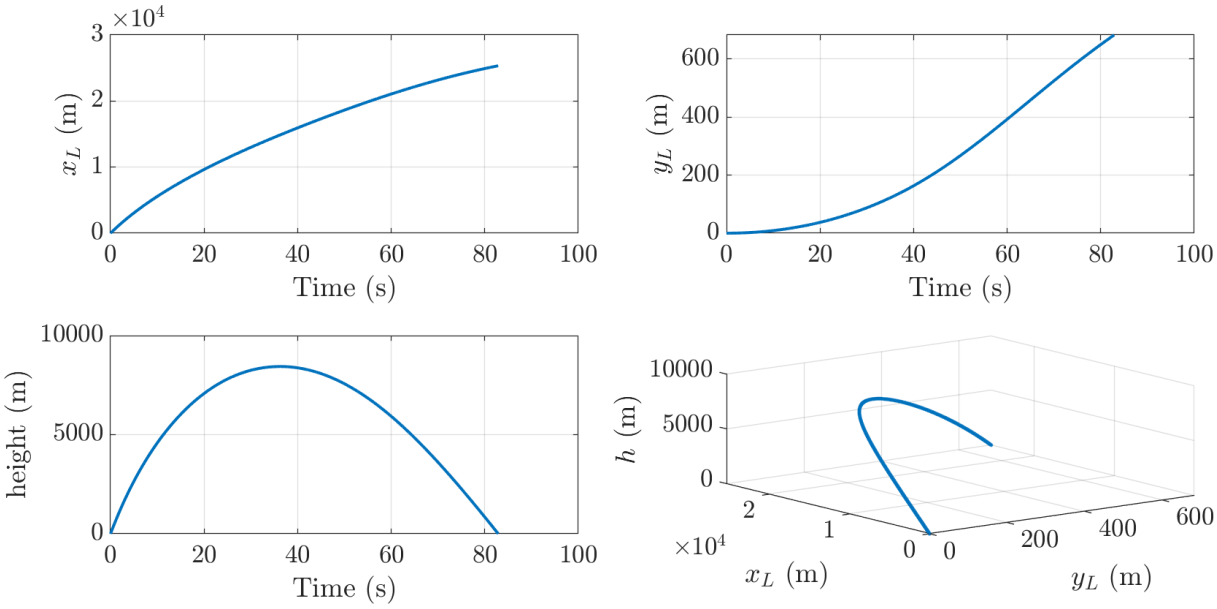

Figure 2.5: Linear positions along a ballistic trajectory

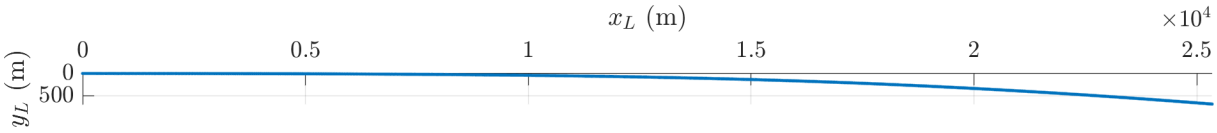

Figure 2.6: Top view of a ballistic trajectory with equally scaled axes

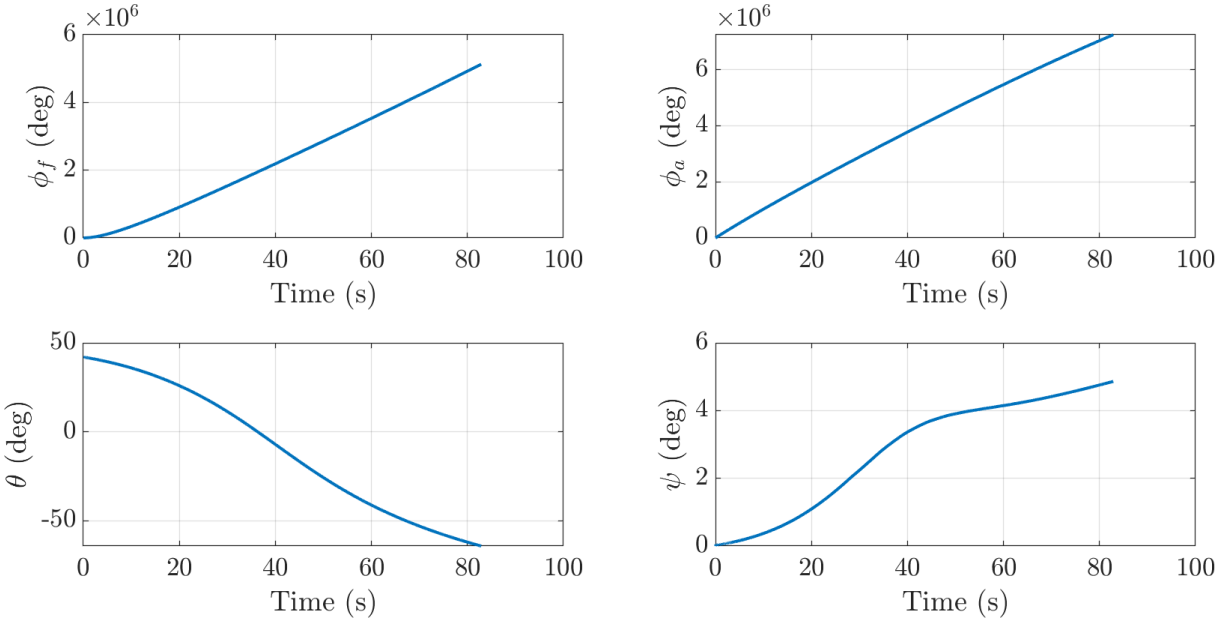

Figure 2.7: Euler angles along a ballistic trajectory

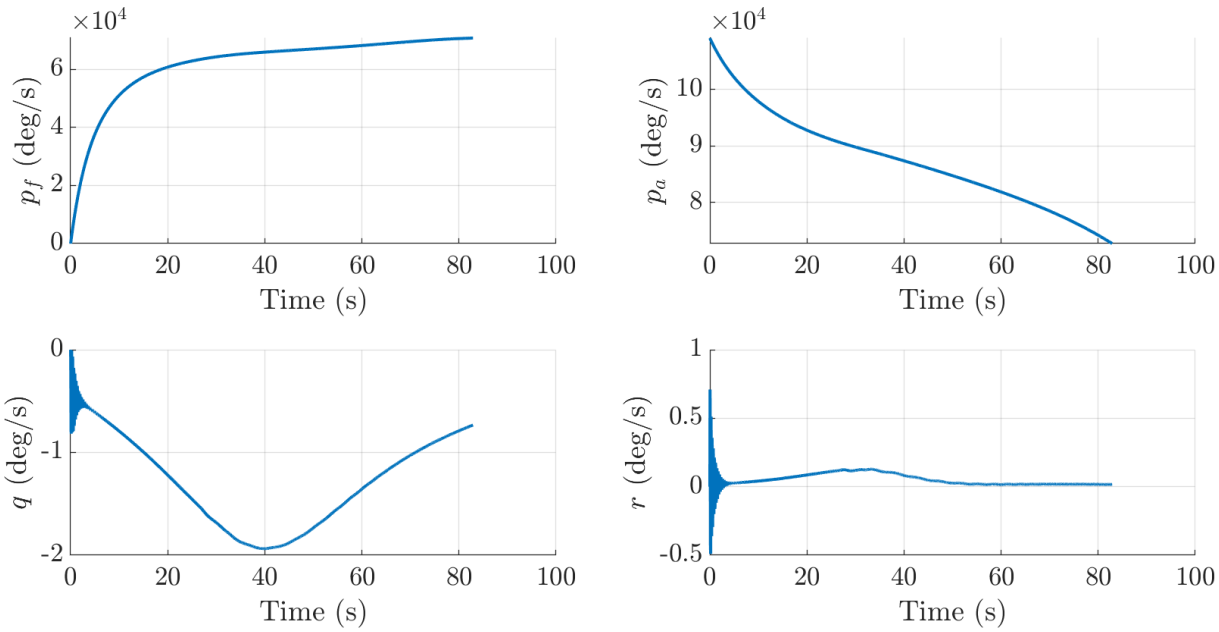

Figure 2.8: Angular rates along a ballistic trajectory

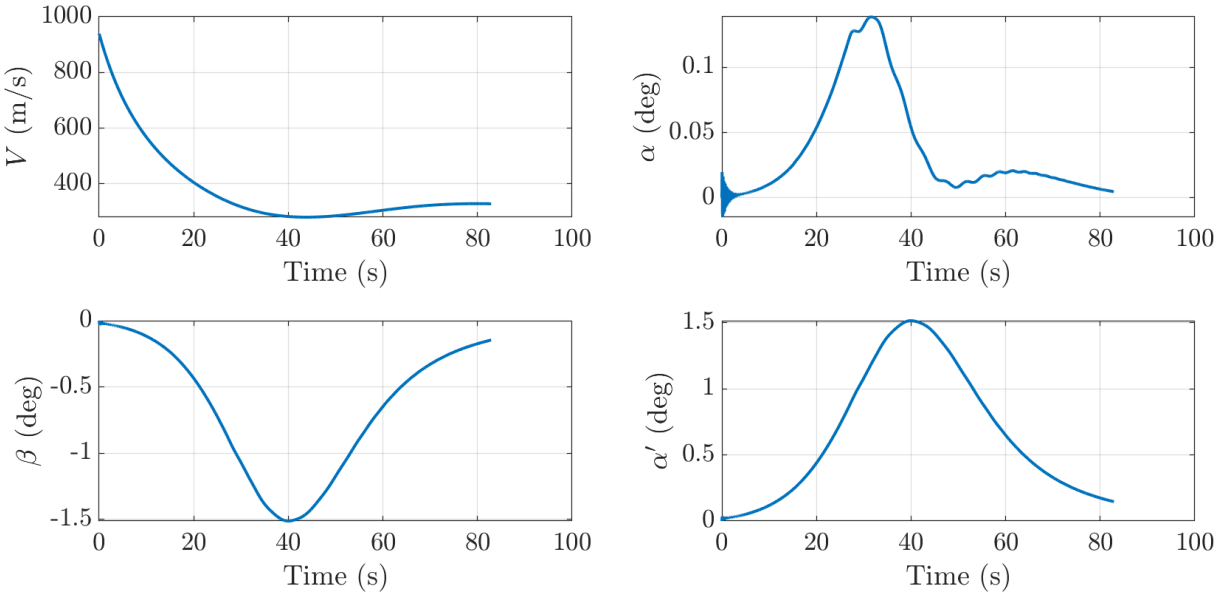

Figure 2.9: Aerodynamic angles and airspeed along a ballistic trajectory

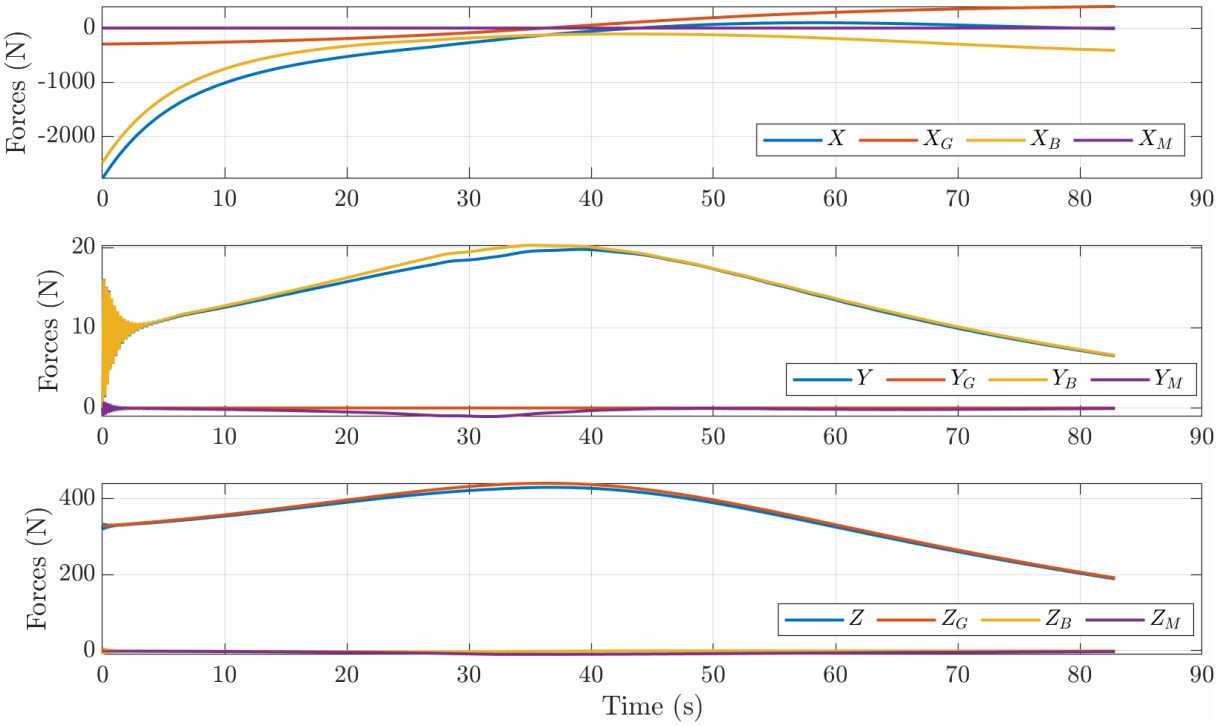

Figure 2.10: Forces along a ballistic trajectory

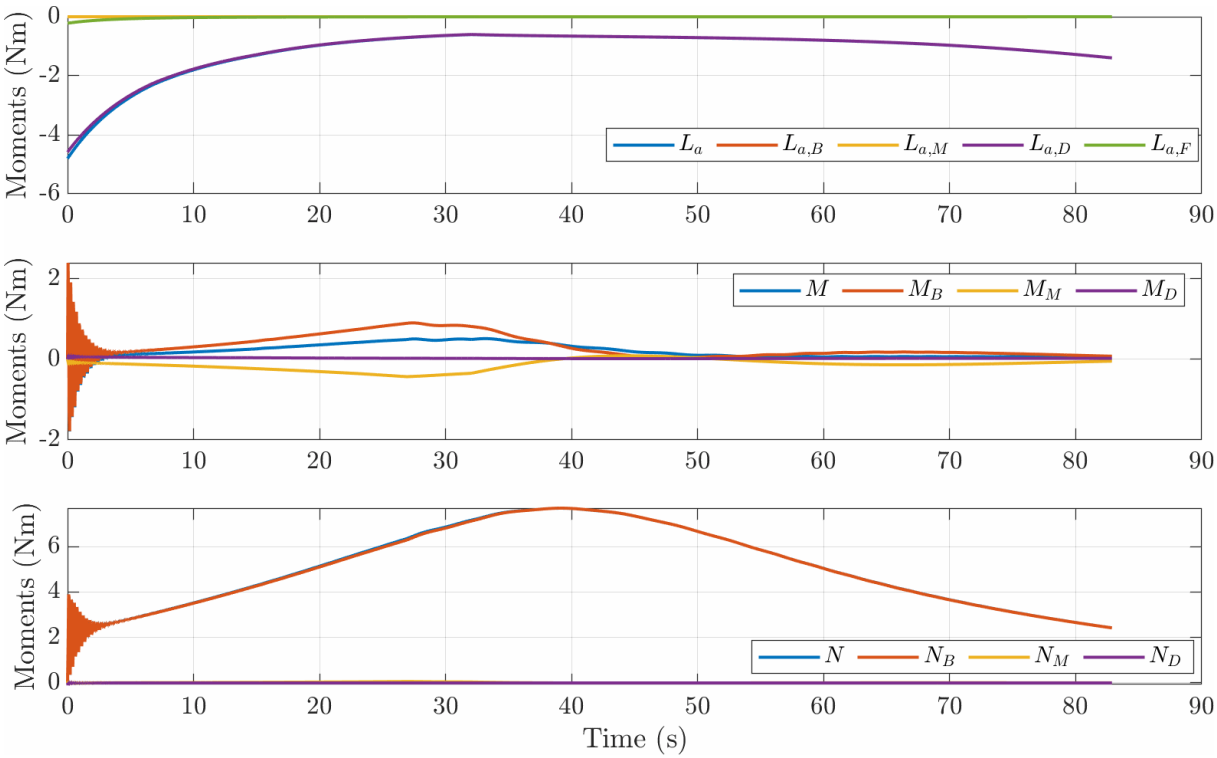

Figure 2.11: Moments along a ballistic trajectory

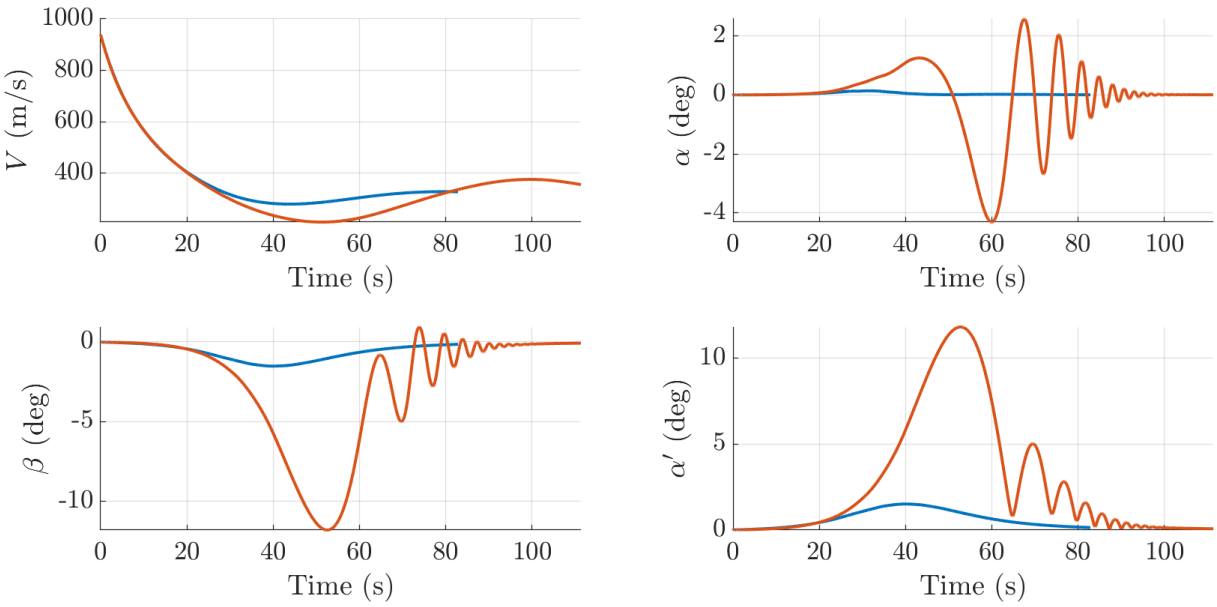

Figure 2.12: Aerodynamic angles and airspeed along a ballistic trajectory for two distinct launch angles (blue: $\theta_0 = 42\,\text{deg}$; orange: $\theta_0 = 62\,\text{deg}$)

Simulations with constant canard angles along the trajectory are also performed. These are useful to confirm the capacity of the canards to modify the trajectory of the projectile. Figure 2.13 shows the impact points obtained with constant canard angles held from $t = 20$ s to the end of the trajectory, where the fuse is set in a '+' configuration ($\phi_f = 0\,\text{deg}$) by removing the contribution of the friction moment. The red points correspond to scenarios with $\delta_r \neq 0$ and $\delta_q = 0$ generated by commanding opposite deflection angles on δ_1 and δ_3. The scenarios for the yellow points use nonzero opposite δ_2 and δ_4 instead to generate $\delta_q \neq 0$ and $\delta_r = 0$. It can be observed that the use of the canards is able to significantly alter the trajectory of the projectile both downrange and laterally.

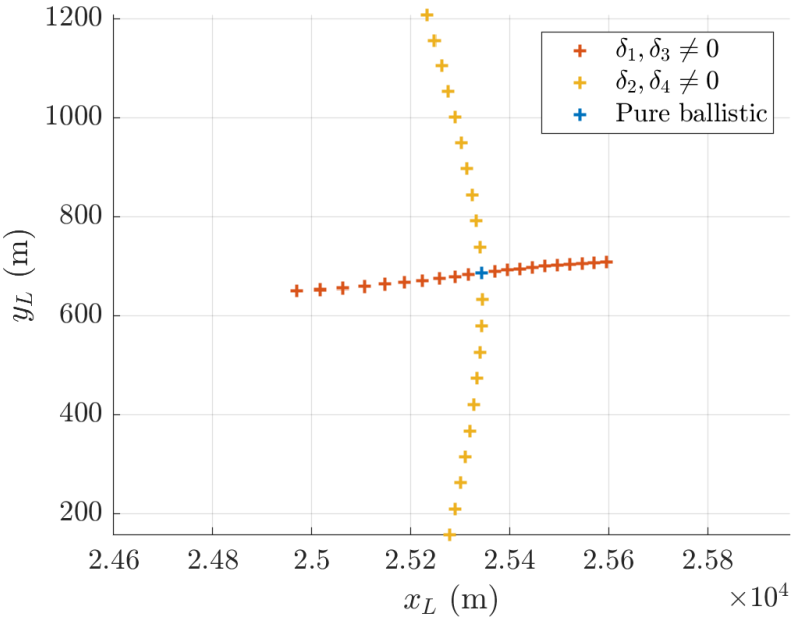

Figure 2.13: Impact points for different deflection angles maintained during the flight

2.4 Linearised models for the roll and pitch/yaw channels

The nonlinear model of the airframe can be decomposed into the roll channel on one hand, and the pitch/yaw channels on the other hand. This decomposition corresponds to the two separate control problems broached in Section 2.2.

2.4.1 LPV model of the roll channel

The states of interest for the control of the roll channel are the roll angle ϕ_f of the fuse and its angular rate p_f. Their dynamics can be extracted from Equations (2.7) and (2.9):

$$\begin{bmatrix} \dot{\phi}_f \\ \dot{p}_f \end{bmatrix} = \begin{bmatrix} p_f + r\tan\theta \\ {I_{xf}}^{-1}(L_{f,C} + L_{f-a}) \end{bmatrix} \tag{2.41}$$

Substituting the moments $L_{f,C}$ and L_{f-a} by their expressions, the system can be rewritten in the following LPV form:

$$\begin{bmatrix} \dot{\phi}_f \\ \dot{p}_f \end{bmatrix} = \begin{bmatrix} 0 & 1 \\ 0 & a_{22}(\boldsymbol{\sigma}_R) \end{bmatrix} \begin{bmatrix} \phi_f \\ p_f \end{bmatrix} + \begin{bmatrix} 0 \\ b_2(\boldsymbol{\sigma}_R) \end{bmatrix} \delta_p + \begin{bmatrix} d_\phi \\ d_p \end{bmatrix} \tag{2.42}$$

where

$$a_{22}(\boldsymbol{\sigma}_R) = -\left(\frac{\overline{q}Sd}{I_{xf}}\right) C_A(\mathcal{M}, \alpha') K_v \tag{2.43}$$

$$b_2(\boldsymbol{\sigma}_R) = -\left(\frac{\overline{q}Sd}{I_{xf}}\right) C_{l\delta}(\mathcal{M}) \tag{2.44}$$

and $\boldsymbol{\sigma}_R = [\alpha' \ V \ h]^T$ is a parameter vector. The time-varying disturbance terms d_ϕ and d_p are given by:

$$d_\phi = r\tan\theta \tag{2.45}$$

$$d_p = \left(\frac{\overline{q}Sd}{I_{xf}}\right) C_A(\mathcal{M}, \alpha')[\text{sign}(p_a - p_f)K_s + K_v p_a] \tag{2.46}$$

Ballistic simulations show that in practical flight conditions, $\alpha' \in [0 \text{ deg}, 15 \text{ deg}]$, and the value of the axial coefficient $C_A(\mathcal{M}, \alpha')$ is predominantly governed by the value of the Mach number, i.e. by the parameters V and h. This observation leads to consider a reduced parameter vector $\boldsymbol{\lambda}_R = [V \ h]^T$.

2.4.2 Linearised model for the pitch/yaw channels

Trimming and Jacobian linearisation

The relevant nonlinear dynamics for the pitch/yaw channels can be rewritten in the generic parameter-dependent form:

$$\begin{cases} \dot{\boldsymbol{x}} = f(\boldsymbol{x}, \boldsymbol{u}, \boldsymbol{\sigma}_{PY}) \\ \boldsymbol{y} = g(\boldsymbol{x}, \boldsymbol{u}, \boldsymbol{\sigma}_{PY}) \end{cases} \tag{2.47}$$

with states $\boldsymbol{x} = [\alpha\ q\ \beta\ r]^T$, inputs $\boldsymbol{u} = [\delta_q\ \delta_r]^T$, outputs $\boldsymbol{y} = [n_z\ n_y\ q\ r]^T$, and parameters $\boldsymbol{\sigma}_{PY} = [V\ h\ p_a\ \theta]^T$. The outputs n_z and n_y are the normal and lateral load factors respectively, defined as:

$$\begin{bmatrix} n_z \\ n_y \end{bmatrix} = \frac{1}{mg} \begin{bmatrix} Z - Z_G \\ Y - Y_G \end{bmatrix} \tag{2.48}$$

and commonly expressed in g, despite being dimensionless quantities.

In view of designing a gain scheduled controller, a Jacobian linearisation around trim points is performed on the nonlinear model [Rugh and Shamma, 2000; Leith and Leithead, 2000]. The procedure starts with the computation of trim points for fixed values $\overline{\boldsymbol{\sigma}}_{PY} = \left[\overline{V}\ \overline{h}\ \overline{p_a}\ \overline{\theta}\right]^T$ of the parameter vector. That is, we seek the solutions $(\overline{\boldsymbol{x}}, \overline{\boldsymbol{u}})$ of the equation:

$$f(\overline{\boldsymbol{x}}, \overline{\boldsymbol{u}}, \overline{\boldsymbol{\sigma}}_{PY}) = 0 \tag{2.49}$$

However, the above system is underdetermined, since it consists of four equations with six unknown variables. To overcome this issue, additional variables must be given fixed values. Thus we define an extended trimming vector $\overline{\boldsymbol{\rho}} = \left[\overline{V}\ \overline{h}\ \overline{p_a}\ \overline{\theta}\ \overline{\alpha}\ \overline{\beta}\right]^T$ by also imposing the values of the AoA and AoS. The solutions $(\overline{\boldsymbol{x}}, \overline{\boldsymbol{u}})$ can then be computed, and are also exploited to compute the corresponding equilibrium outputs $\overline{\boldsymbol{y}}$ (see [Theodoulis et al., 2013] for details on the resolution).

Next, we define the deviation variables:

$$\boldsymbol{x}_\varepsilon = \boldsymbol{x} - \overline{\boldsymbol{x}} \qquad \boldsymbol{u}_\varepsilon = \boldsymbol{u} - \overline{\boldsymbol{u}} \qquad \boldsymbol{y}_\varepsilon = \boldsymbol{y} - \overline{\boldsymbol{y}} \tag{2.50}$$

The nonlinear dynamics can then be rewritten as:

$$\begin{cases} \dot{\boldsymbol{x}}_\varepsilon = f(\overline{\boldsymbol{x}} + \boldsymbol{x}_\varepsilon, \overline{\boldsymbol{u}} + \boldsymbol{u}_\varepsilon) \\ \boldsymbol{y}_\varepsilon = g(\overline{\boldsymbol{x}} + \boldsymbol{x}_\varepsilon, \overline{\boldsymbol{u}} + \boldsymbol{u}_\varepsilon) \end{cases} \tag{2.51}$$

For small values of the deviation variables, this system can be approximated by its first-order Taylor expansion and subsequently written in state-space form.

$$\begin{cases} \dot{\boldsymbol{x}}_\varepsilon = \boldsymbol{A}(\overline{\boldsymbol{\rho}})\boldsymbol{x}_\varepsilon + \boldsymbol{B}(\overline{\boldsymbol{\rho}})\boldsymbol{u}_\varepsilon \\ \boldsymbol{y}_\varepsilon = \boldsymbol{C}(\overline{\boldsymbol{\rho}})\tilde{\boldsymbol{x}}_\varepsilon + \boldsymbol{D}(\overline{\boldsymbol{\rho}})\boldsymbol{u}_\varepsilon \end{cases} \tag{2.52}$$

For simplicity, the aerodynamic coefficients are taken as constant when computing the Jacobian matrices, and their dependency to the Mach number and AoI is omitted for brevity. The state-space matrices are then computed as:

$$\begin{aligned} \boldsymbol{A}(\overline{\boldsymbol{\rho}}) &= \frac{\partial f}{\partial \boldsymbol{x}}(\overline{\boldsymbol{x}}, \overline{\boldsymbol{u}}, \overline{\boldsymbol{\sigma}}_{PY}) \\ &= \begin{bmatrix} Z_{\alpha\alpha} & 1 & Z_{\alpha\beta} & (\cos\alpha\tan\theta - \sin\alpha)\tan\beta \\ \left(\frac{\overline{q}Sd}{I_t}\right)C_{m\alpha} & \left(\frac{\overline{q}Sd}{I_t}\right)\left(\frac{d}{2V}\right)C_{mq} & \left(\frac{\overline{q}Sd}{I_t}\right)\left(\frac{p_a d}{2V}\right)C_{np\alpha} & -2r\tan\theta - \left(\frac{I_{xa}}{I_t}\right)p_a \\ Z_{\beta\alpha} & 0 & Z_{\beta\beta} & -\cos\alpha - \sin\alpha\tan\beta \\ \left(\frac{\overline{q}Sd}{I_t}\right)\left(\frac{p_a d}{2V}\right)C_{np\alpha} & r\tan\theta + \left(\frac{I_{xa}}{I_t}\right)p_a & -\left(\frac{\overline{q}Sd}{I_t}\right)C_{m\alpha} & \left(\frac{\overline{q}Sd}{I_t}\right)\left(\frac{d}{2V}\right)C_{mq} + q\tan\theta \end{bmatrix} \end{aligned} \tag{2.53}$$

$$\boldsymbol{B}(\overline{\boldsymbol{\rho}}) = \frac{\partial f}{\partial \boldsymbol{u}}(\overline{\boldsymbol{x}}, \overline{\boldsymbol{u}}, \overline{\boldsymbol{\sigma}}_{PY}) = \begin{bmatrix} -\left(\frac{\overline{q}S}{mV}\right)\left(\frac{\cos\alpha}{\cos\beta}\right)C_{N\delta} & 0 \\ \left(\frac{\overline{q}Sd}{I_t}\right)C_{m\delta} & 0 \\ \left(\frac{\overline{q}S}{mV}\right)\sin\alpha\sin\beta C_{N\delta} & -\left(\frac{\overline{q}S}{mV}\right)\cos\beta C_{N\delta} \\ 0 & -\left(\frac{\overline{q}Sd}{I_t}\right)C_{m\delta} \end{bmatrix} \tag{2.54}$$

$$\boldsymbol{C}(\overline{\boldsymbol{\rho}}) = \frac{\partial g}{\partial \boldsymbol{x}}(\overline{\boldsymbol{x}}, \overline{\boldsymbol{u}}, \overline{\boldsymbol{\sigma}}_{PY}) = \begin{bmatrix} -\left(\frac{\overline{q}S}{mg}\right)C_{N\alpha} & 0 & -\left(\frac{\overline{q}S}{mg}\right)\left(\frac{p_a d}{2V}\right)C_{Yp\alpha} & 0 \\ \left(\frac{\overline{q}S}{mg}\right)\left(\frac{p_a d}{2V}\right)C_{Yp\alpha} & 0 & -\left(\frac{\overline{q}S}{mg}\right)C_{N\alpha} & 0 \\ 0 & 1 & 0 & 0 \\ 0 & 0 & 0 & 1 \end{bmatrix} \tag{2.55}$$

$$\boldsymbol{D}(\overline{\boldsymbol{\rho}}) = \frac{\partial g}{\partial \boldsymbol{u}}(\overline{\boldsymbol{x}}, \overline{\boldsymbol{u}}, \overline{\boldsymbol{\sigma}}_{PY}) = \begin{bmatrix} -\left(\frac{\overline{q}S}{mg}\right)C_{N\delta} & 0 \\ 0 & -\left(\frac{\overline{q}S}{mg}\right)C_{N\delta} \\ 0 & 0 \\ 0 & 0 \end{bmatrix} \tag{2.56}$$

The elements $Z_{\alpha\alpha}$, $Z_{\alpha\beta}$, $Z_{\beta\alpha}$, and $Z_{\beta\beta}$ of Equation (2.53) are given by:

$$\begin{aligned} Z_{\alpha\alpha} = {} & \left(\frac{1}{mV}\right)\left[-\left(\frac{\cos\alpha}{\cos\beta}\right)X - \left(\frac{\sin\alpha}{\cos\beta}\right)Z + \left(\frac{\cos\alpha}{\cos\beta}\right)\frac{\partial Z}{\partial\alpha}\right] \\ & - r\tan\beta(\sin\alpha\tan\theta + \cos\alpha) \end{aligned} \tag{2.57}$$

$$\begin{aligned} Z_{\alpha\beta} = {} & \left(\frac{1}{mV}\right)\left[-\left(\frac{\sin\alpha\sin\beta}{\cos^2\beta}\right)X + \left(\frac{\cos\alpha\sin\beta}{\cos^2\beta}\right)Z + \left(\frac{\cos\alpha}{\cos\beta}\right)\frac{\partial Z}{\partial\beta}\right] \\ & + \left(\frac{r}{\cos^2\beta}\right)(\cos\alpha\tan\theta - \sin\alpha) \end{aligned} \tag{2.58}$$

$$\begin{aligned} Z_{\beta\alpha} = {} & \left(\frac{1}{mV}\right)\left[\sin\alpha\sin\beta X + \cos\beta\frac{\partial Y}{\partial\alpha} - \cos\alpha\sin\beta Z - \sin\alpha\sin\beta\frac{\partial Z}{\partial\alpha}\right] \\ & + r(\sin\alpha - \cos\alpha\tan\theta) \end{aligned} \tag{2.59}$$

$$\begin{aligned} Z_{\beta\beta} = {} & \left(\frac{1}{mV}\right)\left[-\cos\alpha\cos\beta X - \sin\beta Y + \cos\beta\frac{\partial Y}{\partial\beta} - \sin\alpha\cos\beta Z\right. \\ & \left. - \sin\alpha\sin\beta\frac{\partial Z}{\partial\beta}\right] \end{aligned} \tag{2.60}$$

with:

$$\begin{aligned} \frac{\partial Z}{\partial\alpha} &= -\overline{q}SC_{N\alpha} & \frac{\partial Z}{\partial\beta} &= -\overline{q}S\left(\frac{p_a d}{2V}\right)C_{Yp\alpha} \\ \frac{\partial Y}{\partial\alpha} &= \overline{q}S\left(\frac{p_a d}{2V}\right)C_{Yp\alpha} & \frac{\partial Y}{\partial\beta} &= -\overline{q}SC_{N\alpha} \end{aligned} \tag{2.61}$$

Since the trimming vector used to compute equilibrium points contain state variables, and using a common abuse of language, the bank of LTI models described by Equation (2.52) and parametrised by $\boldsymbol{\rho}$ is referred to as a quasi-LPV model.

To validate the linearisation process, the quasi-LPV model is evaluated along a ballistic trajectory. To do so, first a nonlinear simulation is performed. The values taken by the trimming variables are then used for the trimming and linearisation procedure. Since the trajectory points are not necessarily equilibrium points, the trimming procedure is slightly modified by setting the right-hand side of Equation (2.49) to the values of the time-derivative of the state vector. This

results in an LTV model in the deviation variables, which is subsequently simulated. The states and outputs are recovered using Equation (2.50) and the computed trimming values, and are then compared to the states and outputs from the nonlinear simulation. As shown in Figure 2.14, the results are almost identical.

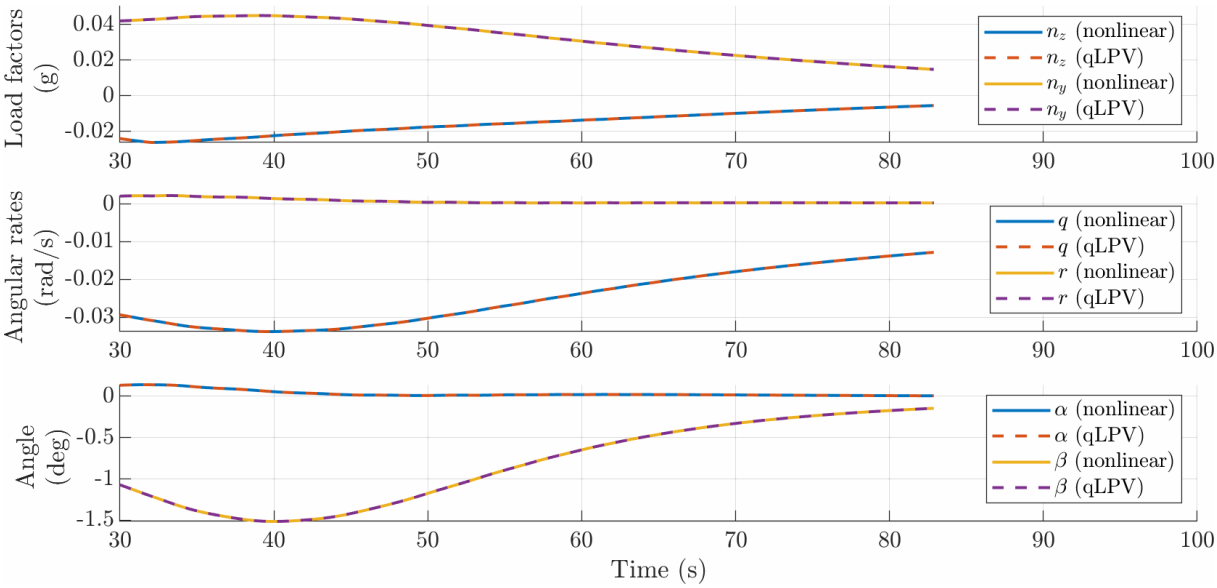

Figure 2.14: Pitch/yaw outputs and states along a ballistic trajectory: nonlinear model VS quasi-LPV model

Analysis of the quasi-LPV model

The quasi-LPV model of the pitch/yaw dynamics can be used to study open-loop stability properties around trim points, and allows to make several links with classical aeroballistic theory.

Spin-stabilised projectiles are known to feature tightly coupled pitch and yaw channel dynamics. This property is visible from the state matrix $\boldsymbol{A}(\boldsymbol{\rho})$, which features nonzero off-diagonal blocks. Moreover, the coefficients of these blocks contain the body roll rate p_a, which is very high for these systems. This prevents the design of separate control loops for each axis, as is typically done in missile autopilots.

Figure 2.15 shows the singular values and poles obtained at trim points corresponding to a ballistic trajectory. Two modes can be identified from the peaks of singular values and from the two pairs of conjugate eigenvalues of the system. These modes can be linked to two known phenomena from aeroballistic theory regarding spinning bodies[McCoy, 1999], which are a low-frequency motion of the axis of rotation called precession, and a higher-frequency motion called nutation. It can be seen that the low-frequency poles associated to precession get very close to the imaginary axis during the trajectory, roughly when the projectile reaches its apogee.

The role of the spin rate p_a in providing gyroscopic stability can also be illustrated by investigating the poles of the system for decreasing values of p_a. As shown in Figure 2.16, the poles associated to the precession mode move towards the right-half plane as p_a decreases, eventually becoming unstable.

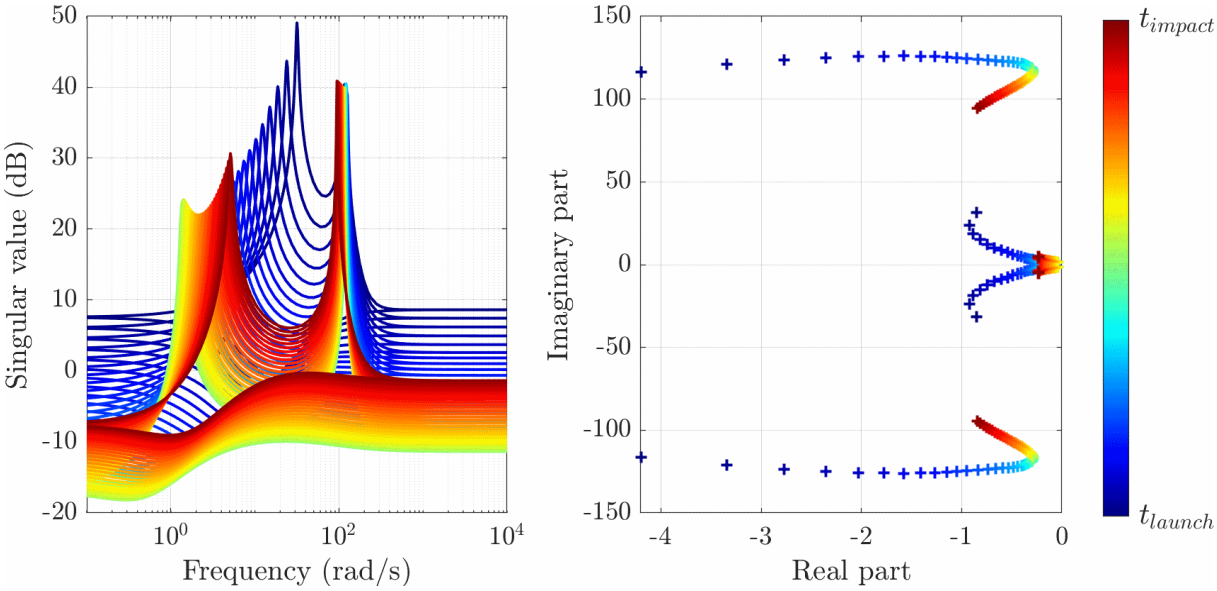

Figure 2.15: Singular values (left) and poles (right) of the linearised pitch/yaw channels along a ballistic trajectory

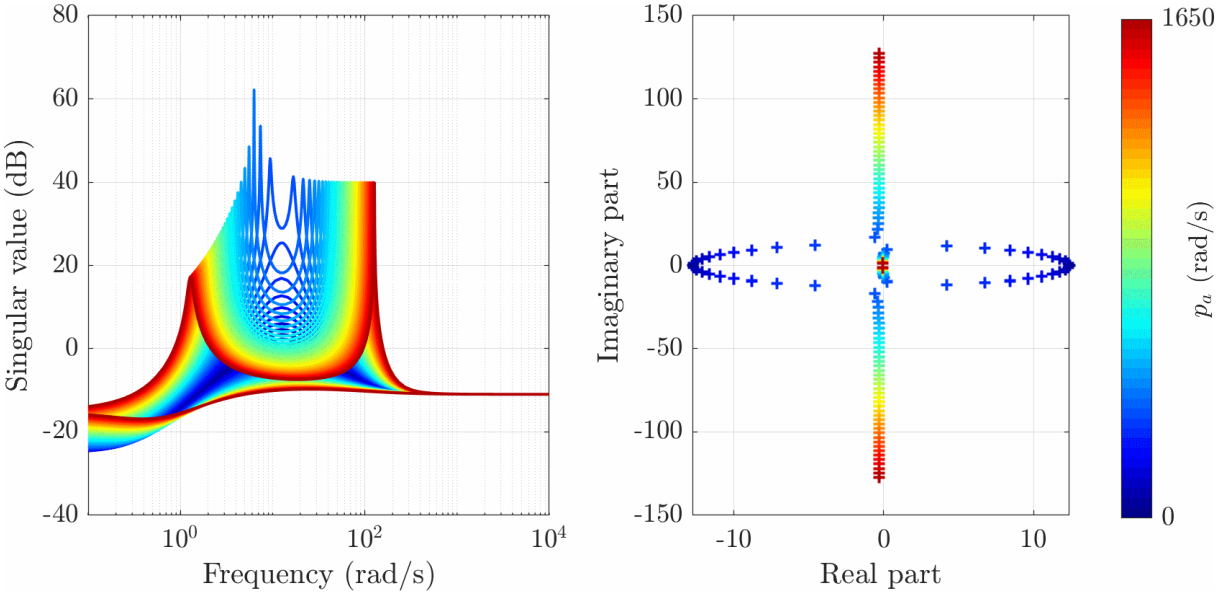

Figure 2.16: Singular values (left) and poles (right) of the linearised pitch/yaw channels for increasing values of p_a

Reduction of the dimension of the flight envelope

The quasi-LPV model of the pitch/yaw channels is parametrised by the six-dimensional vector $\boldsymbol{\rho} = [V\ h\ p_a\ \theta\ \alpha\ \beta]^T$. The corresponding flight envelope can be estimated by performing ballistic simulations using a set of admissible initial conditions. The values taken by the trim variables are shown in Figure 2.17 for simulations corresponding to the four possible launch velocities of the projectile, and with initial pitch angle $\theta_0 \in [16\,\text{deg}, 62\,\text{deg}]$. The plots start at $t = 30$ s when pitch/yaw guidance and control is initiated.

The six-dimensional flight envelope is ill-suited to design a gain scheduled controller, because a large number of local syntheses are required to cover it with a sufficiently thin grid. In order to reduce the computational burden of the controller synthesis step, it is of interest to reduce the number of scheduling variables by keeping only the most influential ones. Following this strategy, and exploiting the simulation-based sensitivity analysis done in [Sève et al., 2017a], the reduced trim vector $\boldsymbol{\lambda}_{PY} = [V\ h\ p_a]^T$ is considered. The three-dimensional flight envelope is described by the intervals $V \in [140\text{ m/s}, 380\text{ m/s}]$, $h \in [0\text{ m}, 15000\text{ m}]$, and $p_a \in [750\text{ rad/s}, 1650\text{ rad/s}]$, with the remaining parameters fixed to: $\theta = -17.5\,\text{deg}$, $\alpha = 0\,\text{deg}$, and $\beta = 0\,\text{deg}$.

Figure 2.18 shows a comparison of the singular value plots and poles obtained with the full and reduced trim vectors along a ballistic trajectory. The blue data correspond to the LTI models obtained when using the full trim vector, while the orange data are obtained by linearising at $\boldsymbol{\rho} = [V\ h\ p_a\ -17.5\,\text{deg}\ 0\ 0]^T$. Both singular values and poles are very well approximated by the reduced quasi-LPV model, justifying its use as the basis for control design.

2.5 Definition of the actuator and sensor models

2.5.1 Actuator models

The four servomotors actuating the canards are modelled as identical second-order systems, whose transfer function is:

$$G_{act,i}(s) = \frac{\omega_{act}^2}{s^2 + 2\xi_{act}\omega_{act}s + \omega_{act}^2} \qquad i \in \{1, 2, 3, 4\} \tag{2.62}$$

In addition, a position saturation δ_{sat} is introduced at the input of each actuator, as shown in Figure 2.19, where $\delta_{i,c}$ is the deflection angle commanded by the autopilot, for $i \in \{1, 2, 3, 4\}$, while no rate saturation is considered. This modelling of the saturations is motivated by the fact that they do not stem from mechanical limitations. Instead, they come from considerations regarding the validity of the aerodynamic model, and specifically the expressions of the canard forces and moments which rely on a small angle assumption. The actuator output signals are converted into the virtual control signals using Equation (2.37).

Since the roll and pitch/yaw control problems are treated separately, it is natural to consider the roll autopilot output as a commanded value on the virtual signal $\delta_{p,c}$, and the pitch/yaw autopilot output as commanded values on $(\delta_{q,c}, \delta_{r,c})$. The commanded virtual signals must then

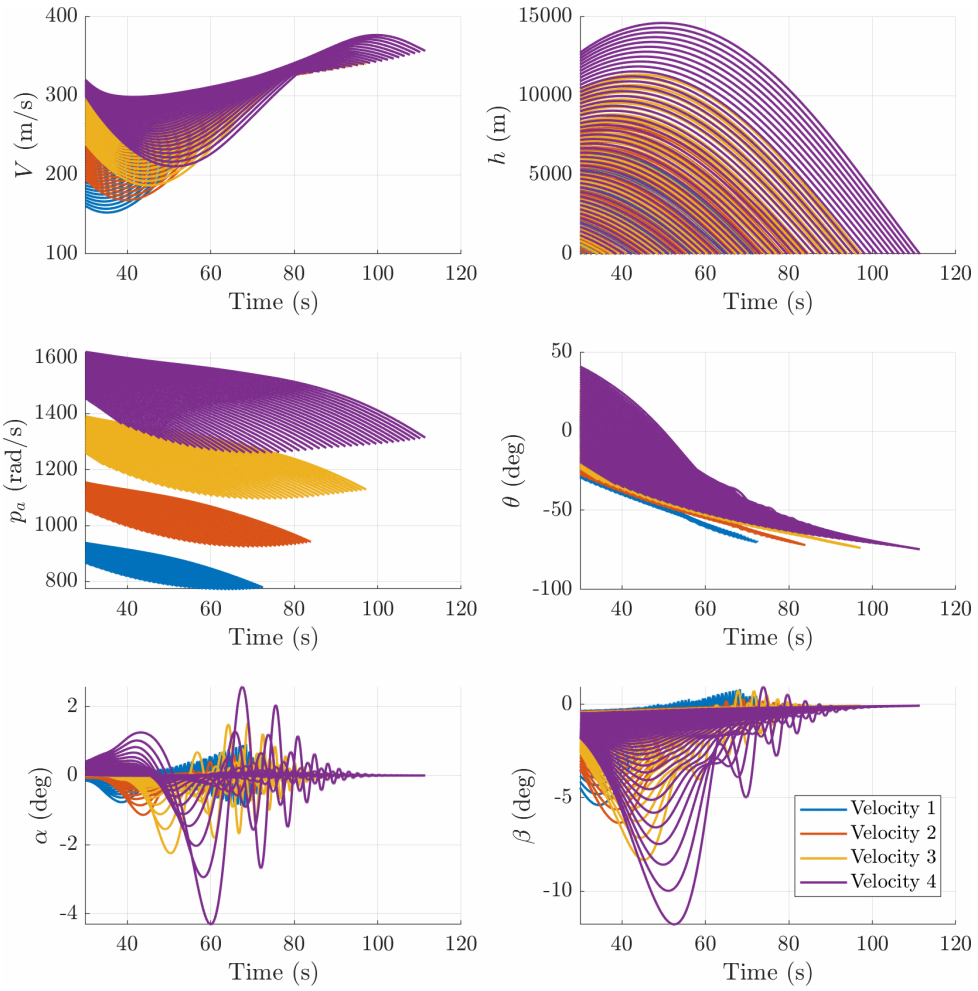

Figure 2.17: Parameter variations for a set of ballistic trajectories used to estimate the flight envelope

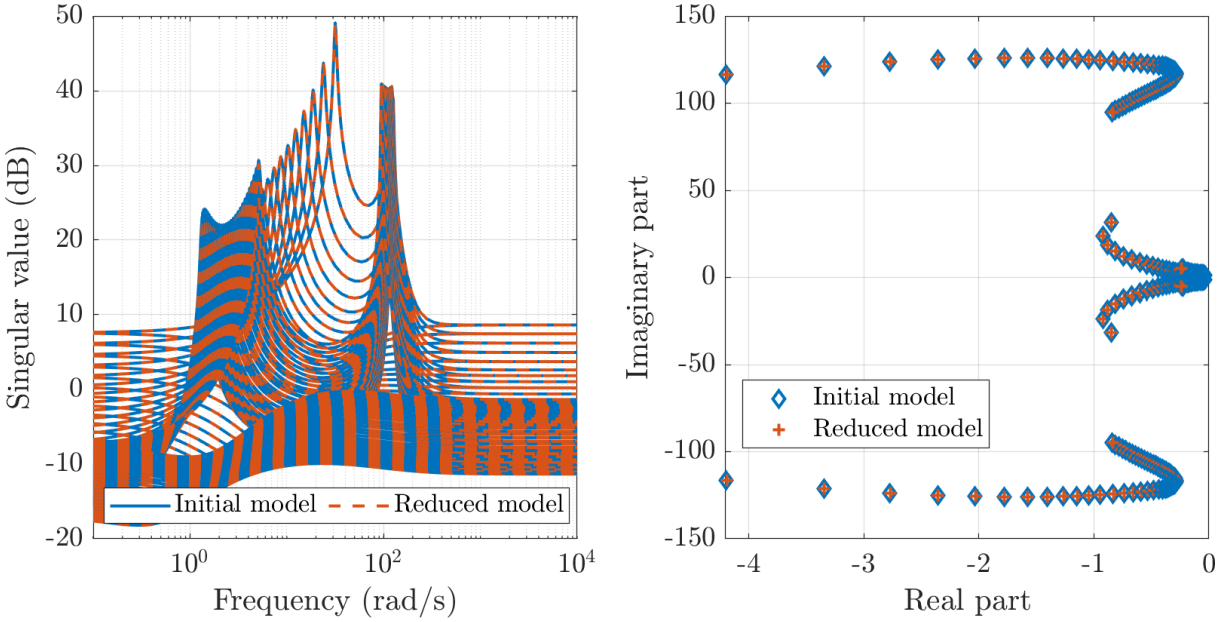

Figure 2.18: Singular values (left) and poles (right) of the linearised pitch/yaw channels along a ballistic trajectory: initial model and reduced model

be allocated to the four actuators. A natural choice for the allocation matrix is:

$$\begin{bmatrix} \delta_{1,c} \\ \delta_{2,c} \\ \delta_{3,c} \\ \delta_{4,c} \end{bmatrix} = T_{VR}(\phi_f)^\dagger \begin{bmatrix} \delta_{p,c} \\ \delta_{q,c} \\ \delta_{r,c} \end{bmatrix} = \begin{bmatrix} 1 & -\sin\phi_f & \cos\phi_f \\ 1 & \cos\phi_f & \sin\phi_f \\ 1 & \sin\phi_f & -\cos\phi_f \\ 1 & -\cos\phi_f & -\sin\phi_f \end{bmatrix} \begin{bmatrix} \delta_{p,c} \\ \delta_{q,c} \\ \delta_{r,c} \end{bmatrix} \tag{2.63}$$

where $T_{VR}(\phi_f)^\dagger = T_{RV}(\phi_f)$ denotes the Moore-Penrose pseudo-inverse of $T_{VR}(\phi_f)$, which in this case is also a right-inverse (i.e. $T_{VR}(\phi_f)T_{RV}(\phi_f) = I_3$).

The characteristics of the servomotor model are gathered in Table 2.1. It is worth noting that the selected natural frequency is relatively small compared to the typical natural frequency of actuators embedded in highly manoeuvrable missiles, which is around 40 Hz [Tsourdos and White, 2005; Jackson, 2010].

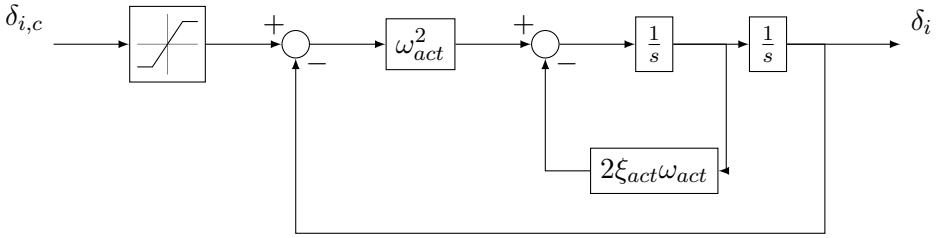

Figure 2.19: Block-diagram representation of a canard servomotor with position saturation

Table 2.1: Actuator parameters

Symbol	Parameter	Value
ω_{act}	Frequency	$2\pi \cdot 20$ rad/s
ξ_{act}	Damping ratio	0.781
δ_{sat}	Amplitude saturation	± 10 deg

2.5.2 Sensor models

The fuse is equipped with accelerometers providing measurements $(n_{z,m}, n_{y,m})$ of the load factors, and with gyroscopes providing measurements $(p_{f,m}, q_m, r_m)$ of the angular rates. In addition, sensors from the servomotors give measurements $(\delta_{1,m}, \delta_{2,m}, \delta_{3,m}, \delta_{4,m})$ of the canard deflection angles. Equation (2.37) can then be used to obtain measurements $(\delta_{p,m}, \delta_{q,m}, \delta_{r,m})$ of the virtual control signals. For simplicity, all sensors are given the same dynamics, described by a first-order model of natural frequency $\omega_s = 2\pi \cdot 133$ rad/s.

Remark 2. *The impact of the position of the sensors is not taken into account in this study. The signals $(n_{z,m}, n_{y,m})$ then correspond to the measured load factors at the projectile centre of mass. A more representative model could be obtained by applying the Grubin transformation [Zipfel, 2007], as done in [Sève et al., 2017b].*

2.6 Uncertainty modelling

2.6.1 Airframe parametric uncertainties

Uncertainties on the airframe dynamics originate primarily from uncertainties on the aerodynamic coefficients. These are due to limitations on wind-tunnel measurements and computational fluid dynamics results. The uncertainty levels are given in Table 2.2, based on values reported by PRODAS [Arrow Tech Associates, 1999-2021] for a spin-stabilised projectile. In addition, a 40% uncertainty is considered on the viscous friction coefficient K_v, affecting the roll channel.

Table 2.2: Aerodynamic coefficient uncertainties

Coefficient	Uncertainty (%)	Coefficient	Uncertainty (%)
C_A	3	-	-
$C_{N\alpha}$	6	$C_{m\alpha}$	3
$C_{Yp\alpha}$	33	$C_{np\alpha}$	25
-	-	C_{lp}	15
-	-	C_{mq}	15
$C_{N\delta}$	15	$C_{l\delta}$	15
-	-	$C_{m\delta}$	15

Remark 3. *Norm-bounded dynamic uncertainties could be added to the actuator models, representing high-order neglected dynamics. However, such LTI uncertainties were found to have little impact on nonlinear closed-loop simulation results.*

2.6.2 LFR modelling

A convenient way to represent uncertain LTI systems is to gather and separate all uncertainties from the nominal system $M(s)$ into a block-diagonal operator of the form:

$$\Delta(s) = \text{diag}(\Delta_1(s), \ldots, \Delta_N(s)) \tag{2.64}$$

where each $\Delta_i(s)$ can be:

- either a time-invariant diagonal matrix $\Delta_i(s) = \delta_i I_{n_i}$, where δ_i is a real or complex parametric uncertainty,
- or a stable and proper real-rational unstructured transfer function, representing neglected dynamics.

The set of matrices with the block-diagonal structure described above is denoted $\mathbf{\Delta}$, and corresponds to the set of physically meaningful uncertainties. The resulting $(M(s), \Delta(s))$ interconnection, which is shown in Figure 2.20, is called a Linear Fractional Representation (LFR). If all uncertainties are bounded, the LFR can be normalised so that physically meaningful uncertainties are restricted to $\mathcal{B}_{\mathbf{\Delta}} = \{\Delta(s) \in \mathbf{\Delta} : \|\Delta(s)\|_\infty \leq 1\}$.

With respect to the generic notation used on Figure 2.20, the transfer function from the input u to the output y of the system is then given by the upper Linear Fractional Transformation

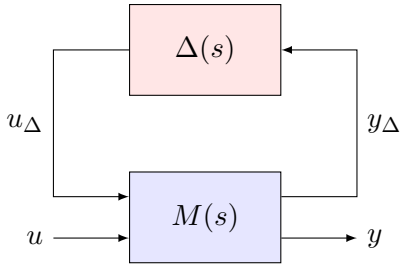

Figure 2.20: LFR of an uncertain system

(LFT):

$$\mathcal{T}_{u\to y}(s) = \mathcal{F}_u(M(s), \Delta(s)) = M_{22}(s) + M_{21}(s)\Delta(s)I - M_{11}(s)\Delta(s)^{-1}M_{12}(s) \tag{2.65}$$

where $M(s) = \begin{bmatrix} M_{11}(s) & M_{12}(s) \\ M_{21}(s) & M_{22}(s) \end{bmatrix}$ is a partitioning of $M(s)$ compatible with the dimensions of $\Delta(s)$ and of the signals u and y.

Systematic methods exist to go from a state-space representation with uncertain coefficients to an LFR, although these methods give no guarantee of minimality for the size of $\boldsymbol{\Delta}$. This can become an issue, since the size of $\boldsymbol{\Delta}$ can have a significant impact not only on computational time, but also on the conservatism of robustness analysis methods. In this context, the GSS library of the SMAC toolbox [Biannic and Roos, 2012-2021] implements a method based on Kalman decomposition [D'Andrea and Khatri, 1997] to build LFRs that may not always be minimal, but are generally of reasonable complexity.

The GSS library is therefore used to obtain, for fixed values of the reduced parameter vectors ($\boldsymbol{\lambda}_R$ for the roll channel, and $\boldsymbol{\lambda}_{PY}$ for the pitch/yaw channels), LFRs including the actuator, airframe, and sensor dynamics, along with the aerodynamic uncertainties.

The open-loop model for the roll channel is thus described by a family of upper LFT parametrised by $\boldsymbol{\lambda}_R$:

$$\mathcal{T}_{\boldsymbol{u}_R\to\boldsymbol{y}_R}(s, \boldsymbol{\lambda}_R) = \mathcal{F}_u(M_R(s, \boldsymbol{\lambda}_R), \Delta_R) \tag{2.66}$$

with:

- input $\boldsymbol{u}_R = \delta_{p,c}$ and outputs $\boldsymbol{y}_R = [\phi_{f,m}\ p_{f,m}]^T$,
- $M_R(s, \boldsymbol{\sigma}_R)$ an LTI system with 12 states (actuators + airframe roll channel + sensors: $8 + 2 + 2$),
- the uncertainty block Δ_R a 3×3 block belonging to the set:

$$\mathcal{B}_{\boldsymbol{\Delta}R} = \{\text{diag}(\delta_{C_A}, \delta_{C_{l\delta}}, \delta_{K_v}) \colon \delta_\bullet \in [-1, 1]\} \tag{2.67}$$

  and containing 3 real parametric blocks of size 1×1.

Similarly, a family of upper LFT parametrised by $\boldsymbol{\lambda}_{PY} = [V\ h\ p_a]^T$ is computed for the pitch/yaw channels:

$$\mathcal{T}_{\boldsymbol{u}_{PY}\to\boldsymbol{y}_{PY}}(s, \boldsymbol{\lambda}_{PY}) = \mathcal{F}_u(M_{PY}(s, \boldsymbol{\lambda}_{PY}), \Delta_{PY}) \tag{2.68}$$

with:

- inputs $\boldsymbol{u}_{PY} = [\delta_{q,\varepsilon,c}\ \delta_{r,\varepsilon,c}]^T$ the deviation of the commanded virtual control signals to the trim values, and outputs $\boldsymbol{y}_{PY} = [n_{z,\varepsilon,m}\ n_{y,\varepsilon,m}\ q_{\varepsilon,m}\ r_{\varepsilon,m}\ \delta_{q,\varepsilon,m}\ \delta_{r,\varepsilon,m}]^T$ the relevant measurements for pitch/yaw control,
- $M_{PY}(s, \boldsymbol{\lambda}_{PY})$ an LTI system with 20 states (actuators + airframe pitch/yaw channel + sensors: $8 + 4 + 8$),
- the uncertainty block Δ_{PY} a 16×16 block belonging to the set:

$$\begin{aligned}\mathcal{B}_{\boldsymbol{\Delta}PY} = \Big\{ &\mathrm{diag}(\delta_{C_{N\alpha}} I_2, \delta_{C_{N\delta}} I_2, \delta_{C_A} I_2, \delta_{C_{Yp\alpha}} I_2, \delta_{C_{m\alpha}} I_2, \\ &\delta_{C_{mq}} I_2, \delta_{C_{m\delta}} I_2, \delta_{C_{np\alpha}} I_2) \colon \delta_\bullet \in [-1, 1] \Big\}\end{aligned} \tag{2.69}$$

  and containing 8 real parametric blocks of size 2×2.

2.7 Conclusion

In this chapter, an open-loop model of a dual-spin projectile compatible with gain scheduling control design techniques has been developed. The projectile concept and flight scenario are presented, and two separate control problems are identified. The first control problem is dedicated to the stabilisation of the fuse roll angle. The second one relates to the guided phase and to the pitch/yaw channels. Nonlinear equations describing the airframe are first established using flight mechanics and aeroballistics theory, and expressed in a non-rolling frame adapted to the application. These equations are implemented in Matlab/Simulink to build a ballistics trajectory simulator, which also allows to evaluate the trajectory deviation induced by constant canard deflections.

The relevant roll and pitch/yaw dynamics are separately linearised, reflecting the two previously mentioned control problems. The linearisation process leads to an LPV model for the roll channel, and a quasi-LPV model for the pitch/yaw channels. The latter is validated through an LTV simulation, and displays properties which are illustrative of well-known phenomena specific to spin-stabilised projectile. In order to decrease the number of scheduling variables for control design, a reduced yet accurate quasi-LPV model is considered, parametrised by the three most influential variables.

The airframe models are then augmented with actuator and sensor models, as well as with aerodynamic uncertainties. Complete open-loop models for the roll and pitch/yaw channels are subsequently obtained as parametrised LFRs. These LFRs constitute the entry point to the development of a gain scheduled baseline autopilot, which is the focus of the next chapter.

References

Arrow Tech Associates (1999-2021). *PRODAS V3*. Tech. rep. URL: `http://www.prodas.com`.

Biannic, J.-M. and Apkarian, P. (1999). "Missile autopilot design via a modified LPV synthesis technique". In: *Aerospace Science and Technology* 3.3, pp. 153–160.

Biannic, J.-M. and Roos, C. (2012-2021). *Generalized State Space: a new Matlab class to model uncertain and nonlinear systems as Linear Fractional Representations*. URL: `http://w3.onera.fr/smac/gss`.

Burchett, B., Peterson, A., and Costello, M. (2002). "Prediction of swerving motion of a dual-spin projectile with lateral pulse jets in atmospheric flight". In: *Mathematical and computer modelling* 35.7-8, pp. 821–834.

Cooper, G. R. and Costello, M. (2011). "Trajectory prediction of spin-stabilized projectiles with a liquid payload". In: *Journal of Spacecraft and Rockets* 48.4, pp. 664–670.

D'Andrea, R. and Khatri, S. (1997). "Kalman decomposition of linear fractional transformation representations and minimality". In: *Proceedings of the 1997 American Control Conference*. IEEE.

Davis, B., Malejko, G., Dohrn, R., Owens, S., Harkins, T., and Bischer, G. (2009). *Addressing the challenges of a thruster-based precision guided mortar munition with the use of embedded telemetry instrumentation*. Tech. rep. Army Research Lab Aberdeen Proving Ground MD.

Frost, G. and Costello, M. (2006). "Control Authority of a Projectile Equipped With an Internal Unbalanced Part". In: *Journal of Dynamic Systems, Measurement, and Control* 128.4, p. 1005.

Hahn, P. V., Frederick, R. A., and Slegers, N. (2009). "Predictive guidance of a projectile for hit-to-kill interception". In: *IEEE Transactions on Control Systems Technology* 17.4, pp. 745–755.

ISO2533 (1975). *International Standard Atmosphere*. International Organization for Standardization.

Jackson, P. (2010). "Overview of missile flight control systems". In: *Johns Hopkins APL Technical Digest (Applied Physics Laboratory)* 29, pp. 9–24.

Jitpraphai, T. and Costello, M. (2001). "Dispersion reduction of a direct fire rocket using lateral pulse jets". In: *Journal of Spacecraft and Rockets* 38.6, pp. 929–936.

Leith, D. J. and Leithead, W. E. (2000). "Survey of gain-scheduling analysis and design". In: *International Journal of Control* 73.11, pp. 1001–1025.

McCoy, R. L. (1999). *Modern Exterior Ballistics: The Launch and Flight Dynamics of Symmetric Projectiles*. Schiffer Publishing.

Mracek, C. and Ridgely, D. (2005). "Missile longitudinal autopilots: connections between optimal control and classical topologies". In: *AIAA guidance, navigation, and control conference and exhibit*, p. 6381.

Pellanda, P. C., Apkarian, P., and Tuan, H. D. (2002). "Missile autopilot design via a multi-channel LFT/LPV control method". In: *International Journal of Robust and Nonlinear Control* 12.1, pp. 1–20.

Rogers, J. and Costello, M. (2009). "A variable stability projectile using an internal moving mass". In: *Proceedings of the Institution of Mechanical Engineers, Part G: Journal of Aerospace Engineering* 223.7, pp. 927–938.

Rugh, W. J. and Shamma, J. S. (2000). "Research on gain scheduling". In: *Automatica* 36.10, pp. 1401–1425.

Sève, F., Theodoulis, S., Wernert, P., Zasadzinski, M., and Boutayeb, M. (2017a). "Flight dynamics modeling of dual-spin guided projectiles". In: *IEEE Transactions on Aerospace and Electronic Systems* 53.4, pp. 1625–1641.

Sève, F., Theodoulis, S., Wernert, P., Zasadzinski, M., and Boutayeb, M. (2017b). "Gain-scheduled H_∞ loop-shaping autopilot design for spin-stabilized canard-guided projectiles". In: *AerospaceLab Journal* Issue 13, December 2017, ISSN: 2107–6596.

Shamma, J. S. and Cloutier, J. R. (1993). "Gain-scheduled missile autopilot design using linear parameter varying transformations". In: *Journal of guidance, Control, and dynamics* 16.2, pp. 256–263.

Siouris, G. M. (2004). *Missile Guidance and Control Systems*. Springer.

Theodoulis, S., Gassmann, V., Brunner, T., and Wernert, P. (2013). "Fixed structure robust control design for the 155mm canard-guided projectile roll-channel autopilot". In: *21st Mediterranean Conference on Control and Automation*. IEEE.

Theodoulis, S. and Wernert, P. (2017). "Flight dynamics & control for smart munition: the ISL contribution". In: *IFAC-PapersOnLine* 50.1, pp. 15512–15517.

Tsourdos, A. and White, B. A. (2005). "Adaptive flight control design for nonlinear missile". In: *Control Engineering Practice* 13.3, pp. 373–382.

Wernert, P. (2005). *Simulations de trajectoires de projectiles à 6 degrés de liberté dans le cadre de la mécanique du vol avion. Partie 2 : validation dans le cas d'un projectile empenné de calibre 38 mm et d'un projectile gyroscopé de calibre 155 mm*. Tech. rep. ISL.

Wernert, P., Theodoulis, S., and Morel, Y. (2010). "Flight dynamics properties of 155 mm spin-stabilized projectiles analyzed in different body frames". In: *AIAA Atmospheric Flight Mechanics Conference*.

White, B. A., Bruyere, L., and Tsourdos, A. (2007). "Missile autopilot design using quasi-LPV polynomial eigenstructure assignment". In: *IEEE Transactions on Aerospace and Electronic Systems* 43.4, pp. 1470–1483.

Wise, K. A. (1990). "Bank-to-turn missile autopilot design using loop transfer recovery". In: *Journal of Guidance, control, and Dynamics* 13.1, pp. 145–152.

Wise, K. A. and Roy, D. J. B. (1998). "Agile missile dynamics and control". In: *Journal of Guidance, Control, and Dynamics* 21.3, pp. 441–449.

Zipfel, P. H. (2007). *Modeling and Simulation of Aerospace Vehicle Dynamics*. Second. American Institute of Aeronautics and Astronautics.

Chapter 3

Development of a gain scheduled baseline autopilot

Contents

3.1 Introduction

In the context of the studied application, the systems to control are an LPV system for the roll channel and a quasi-LPV system for the pitch/yaw channels. In accordance with the envisioned nominal flight scenario, two autopilots must be designed. The first one is dedicated

to the roll channel. Its role is to ensure fixed position of the fuse along the trajectory. In particular, it must counteract the mechanical friction between the spinning body and the fuse, and any other external disturbances that may occur. The second autopilot to design is associated to the pitch/yaw channels, and is responsible for the trajectory modification. Both problems feature a combination of parameter-dependency, model uncertainties, and potentially saturations, which are difficult to address simultaneously given existing design tools. To get around this difficulty, saturations are ignored in this chapter, leading to a so-called baseline autopilot. The resulting unconstrained closed-loop serves as the basis to the treatment of saturations through anti-windup compensation, which is addressed in Chapter 4. To deal with parameter-dependency, a gain scheduling approach is adopted. This choice is motivated by the simplicity and lack of conservatism of the approach, which makes it particularly suited for preliminary design.

This chapter is organised as follows. Section 3.2 contains reminders on gain scheduling techniques and robust control theory which will be used for controller synthesis and analysis in the application. Structured $\mathcal{H}_\infty$ synthesis is of particular interest to reduce the number of gains to be interpolated, and μ-analysis will be used to assess robustness against parametric uncertainties. In Section 3.3, theoretical contributions to a probabilistic extension of μ-analysis are presented and integrated into novel branch-and-bound algorithms for robustness analysis. Finally, the design and validation of the roll and pitch/yaw autopilots are addressed in Section 3.4 and Section 3.5 respectively, by using the reviewed $\mathcal{H}_\infty$, interpolation, and μ-analysis techniques.

3.2 Reminders on gain scheduling and robust control theory

3.2.1 Overview of the $\mathcal{H}_\infty$ control problem

The field of robust control theory emerged in the late 1970s and early 1980s [Dorato, 1987; Safonov, 2012], in part in response to the shortcomings of LQG (Linear-Quadratic-Gaussian) controllers [Athans et al., 1977; Doyle, 1978]. Attempts to address the lack of robustness of LQG controllers led to the LQG/LTR (Loop Transfer Recovery) methodology [Doyle and Stein, 1981; Stein and Athans, 1987], and to the more general $\mathcal{H}_2$ control framework. Meanwhile, the formulation of the $\mathcal{H}_\infty$ synthesis problem by [Zames, 1981] led to the development of $\mathcal{H}_\infty$ methods, which we outline hereafter.

Let us consider the system of Figure 3.1, which is described by:

$$\begin{aligned} \begin{bmatrix} z \\ y \end{bmatrix} &= P(s) \begin{bmatrix} w \\ u \end{bmatrix} = \begin{bmatrix} P_{11}(s) & P_{12}(s) \\ P_{21}(s) & P_{22}(s) \end{bmatrix} \begin{bmatrix} w \\ u \end{bmatrix} \\ u &= K(s)y \end{aligned} \tag{3.1}$$

where $P(s)$ is a model of the plant, and $K(s)$ is the controller, with both $P(s)$ and $K(s)$ real rational transfer matrices. In practice, $P(s)$ is an augmented plant, containing the open-loop system to control $G(s)$ and additional weighting functions capturing design specifications, as shown in Figure 3.2. Weighting functions are typically specified as first-order stable and proper systems of the form:

$$W(s) = \frac{s + \omega^*}{k_{HF}s + k_{LF}\omega^*} \tag{3.2}$$

which is such that $1/|W(j\omega)|$ is equal to k_{LF} at low frequencies, is equal to k_{HF} at high frequencies, and ω^* is the -3 dB cutoff frequency. Higher-order weights can be selected in order to have steeper slopes, and potentially improve performance [Skogestad and Postlethwaite, 2005].

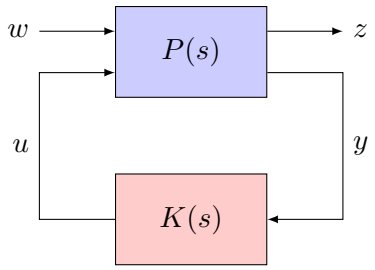

Figure 3.1: Standard interconnection for the $\mathcal{H}_\infty$ problem

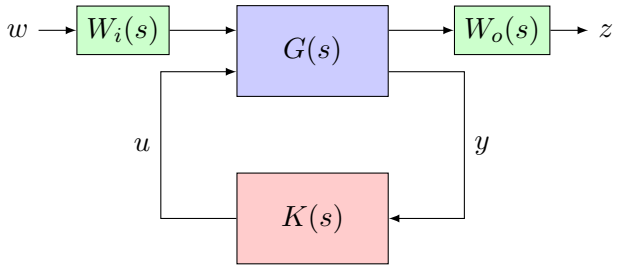

Figure 3.2: Weighted problem

The transfer function from the exogenous input w to the exogenous output z is given by the lower LFT:

$$\mathcal{T}_{w\to z}(s) = \mathcal{F}_l(P(s), K(s)) = P_{11}(s) + P_{12}(s)K(s)(I - P_{22}(s)K(s))^{-1}P_{21}(s) \tag{3.3}$$

The $\mathcal{H}_\infty$ control problem consists in solving an optimisation problem of the form:

$$\begin{aligned} \underset{K}{\text{minimise}} \quad & \left\|\mathcal{F}_l(P(s), K(s))\right\|_\infty \\ \text{subject to} \quad & K(s) \text{ stabilises } P(s) \\ & K(s) \in \mathcal{K} \end{aligned} \tag{3.4}$$

where $\mathcal{K}$ is the set where solutions $K(s)$ are sought. An interpretation in the time-domain of the minimisation of $\left\|\mathcal{F}_l(P(s), K(s)\right\|_\infty = \left\|\mathcal{T}_{w\to z}(s)\right\|_\infty$ is provided by:

$$\left\|\mathcal{T}_{w\to z}(s)\right\|_\infty = \max_{w(t)\neq 0} \frac{\|z(t)\|_2}{\|w(t)\|_2} \tag{3.5}$$

where the $\mathcal{L}_2$ norm of a signal x is defined as:

$$\|x(t)\|_2 = \left(\int_0^\infty \sum_i |x_i|^2 dt\right)^{\frac{1}{2}} = \sqrt{\int_0^\infty x(t)^T x(t) dt} \tag{3.6}$$

In other words, the $\mathcal{H}_\infty$ problem looks for a controller $K(s)$ which minimises the amplification factor $\left\|\mathcal{T}_{w\to z}(s)\right\|_\infty$ between the energy of the input w and the energy of the output z. In

applications, appropriate choice of the exogenous signals w and z and of the weighting functions in $P(s)$ allow to express typical control requirements, such as rejection of low-frequency disturbance, high-frequency noise attenuation, reference tracking/model matching in the low to mid-frequencies.

The resolution of the $\mathcal{H}_\infty$ problem has been a long studied problem. In [Doyle et al., 1988], an efficient solution using state-space methods is proposed, which relies on the resolution of two algebraic Riccati equations. However, this method requires the plant to satisfy some regularity assumptions. Later approaches reduce the problem to an LMI and are able to treat non-regular plants [Gahinet and Apkarian, 1994; Iwasaki and Skelton, 1994]. The above methods are implemented in the Matlab routine `hinfsyn` of the Robust Control Toolbox. Their main drawback is that they result in full-order (or unstructured) controllers, i.e. controllers that have same order as the plant $P(s)$. This makes them less appealing for industrial applications, where structured controllers (PIDs, lead-lag compensators, observer-based) are usually preferred. On the other hand, adding structural constraints in the set $\mathcal{K}$ leads to a BMI (bilinear matrix inequality) and a loss of convexity as a result.

A major breakthrough in structured controller synthesis comes from [Apkarian and Noll, 2006], where nonsmooth optimisation techniques are used. In Matlab, this development led to the `hinfstruct` routine, included in the Robust Control Toolbox. Although only local solutions are obtained, this inconvenience can be mitigated by resorting to multiple random initialisations. The flexibility of the approach is further increased with multi-objective and multi-model synthesis, implemented in the `systune` routine [Apkarian et al., 2014; Apkarian and Noll, 2017]. It allows to combine soft goals (cost to optimise) and hard goals (mandatory constraints) of different nature ($\mathcal{H}_\infty$, $\mathcal{H}_2$, or time-domain constraints). Both `hinfstruct` and `systune` allow to optimise the gains of a structured controller, rather than tune them as is classically done. However, the tuning effort is not entirely removed, and it may be necessary to adjust the requirements and weighting functions for the algorithms to converge to a satisfactory design. In this context, design procedures such as mixed-sensitivity, signal-based, or $\mathcal{H}_\infty$ loop-shaping remain relevant to manage the trade-off between conflicting requirements [Kwakernaak, 2002; Glover and McFarlane, 1989; Skogestad and Postlethwaite, 2005].

3.2.2 Review of interpolation methods for gain scheduling

In the context of designing a gain scheduled autopilot, $\mathcal{H}_\infty$ techniques are useful to compute local controllers at synthesis points taken in a grid of the flight envelope of the system. An interpolation method must then be chosen to determine the behaviour of the controller when the operating point does not belong to the set of synthesis points. A wide array of interpolation methods exist [Leith and Leithead, 2000; Rugh and Shamma, 2000], and a first distinction that can be made is between ad hoc methods on one hand, and methods that provide stability or performance guarantees on the other hand. Other properties impacted by the chosen interpolation method are the smoothness and continuity of the control signals, or the number of on-line operations.

Ad hoc interpolation methods include the following:

- controller switching: a partitioning of the flight envelope is done, such that each component

of the partition corresponds to one of the local controllers. The control signal is then computed as the output of one local controller at a time, which is switched based on the trajectory of the scheduling variables. The switching process may cause discontinuity of the control signals, although this can be avoided through an appropriate initialisation of the controller states. This interpolation method is exploited in [Hyde and Glover, 1990; Shimomura, 2003] for aircraft control.

- gain blending: this method applies when the local controllers share a common structure consisting of a potentially small number of gains, a typical example being the PID structure. The controller corresponding to an operating point is then obtained by interpolating the controller gains. Suppose for instance that we want to schedule a controller gain $K(a, b)$ according to the values of two parameters a and b. For $a_i \leq a < a_{i+1}$ and $b_j \leq b < b_{j+1}$, with (a_i, b_j), (a_i, b_{j+1}), (a_{i+1}, b_j), (a_{i+1}, b_{j+1}) being synthesis points, the value of $K(a, b)$ is computed as:

$$K(a, b) = (1 - k_b) \cdot K(a, b_j) + k_b \cdot K(a, b_{j+1}) \tag{3.7}$$

  where

$$K(a, b_j) = (1 - k_a) \cdot K(a_i, b_j) + k_a \cdot K(a_{i+1}, b_j) \tag{3.8}$$

$$K(a, b_{j+1}) = (1 - k_a) \cdot K(a_i, b_{j+1}) + k_a \cdot K(a_{i+1}, b_{j+1}) \tag{3.9}$$

  and

$$k_a = \frac{a - a_i}{a_{i+1} - a_i} \qquad k_b = \frac{b - b_j}{b_{j+1} - b_j} \tag{3.10}$$

  The computation generalises in a straightforward manner to the case where more than two scheduling variables are involved. This method has been applied with PID controllers in [Theodoulis and Duc, 2007b], [Theodoulis and Duc, 2008], respectively for a missile autopilot and a re-entry vehicle autopilot.

- controller output blending: the control signal at an operating point is obtained by interpolating the outputs of the neighbouring local controllers. This method requires 2^n controllers to run simultaneously (where n is the number of scheduling variables). An advantageous feature of this method is that it is applicable even in the case where the local controllers do not share the same structure. On the downside, some undesirable transient behaviours can appear when the scheduling variable crosses the boundary between regions, as some controllers are switched off and others are switched on. These effects can be mitigated through an appropriate initialisation of the controller states, but the process is not trivial. This method is applied in e.g. [Lawrence et al., 1998; Buschek and Dold, 2001; Theodoulis and Duc, 2007a] for the design of missile autopilots.

- methods interpolating various parameters characterising the local controllers: zeros/poles, transfer function coefficients, state-space coefficients, or solutions of algebraic Riccati equations.

While ad hoc techniques work well in many industrial applications, they rely on a grid of the operating domain and, more importantly, ignore the nonstationary nature of parameter

variations, leading to a lack of stability and performance guarantees. This shortcoming motivated the development of theoretically justified interpolation methods. An early work in this direction is the pole placement procedure of [Shahruz and Behtash, 1992] for state feedback control. More general approaches are proposed in [Stilwell and Rugh, 1999; Stilwell and Rugh, 2000], where stability-preserving interpolation techniques for observer-based controllers, transfer functions, and state-space matrices are presented. These techniques require that the local controllers satisfy a stability covering condition, and allow to ensure closed-loop stability of the scheduled system for slowly varying parameters. Other interpolation methods relying on the Youla-Kucera parametrisation are reported in [Rasmussen and Alleyne, 2009; Bianchi and Sánchez-Peña, 2011].

3.2.3 Reminders on μ-analysis

Robustness analysis aims to check whether the stability or performance of the closed-loop system is preserved when modelling errors affect the system. As described in Section 2.6, uncertainties can be gathered in an operator $\Delta(s)$ belonging to a block-diagonal structure $\mathbf{\Delta}$. Such uncertain closed-loop systems can be represented as the general interconnection of Figure 3.3. For robust stability analysis, the exogenous signals w and z can be removed, and the interconnection is rewritten as the LFR $(M(s), \Delta(s))$ of Figure 3.4.

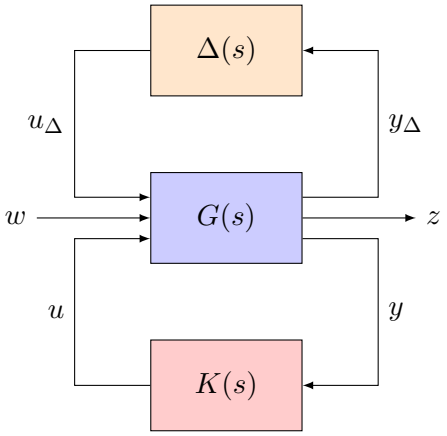

Figure 3.3: Uncertain closed-loop system

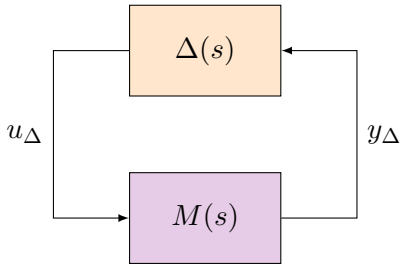

Figure 3.4: LFR for robust stability analysis

Following this modelling step, a first stability result is provided by the small gain theorem [Zames, 1966; Zhou and Doyle, 1998]:

Theorem 3.1 (Small gain theorem)**.** *The $(M(s), \Delta(s))$ interconnection is stable for all uncertainties $\Delta(s)$ such that $\|\Delta(s)\|_\infty < k$ if and only if*

$$\|M(s)\|_\infty \leq \frac{1}{k} \tag{3.11}$$

However, this result ignores the fact that $\Delta(s) \in \mathbf{\Delta}$ and is thus conservative. For a more relevant analysis, the values taken by $\Delta(s)$ should be restricted to the set $\mathbf{\Delta}$ of physically meaningful uncertainties. This can be achieved by using the structured singular value, which was introduced by [Doyle, 1982; Safonov, 1982] and is defined below:

Definition 3.2 (Structured singular value)**.** *Let $\omega \in \mathbb{R}_+$ be a given frequency. If no matrix $\Delta(s) \in \mathbf{\Delta}$ makes the $(M(s), \Delta(s))$ interconnection unstable, then the structured singular value $\mu_{\mathbf{\Delta}}(M(j\omega))$ is defined to be equal to zero. Otherwise:*

$$\mu_{\mathbf{\Delta}}(M(j\omega)) = \frac{1}{\min\limits_{\Delta \in \mathbf{\Delta}} \{\overline{\sigma}(\Delta) \colon \det(I - M(j\omega)\Delta(j\omega)) = 0\}} \tag{3.12}$$

A structured version of the small gain theorem follows.

Theorem 3.3 (Small gain theorem for structured uncertainties)**.** *The $(M(s), \Delta(s))$ interconnection is stable for all uncertainties $\Delta(s) \in k\mathcal{B}_{\mathbf{\Delta}}$ if and only if*

$$\sup_{\omega \in \mathbb{R}_+} \mu_{\mathbf{\Delta}}(M(j\omega)) \leq \frac{1}{k} \tag{3.13}$$

where $k\mathcal{B}_{\mathbf{\Delta}} = \{\Delta(s) \in \mathbf{\Delta} \colon \|\Delta(s)\|_\infty < k\}$.

Finally, we introduce the robust stability margin k_r.

Definition 3.4 (Robust stability margin)**.** *The robust stability margin k_r is defined as the largest value of k for which Equation* (3.13) *holds, i.e.*

$$k_r = \frac{1}{\sup\limits_{\omega \in \mathbb{R}_+} \mu_{\mathbf{\Delta}}(M(j\omega))} \tag{3.14}$$

Computation of the robust stability margin is in general NP-hard [Braatz et al., 1994]. For this reason, upper and lower bounds are computed instead, and numerous algorithms have been developed in order to make these bounds as accurate as possible. A lower bound $\underline{k_r}$ provides a guaranteed, but pessimistic, robust stability margin, whereas an upper bound $\overline{k_r}$ gives the size of a destabilising uncertainty. When the uncertainties are assumed to be bounded, it is convenient to normalise the $(M(s), \Delta(s))$ interconnection so that all admissible uncertainties $\Delta(s) \in \mathbf{\Delta}$ lie in the unit ball $\mathcal{B}_{\mathbf{\Delta}} = \{\Delta(s) \in \mathbf{\Delta} \colon \|\Delta(s)\|_\infty < 1\}$. In this case, validation of robust stability amounts to verifying that the system is stable for all $\Delta(s) \in \mathcal{B}_{\mathbf{\Delta}}$, i.e. that $k_r > 1$. We can then conclude on the robustness of the system if:

- $\underline{k_r} > 1$, in which case the system is robustly stable,

- $\overline{k_r} < 1$, in which case the system is not robustly stable.

No conclusion can be drawn if $\underline{k_r} < 1$ and $\overline{k_r} > 1$. This motivates reducing the gap between the bounds as much as possible in order to improve the assessment of robustness. Much work has been done in that sense, see e.g. [Roos and Biannic, 2010; Roos and Biannic, 2015], and some of the most efficient algorithms are implemented in the SMART library of the SMAC toolbox, as detailed in [Roos et al., 2011; Roos, 2013].

The following example is simple enough to allow a graphical representation, and is used here to illustrate the above notion. Let us consider the system given by the state-space representation:

$$\begin{aligned} \dot{x} &= \begin{bmatrix} 0 & 1 \\ -a_1 & -a_2 \end{bmatrix} x + \begin{bmatrix} 0 \\ 1 \end{bmatrix} u \\ y &= \begin{bmatrix} 1 & 0 \end{bmatrix} x \end{aligned} \tag{3.15}$$

where a_1 and a_2 are two uncertain parameters described by:

$$\begin{aligned} a_1 &= 1 + 2\delta_1, \qquad |\delta_1| \leq 1 \\ a_2 &= 0.8 + \delta_2, \qquad |\delta_2| \leq 1 \end{aligned} \tag{3.16}$$

In this particular case, the stability and instability domains can be calculated analytically (for instance using the Routh criterion). These are represented on Figure 3.5 in green and red respectively. Meanwhile, the stability domain obtained from computing the robust stability margin $k_r = 0.5$ is delimited by the black square and is clearly conservative.

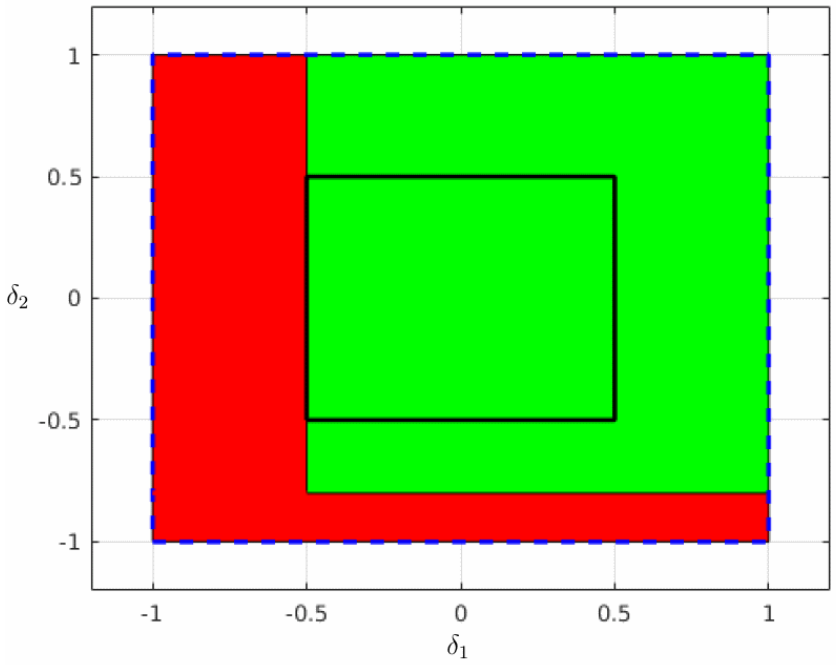

Figure 3.5: Stability and instability domains on an academic example

A way to address this issue is to implement a branch-and-bound algorithm to explore the whole parametric uncertainty domain and get a more precise picture of the stability domain [Newlin and Young, 1992]. The idea is to partition the unit ball $\mathcal{B}_\delta = [-1, 1]^N$, with N the

number of real parametric uncertainties[1], into smaller boxes until each box of the partitioning has either guaranteed stability, or is deemed sufficiently small to be neglected. Taking the union of the boxes with guaranteed stability leads to an approximation D_s of the stability domain. Algorithm 1 implements this approach in a basic way.

Algorithm 1 Branch-and-bound μ-analysis

Inputs: $M(s)$, $\mathbf{\Delta}, l_{min}$
Output: D_s
$\mathcal{L} \leftarrow \{\mathcal{B}_{\boldsymbol{\delta}}\}$ ▷ $\mathcal{L}$ is the list of all boxes left to investigate
$D_s \leftarrow \emptyset$
while $\mathcal{L} \neq \emptyset$ **do**
    select and remove a box $\tilde{\Theta}$ from $\mathcal{L}$
    compute the interconnection $\left(\tilde{M}(s), \tilde{\Delta}\right)$ normalised w.r.t. $\tilde{\Theta}$
    compute a guaranteed robust stability margin $\underline{k_r}$ for $(\tilde{M}(s), \tilde{\Delta})$
    if $(\tilde{M}(s), \tilde{\Delta})$ is nominally stable and $\underline{k_r} \geq 1$ **then**
        add $\tilde{\Theta}$ to D_s
    else if the longest edge of $\tilde{\Theta}$ is longer than l_{min} **then**
        bisect $\tilde{\Theta}$ along its longest edge
        add the boxes obtained by partitioning $\tilde{\Theta}$ into $\mathcal{L}$
    end if
end while

Normalisation of the interconnections is done such that the parametric uncertainties within Δ cover the desired box $\tilde{D}$ when $\tilde{\Delta}$ covers the unit ball. Suppose to simplify notations that $\Delta(s)$ only contains real parametric uncertainties:

$$\Delta(s) = \Delta = \mathrm{diag}(\delta_1 I_{n_1}, \ldots, \delta_N I_{n_N}) \tag{3.17}$$

Then normalisation can be achieved using an affine transformation $\Delta = \tilde{\Delta} Q + R$, where:

$$Q = \mathrm{diag}\left(\frac{\overline{\delta}_1 - \underline{\delta}_1}{2} I_{n_1}, \ldots, \frac{\overline{\delta}_N - \underline{\delta}_N}{2} I_{n_N}\right) \tag{3.18}$$

$$R = \mathrm{diag}\left(\frac{\overline{\delta}_1 + \underline{\delta}_1}{2} I_{n_1}, \ldots, \frac{\overline{\delta}_N + \underline{\delta}_N}{2} I_{n_N}\right) \tag{3.19}$$

and $\underline{\delta}_i$, $\overline{\delta}_i$ correspond to the lower and upper bounds on δ_i in the box $\tilde{\Theta}$. In the case where $\Delta(s)$ contains LTI or complex uncertainties, the corresponding blocks are kept identical through the normalisation.

When applied to the same example as above, Algorithm 1 leads to the partitioning depicted in Figure 3.6, and it can be observed that the computed stability domain is a very good approximation of the exact one. A major drawback of this strategy is the number of generated boxes, which can lead to prohibitive computational time. In particular, the treatment of boxes where the interconnection is unstable is unsatisfactory, because these domains are never identified as such by the algorithm. This is materialised by the use of the blue colour instead of the red one, which represents domains of undetermined stability. This leads to unnecessary robust stability

[1]The distinction between $\mathcal{B}_{\mathbf{\Delta}}$ and $\mathcal{B}_{\boldsymbol{\delta}}$ is that the former denotes the operator in the normalised LFR, in which uncertain parameters may be repeated, while the latter is the set of admissible values of the uncertainties.

margin computations and box generations until the generated boxes reach a negligible size. This issue will be addressed in Section 3.3.

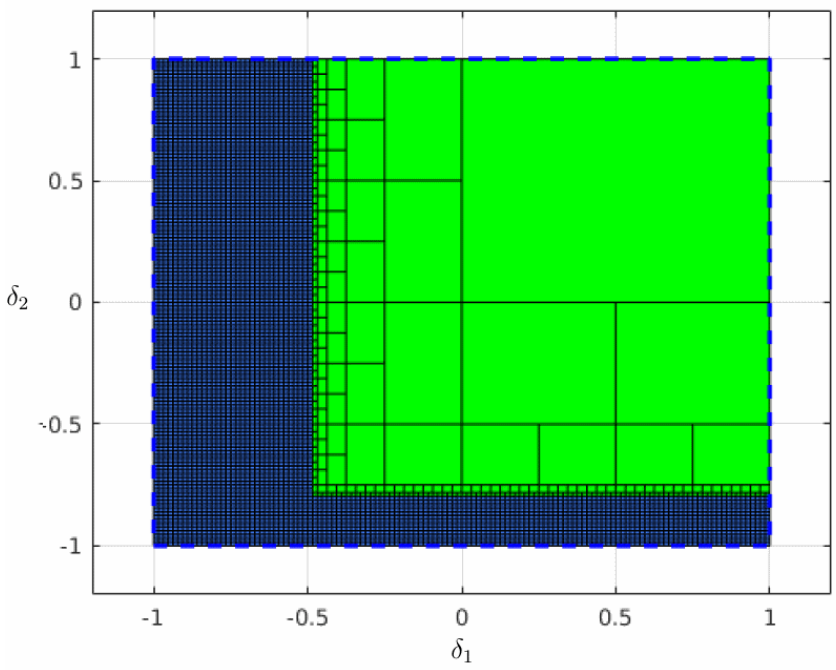

Figure 3.6: Guaranteed stability domain (green) obtained with branch-and-bound

Algorithm 1 features a simple partitioning scheme based on the longest edge. This is done because it is unreasonable in general to bisect along all directions, as this would generate 2^N additional boxes at each inconclusive iteration of the algorithm. Thus selecting one, or at least a small number of directions, is required to prevent computational time from becoming prohibitive. However, taking the direction of the longest edge is not necessarily the best choice, and μ-sensitivities, introduced by [Braatz and Morari, 1991], can be used as an alternative heuristics.

Definition 3.5 (μ-sensitivities)**.** *Let $M = M(j\omega)$ be the frequency response of $M(s)$ at a given frequency ω. Pre- and post-multiply Δ by a diagonal matrix $A(\varepsilon_j) = \mathrm{diag}(I_{n_1}, \ldots, (1-\varepsilon_j)I_{n_j}, \ldots, I_{n_N})$ so that the jth uncertainty is multiplied by $(1-\varepsilon_j)^2$, while the other uncertainties stay at their nominal values. The jth μ-sensitivity is then defined as:*

$$S_j^\mu = \frac{\partial}{\partial \varepsilon_j} \overline{\mu}_{\mathbf{\Delta}}(M_{\varepsilon_j}) = \lim_{\varepsilon_j \to 0^+} \frac{\left| \overline{\mu}_{\mathbf{\Delta}}(M) - \overline{\mu}_{\mathbf{\Delta}}(M_{\varepsilon_j}) \right|}{\varepsilon_j} \tag{3.20}$$

where $\overline{\mu}_{\mathbf{\Delta}}$ is a μ-upper bound and $M_{\varepsilon_j} = A(\varepsilon_j) M A(\varepsilon_j)$.

Intuitively, higher values of S_j^μ characterise a greater influence of the jth uncertainty on the value of $\overline{\mu}_{\mathbf{\Delta}}(M)$. It is thus fairly natural to consider the edge corresponding to the highest μ-sensitivity as a candidate for the bisection, and good results using this method have been reported in [Lesprier et al., 2015].

3.2.4 Reminders on the skewed structured singular value

The skewed structured singular value

The skewed structured singular value is a useful generalisation of the structured singular value that serves as the basis to tackle other robustness analysis problems, such as the worst-case $\mathcal{H}_\infty$ performance and worst-case input-output margins [Fan and Tits, 1992; Roos, 2010; Lescher and Roos, 2011]. The structure $\mathbf{\Delta}$ is now split into two distinct block structures $\mathbf{\Delta} = \text{diag}(\mathbf{\Delta}_1, \mathbf{\Delta}_2)$, and admissible uncertainties are taken in $\mathbf{\Delta}_s = \text{diag}(\mathcal{B}_{\mathbf{\Delta}_1}, \mathbf{\Delta}_2)$. Thus, the distinction is made between bounded and unbounded uncertainties, and the classical case is recovered if $\mathbf{\Delta}_1$ is empty. This framework leads to analogous definitions of the structured singular value and robust stability margin in the skewed case that can be found in [Fan and Tits, 1992] and are recalled here.

Definition 3.6 (Skewed structured singular value)**.** *Let $\omega \in \mathbb{R}_+$ be a given frequency. If no matrix $\Delta = \text{diag}(\Delta_1, \Delta_2) \in \mathbf{\Delta}_s$ makes the interconnection unstable, then the skewed structured singular value $\nu_{\mathbf{\Delta}_s}(M(j\omega))$ is defined to be equal to zero. Otherwise:*

$$\nu_{\mathbf{\Delta}_s}(M(j\omega)) = \frac{1}{\min\limits_{\Delta \in \mathbf{\Delta}_s} \{\overline{\sigma}(\Delta_2), \det(I - M(j\omega)\Delta) = 0\}} \tag{3.21}$$

Theorem 3.7 (Skewed robust stability margin)**.** *The $(M(s), \Delta(s))$ interconnection is stable for all uncertainties $\Delta \in k_s \mathcal{B}_{\mathbf{\Delta}_s}$, where k_s is the skewed robust stability margin, defined as:*

$$k_s = \frac{1}{\sup\limits_{\omega \in \mathbb{R}_+} \nu_{\mathbf{\Delta}_s}(M(j\omega))} \tag{3.22}$$

The computation of k_s is also NP hard in the general case, and lower and upper bounds are computed instead. The SMART library implements methods to compute these bounds, as detailed in [Roos, 2013].

Worst-case $\mathcal{H}_\infty$ performance

With reference to Figure 3.7, worst-case $\mathcal{H}_\infty$ performance analysis consists in verifying that the performance level of the system remains satisfactory for all possible values of the uncertainties, i.e. for a given $\gamma > 0$, we have:

$$\max_{\Delta \in \mathcal{B}_{\mathbf{\Delta}}} \|\mathcal{F}_u(M(s), \Delta(s)\|_\infty \leq \gamma \tag{3.23}$$

It can be assumed without loss of generality that both w and z are q-dimensional signals. The idea to tackle this problem is to consider an augmented uncertainty $\Delta_a \in \mathbf{\Delta}_a$, where $\mathbf{\Delta}_a = \text{diag}(\mathcal{B}_{\mathbf{\Delta}}, \mathbb{C}^{q \times q})$, the additional block $\mathbb{C}^{q \times q}$ being associated to the performance channel $\mathcal{T}_{w \to z}$. By the main loop theorem [Packard and Doyle, 1993]:

Proposition 3.8. *The following statements are equivalent:*

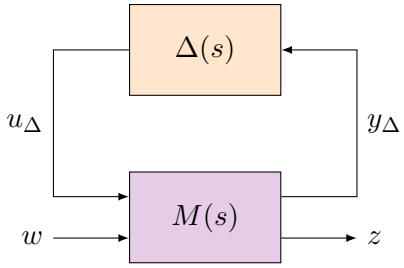

Figure 3.7: LFR for robust performance analysis

1. $\max_{\Delta \in \mathcal{B}_{\boldsymbol{\Delta}}} \|\mathcal{F}_u(M(s), \Delta)\|_\infty \leq \gamma$
2. $\forall \omega \in \mathbb{R}_+, \mu_{\boldsymbol{\Delta}_a}(WM(j\omega)) \leq 1$, *where* $W = \text{diag}(I_n, I_q/\gamma)$
3. $\forall \omega \in \mathbb{R}_+, \nu_{\boldsymbol{\Delta}_a}(M(j\omega)) \leq \gamma$

Thus, worst-case $\mathcal{H}_\infty$ performance analysis can be reformulated as a skew-μ problem, for which resolution methods are known.

3.3 Contribution to probabilistic μ-analysis

3.3.1 Motivation and framework

The structured singular value μ and its skewed version, presented in Section 3.2.3 and 3.2.4, are the preferred robustness analysis tool for uncertain linear dynamical systems within the control community. It allows a deterministic assessment of the bounds on the robust stability margin of an uncertain linear system in the presence of parametric uncertainties. However, despite its efficiency, a common criticism for the use of standard μ or skew μ-analysis in the clearance and certification processes is the lack of quantitative measures on the likelihood occurrence of the identified worst-cases. Therefore, for many problems the worst-case paradigm based on μ can be overly conservative [Khatri and Parrilo, 1998] because of the implicit assumption that each of the real uncertain parameters in the model has uniform probability distribution. In practice, it may be preferable to focus on assessing the risk of unlikely events to occur.

This explains why the Monte Carlo approach [Helton et al., 2006; Landau and Binder, 2014] remains the industrial standard. It is indeed rather simple and very close to the industrial needs, since it only involves an indirect simulation-based strategy where no analytical representation of the system is needed. It performs statistical modelling based on random sampling of the various uncertain parameters of the system. Subsequently, the probability that a given requirement satisfies a specific threshold is computed based on the probability distributions on the parameters. However, Monte Carlo methods can only provide soft bounds on the system requirement satisfaction, characterised by both an accuracy and a confidence level. A large sample size is needed to reach sufficient accuracy and confidence levels, leading to a significant computational effort.

In order to address the aforementioned shortcomings of classical μ-analysis and Monte Carlo techniques, researchers started in the 1990s to investigate probabilistic robustness analysis, and

notably probabilistic μ [Zhu et al., 1996; Khatri and Parrilo, 1998]. The primary drivers are to reduce conservatism and computational load. These approaches seek to combine worst-case bounds with probabilistic information, so as to overcome issues related to the conservatism of the μ-analysis paradigm. In this way, both probabilistic and deterministic aspects of the performance of a system may be assessed. In contrast to stochastic methods, probabilistic μ-analysis is deterministic and exhaustive in the exploration of the parametric space. However, instead of computing the conservative worst-case μ value, the goal is to compute the probability distribution of μ, given a probability distribution on the set of uncertainties.

3.3.2 Enhanced branch-and-bound algorithm for robust stability assessment

With respect to Figure 3.4, suppose for simplicity that $\Delta(s)$ contains only real parametric uncertainties $\boldsymbol{\delta} = (\delta_1, \ldots, \delta_N)$ as in Equation (3.17). The latter are assumed to be independent random variables described by their probability density functions $\boldsymbol{f} = (f_1, \ldots, f_N)$. Then probabilistic robust stability analysis can be formalised as follows:

Problem 3.9 (Probabilistic robust stability)**.** *Compute the probability* $\overline{P}_{\boldsymbol{\Delta},f}(M(s))$ *that the interconnection* $(M(s), \Delta)$ *is unstable when* $\Delta \in \mathcal{B}_{\boldsymbol{\Delta}}$*.*

While exact computation is unsurprisingly not achievable in the general case, Algorithm 1 provides a domain $D_s \subset \mathcal{B}_{\boldsymbol{\delta}}$ of guaranteed stability, which can then lead to an upper bound on the sought probability, and thus validate the current design if the latter is smaller than a tolerance level ε. Moreover, this domain D_s of guaranteed stability conveniently takes the form of a finite union of disjoint boxes $D_s^{(k)}$:

$$D_s = \bigcup_k D_s^{(k)} \text{ where } D_s^{(k)} = \left[\underline{\delta}_1^{(k)}, \overline{\delta}_1^{(k)}\right] \times \cdots \times \left[\underline{\delta}_N^{(k)}, \overline{\delta}_N^{(k)}\right] \tag{3.24}$$

making its associated probability measure, noted $p(D_s)$, straightforward to compute:

$$p(D_s) = \sum_k p\Big(D_s^{(k)}\Big) \tag{3.25}$$

where:

$$p\Big(D_s^{(k)}\Big) = \Pr\Big(\underline{\delta}_i^{(k)} \leq \delta_i \leq \overline{\delta}_i^{(k)}, i = 1, \ldots, N\Big) = \prod_{i=1}^{N} \int_{\underline{\delta}_i^{(k)}}^{\overline{\delta}_i^{(k)}} f_i(\delta_i) d\delta_i \tag{3.26}$$

This approach was proposed for instance in [Falcoz et al., 2017].

It is worth stressing at this point that there is much interest in also calculating a lower bound on $\overline{P}_{\boldsymbol{\Delta},f}(M(s))$, not only to get a more accurate picture of the stability domain, but also potentially to quickly invalidate the current design with respect to the tolerance level ε. In this perspective, the computation of a domain of guaranteed instability $D_{\overline{s}}$ is desirable, so that $\overline{P}_{\boldsymbol{\Delta},f}(M(s))$ can be bounded as follows:

$$p(D_{\overline{s}}) \leq \overline{P}_{\boldsymbol{\Delta},f}(M(s)) \leq 1 - p(D_s) \tag{3.27}$$

The computation of $D_{\overline{s}}$ proves to be straightforward if one realises that μ-analysis based

methods consist essentially in detecting when some poles of the nominally stable system $M(s)$ reach the imaginary axis as the size of Δ increases. Indeed, the same methods applied to a nominally unstable system lead to a "robustness margin for instability". Algorithm 2, which was presented in [Thai et al., 2019], describes an enhanced branch-and-bound algorithm integrating both probabilistic aspects and this additional μ-analysis based instability test. Its termination is ensured by a user-defined thresholds $p_{min} \in [0, 1]$, which is the probability below which a box is not partitioned and declared of undetermined stability. Its primary role is to limit the number of generated boxes, and consequently the computational time of the algorithm. The drawback is that even if p_{min} is set very low, the union of all the neglected boxes may represent a significant probability measure if there is a large number of them. The algorithm outputs a partition of $\mathcal{B}_{\boldsymbol{\delta}}$ of the form:

$$\mathcal{B}_{\boldsymbol{\delta}} = D_s \cup D_{\overline{s}} \cup D_{s_u} \tag{3.28}$$

as well as the probability measure of each of the three components. These correspond to the domains of guaranteed stability, guaranteed instability, and undetermined stability respectively. The presence of the third domain D_{s_u} stems from the fact that in practice, the branch-and-bound algorithm can only approximate the domains of stability and instability, and not compute them exactly. Ideally, D_{s_u} should be as small as possible, although depending on the validation requirements, a coarse result can be sufficient to decide whether the considered system is stable enough.

Remark 4. *In practice, other stopping criteria can be considered for Algorithm 2. For instance, one can stop the algorithm when the probability of instability is guaranteed to be either below or above a given threshold p_{fail}. Another possibility is to exit the main loop when the probability of undetermined stability is guaranteed to be below a given threshold p_{undet}. These criteria can also be used in combination.*

Application of Algorithm 2 to the academic example of Section 3.2.3, with $p_{min} = 10^{-5}$ and assuming a uniform distribution of the uncertainties, leads to the partitioning of Figure 3.8, from which hard bounds on the probability $\overline{P}_{\boldsymbol{\Delta},f}(M(s))$ of instability can be deduced:

$$31.895\% = p(D_{\overline{s}}) \leq \overline{P}_{\boldsymbol{\Delta},f}(M(s)) \leq p(D_{\overline{s}}) + p(D_{s_u}) = 1 - p(D_s) = 32.968\% \tag{3.29}$$

This is a clear improvement over the analysis result shown of Figure 3.6. In particular, the computation of a domain of guaranteed instability, beside its relevance to robustness analysis, drastically reduces CPU time.

Interestingly, updating the probabilities with other distributions does not require to recompute a new partition of $\mathcal{B}_{\boldsymbol{\delta}}$, but only the probabilities associated to the boxes which form D_s, $D_{\overline{s}}$, and D_{s_u}. Assuming for example that the uncertainties δ_1 and δ_2 follow a truncated normal distribution of mean $m = 0$ and variance $\sigma^2 = 1/9$, the bounds on $\overline{P}_{\boldsymbol{\Delta},f}(M(s))$ become:

$$6.875\% = p(D_{\overline{s}}) \leq \overline{P}_{\boldsymbol{\Delta},f}(M(s)) \leq p(D_{\overline{s}}) + p(D_{s_u}) = 1 - p(D_s) = 7.532\% \tag{3.30}$$

These bounds are much more optimistic compared to those of Equation (3.29), highlighting the interest and potential of the probabilistic framework in reducing the conservatism of μ-analysis.

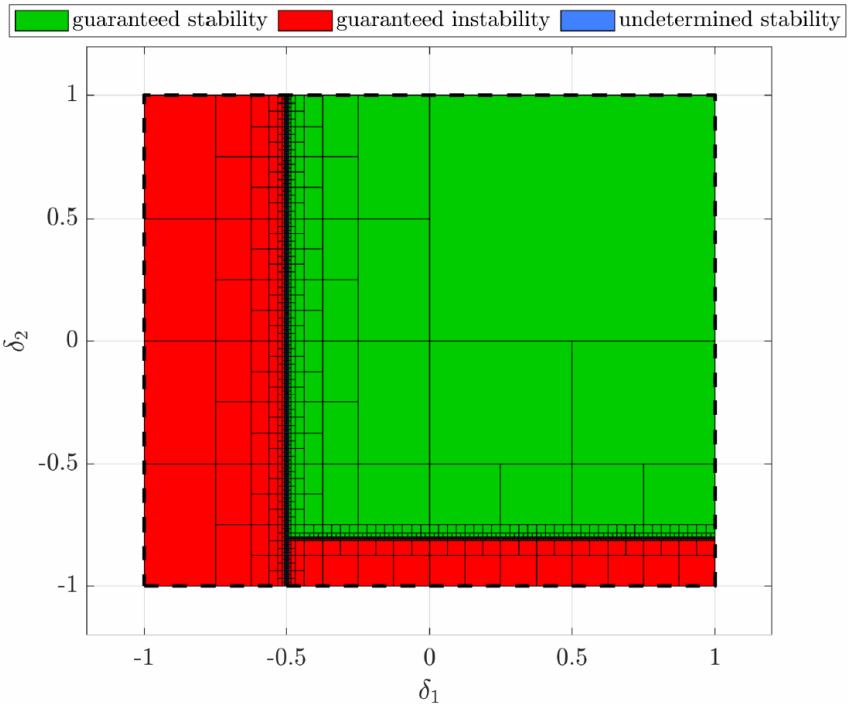

Figure 3.8: Branch-and-bound robust stability analysis (CPU time = 4.8 s)

Algorithm 2 Probabilistic μ-analysis for stability

Inputs: $M(s)$, $\mathbf{\Delta}$, $f_i(\delta_i)$ for $i = 1, \ldots, N$, p_{min}
Outputs: D_s, $D_{\bar{s}}$, D_{s_u}, $p(D_s), p(D_{\bar{s}}), p(D_{s_u})$
$\mathcal{L} \leftarrow \{\mathcal{B}_{\boldsymbol{\delta}}\}$ ▷ $\mathcal{L}$ constitutes the list of all boxes left to investigate
$D_s, D_{\bar{s}}, D_{s_u} \leftarrow \emptyset$
$p(D_s), p(D_{\bar{s}}), p(D_{s_u}) \leftarrow 0$
while $\mathcal{L} \neq \emptyset$ **do**
    select and remove the box $\tilde{D}$ from $\mathcal{L}$ with highest probability measure
    compute the interconnection $\left(\tilde{M}(s), \tilde{\Delta}\right)$ normalised wrt $\tilde{D}$
    compute a guaranteed robust stability margin $\underline{k_r}$ for $\left(\tilde{M}(s), \tilde{\Delta}\right)$
    if $\underline{k_r} \geq 1$ **then**
        if $\mathcal{F}_u(\tilde{M}(s), \tilde{\Delta})$ is nominally stable **then**
            add $\tilde{D}$ to D_s
            $p(D_s) \leftarrow p(D_s) + p(\tilde{D})$
        else
            add $\tilde{D}$ to $D_{\bar{s}}$
            $p(D_{\bar{s}}) \leftarrow p(D_{\bar{s}}) + p(\tilde{D})$
        end if
    else ▷ analysis was inconclusive on the current box
        if $p(\tilde{D}) > p_{min}$ **then**
            select a direction for cutting $\tilde{D}$
            partition $\tilde{D}$
            add the boxes obtained by partitioning $\tilde{D}$ into $\mathcal{L}$
        else
            add $\tilde{D}$ to D_{s_u}
            $p(D_{s_u}) \leftarrow p(D_{s_u}) + p(\tilde{D})$
        end if
    end if
end while

3.3.3 Probabilistic μ-analysis for worst-case $\mathcal{H}_\infty$ performance

Let us now focus on performance, and consider the standard interconnection of Figure 3.7, which is assumed to be stable on $\mathcal{B}_{\mathbf{\Delta}}$. Probabilistic worst-case $\mathcal{H}_\infty$ performance analysis can be formalised as follows:

Problem 3.10 (Probabilistic worst-case $\mathcal{H}_\infty$ performance)**.** *Given a performance level $\gamma > 0$, compute the probability $\overline{P}^{\gamma}_{\mathbf{\Delta},f}(M(s))$ that $\|\mathcal{T}_{w\to z}(s)\|_\infty > \gamma$ when $\Delta \in \mathcal{B}_{\mathbf{\Delta}}$.*

As with robust stability, the idea is to combine branch-and-bound with μ-analysis to compute both a domain of guaranteed performance satisfaction D_γ and a domain of guaranteed performance violation $D_{\overline{\gamma}}$, as well as associated probability measures. But despite the similarities, an additional difficulty arises. Indeed, distinguishing between stability and instability domains boils down to locating the poles of the nominal system either in the open left-half plane or in the right-half plane respectively. By contrast, while verifying performance satisfaction on the unit ball $\mathcal{B}_{\mathbf{\Delta}}$ can be done using Proposition 3.8, performance violation on $\mathcal{B}_{\mathbf{\Delta}}$ is equivalent to:

$$\min_{\Delta\in\mathcal{B}_{\mathbf{\Delta}}} \|\mathcal{F}_u(M(s),\Delta)\|_\infty > \gamma \tag{3.31}$$

which, as a minimax problem, is much more complicated than verifying performance satisfaction.

With the assumption that the performance channel is scalar (i.e. $q = 1$), the problem of verifying performance violation on $\mathcal{B}_{\mathbf{\Delta}}$ can be reformulated as follows:

Problem 3.11. *Given a performance level $\gamma > 0$, and assuming $\sup_{\omega\in\mathbb{R}_+} |M_{22}(j\omega)| > \gamma$, check whether*

$$\min_{\Delta\in\mathcal{B}_{\mathbf{\Delta}}} \sup_{\omega\in\mathbb{R}_+} |\mathcal{F}_u(M(j\omega),\Delta)| > \gamma \tag{3.32}$$

As a preliminary step to deriving a sufficient condition for performance violation, a useful property on LFT inversion is reminded (see e.g. [Doyle et al., 1991]).

Lemma 3.12. *Let $M = \begin{bmatrix} M_{11} & M_{12} \\ M_{21} & M_{22} \end{bmatrix}$, and assume that M_{22} is nonsingular. Then:*

$$(\mathcal{F}_u(M,\Delta))^{-1} = \mathcal{F}_u(N,\Delta) \tag{3.33}$$

with N given by:

$$N = \begin{bmatrix} M_{11} - M_{12}M_{22}^{-1}M_{21} & -M_{12}M_{22}^{-1} \\ M_{22}^{-1}M_{21} & M_{22}^{-1} \end{bmatrix} \tag{3.34}$$

The following proposition from [Thai et al., 2019] is then introduced. It is the key result, which derives a sufficient condition for Inequality (3.32) to hold, in the form of a skew-μ calculation of the inverse transfer $\mathcal{T}^{-1}_{w\to z}$.

Proposition 3.13. *Let $\mathcal{I} = \{\omega \in \mathbb{R}_+ : |M_{22}(j\omega)| > \gamma\}$, and for each $\omega \in \mathcal{I}$, let $N(j\omega)$ be*

such that $(\mathcal{F}_u(M(j\omega),\Delta))^{-1} = \mathcal{F}_u(N(j\omega),\Delta)$. *If there exists* $\omega_0 \in \mathcal{I}$ *such that*

$$\nu_{\mathbf{\Delta}_a}(N(j\omega_0)) < \frac{1}{\gamma} \tag{3.35}$$

where $\mathbf{\Delta}_a = \mathrm{diag}(\mathcal{B}_{\mathbf{\Delta}}, \mathbb{C})$, *then Inequality* (3.32) *holds, and performance violation is guaranteed for all* $\Delta \in \mathcal{B}_{\mathbf{\Delta}}$.

Proof. First, note that nominal performance violation in the scalar case is equivalent to

$$\sup_{\omega\in\mathbb{R}_+} |M_{22}(j\omega)| > \gamma \tag{3.36}$$

which guarantees that $\mathcal{I}$ is nonempty, and that $N(j\omega)$ is well-defined for each $\omega \in \mathcal{I}$. Next, assume that there exists $\omega_0 \in \mathcal{I}$ verifying $\nu_{\mathbf{\Delta}_a}(N(j\omega_0)) < \frac{1}{\gamma}$. From the main loop theorem ([Doyle et al., 1991]), this is equivalent to

$$\begin{aligned} &\mu_{\mathbf{\Delta}}(N_{11}(j\omega_0)) < 1 \\ &\max_{\Delta\in\mathcal{B}_{\mathbf{\Delta}}} |\mathcal{F}_u(N(j\omega_0),\Delta)| < \frac{1}{\gamma} \end{aligned} \tag{3.37}$$

Since $|\mathcal{F}_u(N(j\omega_0),\Delta)| = \dfrac{1}{|\mathcal{F}_u(M(j\omega_0),\Delta)|}$ for every $\Delta \in \mathcal{B}_{\mathbf{\Delta}}$, the second inequality of (3.37) can be rewritten as

$$\min_{\Delta\in\mathcal{B}_{\mathbf{\Delta}}} |\mathcal{F}_u(M(j\omega_0),\Delta)| > \gamma \tag{3.38}$$

which is a sufficient condition for Inequality (3.31) to hold. □

Remark 5. *The step to go from Equation* (3.37) *to Equation* (3.38) *cannot be easily generalised to higher performance channel dimension, i.e. to* $q > 1$.

An algorithm to verify performance violation directly follows from Proposition 3.13, as outlined in Algorithm 3.

Algorithm 3 Verification of performance violation

Inputs: $M(s)$, $\mathbf{\Delta}$, γ
Output: `true` if performance violation is guaranteed on $\mathcal{B}_{\boldsymbol{\delta}}$, `false` otherwise
if $\|M_{22}(s)\|_\infty \leq \gamma$ **then**
    return `false`
else
    select $\omega_0 \in \mathcal{I}$
    compute $\overline{\nu}_{\mathbf{\Delta}_a}(N(j\omega_0))$, where $N(j\omega_0)$ is given by Lemma 3.12
    if $\overline{\nu}_{\mathbf{\Delta}_a}(N(j\omega_0)) < 1/\gamma$ **then**
        return `true`
    else
        return `false`
    end if
end if

Note that the output `false` of Algorithm 3 merely means that the analysis is inconclusive, and does not exclude performance violation on $\mathcal{B}_{\mathbf{\Delta}}$. More precisely, inconclusive cases can result from three causes:

1. the sufficient condition of Proposition 3.13 is not necessary,

2. the selected ω_0 in Algorithm 3 is not satisfactory,

3. the computation of the skew-μ upper bound is not sufficiently accurate.

It does not seem possible to quantify the level of conservatism of Proposition 3.13, i.e. to determine whether the condition is far from being necessary or not. The heuristics used to select ω_0 can prove critical. It is readily apparent that exploring a frequency grid would be computationally inefficient, since only one frequency is sought, which is not even guaranteed to exist. On the other hand, the peak frequency of $M_{22}(s)$, while a natural choice for ω_0, offers no guarantee of optimality. Determining the cause of inconclusiveness could allow to determine whether it is of any interest to draw additional frequencies from $\mathcal{I}$. Finally, the method used to calculate the skew-μ upper bound can also affect the results, but given the maturity of μ-based computations, there seems to be comparatively less room for straightforward improvements on this aspect.

The methods to validate performance satisfaction (Proposition 3.8) and performance violation (Proposition 3.13) on a given box are now integrated into a branch-and-bound scheme. The resulting algorithm is outlined in Algorithm 4. Note that all three issues previously raised above on Algorithm 3 are alleviated by the branch-and-bound scheme. Indeed, barring extreme cases of sensitivities to the uncertainties, it is realistic to assume that the transfer $\mathcal{F}_u(M(s), \Delta)$ varies less and less as Δ is taken in smaller and smaller boxes. Thus the sufficient condition of Proposition 3.13 becomes not only more relevant, but also less sensitive to the choice of ω_0 as a result. Moreover, the gap between the bounds of μ is known to become arbitrarily small as the unit ball $\mathcal{B}_{\mathbf{\Delta}}$ is partitioned into smaller boxes [Roos et al., 2011], which resolves item 3. However, relying on this asymptotic behaviour of the branch-and-bound algorithm may not be satisfactory from a computational time point of view, motivating the search for effective heuristics for frequency selection.

Continuing the study of the illustrative example (3.15), Figure 3.9 shows the results of applying Algorithm 4, with a performance level $\gamma = 1.414$. More specifically, performance verification is conducted on the robustly stable subdomains as established by Figure 3.8 through a preliminary stability analysis.

3.3.4 Probabilistic μ-analysis for stability margins

Suppose now that the LFR of Figure 3.7 represents the open-loop plant and controller, with the loop opened at the place where stability (i.e. gain and phase) margins are to be computed. The corresponding closed-loop interconnection is obtained by setting $G = 1$ in Figure 3.10, and probabilistic margin analysis can then be formalised as follows:

Algorithm 4 Probabilistic μ-analysis for performance verification

Inputs: $M(s)$, $\mathbf{\Delta}$, $f_i(\delta_i)$ for $i = 1, \ldots, N$, γ, p_{min}
Outputs: D_γ, $D_{\bar{\gamma}}$, D_{γ_u}, $p(D_\gamma)$, $p(D_{\bar{\gamma}})$, $p(D_{\gamma_u})$
$\mathcal{L} \leftarrow \{\mathcal{B}_{\boldsymbol{\delta}}\}$ ▷ $\mathcal{L}$ constitutes the list of all boxes left to investigate
$D_\gamma, D_{\bar{\gamma}}, D_{\gamma_u} \leftarrow \emptyset$
$p(D_\gamma), p(D_{\bar{\gamma}}), p(D_{\gamma_u}) \leftarrow 0$
while $\mathcal{L} \neq \emptyset$ **do**
    select and remove the box $\tilde{D}$ from $\mathcal{L}$ with the highest probability measure
    compute the interconnection $\left(\tilde{M}(s), \tilde{\Delta}\right)$ normalised wrt $\tilde{D}$
    compute the nominal $\mathcal{H}_\infty$ performance $\left\|\tilde{M}_{22}(s)\right\|_\infty$
    if $\left\|\tilde{M}_{22}(s)\right\|_\infty < \gamma$ **then**
        verify performance satisfaction on $\tilde{D}$ using Proposition 3.8
        if performance is satisfied on all $\tilde{D}$ **then**
            add $\tilde{D}$ to D_γ
            $p(D_\gamma) \leftarrow p(D_\gamma) + p(\tilde{D})$
        else
            declare current iteration as inconclusive
        end if
    else
        verify performance violation on $\tilde{D}$ using Algorithm 3
        if performance is violated on all $\tilde{D}$ **then**
            add $\tilde{D}$ to $D_{\bar{\gamma}}$
            $p(D_{\bar{\gamma}}) \leftarrow p(D_{\bar{\gamma}}) + p(\tilde{D})$
        else
            declare current iteration as inconclusive
        end if
    end if
    if current iteration is inconclusive **then**
        if $p(\tilde{D}) > p_{min}$ **then**
            select a direction for cutting $\tilde{D}$
            partition $\tilde{D}$
            add the boxes obtained by partitioning $\tilde{D}$ into $\mathcal{L}$
        else
            add $\tilde{D}$ to D_{γ_u}
            $p(D_{\gamma_u}) \leftarrow p(D_{\gamma_u}) + p(\tilde{D})$
        end if
    end if
end while

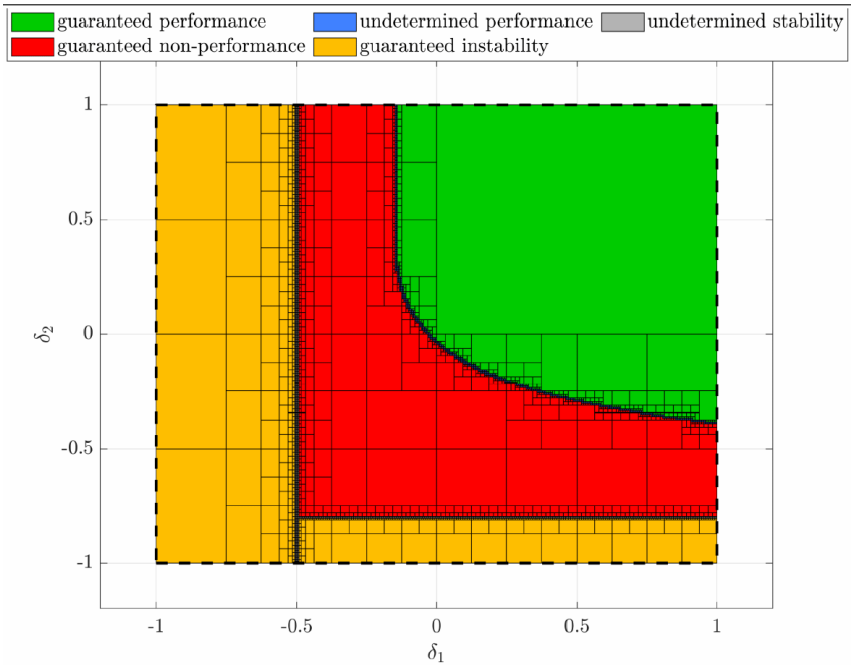

Figure 3.9: Branch-and-bound robust $\mathcal{H}_\infty$ performance analysis (CPU time = 7.6 s)

Problem 3.14 (Probabilistic stability margin)**.** *Given a margin level ϕ, compute the probability $\overline{P}^{\phi}_{\mathbf{\Delta},f}(M(s))$ that the gain, phase or modulus margin is less than ϕ when $\Delta \in \mathcal{B}_{\mathbf{\Delta}}$ for the negative feedback loop obtained by connecting z to w.*

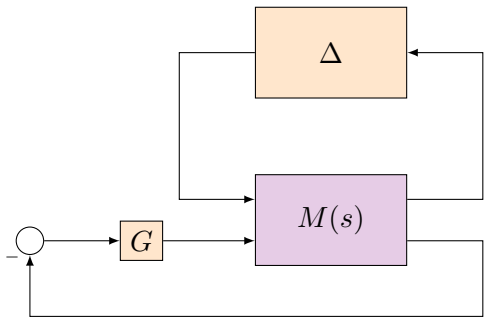

Figure 3.10: Negative feedback loop for gain and phase margin analysis

Once computed, this probability can be confronted to a given tolerance level ε, so as to validate or reject the current design, depending on whether $\overline{P}^{\phi}_{\mathbf{\Delta},f}(M(s))$ is lower or higher than ε. A practical algorithm is introduced below to compute $\overline{P}^{\phi}_{\mathbf{\Delta},f}(M(s))$ in the SISO case, i.e. when $w \in \mathbb{R}$ and $z \in \mathbb{R}$.

Special case of the modulus margin

The modulus margin MM is handled in a different way than the gain and phase margins. It is indeed equal to $\|S(s)\|_\infty^{-1}$ where $S(s)$ denotes the sensitivity function $S(s) = (1 + \mathcal{F}_u(M(s), \Delta))^{-1}$. Once computed, the sensitivity function is normalised as follows:

$$S_n(s) = \sqrt{\phi} S(s) \sqrt{\phi} \tag{3.39}$$

where ϕ is the desired modulus margin. This leads to the following equivalence:

$$\|S_n(s)\|_\infty \leq 1 \iff MM \geq \phi \tag{3.40}$$

Analysing the modulus margin therefore amounts to solving a performance problem, which can be done using Algorithm 4.

Case of the gain and phase margins

The negative feedback loop of Figure 3.10 is first built from the standard open-loop interconnection of Figure 3.7. G represents a gain or a phase shift, the nominal closed-loop uncertain system being obtained for $G = 1$.

The expression of G depends on the considered margin:

- For the gain margin GM, G is a real number which belongs to the interval:

$$G \in \left[10^{\frac{-\phi}{20}}, 10^{\frac{\phi}{20}}\right] \subset \mathbb{R} \tag{3.41}$$

  where ϕ is the desired gain margin in dB. G is normalised as follows:

$$G = G_{dif}\delta_m + G_{nom} \quad \text{where} \quad \begin{cases} G_{dif} & = 0.5 \cdot \left(10^{\frac{\phi}{20}} - 10^{\frac{-\phi}{20}}\right) \\ G_{nom} & = 0.5 \cdot \left(10^{\frac{\phi}{20}} + 10^{\frac{-\phi}{20}}\right) \end{cases} \tag{3.42}$$

  so that G exactly covers the interval (3.41) when δ_m covers the normalised interval $[-1, 1]$.

- For the phase margin PM, G is a complex number of modulus 1 defined as:

$$G = e^{j\tilde{\phi}} \quad \text{where} \quad \tilde{\phi} \in \left[-\frac{\pi\phi}{180}, +\frac{\pi\phi}{180}\right] \subset \mathbb{R} \tag{3.43}$$

  where ϕ is the desired phase margin in deg. When defined as in Equation (3.43), G does not depend on ϕ in a rational way, which prevents the interconnection of Figure 3.10 from being represented as an LFR. The following alternative but equivalent rational formulation is therefore used instead:

$$G = \frac{1 + j\tilde{\delta}}{1 - j\tilde{\delta}} \quad \text{where} \quad \tilde{\delta} \in \left[-\tan\frac{\pi\phi}{360}, +\tan\frac{\pi\phi}{360}\right] \subset \mathbb{R} \tag{3.44}$$

  The last step is to normalise $\tilde{\delta}$ as follows:

$$\tilde{\delta} = \tan\frac{\pi\phi}{360}\delta_m \tag{3.45}$$

  so that G in equation (3.44) exactly covers the circle arc (3.43) in the complex plane when δ_m covers the normalised interval $[-1, 1]$.

In both cases, standard matrix manipulations allow to reformulate the interconnection of Figure 3.10 into that of Figure 3.11, where δ_m is seen as an additional real parametric uncertainty associated with the gain or phase margin.

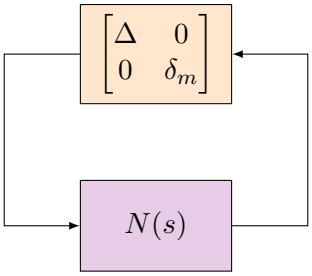

Figure 3.11: Standard interconnection for gain and phase margin analysis

Checking whether a given gain or phase margin requirement is satisfied on an entire box $D \subset \mathcal{B}_{\boldsymbol{\delta}}$ can be done using Proposition 3.15.

Proposition 3.15. *The gain or phase margin is guaranteed to be larger than ϕ on a given box $D \subset \mathcal{B}_{\boldsymbol{\delta}}$ if and only if the interconnection $((N(s), \text{diag}\,(\Delta, \delta_m))$ is stable for all $\Delta \in D$ and for all $\delta_m \in [-1, 1]$.*

This is nothing but a standard μ-analysis problem, which can be solved using existing tools such as those available in the SMART Library of the SMAC Toolbox [Roos, 2013]. If Δ is normalised on D, i.e. if the interconnection $(N(s), \text{diag}\,(\Delta, \delta_m))$ with $\Delta \in D$ is replaced with $(\tilde{N}(s), \text{diag}\left(\tilde{\Delta}, \delta_m\right))$ with $\tilde{\Delta} \in \mathcal{B}_{\boldsymbol{\Delta}}$, then it is sufficient to prove that:

$$\mu(\tilde{N}(j\omega)) < 1 \quad \begin{cases} \forall \omega \geq 0 & \text{for the gain margin} \\ \forall \omega \in \mathbb{R} & \text{for the phase margin} \end{cases} \tag{3.46}$$

The condition on the frequency ω is standard for the gain margin, but it is important to note that negative frequencies must be considered as well for the phase margin. This is because G is a complex number in Equation(3.44), which means that $N(s)$ is a transfer function with complex coefficients. As a result, the eigenvalues of the standard interconnection of Figure 3.11 are not necessarily symmetrical with respect to the real axis in the complex plane. It is therefore necessary to consider the whole frequency range when applying μ-analysis to find values of Δ and δ_m which bring the system at the limit of stability.

Checking whether a given gain or phase margin requirement is violated on an entire box $D \subset \mathcal{B}_{\boldsymbol{\delta}}$ can be done using Proposition 3.16.

Proposition 3.16. *The gain or phase margin is guaranteed to be lower than ϕ on a given box $D \subset \mathcal{B}_{\boldsymbol{\delta}}$ if and only if:*

$$\forall \Delta \in D,\ \exists \hat{\delta}_m \in [-1, 1] \text{ such that the interconnection } \left(N(s), \text{diag}(\Delta, \hat{\delta}_m)\right) \text{ is unstable}$$

The condition in Proposition 3.16 cannot be directly evaluated using μ-based tools. It is thus replaced with the sufficient condition of Proposition 3.17.

Proposition 3.17. *The gain or phase margin is guaranteed to be lower than ϕ on a given*

box $D \subset \mathcal{B}_{\boldsymbol{\delta}}$ *if:*

$$\exists \hat{\delta}_m \in [-1,1],\ \forall \Delta \in D,\ \textit{the interconnection } \left(N(s), \mathrm{diag}(\Delta, \hat{\delta}_m)\right) \textit{ is unstable}$$

Once it is determined, the real parameter $\hat{\delta}_m$ remains constant in Proposition 3.16. It can therefore be integrated into $N(s)$ to form a reduced interconnection $(N_r(s), \Delta)$. The latter is normalised, i.e. $(N_r(s), \Delta), \Delta \in D$ is replaced with $\left(\tilde{N}_r(s), \tilde{\Delta}\right), \tilde{\Delta} \in \mathcal{B}_{\boldsymbol{\Delta}}$. Verifying the sufficient condition of Proposition 3.17 then amounts to checking the stability of $\left(\tilde{N}_r(s), \tilde{\Delta}\right)$, which can be done easily using μ-based tools. The most critical point here is the determination of $\hat{\delta}_m$, if it exists at all. Any value of δ_m which makes the reduced nominal system $\tilde{N}_r(s)$ unstable is a potential candidate, so an obvious strategy is to study the stability of the interconnection $(N(s), \mathrm{diag}(0_{p\times p}, \delta_m))$. This can be done using μ-based tools, but it is not recommended in practice. The problem considered here has indeed a unique real uncertainty, which can create discontinuities in the structured singular value μ. It is even possible that μ is non-zero only at a finite number of frequencies, which usually defeats most classical algorithms. A more efficient though empirical strategy is to consider a finite number of values $(\delta_m^k)_k$ which grid the interval $[-1,1]$, and to choose $\hat{\delta}_m$ as the δ_m^k of largest magnitude which makes the interconnection $\left(N(s), \mathrm{diag}(0_{p\times p}, \delta_m^k)\right)$ unstable. The risk with such an approach is to fail to identify an unstable configuration, although there exists one between some points of the grid. However, this has no other consequence than splitting unnecessarily the uncertainty domain when applying Algorithm 5 below, which is not a critical issue. On the other hand, such a situation means that the system is stable for a gain or phase shift equal to ϕ, but becomes unstable for some values lower than ϕ, which is highly unlikely in practice. The conditions for determining whether a given stability (gain or phase) margin requirement is satisfied (Proposition 3.15) or violated (Proposition 3.17) on an entire box are now integrated into a branch-and-bound scheme described in Algorithm 5 below, which draws heavily from the other branch-and-bound algorithms 2 and 4. This leads to:

$$D_s = D_m \cup D_{\overline{m}} \cup D_{m_u} \tag{3.47}$$

where D_m, $D_{\overline{m}}$ and D_{m_u} are the domains of guaranteed gain/phase margin satisfaction, guaranteed gain/phage margin violation and undetermined gain/phase margin respectively, with probabilities $p(D_m)$, $p(D_{\overline{m}})$ and $p(D_{m_u})$. The investigated domain is limited to the domain of guaranteed stability $D_s \subset \mathcal{B}_{\boldsymbol{\delta}}$, since stability margins analysis only makes sense for stable systems. A preliminary stability analysis is therefore performed with Algorithm 2, leading to:

$$\mathcal{B}_{\boldsymbol{\delta}} = D_s \cup D_{\bar{s}} \cup D_{s_u} \tag{3.48}$$

where $D_{\bar{s}}$ and D_{s_u} are the domains of guaranteed instability and undetermined stability respectively. The following partition of $\mathcal{B}_{\boldsymbol{\delta}}$ is finally obtained by combining (3.47) and (3.48):

$$\mathcal{B}_{\boldsymbol{\delta}} = D_m \cup D_{\overline{m}} \cup D_{m_u} \cup D_{\bar{s}} \cup D_{s_u} \tag{3.49}$$

This leads to bounds on the exact probability $\overline{P}^{\phi}_{\boldsymbol{\Delta},f}(M(s))$ of stability margins violation, thus

solving Problem 3.14:

$$p(D_{\overline{m}}) \leq \overline{P}^{\phi}_{\mathbf{\Delta},f}(M(s)) \leq p(D_{\overline{m}}) + p(D_{m_u}) = p(D_s) - p(D_m) \tag{3.50}$$

Algorithm 5 Probabilistic μ-analysis for stability margins

Inputs: $M(s)$, $\mathbf{\Delta}$, $f_i(\delta_i)$ for $i = 1, \ldots, N$, ϕ, p_{min}
Outputs: D_m, $D_{\overline{m}}$, D_{m_u}, $p(D_m)$, $p(D_{\overline{m}})$, $p(D_{m_u})$
$\mathcal{L} \leftarrow \{\mathcal{B}_{\boldsymbol{\delta}}\}$ ▷ $\mathcal{L}$ constitutes the list of all boxes left to investigate
$D_m, D_{\overline{m}}, D_{m_u} \leftarrow \emptyset$
$p(D_m), p(D_{\overline{m}}), p(D_{m_u}) \leftarrow 0$
while $\mathcal{L} \neq \emptyset$ **do**
    select and remove the box $\tilde{D}$ from $\mathcal{L}$ with the highest probability measure
    compute the interconnection $\left(\tilde{N}(s), \text{diag}\left(\tilde{\Delta}, \delta_m\right)\right)$ normalised on $\tilde{D}$
    check if there exists a $\hat{\delta}_m$ which makes $\tilde{N}_r(s)$ unstable
    if $\hat{\delta}_m$ does not exist **then** ▷ nominal gain or phase margin is $\geq \phi$
        check gain/phase margin satisfaction on $\tilde{D}$ using Proposition 3.15
        if gain/phase margin satisfaction is guaranteed on all $\tilde{D}$ **then**
            add $\tilde{D}$ to D_m
            $p(D_m) \leftarrow p(D_m) + p(\tilde{D})$
        else
            declare current iteration as inconclusive
        end if
    else ▷ nominal gain or phase margin is $< \phi$
        check gain/phase margin violation on $\tilde{D}$ using Proposition 3.17
        if gain/phase margin violation is guaranteed on all $\tilde{D}$ **then**
            add $\tilde{D}$ to $D_{\overline{m}}$
            $p(D_{\overline{m}}) \leftarrow p(D_{\overline{m}}) + p(\tilde{D})$
        else
            declare current iteration as inconclusive
        end if
    end if
    if current iteration is inconclusive **then**
        if $p(\tilde{D}) > p_{min}$ **then**
            select a direction for cutting $\tilde{D}$
            partition $\tilde{D}$ and add the resulting boxes into $\mathcal{L}$
        else
            add $\tilde{D}$ to D_{m_u}
            $p(D_{m_u}) \leftarrow p(D_{m_u}) + p(\tilde{D})$
        end if
    end if
end while

3.4 Roll autopilot design

The elements reviewed in Section 3.2 are now applied to the design of a baseline autopilot for the projectile. The roll channel, described in Section 2.4.1, is addressed first, whereas the pitch/yaw channels from Section 2.4.2 are the topic of the following section.

3.4.1 Control objectives and strategy

The roll autopilot is critical during the ballistic phase of the projectile to stabilise the fuse at a fixed roll angle, and it must also be able to maintain a desired roll angle during the guided phase, in spite of disturbances. To tackle the roll autopilot design problem, the LPV system describing the roll dynamics (cf. Section 2.4.1) is simplified by considering the reduced parameter vector $\boldsymbol{\lambda}_R = [V\ h]^T$ and by neglecting the disturbances $[d_\phi\ d_{p_f}]^T$.

$$\begin{bmatrix} \dot{\phi}_f \\ \dot{p}_f \end{bmatrix} = \begin{bmatrix} 0 & 1 \\ 0 & a_{22}(\boldsymbol{\lambda}_R) \end{bmatrix} \begin{bmatrix} \phi_f \\ p_f \end{bmatrix} + \begin{bmatrix} 0 \\ b_2(\boldsymbol{\lambda}_R) \end{bmatrix} \delta_p \tag{3.51}$$

This system has one pole at 0 and another pole given by $a_{22}(\boldsymbol{\lambda}_R)$. The variations of the parameter-dependent coefficients $a_{22}(\boldsymbol{\lambda}_R)$ and $b_2(\boldsymbol{\lambda}_R)$ are shown in Figure 3.12. A noticeable property is that the variations of the second pole are restricted to a small interval in the left-half plane. It is therefore tempting to approximate this coefficient with a constant $\overline{a_{22}}$. From Equation (3.51), the transfer function from the control input δ_p to $[\phi_f\ p_f]^T$ then takes the form:

$$G_R(s, \boldsymbol{\lambda}_R) = b_2(\boldsymbol{\lambda}_R) \begin{bmatrix} \dfrac{1}{s(s - \overline{a_{22}})} \\ \dfrac{1}{s - \overline{a_{22}}} \end{bmatrix} = b_2(\boldsymbol{\lambda}_R) \hat{G}_R(s) \tag{3.52}$$

Thus, the chosen control strategy consists in designing a controller $\hat{K}_R(s)$ associated to the LTI system $\hat{G}_R(s)$. Then a gain scheduled controller for $G_R(s, \boldsymbol{\lambda}_R)$ is directly obtained as:

$$K_R(s, \boldsymbol{\lambda}_R) = \frac{1}{b_2(\boldsymbol{\lambda}_R)} \hat{K}_R(s) \tag{3.53}$$

Since only one design point is needed, this strategy drastically simplifies the design step, and the relevance of the approximations can be validated with *a posteriori* analyses and simulations. The design point $\boldsymbol{\lambda}_{R0} = [V = 380\ \text{m/s},\ h = 5000\ \text{m}]^T$ is chosen from a 15×16 grid of the reduced flight envelope so as to minimise the distance of $a_{22}(\boldsymbol{\lambda}_{R0})$ to the midpoint $\frac{1}{2}\Big(\max\limits_{\boldsymbol{\lambda}_R} a_{22}(\boldsymbol{\lambda}_R) - \min\limits_{\boldsymbol{\lambda}_R} a_{22}(\boldsymbol{\lambda}_R)\Big)$.

3.4.2 Autopilot structure and tuning

The proposed fixed-structure controller is shown in Figure 3.13. Recall from Section 2.6.2 that the roll autopilot must generate the virtual control signal $\delta_{p,c}$ from the reference roll angle $\phi_{f,g}$ (provided by the guidance module in the complete system) and the roll angle and spin rate measurements $\phi_{f,m}$ and $p_{f,m}$. The controller structure consists of a PI-P controller (gains $K_{p,e}$, $K_{i,e}$, and K_{p,p_f}) with an additional feedforward gain K_{ff} to help with reference tracking.

To deal with disturbance rejection, a signal-based approach is used to attenuate low frequency disturbances d_o at the plant output and high frequency actuator usage. Another requirement is that the transfer from the reference roll angle $\phi_{f,g}$ to the fuse roll angle ϕ_f remains as close as

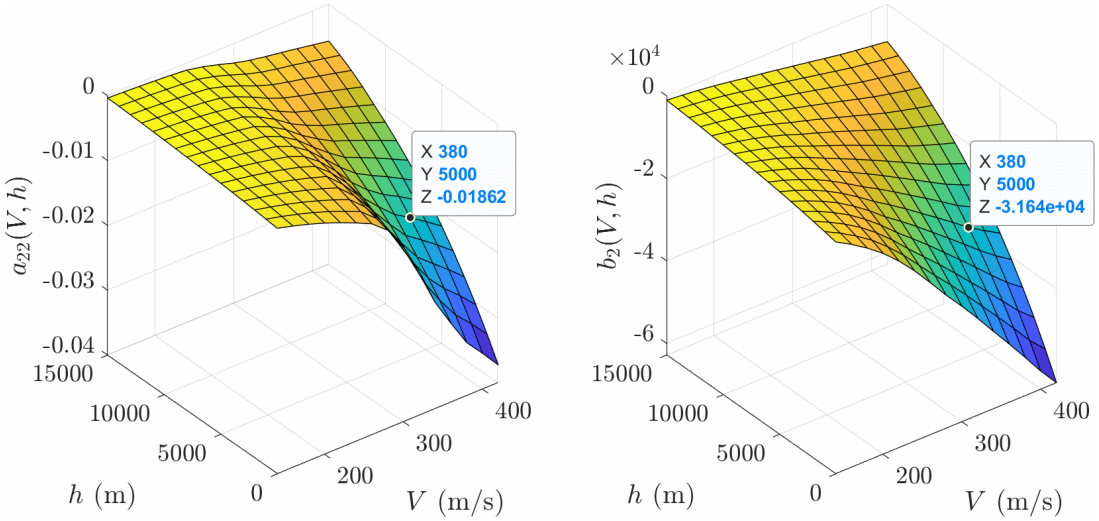

Figure 3.12: Variation of the state-space coefficients over the flight envelope

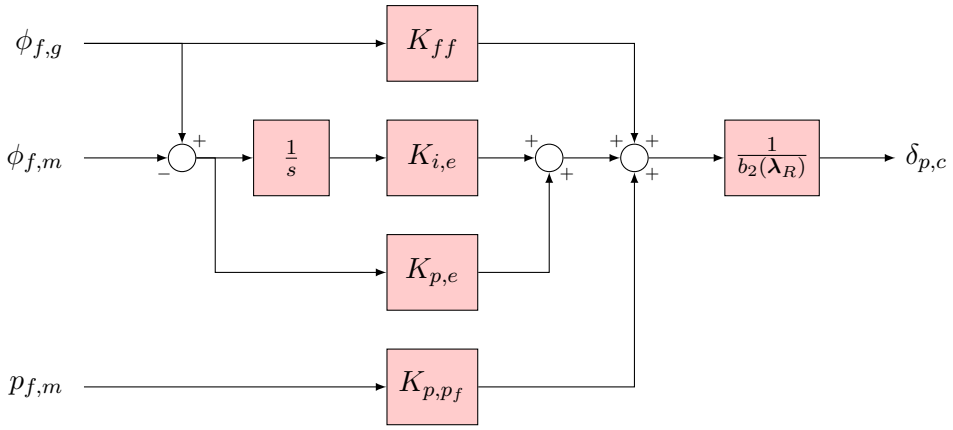

Figure 3.13: Roll autopilot structure

possible to a second-order reference model:

$$T_{ref,R}(s) = \frac{\omega_{ref,R}^2}{s^2 + 2\xi_{ref,R}\omega_{ref,R}s + \omega_{ref,R}^2} \tag{3.54}$$

with $\omega_{ref,R} = 14.3$ rad/s and $\xi_{ref,R} = 0.781$ corresponding to a settling time within 2% of 0.25 s and an overshoot of 2%.

The system is augmented with weighting functions $W_S(s)$, $W_{KS}(s)$, and $W_M(s)$ corresponding to these requirements, as shown in Figure 3.14. Their role is to shape respectively the transfer functions $\mathcal{T}_{d_o\to\phi_f}(s)$, $\mathcal{T}_{d_o\to\delta_{p,c}}(s)$, and $\mathcal{T}_{\phi_{f,g}\to e_{ref}}(s)$. Since an accurate model matching is not perceived as an imperative for the roll autopilot design, the related requirement is given as a soft constraint. Thus, the optimisation problem to solve is:

$$\begin{aligned} \underset{\boldsymbol{\kappa}_R}{\text{minimise}} \quad & \left\| W_M(s)\mathcal{T}_{\phi_{f,g}\to e_{ref}}(s) \right\|_\infty \\ \text{subject to} \quad & \left\| W_S(s)\mathcal{T}_{d_o\to\phi_f}(s) \right\|_\infty < 1 \\ & \left\| W_{KS}(s)\mathcal{T}_{d_o\to\delta_p}(s) \right\|_\infty < 1 \end{aligned} \tag{3.55}$$

where $\boldsymbol{\kappa}_R = [K_{i,e}\ K_{p,e}\ K_{p,p_f}\ K_{ff}]^T$. The weighting functions are selected as follows:

$$W_M(s) = \frac{s+30}{0.15s + 30 \cdot 10^{-4}} \tag{3.56}$$

$$W_S(s) = \frac{s+10}{1.6s + 10 \cdot 10^{-4}} \tag{3.57}$$

$$W_{KS}(s) = \frac{s+40}{10^{-4}s + 40 \cdot 0.5} \tag{3.58}$$

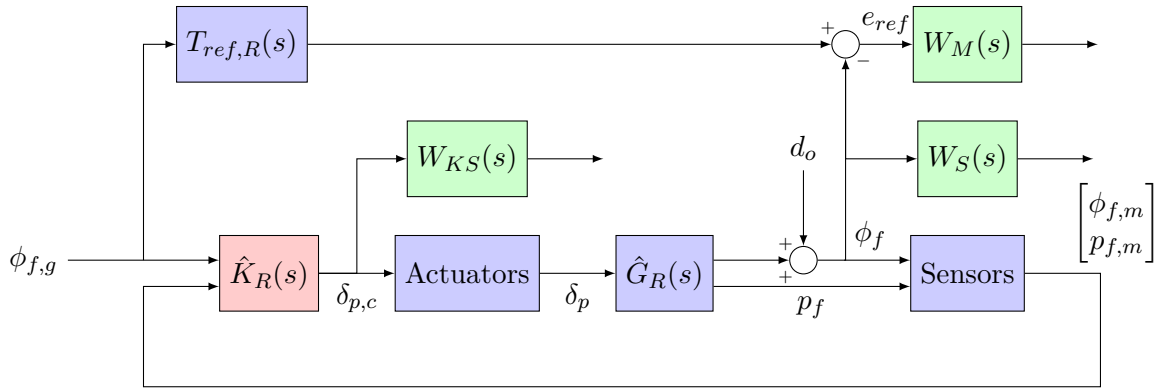

Figure 3.14: Structured $\mathcal{H}_\infty$ synthesis problem for the roll autopilot

Remark 6. *Since d_o enters the system between the plant $\hat{G}_R(s)$ and the sensor model, the transfer function $\mathcal{T}_{d_o \to \phi_f}(s)$ does not correspond to the textbook definition of the sensitivity function. Nevertheless, the weighting functions are named following the conventions of the mixed-sensitivity approach, since the underlying ideas are identical.*

The optimisation problem is successfully solved using `systune`, which yields a performance index (value of the soft constraint) of $\gamma = 0.62$. The resulting shaped transfer functions are shown in Figure 3.15, illustrating the fulfilment of the specifications. The transfer function from $\mathcal{T}_{\phi_{f,g} \to \phi_f}(s)$ is also compared to that of the reference model $T_{ref,R}(s)$, showing a good matching in low to intermediate frequencies. This is further confirmed by the step response shown in Figure 3.16 which is very close to the reference model, despite a higher overshoot (2.6%) and settling time (0.43 s).

3.4.3 Robustness analysis and time-domain simulations

Robustness analysis

The robustness of the closed-loop roll channel is first evaluated by computing the classical gain (GM), phase (PM), and delay margins (DM), as well as the modulus margin (MM) at the output of the autopilot. Satisfactory values are obtained at the design point $\boldsymbol{\lambda}_{R0} = [380\ \text{m/s},\ 5000\ \text{m}]^T$, with $GM = 2.70 \approx 8.61$ dB, $PM = 33.4$ deg, $DM = 12$ ms, and $MM = 0.46$.

Next, robustness with respect to uncertainties is assessed using μ-analysis. As a reminder, the roll channel is affected by three parametric uncertainties $\boldsymbol{\delta}_R = [\delta_{C_A}, \delta_{C_{l\delta}}, \delta_{K_v}]^T \in [-1, 1]^3$, gathered in the block Δ_R whose structure is given in Equation (2.67). The value of the μ upper bound obtained by using the SMART library of the SMAC toolbox equals 0.19, corresponding

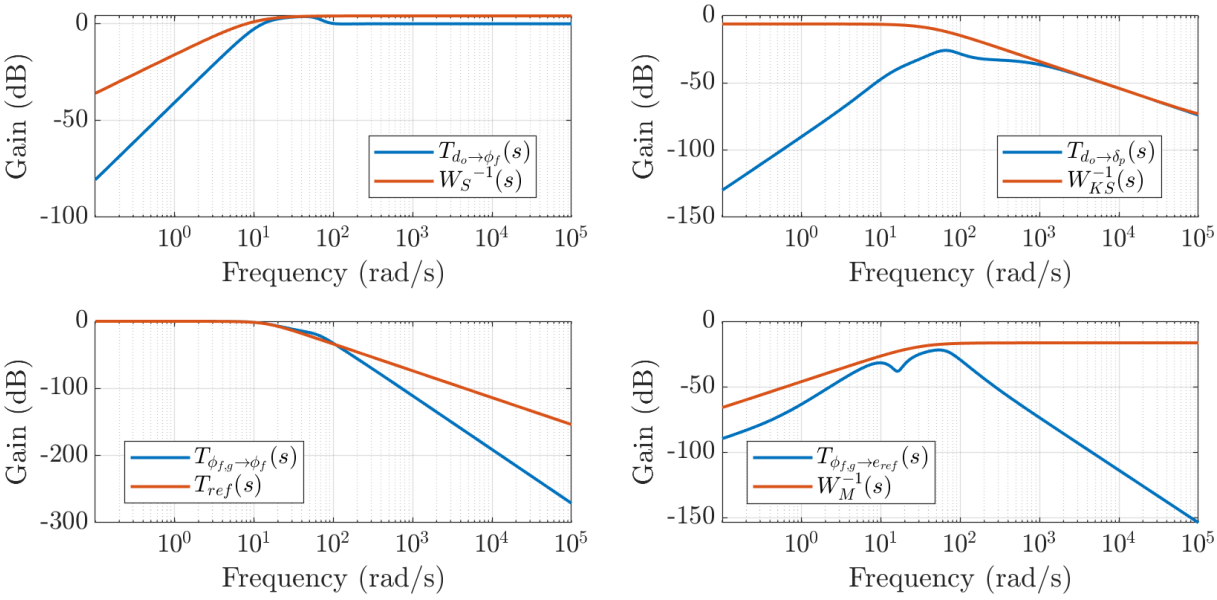

Figure 3.15: Closed-loop transfer functions for disturbance rejection (upper left), control attenuation (upper right), reference tracking (lower left), model matching (lower right)

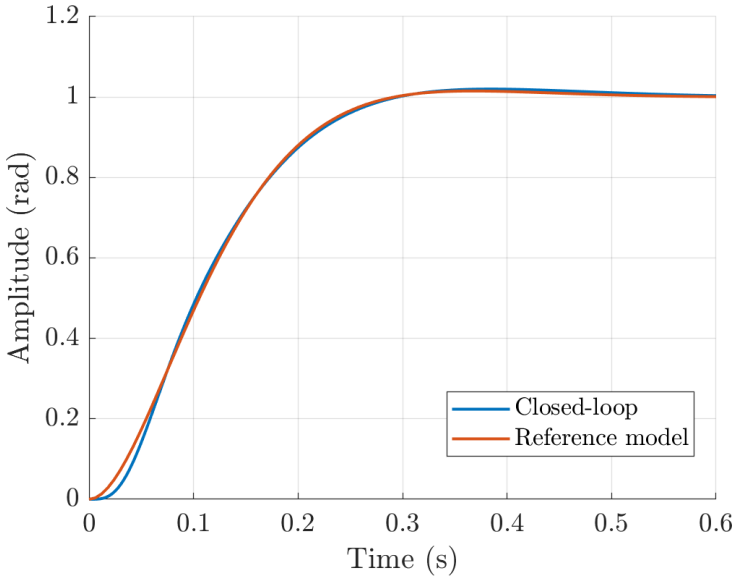

Figure 3.16: Closed-loop system step response

to a lower bound on the robust stability margin $\underline{k_r} = 1/0.19 \approx 5.26 > 1$, thus validating robust stability. Good robust performance is also achieved, with a worst-case $\mathcal{H}_\infty$ performance $\max_{\Delta \in \mathcal{B}_{\mathbf{\Delta}_R}} \left\| \mathcal{T}_{\phi_{f,g} \to e_{ref}} \right\|_\infty < 0.094$ remaining relatively close to its nominal value of[2] $\gamma_{nom} = 0.087$.

Probabilistic μ-analysis allows to push the performance analysis further by computing bounds on the probability of performance satisfaction for a given performance level using Algorithm 4. Figure 3.17 then plots the probability of $\mathcal{H}_\infty$ performance satisfaction for two configurations of the probability density functions of the uncertainties. The first configuration corresponds to a uniform distribution for each of the uncertainties. The second configuration corresponds

[2]Here we give the performance index γ_{nom} without taking into account the weighting filter $W_M(s)$ on model matching.

to a truncated normal distribution, where for each uncertainty, the standard deviation σ is chosen so that 3σ corresponds to the difference between the nominal value and any of the extremal values[3]. Very tight bounds are obtained, illustrating the efficiency of the branch-and-bound algorithm. Moreover, the results illustrate anew that uniform distributions lead to more pessimistic probabilities. From a computational point of view, the plot corresponding to the uniform distributions is obtained by calling Algorithm 4 for 20 values of $\mathcal{H}_\infty$ performance between the nominal and worst-case values, for a total CPU time of 25.8 s. Meanwhile, as already noted in Section 3.3.2, recomputing the probability of interest with another distribution of the uncertainties does not require further calls to the branch-and-bound algorithm, and the data corresponding to the normal distributions are obtained in merely 3.6 s.

Similarly, bounds on the probability of margin violation for different levels of the gain, phase, and modulus margins are computed. The results are shown in Figure 3.18, as before for uniform and normal distributions. A first thing to note is that the worst-case margins remain very satisfactory, at respectively 7.4 dB, 30.3 deg, and 0.40 for the gain, phase, and modulus margins. Interestingly, unlike for $\mathcal{H}_\infty$ performance, normal distributions do not consistently lead to less conservative probabilities compared to uniform ones. In fact, for this system, the plots intersect at the 50% mark, which also corresponds to the nominal margin values. This indicates that half of the parametric uncertainty space actually leads to better margins (at the price of a lower $\mathcal{H}_\infty$ performance). This behaviour can be explained by the fact that only the two state-space coefficients a_{22} and b_2 of the airframe are impacted by the uncertainties, with the former being a negative real pole of the airframe (which can either be pushed left or right by the uncertainties), and the latter merely scaling the control input. This observation is further corroborated by Figure 3.19, which shows the Bode and Nyquist plots for samples of the uncertain system. Probabilistic μ-analysis is however clearly advantageous compared to a statistical analysis of random samples in this case, since it provides guaranteed and tight bounds on the probabilities of margin violation in a short time (57 s for the three margins), which are moreover cheap to update (3.6 s) when considering alternative uncertainty distributions.

The above robustness analysis results pertain only to the design point. The robustness properties must then be checked on the rest of the flight envelope, since the autopilot does not take into account the variations of the state-space coefficient $a_{22}(\boldsymbol{\lambda}_R)$, which is moreover affected by the parametric uncertainties, i.e. we have in fact $a_{22}(\boldsymbol{\lambda}_R, \boldsymbol{\delta}_R)$. Fortunately, nominal and worst-case values ($\mathcal{H}_\infty$ performance and margins) remain almost constant when $\boldsymbol{\lambda}_R$ varies, and the cumulative distribution functions calculated on a few points of the flight envelope keep the same profile as in Figures 3.17 and 3.18, indicating virtually identical robustness properties across the whole flight envelope.

Closed-loop time-domain simulations

The analysis of the closed-loop roll channel is completed with time-domain simulations under several scenarios. Figure 3.20 shows a nominal simulation conducted at the design point, with a step input of 45 deg at 0 s. The simulation also includes a step disturbance $d_o = 20\,\text{deg}$ applied at 1.5 s on ϕ_f which is successfully rejected. Furthermore, the control signal remains small in

[3]It is assumed that the uncertainty range is centred around the nominal value.

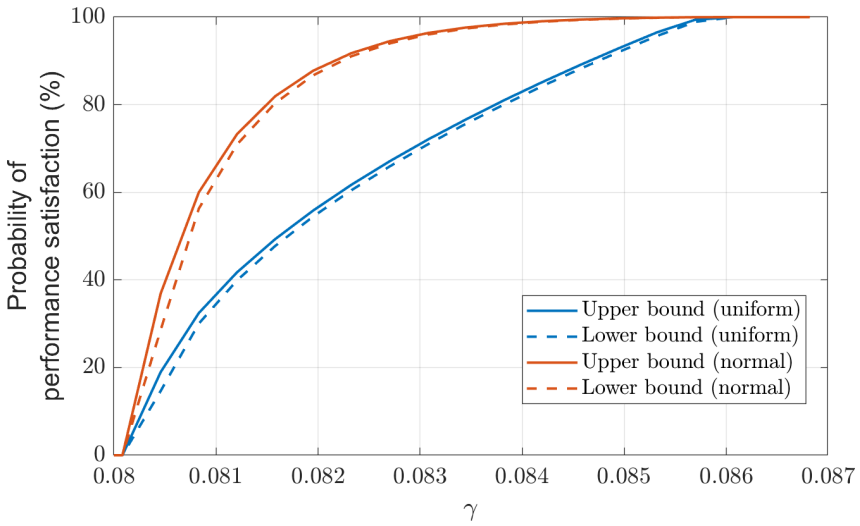

Figure 3.17: Bounds on the probability of $\mathcal{H}_\infty$ performance satisfaction assuming either a uniform (blue) or a normal (orange) distribution of the uncertainties

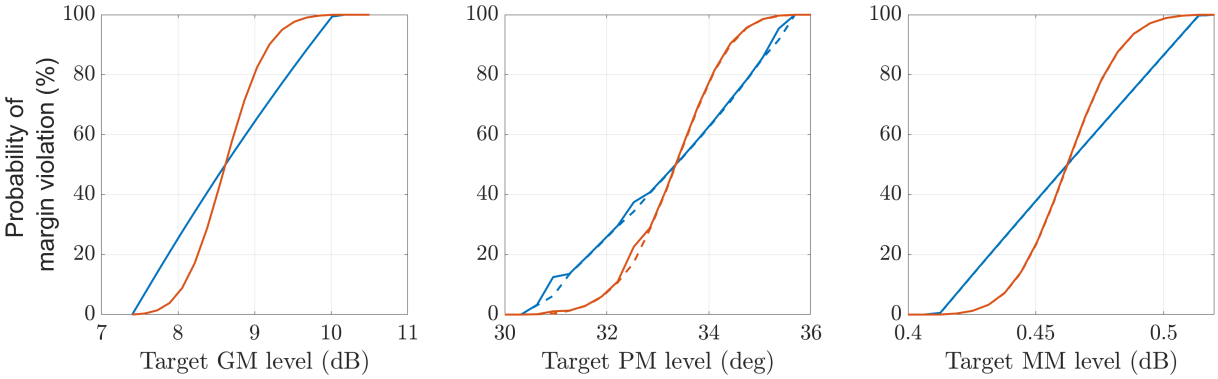

Figure 3.18: Upper (solid) and lower (dashed) bounds on the probability of gain (left), phase (middle), and modulus (right) margin violation assuming either a uniform (blue) or a normal (orange) distribution of the uncertainties

amplitude and far from the saturation level ± 10 deg.

Robustness against parametric uncertainties is illustrated by Figure 3.21, which shows the responses for 300 random samples of the uncertain system. Robust stability and performance are verified since the output responses remain very close to the nominal response with also minimal change to the required control signals. This is consistent with the results obtained previously with μ-analysis.

Lastly, nominal simulations are performed on all points of the 15×16 grid of the reduced flight envelope. The results, as shown in Figure 3.22, are consistent with the scheduling strategy of Section 3.4.1. Indeed, the output responses are virtually identical, while important variations can be observed on the amplitudes of the control signal due to the variations of $b_2(\boldsymbol{\lambda}_R)$. In spite of this, the risk of saturations can be mostly dismissed, since step reference signals for the fuse roll angle are only representative of the ballistic phase of the flight, more specifically the activation of the roll autopilot. In terms of parameter values, this corresponds to $V > 200$ m/s and intermediate altitudes $h < 10000$ m, dismissing the points where the control input signal is significantly scaled up.

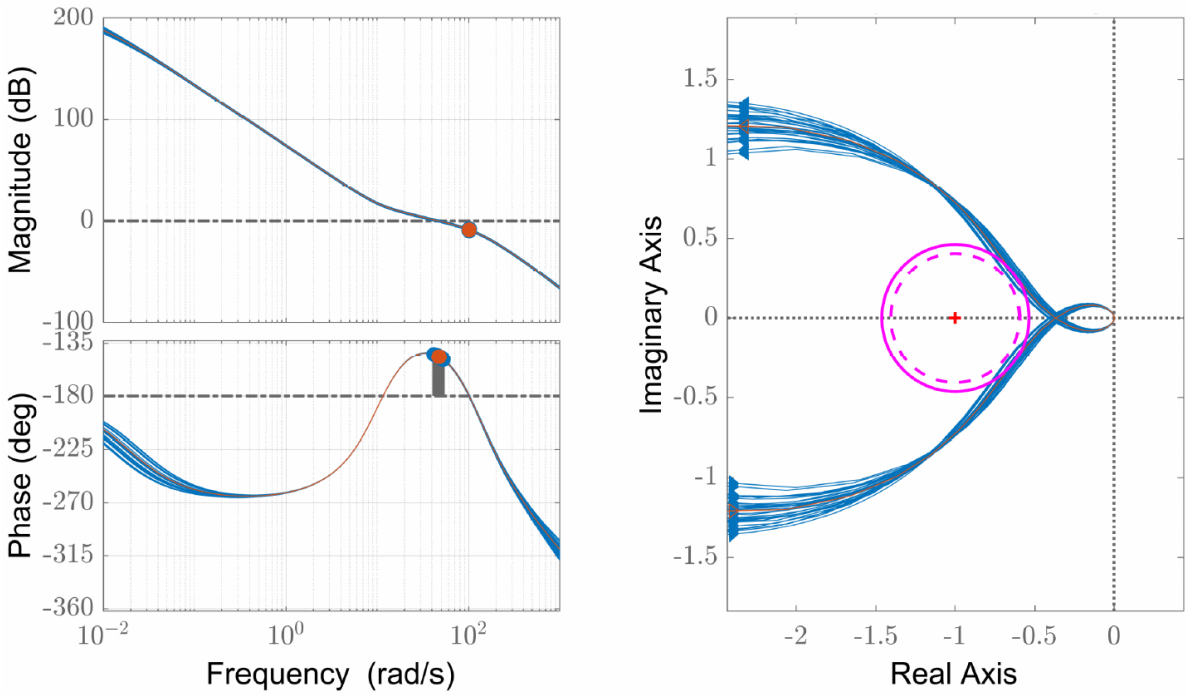

Figure 3.19: Bode plots and Nyquist diagrams: perturbed systems (blue) and nominal system (orange); the magenta circles correspond to the nominal (full line) and worst-case (dashed) modulus margins

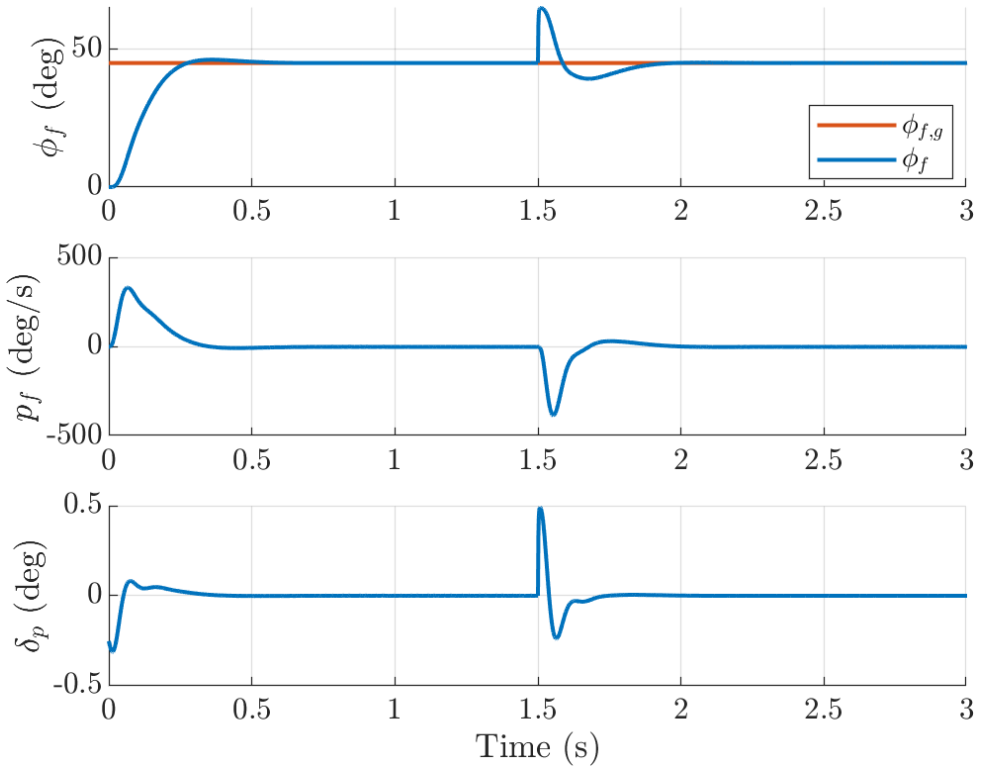

Figure 3.20: Nominal simulation of the closed-loop roll channel at the design point $\boldsymbol{\lambda}_{R0}$: roll angle (top), roll angular rate (middle), virtual roll control signal (bottom)

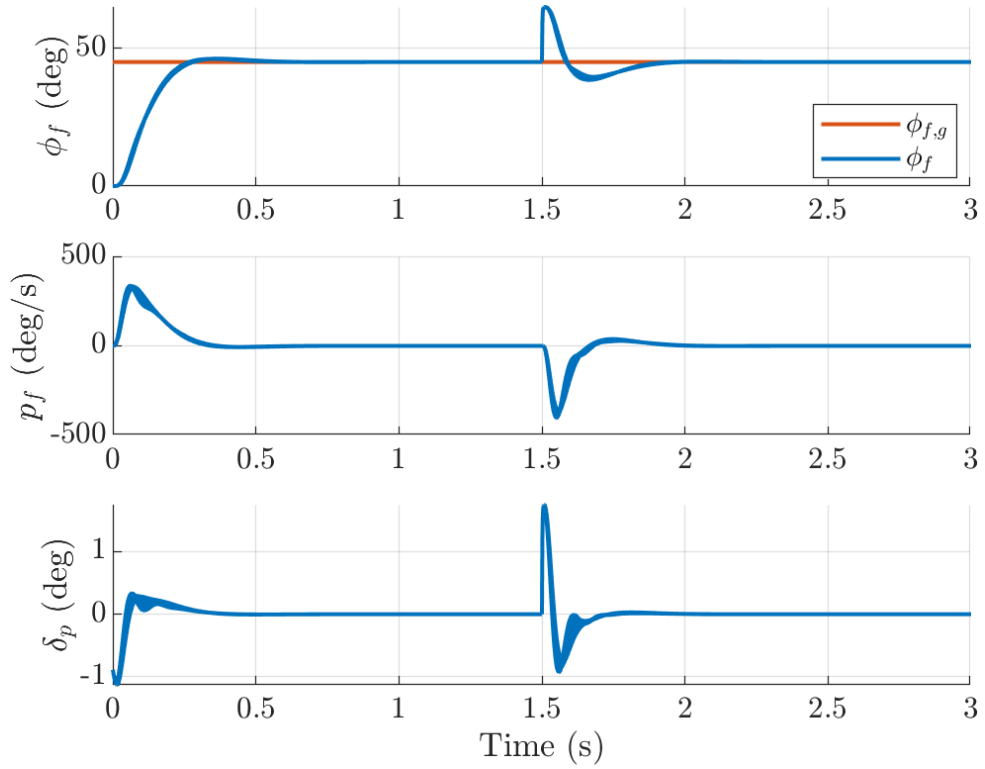

Figure 3.21: Simulation at the design points with model uncertainties: roll angle (top), roll angular rate (middle), virtual roll control signal (bottom)

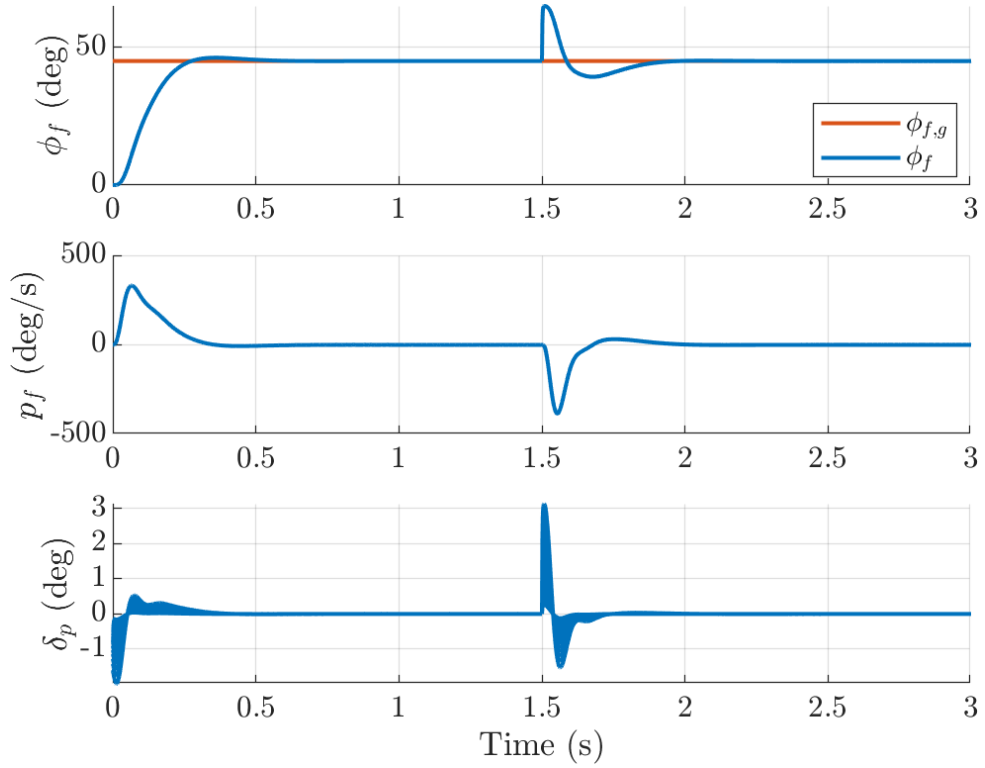

Figure 3.22: Nominal simulations over the flight envelope: roll angle (top), roll angular rate (middle), virtual roll control signal (bottom)

3.5 Pitch/yaw autopilot design

3.5.1 Control objectives and strategy

The pitch/yaw autopilot is responsible for the tracking of the reference normal and lateral loading factors demanded from the guidance module. Recall from Section 2.5.2 that the relevant sensor measurements for the pitch/yaw channels are the measurements of the normal and lateral load factors $\boldsymbol{n}_{zy,m} = [n_{z,m}\ n_{y,m}]^T$, of the angular rates $\boldsymbol{\omega}_{qr,m} = [q_m\ r_m]^T$, and of the virtual control signals $\boldsymbol{\delta}_{qr,m} = [\delta_{q,m}\ \delta_{r,m}]^T$, the latter obtained by combining measurements of the real deflection angles with the measurement of the roll angle. An additional input to the pitch/yaw controller is the guidance signal, which contains the reference normal and lateral load factors $\boldsymbol{n}_{zy,g} = [n_{z,g}\ n_{y,g}]^T$.

Remark 7. *We recall that in the context of a linearisation-based gain scheduling, the inputs, outputs, and states of the investigated LTI systems actually represent deviations from equilibrium values. However, to lighten notations, the related subscript ε is omitted in this section.*

Autopilot design for the pitch/yaw channels is based on the quasi-LPV model established in Section 2.4.2, and more particularly on the bank of LTI models generated from the reduced flight envelope $\boldsymbol{\lambda}_{PY} = [V\ h\ p_a]^T$. The closed-loop settling time must be sufficiently large compared to the settling time of the roll channel (0.43 s), since the pitch/yaw autopilot is designed with the assumption that the roll angle is already settled, but small enough to ensure good tracking of the guidance signal and, ultimately, good accuracy upon impact. Due to the strong coupling between the pitch and yaw axes, a multivariable control problem must be tackled. A low-order structured controller composed of few gains is preferred, so that a simple gain blending approach can be used for controller interpolation. The closed-loop performance and robustness properties must then be checked on the flight envelope. However, controller fine-tuning and an exhaustive validation are premature, since the linear framework lacks the saturations and is not representative of the real system. Rather, the aim here is to design a baseline autopilot with high enough performance to contemplate an anti-windup augmentation.

3.5.2 Autopilot structure and tuning

The proposed fixed-structure controller is presented in Figure 3.23. Symmetries of the airframe model are exploited by imposing corresponding symmetries on the gain matrices of the controller, further reducing the interpolation and implementation effort:

$$\begin{aligned} \mathbf{K}_{i,e} &= \begin{bmatrix} K_{i,e}^{(11)} & K_{i,e}^{(12)} \\ K_{i,e}^{(12)} & -K_{i,e}^{(11)} \end{bmatrix} \quad \mathbf{K}_{p,n} = \begin{bmatrix} K_{p,n}^{(11)} & K_{p,n}^{(12)} \\ K_{p,n}^{(12)} & -K_{p,n}^{(11)} \end{bmatrix} \\ \mathbf{K}_{p,\omega} &= \begin{bmatrix} K_{p,\omega}^{(11)} & K_{p,\omega}^{(12)} \\ -K_{p,\omega}^{(12)} & K_{p,\omega}^{(11)} \end{bmatrix} \quad \mathbf{K}_{p,\delta} = \begin{bmatrix} K_{p,\delta}^{(11)} & K_{p,\delta}^{(12)} \\ K_{p,\delta}^{(12)} & -K_{p,\delta}^{(11)} \end{bmatrix} \end{aligned} \tag{3.59}$$

The eight controller gains are computed by solving a mixed $\mathcal{H}_2/\mathcal{H}_\infty$ controller synthesis problem using the Matlab routine `systune`. As with roll autopilot synthesis, weighting functions $W_S(s)$ and $W_{KS}(s)$ are defined to capture respectively disturbance rejection and control

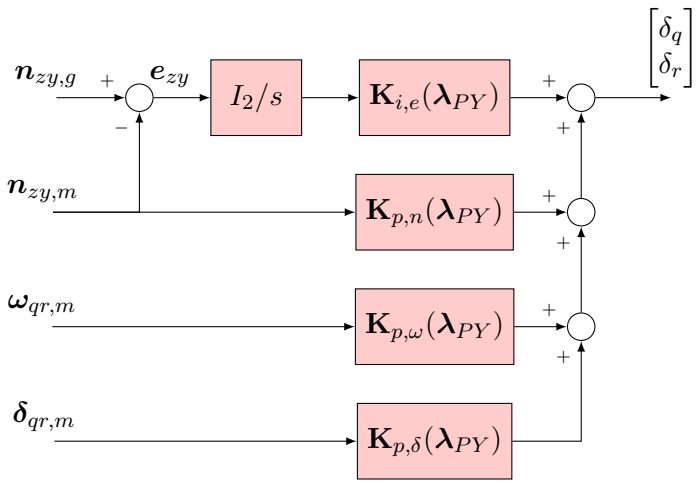

Figure 3.23: Pitch/yaw autopilot structure

attenuation requirements, and a second-order system is used as a reference model for the system response:

$$T_{ref,PY}(s) = \frac{\omega_{ref,PY}^2}{s^2 + 2\xi_{ref,PY}\omega_{ref,PY}s + \omega_{ref,PY}^2} \cdot I_2 \tag{3.60}$$

with $\omega_{ref,PY} = 5$ rad/s and $\xi_{ref,PY} = 0.781$. This reference model corresponds to a settling time within 2% of 0.72 s with an overshoot of 2%. The associated soft goal is specified as a time-domain step tracking goal in `systune`[4]. With respect to the signals defined in Figure 3.24, the quantity to minimise relates to the energy of the step response of the transfer function:

$$\mathcal{T}_{\boldsymbol{n}_{zy,g}\to\boldsymbol{e}_{zy,ref}}(s) = T_{ref,PY}(s) - \mathcal{T}_{\boldsymbol{n}_{zy,g}\to\boldsymbol{n}_{zy}}(s) \tag{3.61}$$

The $\mathcal{H}_2$ norm, which corresponds to the energy of the impulse response of a system[5], is used to express the objective function. More precisely, `systune` minimises the following quantity:

$$f(\boldsymbol{\kappa}_{PY}) = \frac{\left\| \frac{1}{s}\mathcal{T}_{\boldsymbol{n}_{zy,g}\to\boldsymbol{e}_{zy,ref}}(s) \right\|_2}{\eta \left\| \frac{1}{s}[T_{ref,PY}(s) - I] \right\|_2} \tag{3.62}$$

where $\boldsymbol{\kappa}_{PY}$ is the free variables of the problem, i.e. the eight controller gains in this case, and η is a user-defined positive scalar value representing the desired maximum relative matching error (higher values of η decrease the performance index, loosening the requirement), and taken as 0.05 here. Thus, the synthesis problem for a design point $\boldsymbol{\lambda}_{PY}$ of the reduced flight envelope

[4]Using a more standard $\mathcal{H}_\infty$ soft goal of the form $\left\| W_M(s)\mathcal{T}_{\boldsymbol{n}_{zy,g}\to\boldsymbol{e}_{zy,ref}}(s) \right\|_\infty$, as with the roll channel, led to less robust margins, as well as less smooth gain surfaces when performing the synthesis over the flight envelope.

[5]Thus the $\mathcal{H}_2$ norm of $G(s)/s$ corresponds to the energy of the step response of $G(s)$.

takes the form:

$$\begin{aligned} \underset{\boldsymbol{\kappa}_{PY}}{\text{minimise}} \quad & f(\boldsymbol{\kappa}_{PY}) \\ \text{subject to} \quad & \left\| W_S(s)\mathcal{T}_{d_z \to n_z}(s) \right\|_\infty < 1 \\ & \left\| W_S(s)\mathcal{T}_{d_y \to n_y}(s) \right\|_\infty < 1 \\ & \left\| W_{KS}(s, \boldsymbol{\lambda}_{PY})\mathcal{T}_{\boldsymbol{d}_{zy} \to \boldsymbol{\delta}_{qr}}(s) \right\|_\infty < 1 \end{aligned} \tag{3.63}$$

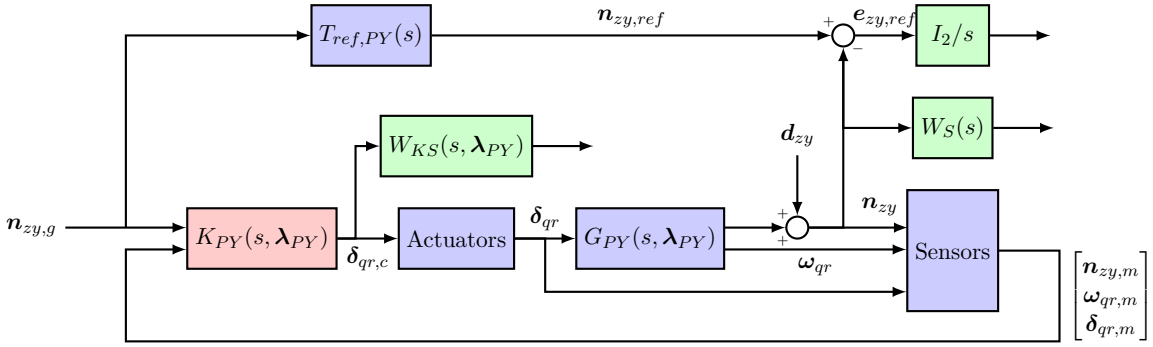

Figure 3.24: Structured $\mathcal{H}_2/\mathcal{H}_\infty$ synthesis problem for the pitch/yaw autopilot

A key aspect to address is the parametrisation of $W_{KS}(s, \boldsymbol{\lambda}_{PY})$. Indeed, since the control authority of the projectile varies significantly across the flight envelope, choosing a unique weighting function for control attenuation is inadequate. On the other hand, it is overly tedious to manually adapt the weighting function to each design point. The proposed strategy relies on introducing a scaling factor $k(\boldsymbol{\lambda}_{PY})$ based on the DC gain of the pitch/yaw airframe model. More precisely, noting $(\boldsymbol{A}(\boldsymbol{\lambda}_{PY}), \boldsymbol{B}(\boldsymbol{\lambda}_{PY}), \boldsymbol{C}(\boldsymbol{\lambda}_{PY}), \boldsymbol{D}(\boldsymbol{\lambda}_{PY}))$ a realisation of the airframe at $\boldsymbol{\lambda}_{PY}$ (cf. Section 2.4.2), and noting

$$\boldsymbol{K}_{DC}(\boldsymbol{\lambda}_{PY}) = \boldsymbol{D}(\boldsymbol{\lambda}_{PY}) - \boldsymbol{C}(\boldsymbol{\lambda}_{PY})\boldsymbol{A}(\boldsymbol{\lambda}_{PY})^{-1}\boldsymbol{B}(\boldsymbol{\lambda}_{PY}) \tag{3.64}$$

the scaling factor $k(\boldsymbol{\lambda}_{PY})$ is selected as the first coefficient of $\boldsymbol{K}_{DC}(\boldsymbol{\lambda}_{PY})$, corresponding to the input δ_q and output n_z. The weighting function $W_{KS}(s, \boldsymbol{\lambda}_{PY})$ is then parametrised as:

$$W_{KS}(s, \boldsymbol{\lambda}_{PY}) = k(\boldsymbol{\lambda}_{PY}) \cdot \hat{W}_{KS}(s) \tag{3.65}$$

with $\hat{W}_{KS}(s)$ to tune.

A design point $\boldsymbol{\lambda}_{PY0}$ corresponding to high velocity $V = 340$ m/s, low altitude $h = 0$ m, and intermediate spin rate $p_a = 1200$ rad/s is then selected to perform a first synthesis. This point corresponds to the end of a trajectory, where performance is critical to guarantee good terminal accuracy. The weighting functions are tuned as follows:

$$W_S(s) = \frac{s + 5}{2s + 5 \cdot 10^{-4}} \tag{3.66}$$

$$\hat{W}_{KS}(s) = \frac{s + 110}{10^{-2}s + 110 \cdot 3} \tag{3.67}$$

The closed-loop step response is shown in Figure 3.25 and corresponds to a soft goal value of 2.52. Figure 3.26 shows the shaped transfer functions, as well as the transfers $\mathcal{T}_{\boldsymbol{n}_{zy,g} \to \boldsymbol{n}_{zy}}(s)$ and

$\mathcal{T}_{\boldsymbol{n}_{zy,g} \to \boldsymbol{e}_{zy,ref}}(s)$. The shape of the latter remains similar to what can be expected with a $\mathcal{H}_\infty$ model matching requirement, despite no such requirement being present in the optimisation problem. This illustrates the relevance of the time-domain step tracking goal.

The same synthesis problem is subsequently solved on a $7 \times 6 \times 5$ grid of the reduced flight envelope (210 points). The hard constraints are satisfied for all design points, while the worst-case value of the soft goal reaches 4.86 at point $(V, h, p_a) = (380\ \text{m/s}, 9000\ \text{m}, 750\ \text{rad/s})$. Nonetheless, the corresponding step response, shown in Figure 3.27, remains satisfactory. Figures 3.28 to 3.32 show the values of the controller gains for all 210 design points, displayed as surfaces in (V, h) for the different values of p_a. The surfaces remain relatively smooth, with the notable exception of the gains $K_{p,\delta}^{(11)}$ and $K_{p,\delta}^{(12)}$. However, this issue is mitigated by the fact that variations of these two gains are in fact restricted to a small interval.

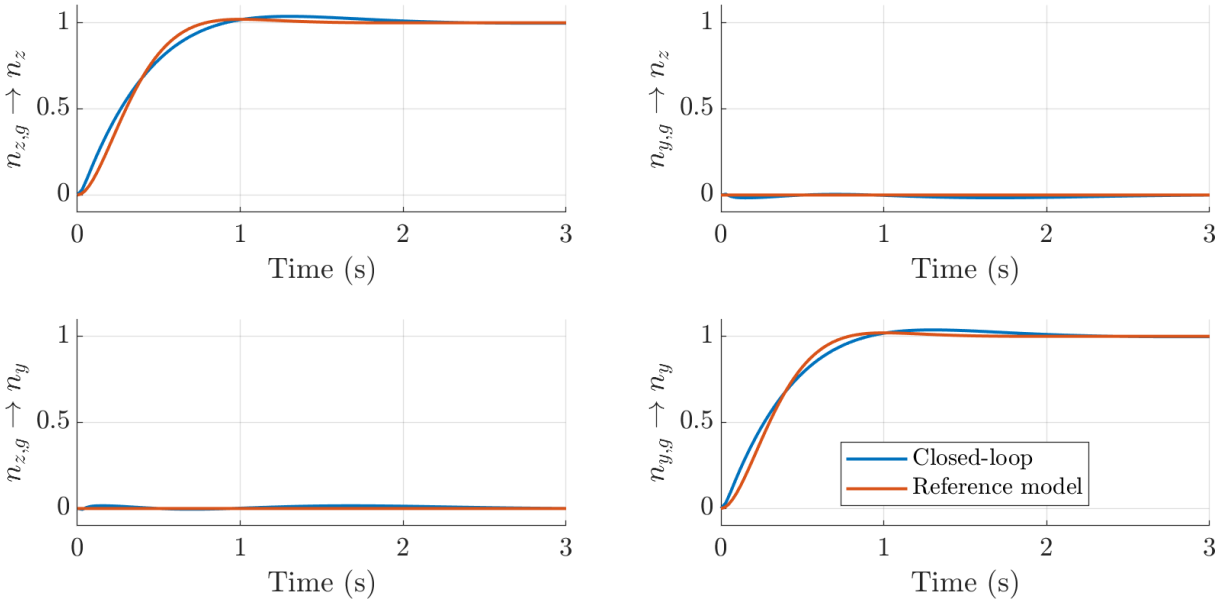

Figure 3.25: Closed-loop system step response at design point ($\gamma = 2.52$)

3.5.3 Robustness analysis and time-domain simulations

Robustness analysis

Robust stability is evaluated at all design points by computing the loop-at-a-time and multivariable margins. The results are summarised in Table 3.1, which shows the minimal values obtained over the design points. The minimal loop-at-a-time gain, phase, and modulus margins remain satisfactory. On the other hand, the values obtained for the delay and multivariable disk-based margins [Seiler et al., 2020] are rather low, and retuning of some points may then be necessary depending on the navigation module and hardware selection, as well as the related potential computational delays and uncertainties. However further fine-tuning of the baseline autopilot is out of the scope of this study.

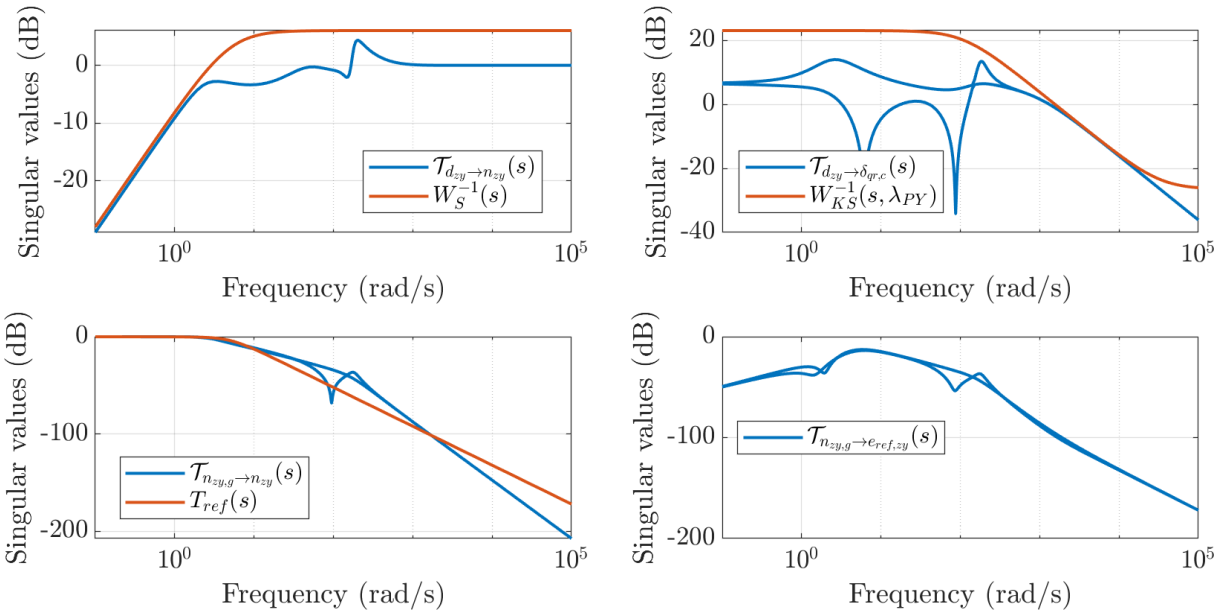

Figure 3.26: Closed-loop transfer functions for disturbance rejection (upper left), control attenuation (upper right), reference tracking (lower left), model matching (lower right)

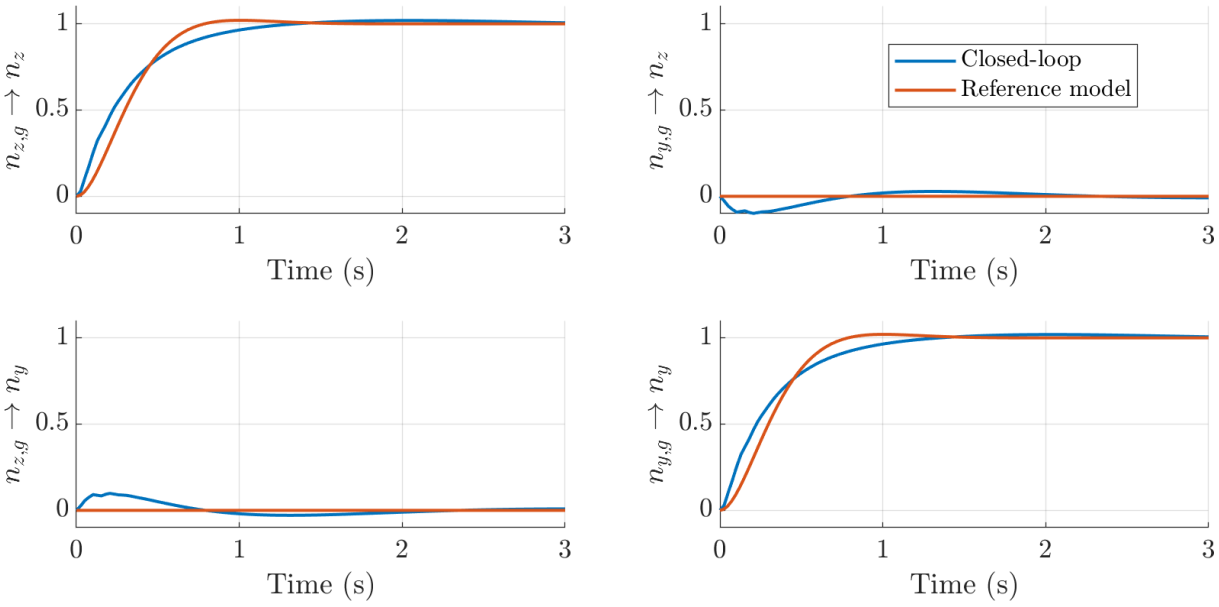

Figure 3.27: Worst-case closed-loop system step response over the design points ($\gamma = 4.86$)

Table 3.1: Minimum loop-at-a-time gain, phase, delay, modulus margins (columns GM, PM, DM, SISO MM), minimum multivariable modulus margin (MIMO MM), and minimum multiloop disk-based margin (DGM, DPM) at the autopilot output

GM	PM	DM	SISO MM	MIMO MM	DGM	DPM
6.05 dB	36.8 deg	0.01 s	0.50	0.25	2.14 dB	14.02 deg

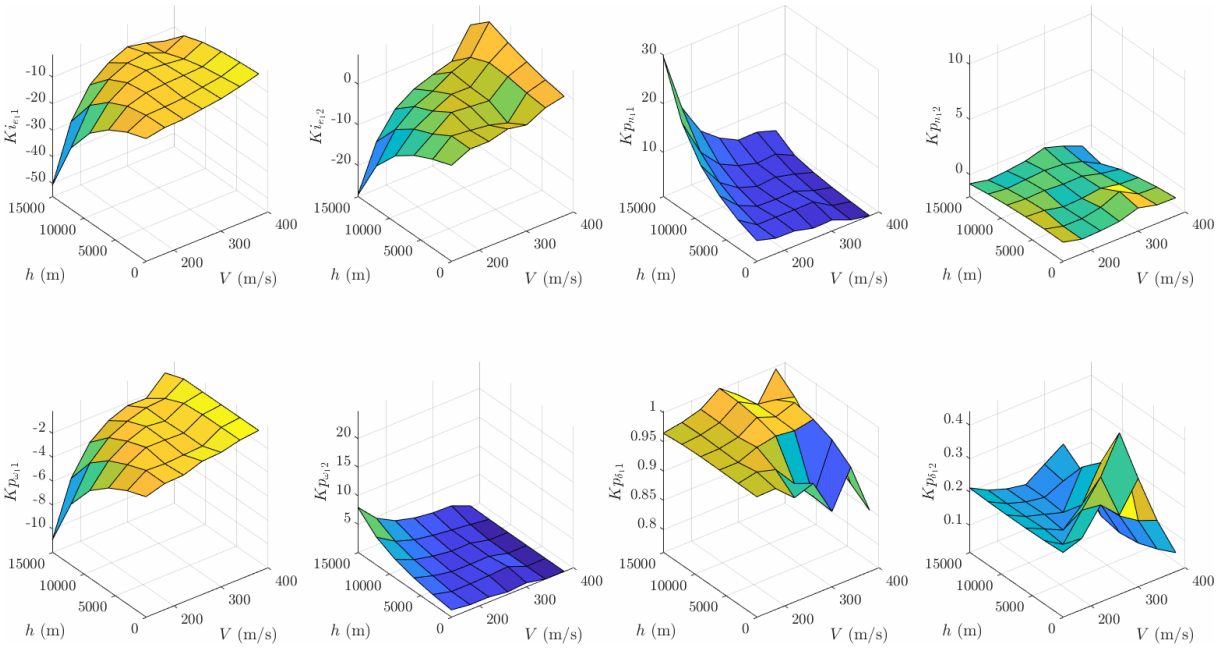

Figure 3.28: Gain surfaces at $p_a = 750$ rad/s

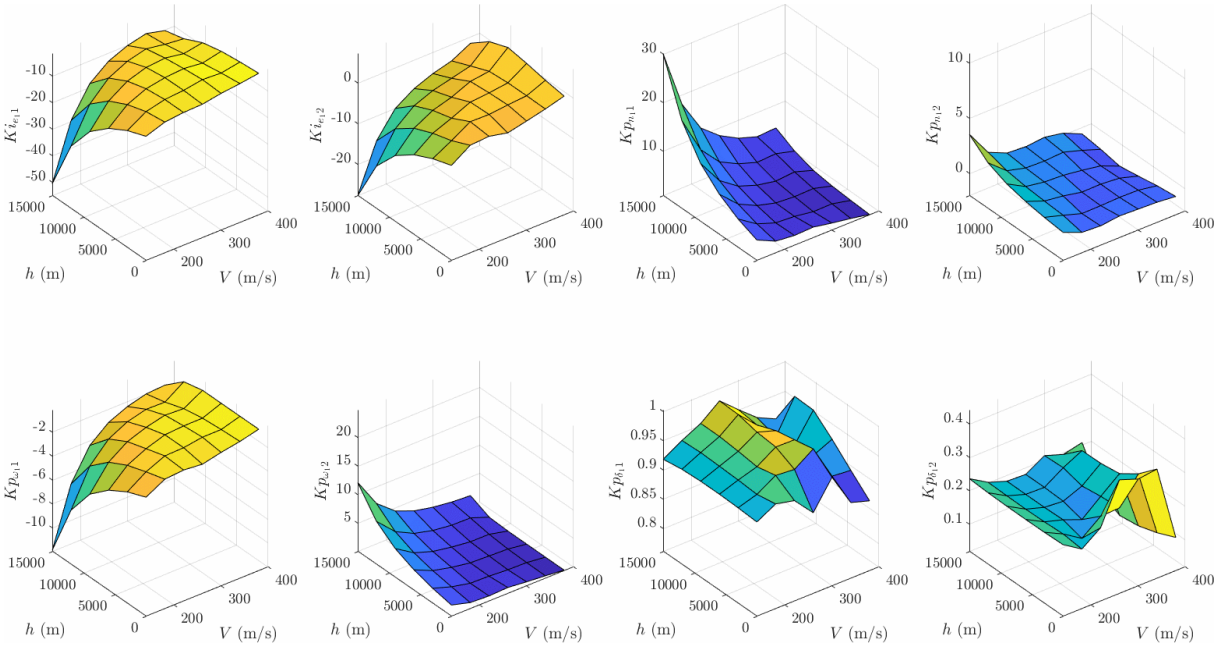

Figure 3.29: Gain surfaces at $p_a = 975$ rad/s

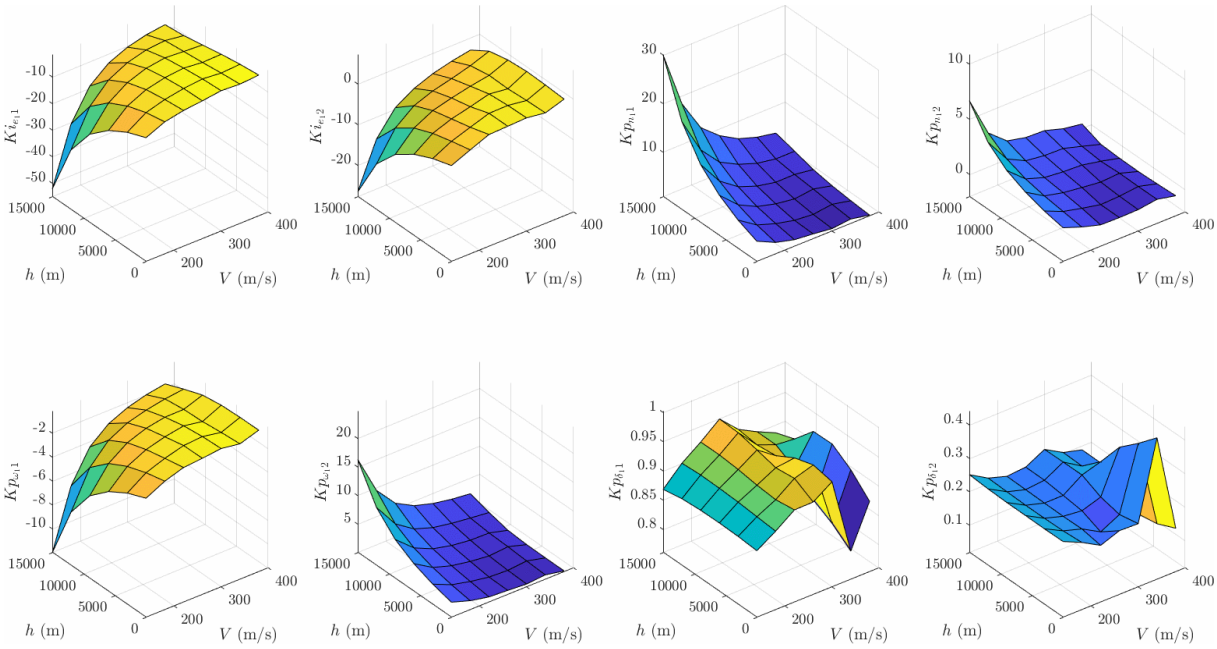

Figure 3.30: Gain surfaces at $p_a = 1200$ rad/s

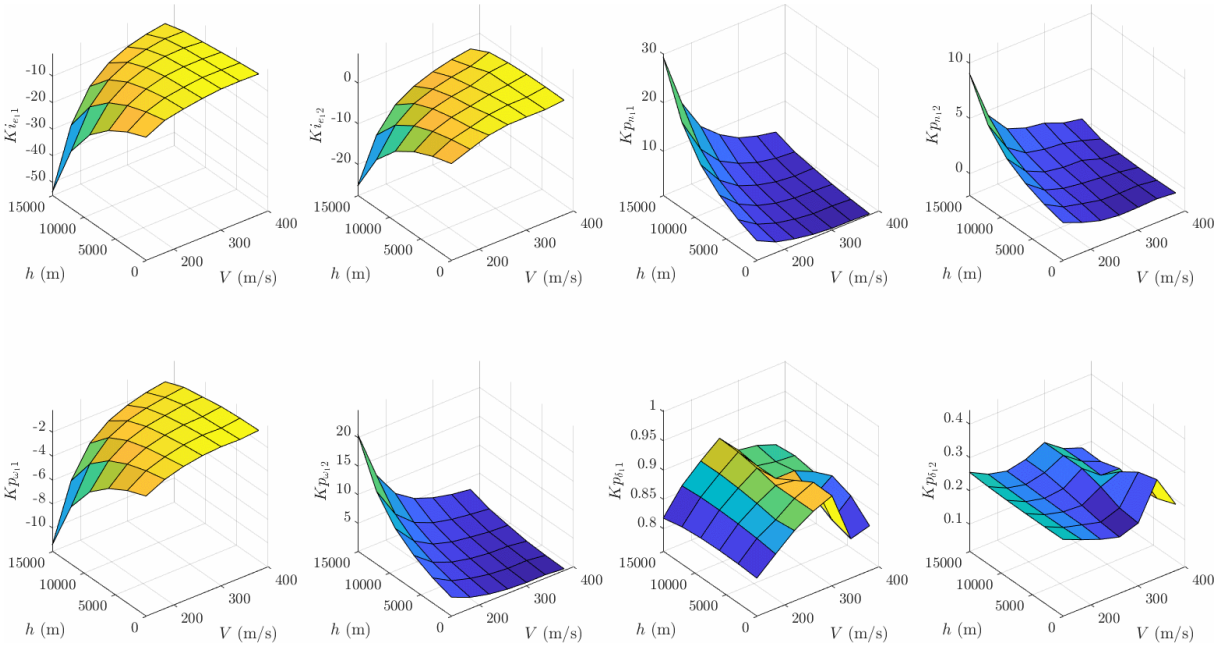

Figure 3.31: Gain surfaces at $p_a = 1425$ rad/s

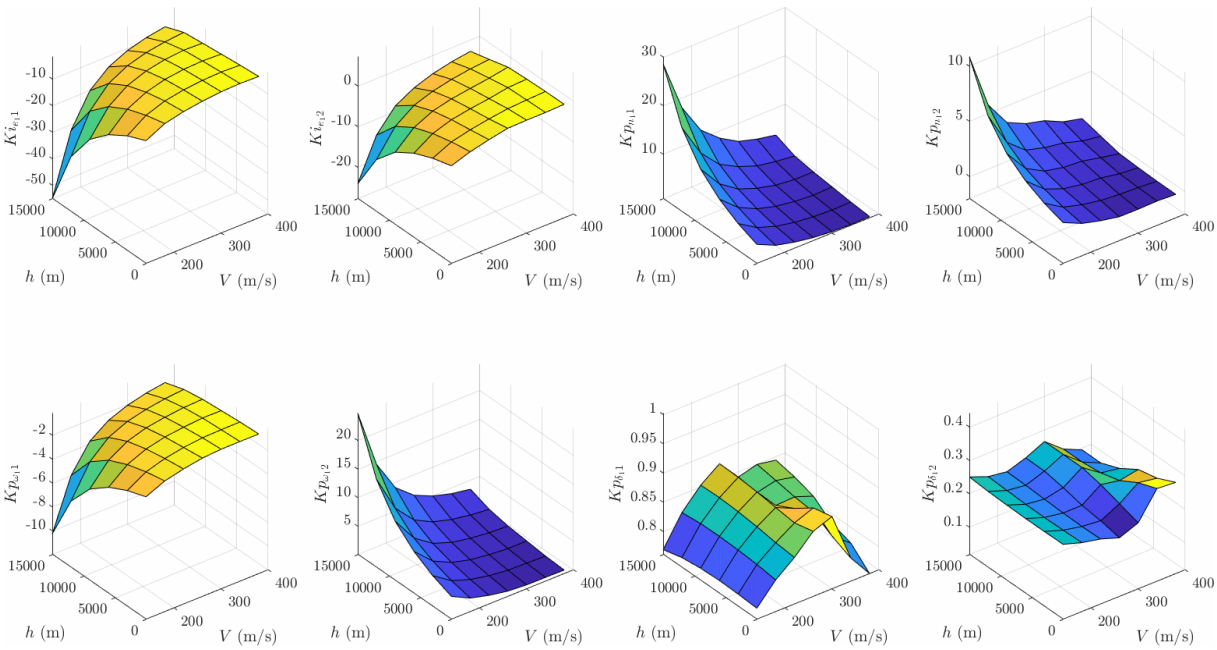

Figure 3.32: Gain surfaces at $p_a = 1650$ rad/s

A μ-analysis is then used to verify local robust stability for all design points. Recall that the pitch/yaw channels are affected by eight parametric uncertainties:

$$\boldsymbol{\delta}_{PY} = [\delta_{C_{N\alpha}}, \delta_{C_{N\delta}}, \delta_{C_A}, \delta_{C_{Yp\alpha}}, \delta_{C_{m\alpha}}, \delta_{C_{mq}}, \delta_{C_{m\delta}}, \delta_{C_{np\alpha}}]^T \in [-1, 1]^8 \tag{3.68}$$

These are gathered in the block Δ_{PY} whose structure is given in Equation (2.69). Only one point fails to validate robust stability, with $\mu \in [1.009,\ 1.02]$ ($k_r \in [0.980,\ 0.991]$), for parameter values $V = 300$ m/s, $h = 3000$ m, and $p_a = 750$ rad/s. Interestingly, the value of the airspeed at this point is a bit below Mach 1, which corresponds to either extrema or strong variations of several aerodynamic coefficients. This is combined with a low value of p_a, for which gyroscopic stability is weaker, thus giving a physical interpretation of why robust stability is not achieved at this point. However, probabilistic μ-analysis allows to show that the probability of instability at this point is in fact very low, with an upper bound at 0.013% assuming a uniform distribution of the uncertainties, and lowering to approximately $9 \cdot 10^{-7}$% when considering truncated normal distributions (where, as before, 3σ corresponds to the difference between the nominal value and any of the extremal values).

Worst-case and probabilistic $\mathcal{H}_\infty$ performance are then investigated on three realistic design points of the same ballistic trajectory, with the following parameter values:

- Point #1 (near apogee): $(V, h, p_a) = (300\text{ m/s}, 9000\text{ m}, 1650\text{ rad/s})$,
- Point #2 (descent): $(V, h, p_a) = (300\text{ m/s}, 6000\text{ m}, 1425\text{ rad/s})$,
- Point #3 (close to impact): $(V, h, p_a) = (340\text{ m/s}, 0\text{ m}, 1200\text{ rad/s})$.

Two scalar performance channels are considered, given respectively by the transfer functions $\mathcal{T}_{n_{z,g} \to e_{z,ref}}(s)$ and $\mathcal{T}_{n_{z,g} \to e_{y,ref}}(s)$. The former evaluates the step tracking performance, while

the latter corresponds to the cross-axis decoupling. Table 3.2 shows the nominal and worst-case $\mathcal{H}_\infty$ performance of these two transfer functions for the three considered design points. Performance degradations are noticeably more important for Point #3. It can also be checked that virtually identical values are obtained for $\mathcal{T}_{n_{y,g}\to e_{y,ref}}(s)$ and $\mathcal{T}_{n_{y,g}\to e_{z,ref}}(s)$, thus confirming the symmetry of the model which was enforced during the synthesis. Probabilistic μ-analysis is then used to compute bounds on the probability of $\mathcal{H}_\infty$ performance satisfaction, for performance levels varying between the nominal and worst-case values. The results are shown in Figure 3.33. Unfortunately, the bounds obtained are not tight, indicating that the branch-and-bound algorithm fails to categorise a significant subdomain of the uncertain parametric space. This is especially true for lower values of the target performance level, where we would expect most of the domain to violate the specification. Thus, this behaviour can be attributed to the use of the sufficient condition of Proposition 3.13 to validate performance violation. Accordingly, the computational effort is significant in this case, at about 2 hours to generate all the data shown in Figure 3.33 when using μ-sensitivities for bisection. Parallel computing offers a promising solution to reduce the computational time. However, the search for more efficient heuristics to validate performance violation and decreasing the guaranteed upper bound on the probability of performance satisfaction remains an open issue. On the other hand, the guaranteed lower bounds remain useful to quantify the conservatism of the worst-case $\mathcal{H}_\infty$ performance values. Indeed, it can be observed that for all the tested performance channels, more than 90% of the uncertain parametric space satisfies a performance level at the middle value of the nominal and worst cases. This constitutes an interesting benchmark against which to compare future autopilot designs for this system.

Table 3.2: Nominal and worst-case $\mathcal{H}_\infty$ performance of the closed-loop pitch/yaw channel at different analysis points

Analysis point	**#1**	**#2**	**#3**
Tracking (nominal, worst-case)	0.24, 0.37	0.24, 0.38	0.22, 0.86
Decoupling (nominal, worst-case)	0.01, 0.23	0.01, 0.28	0.04, 0.82

The above study of probabilistic $\mathcal{H}_\infty$ performance shows some numerical difficulties that can arise in an exhaustive exploration of the uncertainty domain, and which prevent from obtaining tight estimates of the cumulative distribution functions. However, such a strategy is not necessarily relevant for validation purposes. To illustrate this, consider now the case of loop-at-a-time margins, where we want to determine whether a target gain or phase margin value is guaranteed with probability higher than a given threshold $1 - p_{fail}$. This criterion can be taken into account in Algorithm 5, by changing the stopping condition of Line 6 to:

$$\mathcal{L} = \emptyset \text{ or } p(D_m) \geq 1 - p_{fail} \text{ or } p(D_{\overline{m}}) \geq p_{fail} \tag{3.69}$$

This modified condition can potentially allow to conclude quickly. Thus, with $p_{fail} = 10^{-6}$ and a uniform distribution of the uncertainties, the target gain margin value of 6 dB is invalidated for all three analysis points in respectively 0.8 s, 6.4 s, and 7.4 s. Likewise, the target phase margin value 30 deg is invalidated for Points #1 and #2 in respectively 34.1 s and 183.5 s, and is guaranteed on the whole uncertainty domain for Point #3 in 4 s. The relatively high computation

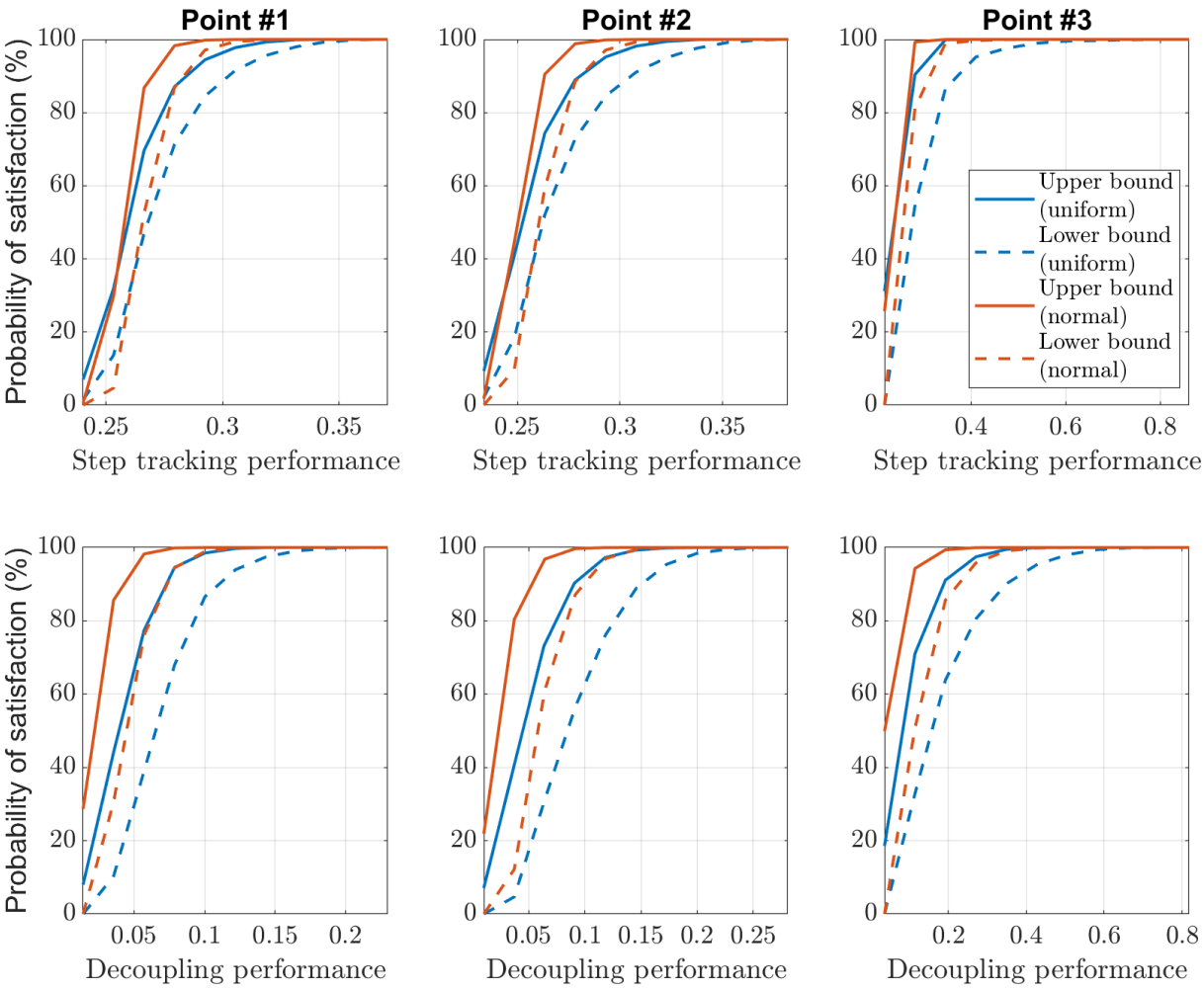

Figure 3.33: Probability of $\mathcal{H}_\infty$ performance satisfaction for step tracking ($\mathcal{T}_{n_{z,g} \to e_{z,ref}}$) and decoupling ($\mathcal{T}_{n_{z,g} \to e_{y,ref}}$) for three design points of the reduced flight envelope

time for Point #2 must be confronted to the fact that the probability of phase margin violation $p(D_{\overline{m}})$ is also established to be below 1.15%, making it a moderately rare event. However, the benefits compared to Monte Carlo techniques may not be obvious. Another modification to the branch-and-bound strategy can then be considered. First, an upper bound on the worst-case phase margin $\overline{\phi}_{wc} = 26.9\,\text{deg}$ is computed by solving a skew-μ-analysis problem, along with the corresponding uncertainty configuration $\boldsymbol{\delta}_{PY} = [1, -1, 1, 1, -1, -1, 1, -1]$. Then Line 7 of Algorithm 5 is modified so that, instead of analysing the box with highest probability measure, we analyse the box whose centre is closest to $\boldsymbol{\delta}_{PY}$. Indeed, with this strategy, the target phase margin value is now invalidated in a mere 3.7 s for Point #2, including the time required to compute $\overline{\phi}_{wc}$. Likewise, applied on Point #1, the target phase margin can now be invalidated in 3.0 s. Thus with these adaptations to the branch-and-bound algorithm, the proposed μ-based method remains very competitive when compared to Monte Carlo techniques to quickly invalidate a requirement. That being said, all three points robustly achieve relaxed requirements of 3 dB and 25 deg, as well as a modulus margin of 0.35, which is deemed sufficient to proceed with the current design.

Closed-loop time-domain simulations

The impact of the uncertainties is visualised in the time-domain simulations of Figure 3.34, which shows the responses of the nominal system and uncertain samples related to Point #3. Confirming the previous μ-analysis, both tracking and decoupling are noticeably degraded in the presence of uncertainties. In addition, larger control signals are required by the autopilot. However, the degradations are overall moderate and the responses remain within a small envelope around the nominal response.

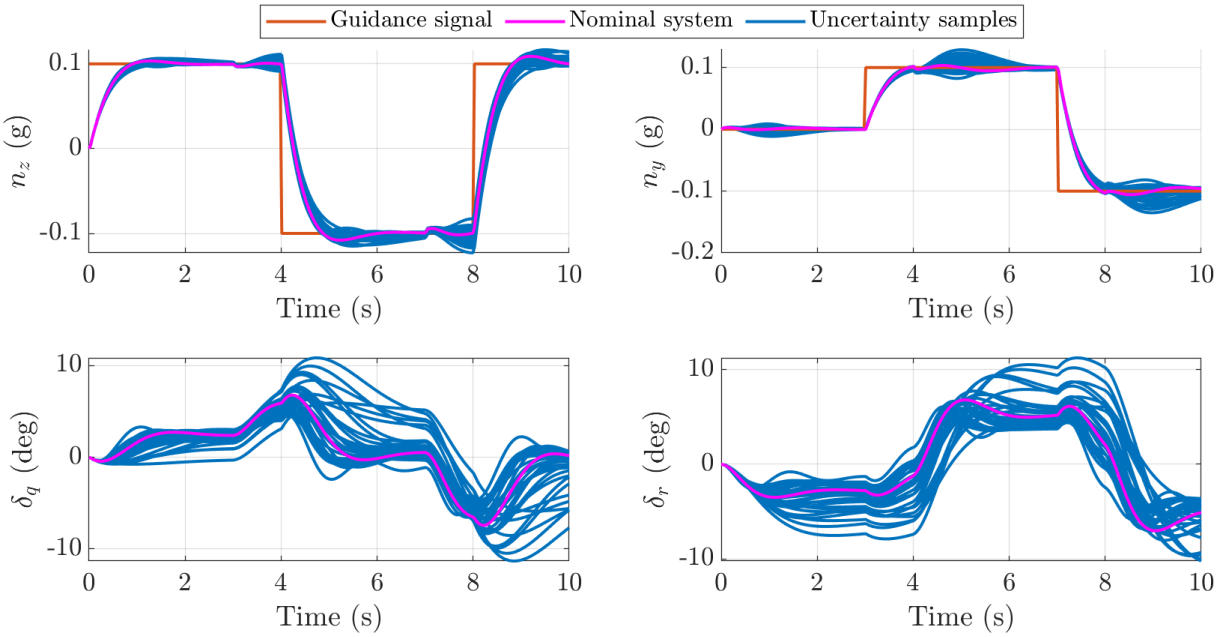

Figure 3.34: Simulation with model uncertainties at the design point

This section concludes with an LTV simulation of the closed-loop pitch/yaw channel for a fixed trajectory of the scheduling variables. The trajectory is given in Figure 3.35, and is taken from a ballistic trajectory. Values of the controller gains outside of the $7 \times 6 \times 5$ design grid are obtained using the linear interpolation scheme of Equation (3.7). Meanwhile, the guidance signals $n_{z,g}$ and $n_{y,g}$ are defined as the ballistic load factors, and thus have order of magnitudes representative of a realistic scenario. Figure 3.36 shows that the gain scheduled autopilot allows to successfully follow the reference signals. Furthermore, this is achieved with low deflection angles, limiting the risk of saturations in nominal scenarios. However, as already hinted by Figure 3.34, and as explicitly shown in Chapter 5, degraded scenarios involving uncertainties on the launch conditions or the aerodynamic coefficients can potentially lead to larger load factors and deflection angles exceeding the saturation level, justifying the need to develop an anti-windup compensator. This is the topic of the next chapter.

3.6 Conclusion

In this chapter, major theoretical contributions to probabilistic μ-analysis have been presented, leading to the development of enhanced branch-and-bound algorithms for stability, $\mathcal{H}_\infty$ performance, and gain/phase/modulus margins. These methods offer a way to quantify the

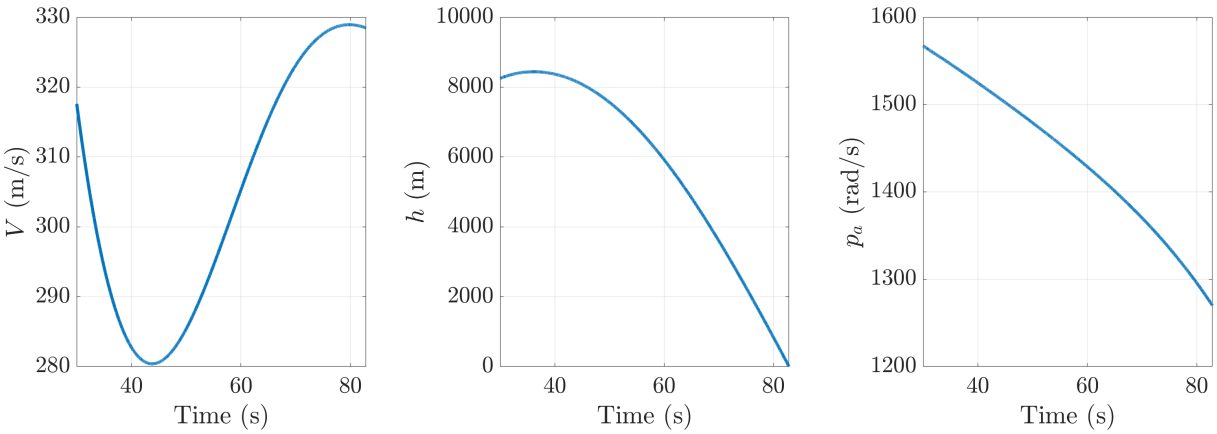

Figure 3.35: Evolution of the scheduling variables along a ballistic trajectory

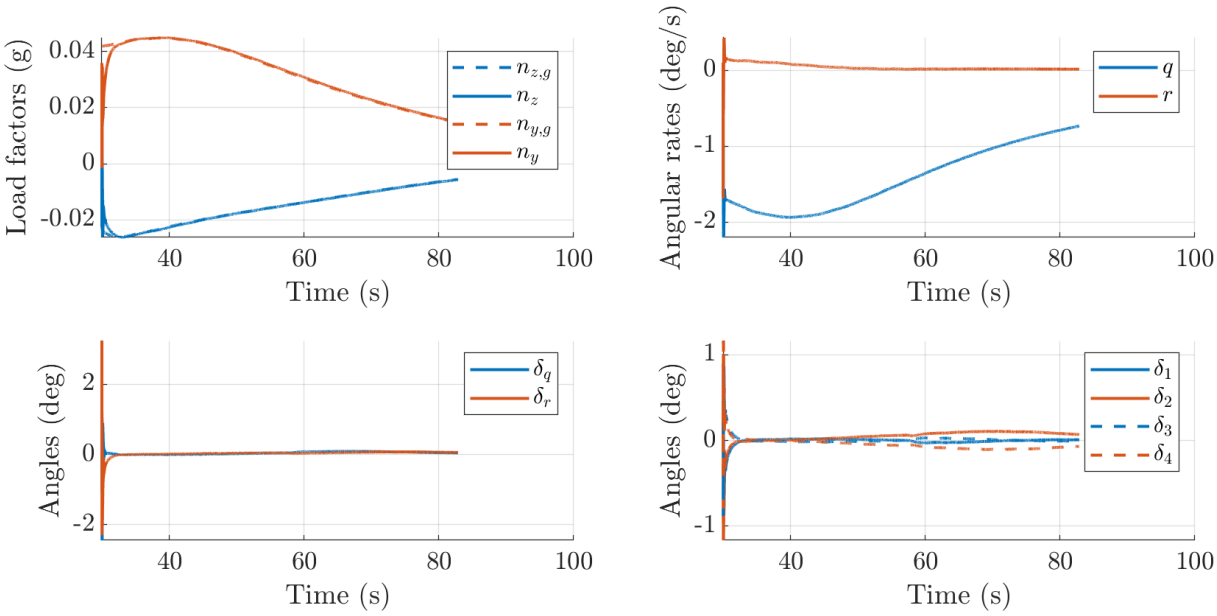

Figure 3.36: Closed-loop simulation of the linearised pitch/yaw channels with parameter variations

conservatism of standard (worst-case) μ-analysis, and, unlike Monte Carlo methods, provide hard upper and lower bounds on the evaluated probabilities. In addition, the obtained bounds are easily updated when different uncertainty distributions are considered. An essential part of the proposed branch-and-bound algorithms lies in the ability to categorise subdomains of the uncertain parameter space violating the tested criterion, and sufficient conditions have been formulated to this effect.

Regarding the guided projectile application, gain scheduled autopilots have been developed for both the roll and the pitch/yaw channels. Simple structures are used for the controllers, whose gains are computed by solving an $\mathcal{H}_\infty$ problem for the roll autopilot, and a $\mathcal{H}_2/\mathcal{H}_\infty$ problem for the pitch/yaw autopilot. A single design point is used to compute the roll autopilot, with the application of a parameter-dependent scaling coefficient ensuring nominal performance across the flight envelope. The resulting closed-loop displays very good robustness properties, and the use of probabilistic μ-analysis on this system allows to compute tight approximations of the $\mathcal{H}_\infty$ performance and margins distributions in very short times. The pitch/yaw autopilot is obtained

by computing local controllers on a grid of the reduced flight envelope, resulting in relatively smooth gain surfaces, and gain scheduling is achieved through linear interpolation. While a single design point that fails to validate local robust stability is found, probabilistic μ-analysis is useful here to establish that the probability of instability is in fact very low, and below a typical validation threshold. Regarding probabilistic $\mathcal{H}_\infty$ performance, while the branch-and-bound algorithm does not provide tight bounds, it still offers a useful quantification of the conservatism of worst-case values. Finally, time-domain simulations are proposed to illustrate the local robustness of the design, and the effectiveness of the interpolation scheme when variations of the scheduling parameters are at play.

References

Apkarian, P. and Noll, D. (2006). "Nonsmooth H_∞ Synthesis". In: *IEEE Transactions on Automatic Control* 51.1, pp. 71–86.

Apkarian, P., Gahinet, P., and Buhr, C. (2014). "Multi-model, multi-objective tuning of fixed-structure controllers". In: *2014 European Control Conference (ECC)*. IEEE.

Apkarian, P. and Noll, D. (2017). "The H_∞ control problem is solved". In: *Aerospace Lab* 13.

Athans, M., Castanon, D., Dunn, K., Greene, C., Lee, W., Sandell, N., and Willsky, A. (1977). "The stochastic control of the F-8C aircraft using a multiple model adaptive control (MMAC) method–Part I: equilibrium flight". In: *IEEE Transactions on Automatic Control* 22.5, pp. 768–780.

Bianchi, F. D. and Sánchez-Peña, R. S. (2011). "Interpolation for gain-scheduled control with guarantees". In: *Automatica* 47.1, pp. 239–243.

Braatz, R. D. and Morari, M. (1991). "μ-sensitivities as an aid for robust identification". In: *1991 American Control Conference*. IEEE.

Braatz, R. P., Young, P. M., Doyle, J. C., and Morari, M. (1994). "Computational complexity of μ calculation". In: *IEEE Transactions on Automatic Control* 39.5, pp. 1000–1002.

Buschek, H. and Dold, R. (2001). "Flight test of a scheduled mu-synthesis autopilot for an air-to-air missile". In: *AIAA Guidance, Navigation, and Control Conference and Exhibit*. American Institute of Aeronautics and Astronautics.

Dorato, P. (1987). "A historical review of robust control". In: *IEEE Control Systems Magazine* 7.2, pp. 44–47.

Doyle, J. (1978). "Guaranteed margins for LQG regulators". In: *IEEE Transactions on Automatic Control* 23.4, pp. 756–757.

Doyle, J., Packard, A., and Zhou, K. (1991). "Review of LFTs, LMIs, and mu". In: *30th IEEE Conference on Decision and Control*. IEEE.

Doyle, J. and Stein, G. (1981). "Multivariable feedback design: Concepts for a classical/modern synthesis". In: *IEEE Transactions on Automatic Control* 26.1, pp. 4–16.

Doyle, J. (1982). "Analysis of feedback systems with structured uncertainties". In: *IEE Proceedings D Control Theory and Applications* 129.6, p. 242.

Doyle, J., Glover, K., Khargonekar, P., and Francis, B. (1988). "State-space solutions to standard H_2 and H_∞ control problems". In: *1988 American Control Conference*. IEEE.

Falcoz, A., Alazard, D., and Pittet, C. (2017). "Probabilistic μ-analysis for system performances assessment". In: *IFAC-PapersOnLine* 50.1, pp. 399–404.

Fan, M. K. H. and Tits, A. L. (1992). "A measure of worst-case H_∞ performance and of largest acceptable uncertainty". In: *Systems & Control Letters* 18.6, pp. 409–421.

Gahinet, P. and Apkarian, P. (1994). "A linear matrix inequality approach to H_∞ control". In: *International Journal of Robust and Nonlinear Control* 4.4, pp. 421–448.

Glover, K. and McFarlane, D. (1989). "Robust stabilization of normalized coprime factor plant descriptions with H_∞-bounded uncertainty". In: *IEEE Transactions on Automatic Control* 34.8, pp. 821–830.

Helton, J. C., Johnson, J. D., Sallaberry, C. J., and Storlie, C. B. (2006). "Survey of sampling-based methods for uncertainty and sensitivity analysis". In: *Reliability Engineering & System Safety* 91.10-11, pp. 1175–1209.

Hyde, R. A. and Glover, K. (1990). "VSTOL aircraft flight control system design using H_∞ controllers and a switching strategy". In: *29th IEEE Conference on Decision and Control*. IEEE.

Iwasaki, T. and Skelton, R. E. (1994). "All controllers for the general H_∞ control problem: LMI existence conditions and state space formulas". In: *Automatica* 30.8, pp. 1307–1317.

Khatri, S. and Parrilo, P. A. (1998). "Guaranteed bounds for probabilistic μ". In: *37th IEEE Conference on Decision and Control)*. IEEE.

Kwakernaak, H. (2002). "Mixed sensitivity design". In: *IFAC Proceedings Volumes* 35.1, pp. 61–66.

Landau, D. P. and Binder, K. (2014). *A guide to Monte Carlo simulations in statistical physics*. Cambridge university press.

Lawrence, D., Kelly, J., and Evers, J. (1998). "Gain scheduled missile autopilot design using a control signal interpolation technique". In: *Guidance, Navigation, and Control Conference and Exhibit*. American Institute of Aeronautics and Astronautics.

Leith, D. J. and Leithead, W. E. (2000). "Survey of gain-scheduling analysis and design". In: *International Journal of Control* 73.11, pp. 1001–1025.

Lescher, F. and Roos, C. (2011). "Robust stability of time-delay systems with structured uncertainties: a μ-analysis based algorithm". In: *50th IEEE Conference on Decision and Control and European Control Conference*. IEEE.

Lesprier, J., Roos, C., and Biannic, J.-M. (2015). "Improved μ upper bound computation using the μ-sensitivities". In: *IFAC-PapersOnLine* 48.14, pp. 215–220.

Newlin, M. P. and Young, P. M. (1992). "Mixed mu problems and branch and bound techniques". In: *31st IEEE Conference on Decision and Control*. IEEE.

Packard, A. and Doyle, J. (1993). "The complex structured singular value". In: *Automatica* 29.1, pp. 71–109.

Rasmussen, B. P. and Alleyne, A. G. (2009). "Gain scheduled control of an air conditioning system using the Youla parametrization". In: *IEEE Transactions on Control Systems Technology* 18.5, pp. 1216–1225.

Roos, C. and Biannic, J.-M. (2015). "A detailed comparative analysis of all practical algorithms to compute lower bounds on the structured singular value". In: *Control Engineering Practice* 44, pp. 219–230.

Roos, C. (2013). "Systems modeling, analysis and control (SMAC) toolbox: an insight into the robustness analysis library". In: *2013 Conference on Computer Aided Control System Design (CACSD)*. IEEE.

Roos, C. (2010). "A practical approach to worst-case H_∞ performance computation". In: *2010 International Symposium on Computer-Aided Control System Design*. IEEE.

Roos, C. and Biannic, J.-M. (2010). "Efficient computation of a guaranteed stability domain for a high-order parameter dependent plant". In: *2010 American Control Conference*. IEEE.

Roos, C., Lescher, F., Biannic, J.-M., Döll, C., and Ferreres, G. (2011). "A set of μ-analysis based tools to evaluate the robustness properties of high-dimensional uncertain systems". In: *2011 International Symposium on Computer-Aided Control System Design (CACSD)*. IEEE.

Rugh, W. J. and Shamma, J. S. (2000). "Research on gain scheduling". In: *Automatica* 36.10, pp. 1401–1425.

Safonov, M. G. (1982). "Stability margins of diagonally perturbed multivariable feedback systems". In: *IEE Proceedings D Control Theory and Applications* 129.6, p. 251.

Safonov, M. G. (2012). "Origins of robust control: Early history and future speculations". In: *Annual Reviews in Control* 36.2, pp. 173–181.

Seiler, P., Packard, A., and Gahinet, P. (2020). *An introduction to disk margins*. URL: `https://arxiv.org/abs/2003.04771`.

Shahruz, S. M. and Behtash, S. (1992). "Design of controllers for linear parameter-varying systems by the gain scheduling technique". In: *Journal of Mathematical Analysis and Applications* 168.1, pp. 195–217.

Shimomura, T. (2003). "Hybrid control of gain-scheduling and switching: a design example of aircraft control". In: *2003 American Control Conference*. IEEE.

Skogestad, S. and Postlethwaite, I. (2005). *Multivariable feedback control: analysis and design*. Wiley-Interscience.

Stein, G. and Athans, M. (1987). "The LQG/LTR procedure for multivariable feedback control design". In: *IEEE Transactions on Automatic Control* 32.2, pp. 105–114.

Stilwell, D. J. and Rugh, W. J. (1999). "Interpolation of observer state feedback controllers for gain scheduling". In: *IEEE Transactions on Automatic Control* 44.6, pp. 1225–1229.

Stilwell, D. J. and Rugh, W. J. (2000). "Stability preserving interpolation methods for the synthesis of gain scheduled controllers". In: *Automatica* 36.5, pp. 665–671.

Thai, S., Roos, C., and Biannic, J.-M. (2019). "Probabilistic μ-analysis for stability and H_∞ performance verification". In: *2019 American Control Conference (ACC)*. IEEE.

Theodoulis, S. and Duc, G. (2007a). "Gain-scheduling techniques for missile autopilot synthesis". In: *2007 European Control Conference (ECC)*. IEEE.

Theodoulis, S. and Duc, G. (2007b). "Static interpolated $H\infty$ loop-shaping controllers for missile autopilot synthesis". In: *2007 46th IEEE Conference on Decision and Control*. IEEE.

Theodoulis, S. and Duc, G. (2008). "Gain scheduled autopilot synthesis for an atmosphere re-entry vehicle". In: *Guidance, Navigation and Control Conference and Exhibit*. American Institute of Aeronautics and Astronautics.

Zames, G. (1966). "On the input-output stability of time-varying nonlinear feedback systems Part one: Conditions derived using concepts of loop gain, conicity, and positivity". In: *IEEE Transactions on Automatic Control* 11.2, pp. 228–238.

Zames, G. (1981). "Feedback and optimal sensitivity: Model reference transformations, multiplicative seminorms, and approximate inverses". In: *IEEE Transactions on Automatic Control* 26.2, pp. 301–320.

Zhou, K. and Doyle, J. C. (1998). *Essentials of Robust Control*. Prentice Hall.

Zhu, X., Huang, Y., and Doyle, J. (1996). "Soft vs. hard bounds in probabilistic robustness analysis". In: *35th Conference on Decision and Control*. IEEE.

Chapter 4

Development of anti-windup compensators

Contents

4.1 Introduction

The objective of this chapter is to address the saturations that were ignored from the baseline pitch/yaw autopilot design of Chapter 3. Saturations are associated with a wide array of undesirable nonlinear phenomena, such as limit cycles, performance loss, or even instability. In the two-step procedure adopted here, the effects of saturations are meant to be mitigated by adding an anti-windup compensator to the baseline autopilot. This additional component becomes active and modifies the closed-loop behaviour when saturations are encountered. On the other hand, the unconstrained closed-loop properties are retained when no saturations occur.

This chapter starts with reminders of theoretical elements related to the study of saturated systems in Section 4.2, including stability and performance analysis, anti-windup design using the DLAW and MRAW frameworks, and robustness analysis using IQCs. Given the vastness of each of these topics, this section does not aim to cover them exhaustively, but focuses

on properties and results that are relevant for the study of the guided projectile application. Section 4.3 then presents the anti-windup design step for the pitch/yaw channels of the projectile, where three local architectures are considered. The first one consists in a static DLAW-based compensator maximising a stability domain. The second and third ones are both LQ-based MRAW compensators, with the latter using a reduced plant model. All three approaches require little tuning, making synthesis over a grid of the flight envelope straightforward. The resulting augmented closed-loops are then evaluated and compared through time-domain simulations and IQC analysis.

4.2 Reminders on the study of saturated systems

4.2.1 Introduction to the anti-windup problem

Saturations are present in all physical systems, and can cause severe degradation of the system performance. A first strategy to avoid this scenario is to design a controller that will not reach the saturation levels, at the cost of lower performance which may be unacceptable in some applications. Another strategy is to allow saturations to occur, all the while modifying the closed-loop dynamics to mitigate their detrimental effects. This second approach usually involves a two-step procedure. In a first step, a linear controller is designed and validated as if saturations were absent from the system. The second step addresses saturations by addition of an anti-windup compensator, which only becomes active when saturations occur, ensuring that nominal performance is unaffected as long as saturations are not reached. The principle of anti-windup compensation is illustrated by the Figure 4.1. The anti-windup problem then consists in designing an anti-windup compensator to achieve satisfactory closed-loop behaviour even when saturations occur.

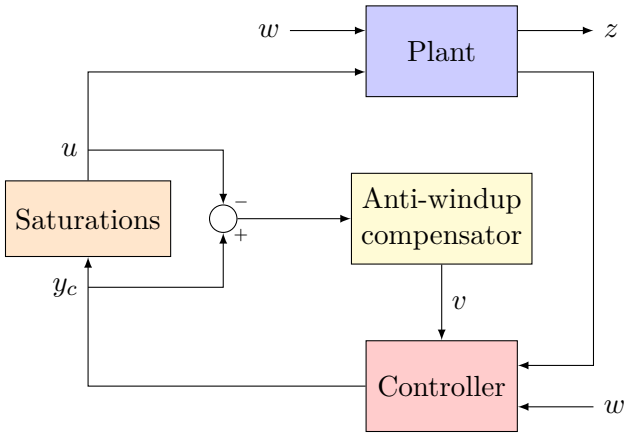

Figure 4.1: Basic anti-windup architecture

Early academic works on the topic date back to the 1950s, although it seems certain that awareness of the problems caused by saturations was already high. In [Lozier, 1956], the impact of saturations on PI control systems are studied. Subsequently, several ad hoc anti-windup schemes for PID controllers were proposed, including back calculation [Fertik and Ross, 1967], Hanus' conditioning techniques [Hanus et al., 1987], and observer-based approaches [Åström

and Rundqwist, 1989]. However, as pointed out by [Doyle et al., 1987], these methods provided neither stability nor performance guarantees.

The topic gained in impetus from a theoretical perspective with the work of [Kothare et al., 1994], where a unifying framework was formulated, encompassing many previously proposed compensation schemes, and inspired by the standard form from robust control. Several methods based on LMI resolutions then started to appear, exploiting increasingly less conservative descriptions of the saturation nonlinearity:

- the so-called classical sector conditions, allowing to treat saturated systems as Lur'e systems [Vidyasagar, 2002; Khalil, 2002] and to exploit theoretical results from absolute stability theory (circle and Popov criteria) [Pittet et al., 2007; Mulder et al., 2001; Saeki and Wada, 2002; Grimm et al., 2003; Hu et al., 2005],
- the polytopic description [Hu et al., 2002; Cao et al., 2002],
- the modified sector conditions of [Gomes da Silva and Tarbouriech, 2005].

The modified sector conditions, which are reviewed in Section 4.2.2, are remarkable since they allow to obtain convex formulations for the anti-windup synthesis problem. The related synthesis techniques are referred to as Direct Linear Anti-Windup (DLAW) in the recent literature [Galeani et al., 2009; Tarbouriech et al., 2011; Zaccarian and Teel, 2011].

An implicit assumption in anti-windup design is that the behaviour of the unconstrained closed-loop system constitutes an ideal response. It is therefore natural to seek to keep track of the distance to this ideal response when saturations occur, and to recover it whenever possible. Early works that explicitly pursued this qualitative objective are [Teel and Kapoor, 1997a; Teel and Kapoor, 1997b]. These papers laid down the key ingredients for another anti-windup paradigm, originally labelled $\mathcal{L}_2$ anti-windup and more recently named Model Recovery Anti-Windup (MRAW).

4.2.2 Analysis of saturated systems

Stability of nonlinear systems with Lyapunov functions

Let us consider an autonomous system described by the first-order differential equation:

$$\begin{cases} \dot{x}(t) = f(x(t)) \\ x(0) = x_0 \in \mathbb{R}^n \end{cases} \tag{4.1}$$

where the function f is supposed to be locally Lipschitz, so as to guarantee the existence and uniqueness of a local solution (or trajectory). For a linear system ($\dot{x}(t) = Ax(t)$), the notion of stability is relatively simple. Indeed, such a system is either globally stable or unstable, and this is easily determined by checking whether all the eigenvalues of A lie in the open left-half complex plane or not. By contrast, stability for nonlinear systems is not as straightforward and can in fact refer to different notions. The most important one is Lyapunov stability theory, introduced by Lyapunov in his PhD thesis in 1892 [Lyapunov, 1992], which focuses on the behaviour of the system around its equilibrium points. The main definitions and results of Lyapunov theory are

given next. These are classical results which can be found e.g. in [Khalil, 2002] or [Vidyasagar, 2002].

Definition 4.1 (Equilibrium point)**.** *A vector $x_e \in \mathbb{R}^n$ is said to be an equilibrium point of the system* (4.1) *if it satisfies $f(x_e) = 0$.*

Any equilibrium point can be brought to the origin through a change of variables. Thus without loss of generality, the following definitions and results are stated with equilibrium point $x_e = 0$.

Definition 4.2 (Stability of an equilibrium point)**.** *The equilibrium point $x_e = 0$ for the system* (4.1) *is said to be:*

- *stable if, for each $\varepsilon > 0$, there exists $\delta > 0$ such that:*

$$\|x_0\| < \delta \implies \|x(t)\| < \varepsilon \ \forall t \geq 0 \tag{4.2}$$

- *attractive if there exists a neighbourhood $\Omega \subset \mathbb{R}^n$ of the origin such that:*

$$x_0 \in \Omega \implies \lim_{t \to \infty} x(t) = 0 \tag{4.3}$$

- *asymptotically stable if x_e is stable and attractive.*

Theorem 4.3 (Lyapunov second method)**.** *Let $x_e = 0$ be an equilibrium point for the system* (4.1)*, and $\Omega \subset \mathbb{R}^n$ a neighbourhood of the origin. Let $V : \Omega \to \mathbb{R}$ be a continuously differentiable function such that:*

$$\forall x \in \Omega \setminus \{0\},\ V(x) > 0 \text{ and } V(0) = 0 \tag{4.4}$$

$$\forall x \in \Omega,\ \dot{V}(x) \leq 0 \tag{4.5}$$

Then $x_e = 0$ is a stable equilibrium point. Moreover, if:

$$\forall x \in \Omega \setminus \{0\},\ \dot{V}(x) < 0 \tag{4.6}$$

then $x_e = 0$ is asymptotically stable.

A function V satisfying conditions (4.4) and (4.5) is called a Lyapunov function. In that case, the domain Ω of the Lyapunov function represents a region of guaranteed stability. A common interpretation is to think of Lyapunov functions as measuring the energy of the state of the system. Then if this energy decreases, the system evolves towards an equilibrium state.

Thus, a strategy to establish the stability of a nonlinear system around the origin consists in finding a Lyapunov function. However, this task is not straightforward to undertake. In practice, the search for Lyapunov functions is restricted to a particular class of functions. A widely used class of functions is that of quadratic functions of the form $V(x) = x^T P x$, where P is a symmetric positive definite matrix (denoted by $P > 0$), thus guaranteeing by construction

the condition (4.4). Although this restriction introduces some conservatism (a notable exception being the LTI case), quadratic functions are nevertheless highly advantageous since they often lead to convex characterisations that can be exploited for synthesis problems. Moreover, their associated domains of stability correspond to ellipsoids:

$$\mathcal{E}(P,\delta) = \left\{x \in \mathbb{R}^n \colon x^T P x \leq \delta^{-1}\right\} \tag{4.7}$$

whose size can be maximised in various ways (e.g. maximisation of the volume, or maximisation in certain directions).

Saturation and deadzone nonlinearities

A saturation function $\mathrm{sat}_l(\cdot)$ is a piecewise linear function given as:

$$\mathrm{sat}_l(y_c) = \mathrm{sign}(y_c) \cdot \min(|y_c|, l) \tag{4.8}$$

where $l > 0$ defines the limits of the saturation. A related function is the deadzone function $\mathrm{dz}_l(\cdot)$ characterised by the identity[1]:

$$\mathrm{dz}_l(y_c) = y_c - \mathrm{sat}_l(y_c) \tag{4.9}$$

Remark 8. *The argument of the saturation and deadzone functions is noted y_c in reference to the fact that the signal entering these nonlinearities is typically the output of the controller.*

The graphs of these functions are given in Figure 4.2. A convenient feature of the deadzone function is that it is nonzero if and only if the saturations are active, and equals zero in the linear domain. Thus the nominal (non-saturated) behaviour of a system is more easily retrieved when deadzone functions, rather than saturations, are used to describe the system.

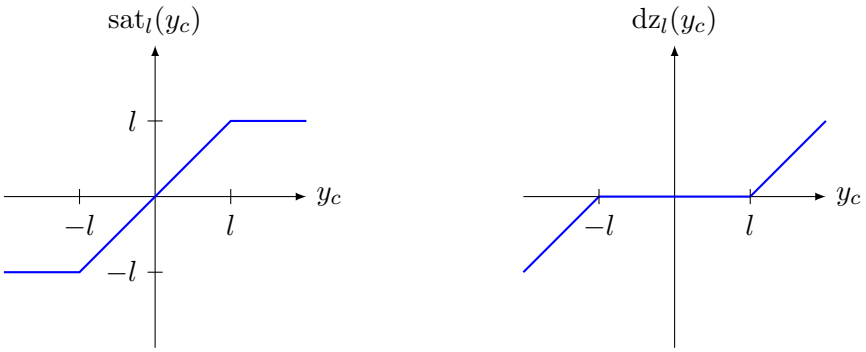

Figure 4.2: Saturation (left) and deadzone (right) nonlinearities

In addition, both functions are easily normalised, i.e. brought down to the case $l = 1$, by weighting their input and output by $1/l$ and l respectively. Normalised saturations and deadzones will be denoted by $\mathrm{sat}(\cdot)$ and $\mathrm{dz}(\cdot)$, dropping the subscript. The notations $\mathrm{Sat}(\cdot)$ and $\mathrm{Dz}(\cdot)$ will be used to denote vector-valued normalised saturation and deadzone nonlinearities in the case

[1] Some authors define the deadzone function as $\mathrm{dz}_l(y_c) = \mathrm{sat}_l(y_c) - y_c$ instead.

of multidimensional signals. Figure 4.3 describes how a saturation can be rewritten using a normalised deadzone.

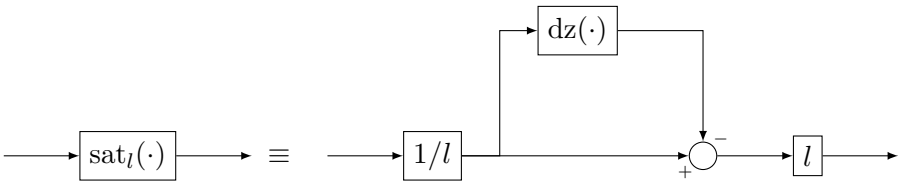

Figure 4.3: Conversion of a saturation into a normalised deadzone

Finally, the deadzone nonlinearity satisfies a number of sector conditions which are useful in the context of system analysis, and which are recalled next. The so-called classical sector condition describes nonlinearities that are inscribed in a conic region [Khalil, 2002]. Indeed, it can be observed that the scalar deadzone function satisfies:

$$\forall y_c \in \mathbb{R},\ \mathrm{dz}(y_c)(\mathrm{dz}(y_c) - y_c) \leq 0 \tag{4.10}$$

which is illustrated by Figure 4.4a. Equivalently, we say that dz$(\cdot)$ belongs to the sector sec$[0, 1]$ globally, denoted dz $\in$ sec$[0, 1]$. However, it is clear from the graph that the class of nonlinearities belonging to sec$[0, 1]$ encompasses more than just the deadzone nonlinearity, resulting in penalising surfaces in terms of conservatism of the description. In fact, this description does not even allow to distinguish between the deadzone and saturation functions, since we also have sat $\in$ sec$[0, 1]$. Thus this approach to stability analysis of saturated systems suffers from some conservatism. The use of a sector sec$[0, \beta]$, with $0 < \beta < 1$ allows to decrease the size of the penalising surfaces, as seen in Figure 4.4b, but the sector condition is then only valid locally, for $|y_c| \leq \frac{1}{1-\beta}$.

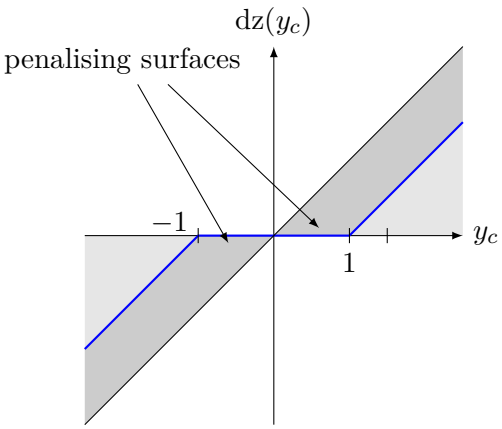

(a) Deadzone nonlinearity in the global sector sec$[0, 1]$

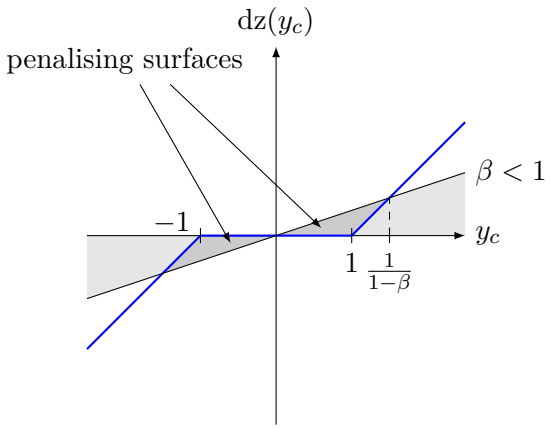

(b) Deadzone nonlinearity in the local sector sec$[0, \beta]$, $0 < \beta < 1$

Figure 4.4: Classical sector conditions applied to the deadzone nonlinearity

The modified sector condition of [Gomes da Silva and Tarbouriech, 2005] directly addresses the aforementioned drawbacks of the classical sector condition. It relies on the following inequalities

which are easily checked from the graph of $\mathrm{dz}(\cdot)$:

$$\forall y_c \in \mathbb{R},\ \forall y_s \in [-y_c - 1, -y_c + 1], \begin{cases} y_c \geq 1 \implies \mathrm{dz}(y_c) + y_s \leq 0 \\ y_c \leq -1 \implies \mathrm{dz}(y_c) + y_s \geq 0 \\ y_c \in [-1, 1] \implies \mathrm{dz}(y_c) = 0 \end{cases} \tag{4.11}$$

Multiplying the left-hand sides of the first two inequalities by $\mathrm{dz}(y_c)$ (which has same sign as y_c), and the left-hand side of the third inequality by $(\mathrm{dz}(y_c) + y_s)$, leads to the following global inequality:

$$\forall y_c \in \mathbb{R},\ \forall y_s \in \mathbb{R},\ |y_c + y_s| \leq 1 \implies \mathrm{dz}(y_c)(\mathrm{dz}(y_c) + y_s) \leq 0 \tag{4.12}$$

Figure 4.5 provides a geometric interpretation of the modified sector condition in the scalar case, illustrating the complete removal of penalising surfaces. In the multidimensional case, the modified sector condition generalises to:

$$\forall y_c \in \mathbb{R}^m,\ \forall y_s \in \mathbb{R}^m,\ (\forall i \in \{1, \ldots, m\}, |y_{c,i} + y_{s,i}| \leq 1) \implies \mathrm{Dz}(y_c)^T \Lambda (\mathrm{Dz}(y_c) + y_s) \leq 0 \tag{4.13}$$

for any diagonal positive definite matrix $\Lambda \in \mathbb{R}^{m \times m}$.

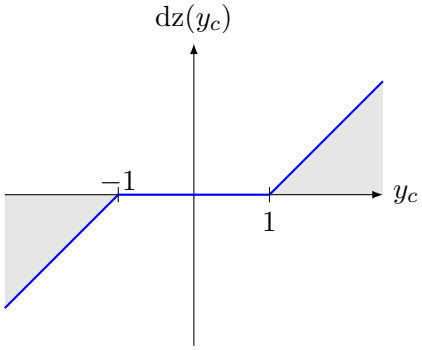

Figure 4.5: Deadzone nonlinearity in the modified sector condition

Analysis of saturated systems using the modified sector condition

Let us now consider the interconnection of a stable LTI system $M(s)$ with a normalised deadzone nonlinearity as depicted in Figure 4.6. This interconnection is described by the set of equations:

$$\begin{cases} \dot{x} = Ax + B_u \tilde{u} + B_w w \\ y_c = C_y x + D_{yu} \tilde{u} + D_{yw} w \\ z = C_z x + D_{zu} \tilde{u} + D_{zw} w \\ \tilde{u} = \mathrm{Dz}(y_c) \end{cases} \tag{4.14}$$

with $x \in \mathbb{R}^{n_x}$, $\tilde{u}, y_c \in \mathbb{R}^{n_u}$, $z \in \mathbb{R}^{n_z}$, and $w \in \mathbb{R}^{n_w}$.

Remark 9. *In the context of a closed-loop system, the control signal is typically $u = \mathrm{Sat}(y_c)$ with y_c the output of the controller. This motivates choosing another notation, here $\tilde{u}$, for the*

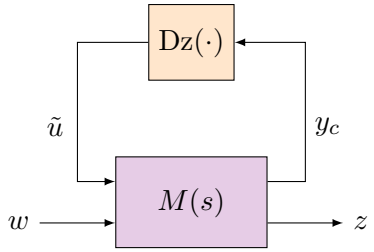

Figure 4.6: Standard interconnection for the analysis of a saturated system

output of the deadzone function.

Let us consider a quadratic candidate Lyapunov function $V(x) = x^T P x$. The condition $\dot{V}(x) < 0$ is given by:

$$\dot{V}(x) = x^T P \dot{x} + \dot{x}^T P x = x^T (A^T P + PA)x + 2x^T P B_u \tilde{u} < 0 \tag{4.15}$$

or, in matrix form:

$$\begin{bmatrix} x \\ \tilde{u} \end{bmatrix}^T \begin{bmatrix} A^T P + PA & PB_u \\ \star & 0 \end{bmatrix} \begin{bmatrix} x \\ \tilde{u} \end{bmatrix} < 0 \tag{4.16}$$

where we use the symbol $\star$ to denote matrix blocks that can be inferred by symmetry. This inequality is not easily exploitable to derive a stability domain due to the nonlinear relation between $\tilde{u}$ and x. This difficulty can be overcome by using the modified sector condition. A key idea is to link the free vector y_s to the state vector x. A relevant choice is to write $y_s = Hx - y_c$, where $H \in \mathbb{R}^{n_u \times n_x}$ is an arbitrary matrix[2], so that $y_c + y_s = Hx$. We then introduce the polyhedral set:

$$\mathcal{S} = \{x \in \mathbb{R}^{n_x} : \forall i = 1, \ldots, n_x,\ |H_i x| \leq 1\} \tag{4.17}$$

where H_i denotes the ith row of H respectively. We then have:

$$\forall x \in \mathcal{S},\ \tilde{u}^T \Lambda (\tilde{u} + Hx - y_c) \leq 0 \tag{4.18}$$

Application of the S-procedure and Schur complements (see e.g. [Boyd et al., 1994; Scherer and Weiland, 2000]) along with other elementary matrix manipulations then allow to derive LMI constraints so that $\mathcal{E}(P,1) \subset \mathcal{S}$ on one hand, and $\dot{V}(x) < 0$ for $x \in \mathcal{E}(P,1)$ on the other hand. This reasoning can be extended to obtain an upper bound on the $\mathcal{L}_2$-gain of the transfer from w to z, by considering the inequality $\dot{V}(x) + \frac{1}{\gamma^2} z^T z - w^T w < 0$. This leads to the following proposition from [Gomes da Silva and Tarbouriech, 2005; Galeani et al., 2009] For a detailed proof, the interested reader can refer to [Tarbouriech et al., 2011].

Proposition 4.4 (Stability and $\mathcal{L}_2$-gain analysis)**.** *Suppose that there exist matrices* $Q = Q^T > 0 \in \mathbb{R}^{n_x \times n_x}$, $S > 0 \in \mathbb{R}^{n_u \times n_u}$ *a diagonal matrix,* $Z \in \mathbb{R}^{n_u \times n_x}$, *and* $\gamma > 0$

[2] An alternative is to select $y_s = Hx - D_{yu}\tilde{u}$, which leads to $y_c + y_s = (H + C_y)x$.

satisfying the following LMI constraints:

$$\begin{bmatrix} AQ + QA^T & B_uS + QC_y^T - Z^T & B_w & QC_z^T \\ \star & -2S + D_{yu}S + SD_{yu}^T & D_{yw} & SD_{zu}^T \\ \star & \star & -I & D_{zw} \\ \star & \star & \star & -\gamma^2 I \end{bmatrix} < 0 \tag{4.19}$$

$$\begin{bmatrix} Q & Z_i^T \\ \star & \delta \end{bmatrix} \geq 0, \quad i = 1, \ldots, n_u \tag{4.20}$$

then:

1. *if $w = 0$, the nonlinear closed-loop system (4.14) remains stable for all initial conditions $x(0) \in \mathcal{E}_P$, with $P = Q^{-1}$.*
2. *if $w \neq 0$, $\|w\|_2^2 \leq \delta^{-1}$ and $x(0) = 0$, then:*
   - *the closed-loop trajectories remain bounded in the set $\mathcal{E}(P, \delta)$;*
   - *the transfer from w to z is finite $\mathcal{L}_2$-gain stable, with:*

$$\forall T \geq 0, \ \int_0^T z^T z dt \leq \gamma^2 \int_0^T w^T w dt \tag{4.21}$$

Remark 10. *Conditions for global stability are obtained by selecting $y_s = -y_c$ in the modified sector condition. This is equivalent to conducting the analysis with the classical global sector condition and leads to a state-space formulation of the MIMO circle criterion.*

Proposition 4.4 is formulated as a feasibility problem, but it can be cast into an optimisation problem. For stability analysis, we then seek to maximise a certain geometric characteristic of the ellipsoid, such as its volume $J = -\ln(\det(\delta^{-1}Q))$, the length of the minor axis $J = -\lambda$ with $Q \geq \lambda I_{n_x}$, or its length along certain directions [Hu and Lin, 2001]. Performance analysis consists in minimising the upper bound γ on the $\mathcal{L}_2$-gain for a given bound δ^{-1} on the exogenous input energy.

A drawback of this approach regarding performance analysis is that the class of $\mathcal{L}_2$-bounded signals is very large and may not be fully relevant in practice. From this observation, [Biannic et al., 2006] suggests to consider a specific subset $\mathcal{W}(\lambda, \rho)$ of step-like exogenous inputs, as shown on Figure 4.7, given by:

$$\mathcal{W}(\lambda, \rho) = \left\{ w \colon \mathbb{R}^{n_w} \to \mathbb{R}^{n_w} : \forall t \geq 0, \ w(t) = w_0 e^{-\lambda t} \text{ and } \|w_0\| \leq \rho \right\} \tag{4.22}$$

Any signal $w \in \mathcal{W}(\lambda, \rho)$ is $\mathcal{L}_2$-bounded, with $\|w\|_2 = \frac{\|w_0\|_2}{2\lambda}$, and can conveniently be generated by an autonomous linear system $W(s)$ with nonzero initial state w_0:

$$\dot{w} = -\lambda w \qquad w(0) = w_0 \tag{4.23}$$

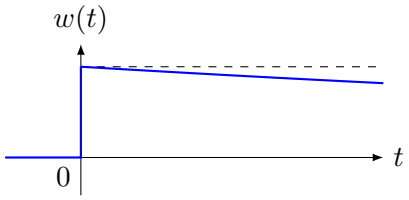

Figure 4.7: Approximation of a step input by a slowly decreasing exponential function

The exogenous signal w in the interconnection of Figure 4.6 can then be replaced by the system $W(s)$, leading to the augmented system $\tilde{M}(s)$ depicted in Figure 4.8 and given by:

$$\tilde{M}(s):\begin{cases}\dot{\zeta} = \tilde{A}\zeta + \tilde{B}\tilde{u}\\ y_c = \tilde{C}_y\zeta + \tilde{D}_{yu}\tilde{u}\\ z = \tilde{C}_z\zeta + \tilde{D}_{zu}\tilde{u}\end{cases} \tag{4.24}$$

with state $\zeta = [w \quad x]^T \in \mathbb{R}^{n_x+n_w}$ and state-space matrices:

$$\begin{aligned}\tilde{A} &= \begin{bmatrix}-\lambda I & 0\\ B_w & A\end{bmatrix} \quad \tilde{B} = \begin{bmatrix}0\\ B_u\end{bmatrix}\\ \tilde{C}_y &= \begin{bmatrix}D_{yw} & C_y\end{bmatrix} \quad \tilde{D}_{yu} = D_{yu}\\ \tilde{C}_z &= \begin{bmatrix}D_{zw} & C_z\end{bmatrix} \quad \tilde{D}_{zu} = D_{zu}\end{aligned} \tag{4.25}$$

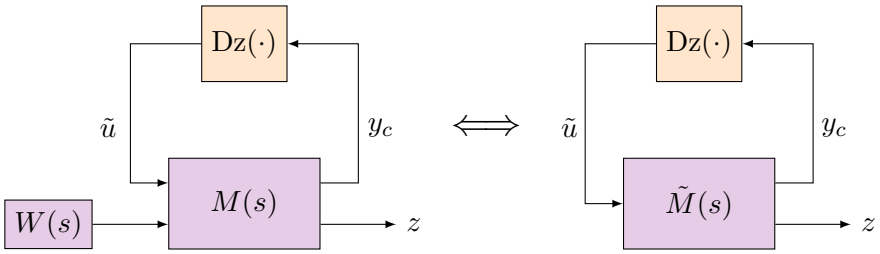

Figure 4.8: Interconnection for analysis against step-like inputs

This leads to the following proposition [Biannic et al., 2006].

Proposition 4.5 (Analysis against step-like inputs)**.** *If there exist matrices $Q = Q^T > 0 \in \mathbb{R}^{(n_x+n_w)\times(n_x+n_w)}$, $S > 0 \in \mathbb{R}^{n_u\times n_u}$ diagonal, $Z \in \mathbb{R}^{n_u\times(n_x+n_w)}$, and positive real numbers γ and $\overline{\rho}$ satisfying the following LMI constraints:*

$$\begin{bmatrix}Q & \begin{bmatrix}\overline{\rho}I\\ 0\end{bmatrix}\\ \star & I\end{bmatrix} > 0 \tag{4.26}$$

$$\begin{bmatrix}\tilde{A}Q + Q\tilde{A}^T & \tilde{B}S + Q\tilde{C}_y^T - Z^T & Q\tilde{C}_z^T\\ \star & -2S + D_{yu}S + SD_{yu}^T & SD_{zu}^T\\ \star & \star & -\gamma^2 I\end{bmatrix} < 0 \tag{4.27}$$

$$\begin{bmatrix} Q & Z_i^T \\ \star & 1 \end{bmatrix} > 0, \quad i = 1, \dots, m \tag{4.28}$$

where Z_i denotes the ith row of Z, then for every $\rho \leq \overline{\rho}$ and for every $w \in \mathcal{W}(\lambda, \rho)$, the interconnection of Figure 4.6 is asymptotically stable for any initial condition ζ_0 in the ellipsoid:

$$\mathcal{E}_P = \left\{ x \in \mathbb{R}^{n_x} : \begin{bmatrix} \rho \\ x \end{bmatrix}^T P \begin{bmatrix} \rho \\ x \end{bmatrix} \leq 1 \right\} \tag{4.29}$$

with $P = Q^{-1}$. Moreover, the energy of the performance output satisfies:

$$\int_0^\infty z^T z dt \leq \gamma^2 \tag{4.30}$$

Compared to Proposition 4.4, the additional constraint (4.26) guarantees that the initial condition $\zeta_0 = [w_0 \quad 0]^T$ belongs to the ellipsoid of guaranteed stability. As before, the feasibility problem can be turned into an optimisation problem. Standard objectives are to minimise the performance index γ for a fixed $\overline{\rho}$, or to maximise $\overline{\rho}$.

4.2.3 Anti-windup design in the DLAW framework

In its modern formulation, DLAW exploits Propositions 4.4 and 4.5 to derive anti-windup synthesis algorithms. Consider the interconnection of Figure 4.9 corresponding to the standard anti-windup architecture where the plant, controller, and anti-windup compensator are assumed to be linear. The interconnection is described by the set of equations:

$$\begin{aligned}
P(s): &\begin{cases} \dot{x}_p = A_p x_p + B_{pu} u + B_{pw} w \\ z = C_z x_p + D_{zu} u + D_{zw} w \\ y = C_y x_p \qquad\quad + D_{yw} w \end{cases} \\
K(s): &\begin{cases} \dot{x}_c = A_c x_c + B_{cy} y + B_{cw} w + v_1 \\ y_c = C_c x_c + D_{cy} y + D_{cw} w + v_2 \end{cases} \\
AW(s): &\begin{cases} \dot{x}_{aw} = A_{aw} x_{aw} + B_{aw} \,\mathrm{Dz}(y_c) \\ v_1 = C_{aw,1} x_{aw} + D_{aw,1} \,\mathrm{Dz}(y_c) \\ v_2 = C_{aw,2} x_{aw} + D_{aw,2} \,\mathrm{Dz}(y_c) \end{cases} \\
&\quad u = \mathrm{Sat}(y_c)
\end{aligned} \tag{4.31}$$

Remark 11. *The feedthrough term D_{yu} of the plant is assumed to be zero. This is often verified in practice, and simplifies some of the mathematical developments. Notably, it guarantees well-posedness of the system and avoids a potential algebraic loop which can lead to nested saturations.*

Remark 12. *The signal v_2 can potentially introduce an algebraic loop in the closed-loop system. In anti-windup synthesis algorithms, the well-posedness of the algebraic loop can be enforced with additional LMI constraints [Zaccarian and Teel, 2011]. However, this gives no indication on*

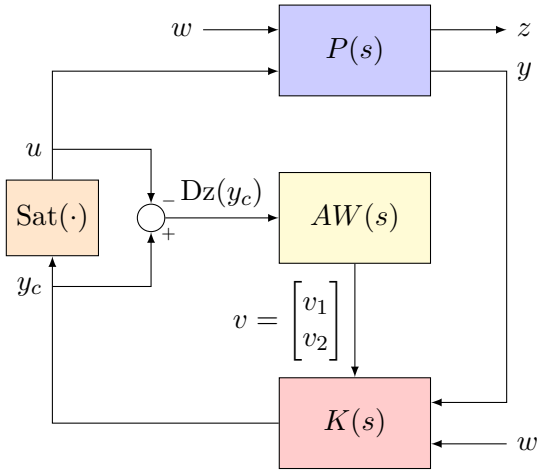

Figure 4.9: Closed-loop system with anti-windup compensation

how to solve the algebraic loop, which can be an issue during simulations. The problem can be avoided altogether by considering a simplified anti-windup architecture where $v_2 = 0$*. Another way consists in filtering the signal* v_2 *with a low-pass filter [Biannic and Tarbouriech, 2009].*

This system can then be put in the standard form of Figure 4.6 with some basic manipulations, resulting in the system [Galeani et al., 2009]:

$$\begin{aligned} \dot{x} &= \mathcal{A}x + \mathcal{B}_u \,\mathrm{Dz}(y_c) + \mathcal{B}_w w \\ y_c &= \mathcal{C}_y x + \mathcal{D}_{yu} \,\mathrm{Dz}(y_c) + \mathcal{D}_{yw} w \\ z &= \mathcal{C}_z x + \mathcal{D}_{zu} \,\mathrm{Dz}(y_c) + \mathcal{D}_{zw} w \end{aligned} \tag{4.32}$$

with state $x = [x_p \quad x_c \quad x_{aw}]^T$, and:

$$\begin{aligned} \mathcal{A} &= \begin{bmatrix} A_p + B_{pu} D_{cy} C_y & B_{pu} C_c & B_{pu} C_{aw,2} \\ B_{cy} C_y & A_c & C_{aw,1} \\ 0 & 0 & A_{aw} \end{bmatrix} \\ \mathcal{B}_u &= \begin{bmatrix} B_{pu}(D_{aw,2} - I) \\ D_{aw,1} \\ B_{aw} \end{bmatrix} \qquad \mathcal{B}_w = \begin{bmatrix} B_{pu}(D_{cw} + D_{cy} D_{yw}) + B_{pw} \\ B_{cy} D_{yw} + B_{cw} \\ 0 \end{bmatrix} \\ \mathcal{C}_y &= \begin{bmatrix} D_{cy} C_y & C_c & C_{aw,2} \end{bmatrix} \qquad \mathcal{D}_{yu} = D_{aw,2} \qquad \mathcal{D}_{yw} = D_{cy} D_{yw} + D_{cw} \\ \mathcal{C}_z &= \begin{bmatrix} C_z + D_{zu} D_{cy} C_y & D_{zu} C_c & D_{zu} C_{aw,2} \end{bmatrix} \qquad \mathcal{D}_{zu} = D_{zu}(D_{aw,2} - I) \\ \mathcal{D}_{zw} &= D_{zw} + D_{zu}(D_{cy} D_{yw} + D_{cw}) \end{aligned} \tag{4.33}$$

If the anti-windup state-space matrices A_{aw}, B_{aw}, $C_{aw} = [C_{aw,1} \; C_{aw,2}]^T$, and $D_{aw} = [D_{aw,1} \; D_{aw,2}]^T$ are provided, this puts us in position to exploit the analysis results from Section 4.2.2. However, the goal here is to compute these matrices, which then become free variables in the inequalities of Propositions 4.4 and 4.5. It results that the analysis variables and the matrices $A_{aw}, B_{aw}, C_{aw}, D_{aw}$ have to be computed simultaneously. The resulting problem is in general no longer convex. However, convexity is recovered in the following cases:

- the anti-windup compensator is static, i.e. only D_{aw} is non-empty;

- the anti-windup compensator has order $n_{aw} = n_p + n_c$, where n_p and n_c denote respectively the orders of the plant and of the controller. The proof of this result makes use of the projection (or elimination) lemma [Gahinet and Apkarian, 1994]. This case is referred to as full-order anti-windup. Furthermore, [Roos and Biannic, 2008] shows that an upper bound can be introduced on the real part of the anti-windup poles to avoid slow dynamics.

- the matrices A_{aw} and C_{aw} are fixed, which allows to consider reduced-order anti-windup synthesis. The choice of the matrices A_{aw} and C_{aw} can be carried out based on the poles of the full-order anti-windup compensator, typically by eliminating slow and fast dynamics relative to the system bandwidth [Biannic et al., 2007; Kerr et al., 2008; Biannic and Tarbouriech, 2009].

Note that another common architecture consists in injecting anti-windup signals $\tilde{v}_1$ and $\tilde{v}_2$ in the controller dynamics as follows:

$$\begin{aligned} \dot{x}_c &= A_c x_c + B_{cy}(y + \tilde{v}_1) + B_{cw} w \\ y_c &= C_c x_c + D_{cy}(y + \tilde{v}_1) + D_{cw} w + \tilde{v}_2 \end{aligned} \tag{4.34}$$

[Zaccarian and Teel, 2011] refers to this architecture as external anti-windup, and calls the architecture described by Equation (4.31) full-authority anti-windup. In particular, the MRAW framework presented in Section 4.2.4 is more naturally formulated using the external architecture. Full-authority anti-windup is slightly more general: if $\tilde{v} = [\tilde{v}_1 \quad \tilde{v}_2]^T$ is the output of an external anti-windup compensator $AW_{ext}(s)$, then the output of an equivalent full-authority anti-windup compensator $AW(s)$ is obtained as:

$$v = \begin{bmatrix} v_1 \\ v_2 \end{bmatrix} = \begin{bmatrix} B_{cy}\tilde{v}_1 \\ D_{cy}\tilde{v}_1 + \tilde{v}_2 \end{bmatrix} \tag{4.35}$$

and the inverse conversion can be done provided that B_{cy} has full rank. This conversion is illustrated in Figure 4.10. From an implementation point of view, it is worth noting that full-authority anti-windup requires acting directly on the states of the controller, and results from synthesis algorithms become dependent on the chosen state-space representation of the controller.

4.2.4 Anti-windup design in the MRAW framework

As already mentioned, the MRAW framework seeks to keep track of the distance to the ideal response, defined by the unconstrained system. This is done by embedding a model $\hat{P}(s)$ of the plant in the anti-windup compensator [Galeani et al., 2009; Zaccarian and Teel, 2011], as illustrated by Figure 4.11. Noting $(A_p, B_{pu}, C_y, 0)$ a realisation of the plant (not taking into

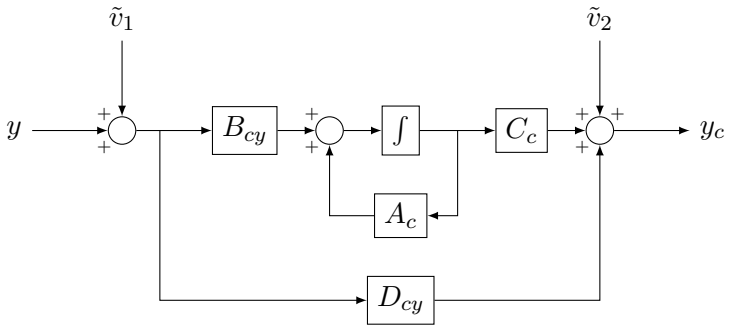

(a) Injection of external anti-windup signals in the controller dynamics

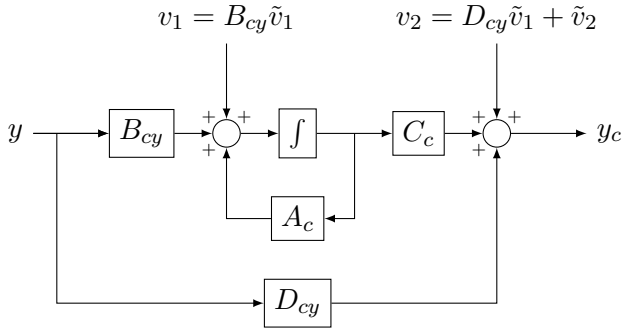

(b) Injection of full-authority anti-windup signals in the controller dynamics

Figure 4.10: External and full-authority anti-windup

account the exogenous input w), we have:

$$\hat{P}(s): \begin{cases} \dot{x}_{aw} = A_p x_{aw} + B_{pu}(\tilde{v}_2 - \mathrm{Dz}(y_c)) \\ z_{aw} = C_z x_{aw} + D_{zu}(\tilde{v}_2 - \mathrm{Dz}(y_c)) \\ y_{aw} = C_y x_{aw} \\ \tilde{v}_2 \text{ to be designed} \end{cases} \tag{4.36}$$

It follows that:

$$\begin{cases} \dot{x}_p - \dot{x}_{aw} = A_p(x_p - x_{aw}) + B_{pu}(u - \tilde{v}_2 + \mathrm{Dz}(y_c)) + B_{pw} w \\ z - z_{aw} = C_z(x_p - x_{aw}) + D_{zu}(u - \tilde{v}_2 + \mathrm{Dz}(y_c)) + D_{zw} w \\ y - y_{aw} = C_y(x_p - x_{aw}) + D_{yw} w \end{cases} \tag{4.37}$$

The above fictitious system with state $x_p - x_{aw}$ shares the plant dynamics. Moreover, note that its input $u - \tilde{v}_2 + \mathrm{Dz}(y_c) = \mathrm{Sat}(y_c) - \tilde{v}_2 + \mathrm{Dz}(y_c) = \tilde{y}_c$ coincides with the output of the controller before injection of the anti-windup signals, and its output coincides with the input of the controller. Thus the response of this fictitious system is that of the plant in the unconstrained closed-loop system. In other words, the system $\hat{P}(s)$ tracks the mismatch between the plant response and the ideal, unconstrained response. A natural objective is then to bring x_{aw} to 0 to recover the behaviour of the unconstrained system. This is achieved by way of the signal $\tilde{v}_2$, which constitutes the degree of freedom of this anti-windup architecture. While it is possible to design $\tilde{v}_2$ as a nonlinear function of the anti-windup state [Galeani et al., 2007b; Galeani et al.,

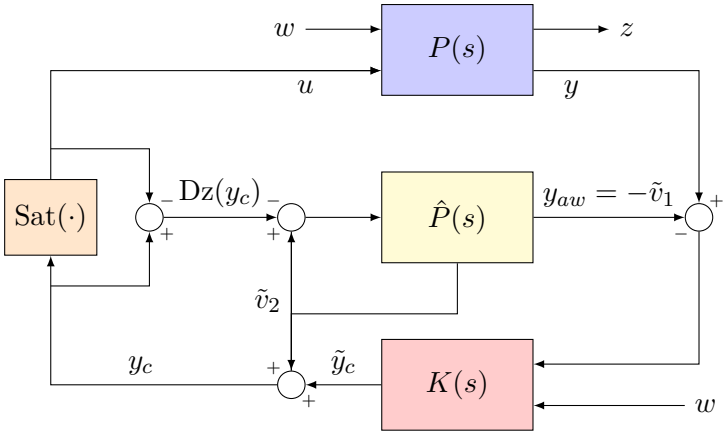

Figure 4.11: MRAW architecture

2007c; Cristofaro et al., 2019], many MRAW designs build this signal linearly as:

$$\tilde{v}_2 = Kx_{aw} + L(\tilde{v}_2 - \mathrm{Dz}(y_c)) \tag{4.38}$$

for some suitable matrices K and L. This relation can be rewritten explicitly as:

$$\tilde{v}_2 = (I - L)^{-1}Kx_{aw} - (I - L)^{-1}L\,\mathrm{Dz}(y_c) \tag{4.39}$$

The corresponding external anti-windup compensator $AW_{ext}(s)$, with input $\mathrm{Dz}(y_c)$, then admits the following state-space representation:

$$AW_{ext}(s):\begin{cases} \dot{x}_{aw} = (A_p + B_{pu}(I - L)^{-1}K)x_{aw} - B_{pu}(I - L)^{-1}\,\mathrm{Dz}(y_c) \\ \tilde{v}_1 = -y_{aw} = -C_y x_{aw} \\ \tilde{v}_2 = (I - L)^{-1}Kx_{aw} - (I - L)^{-1}L\,\mathrm{Dz}(y_c) \end{cases} \tag{4.40}$$

This state-space representation highlights a notable feature of MRAW compensators, namely that they do not depend on the controller dynamics. A drawback of this approach is that MRAW compensators are, by construction, of the order of the plant, which can be high. This can be mitigated by using order-reduction techniques. While the approximation error clearly means that the model recovery feature of the architecture is lost, this is not necessarily an issue: as discussed in [Zaccarian and Teel, 2011], even if the embedded plant model $\hat{P}(s)$ is approximated, stabilisation of the MRAW compensator dynamics remains meaningful to achieve good closed-loop performance properties. For the same reason, the MRAW architecture is intrinsically robust to plant uncertainties, although the exact amount of tolerable uncertainties is problem specific.

Many algorithms are available to compute the matrices K and L characterising the MRAW anti-windup signal $\tilde{v}_2$. A few are mentioned and briefly described next, and we refer to [Galeani et al., 2009; Zaccarian and Teel, 2011] for further details. For exponentially stable plants, global exponential stability can be guaranteed. In this case, some noteworthy MRAW schemes are:

- IMC-based (internal model control) MRAW [Zheng et al., 1994; Teel and Kapoor, 1997a]: this is the simplest MRAW scheme and consists in taking $\tilde{v}_2 = 0$. Consequently, the controller produces the same signal that it would do in the absence of saturations. This

scheme was first described in [Morari and Zafiriou, 1989].

- LQ-based [Zaccarian and Teel, 2002]: the anti-windup gains are computed to guarantee closed-loop global stability (using classical sector conditions) while simultaneously minimising an LQ performance index:

$$J = \int_0^\infty \left(x_{aw}^T Q_p x_{aw} + \tilde{v}_2^T R_p \tilde{v}_2 \right) dt \tag{4.41}$$

  with Q_p and R_p positive definite.

For unstable plants, some available MRAW synthesis methods are:

- LQ-based [Teel and Kapoor, 1997a]: the signal $\tilde{v}_2$ is simply computed as $\tilde{v}_2 = K_{lqr} x_{aw}$ so as to minimise the LQ performance index (4.41). This method effectively ignores the saturations, and as such it does not provide any stability or performance guarantees, and the associated stability regions can be small.

- LMI-based [Galeani et al., 2007a]: this uses the modified sector conditions; as such, it can be seen as a particular fixed-order DLAW synthesis where parts of the anti-windup compensator is determined by the MRAW architecture.

4.2.5 Other strategies to address saturations

While the DLAW and MRAW approaches allow to unify the presentation of a large number of compensation schemes, it should be noted that some anti-windup techniques do not fall in these frameworks.

In [Boada et al., 2010], an architecture combining an MRAW compensator with a static DLAW compensator is proposed (called Extended MRAW, or EMRAW). The synthesis problem involves the resolution of a BMI, which can be solved iteratively using a coordinate-descending algorithm. Alternatively, the MRAW signal $\tilde{v}_2$ and DLAW static gain are computed independently in a first step, and the constraints are checked a posteriori, eventually leading to a tuning phase.

A significant research effort has also been dedicated to deferred or anticipatory anti-windup [Sajjadi-Kia and Jabbari, 2011; Wu and Lin, 2012b; Wu and Lin, 2012a; Turner and Herrmann, 2014; Turner et al., 2016]. It consists in defining different bounds between the deadzone nonlinearity responsible for activating the anti-windup compensator, and the saturation located at the input of the actuators. While these schemes do not consistently lead to better performance than standard immediate anti-windup, improvements have been noted in some cases [Turner et al., 2016].

Another approach is the switching strategy proposed in [Li and Lin, 2015; Li and Lin, 2016], where the input space is partitioned so that different anti-windup gains are used depending on which control signals saturate. Piecewise quadratic Lyapunov functions and extended sector conditions involving the derivative of the deadzone function are then used to formulate the anti-windup synthesis problem as a BMI, for which solutions are sought using LMI-based iterative algorithms. This approach can lead to larger domains of guaranteed stability, but remains computationally intensive.

In [Turner and Kerr, 2018], a nonlinear modification to pre-designed anti-windup compensators is proposed, with the aim to reduce anti-windup action when saturation ceases. This can be seen as an alternative way to address undesirable slow dynamics of anti-windup compensators. However, the proposed method does not scale well with the number of saturation nonlinearities.

Another paradigm worth mentioning to handle saturations is the reference governor approach [Bemporad, 1998; Garone et al., 2017]. Similarly to anti-windup compensation, it consists in adding a component to a pre-designed controller. However, the modification brought by reference governors directly acts on the exogenous reference signal rather than the controller output.

4.2.6 Robustness analysis with integral quadratic constraints

Section 4.2.2 gives results allowing to investigate (either globally or locally) stability and performance of a stable LTI system interconnected with deadzone nonlinearities. Meanwhile, μ-analysis, which is extensively described in Section 3.2.3, provides efficient tools to evaluate the robustness properties of an LTI system subject to real parametric and LTI uncertainties. But these methods become inadequate when both deadzone nonlinearities and uncertainties affect the system simultaneously.

In this context, Integral Quadratic Constraints (IQC) provide a relevant approach to perform robustness analysis. This framework was introduced in [Megretski and Rantzer, 1997], and can be seen as a unification of ideas taken from absolute stability theory, input-output theory (e.g. small gain and passivity theorems), and robust control. It also relies on an interconnection of a stable LTI system $M(s)$ with an operator Δ. The latter is not necessarily linear, and the IQC framework merely requires that Δ be causal and bounded.

To present the IQC approach, we start by recalling some standard notations on function spaces and operators:

- For $n \in \mathbb{N}$, $\mathcal{L}_2^n$ is the space of $\mathbb{R}^n$-valued functions which are square integrable on $[0, \infty)$. It is a subset of the set $\mathcal{L}_{2e}^n$ of locally square integrable functions, i.e. square integrable on any finite interval.
- $\mathcal{RH}_\infty^{n_y \times n_u}$ is the set of $m \times n$ proper transfer matrices without poles in the closed right-half plane, or in other words the set of stable $n_y \times n_u$ LTI systems.
- An operator $\Delta \colon \mathcal{L}_{2e}^{n_y} \to \mathcal{L}_{2e}^{n_u}$ is bounded if the gain defined as:

$$\|\Delta\| = \sup_{f \in \mathcal{L}_2^{n_y}, f \neq 0} \frac{\|\Delta(f)\|_2}{\|f\|_2} \tag{4.42}$$

  is finite. Note that although this definition of boundedness is expressed in terms of $f \in \mathcal{L}_2$, it implies boundedness on $\mathcal{L}_{2e}$. This can be demonstrated using the truncation operator [Jönnson, 2001].

Integral quadratic constraints are defined next.

Definition 4.6 (Signals satisfying an IQC)**.** *Let $p \in \mathcal{L}_2^{n_p}$ and $q \in \mathcal{L}_2^{n_q}$, and $\Pi \colon j\mathbb{R} \to \mathbb{C}^{(n_p+n_q)\times(n_p+n_q)}$ a measurable Hermitian-valued function. We say that p and q satisfy the*

IQC defined by Π *provided that:*

$$\int_{-\infty}^{\infty} \begin{bmatrix} \hat{p}(j\omega) \\ \hat{q}(j\omega) \end{bmatrix}^* \Pi(j\omega) \begin{bmatrix} \hat{p}(j\omega) \\ \hat{q}(j\omega) \end{bmatrix} d\omega \geq 0 \tag{4.43}$$

where $\hat{p}(j\omega)$ *and* $\hat{q}(j\omega)$ *denote respectively the Fourier transforms of* p *and* q*, that is:*

$$\hat{p}(j\omega) = \int_0^{\infty} e^{-j\omega t} p(t) dt \quad \text{and} \quad \hat{q}(j\omega) = \int_0^{\infty} e^{-j\omega t} q(t) dt \tag{4.44}$$

To lighten notation, the inequality (4.43) *is denoted by* $I(\Pi, p, q) \geq 0$*.*

Definition 4.7. *A bounded operator* $\Delta \colon \mathcal{L}_{2e}^{n_p} \to \mathcal{L}_{2e}^{n_q}$ *is said to satisfy the IQC defined by* Π *if:*

$$\forall p \in \mathcal{L}_2^{n_p}, \ I(\Pi, p, \Delta(p)) \geq 0 \tag{4.45}$$

Consider now the interconnection of a stable linear system $M(s) \in \mathcal{RH}_\infty^{n_y \times n_u}$ with a bounded causal operator $\Delta \colon \mathcal{L}_{2e}^{n_y} \to \mathcal{L}_{2e}^{n_u}$. In this context, well-posedness of the interconnection means that the operator $(I - M\Delta)$ has a causal inverse, and stability means furthermore that this inverse is bounded. We can now state the IQC stability theorem from [Megretski and Rantzer, 1997].

Theorem 4.8 (IQC stability theorem)**.** *Let* $M(s) \in \mathcal{RH}_\infty^{n_y \times n_u}$*, and* $\Delta \colon \mathcal{L}_{2e}^{n_y} \to \mathcal{L}_{2e}^{n_u}$ *a bounded causal operator. Let* $\Pi \colon j\mathbb{R} \to \mathbb{C}^{(n_y+n_u)\times(n_y+n_u)}$ *a measurable Hermitian-valued function. Assume that:*

i) for every $\tau \in [0, 1]$*, the interconnection of* M *and* $\tau\Delta$ *is well-posed;*

ii) for every $\tau \in [0, 1]$*, the IQC defined by* Π *is satisfied by* $\tau\Delta$*;*

iii) there exists $\varepsilon > 0$ *such that:*

$$\forall \omega \in \mathbb{R} \quad \begin{bmatrix} M(j\omega) \\ I \end{bmatrix}^* \Pi(j\omega) \begin{bmatrix} M(j\omega) \\ I \end{bmatrix} \leq -\varepsilon I \tag{4.46}$$

Then the feedback interconnection of $M(s)$ *and* Δ *is stable.*

The first assumption holds in most practical cases. The second assumption can be enforced by selecting a multiplier $\Pi = \begin{bmatrix} \Pi_{11} & \Pi_{12} \\ \Pi_{12}^* & \Pi_{22} \end{bmatrix}$ verifying $\Pi_{11} \geq 0$ and $\Pi_{22} \leq 0$. Hence, in practice, IQC stability analysis consists in finding a multiplier Π capturing some properties of the Δ operator through the relation (4.45) and simultaneously satisfying the frequency-dependent inequalities (4.46). The numerous works on IQC theory provide multipliers for a wide variety of uncertainties [Veenman et al., 2016], including but not restricted to:

- uncertain LTI dynamics and time-invariant parametric uncertainties, using multipliers stemming from μ-analysis (D- and DG-scalings) [Packard and Doyle, 1993],

- arbitrarily fast or rate-bounded LTV parametric uncertainties [Köroğlu and Scherer, 2007],
- sector bounded nonlinearities, using the circle and Popov criteria, and their full-block version [Fetzer and Scherer, 2017]
- slope-restricted nonlinearities, using Zames-Falb multipliers [Zames and Falb, 1968; Carrasco et al., 2016; Fetzer and Scherer, 2017; Turner, 2021]
- time-delays [Jun and Safonov, 2001; Polat and Scherer, 2012; Scorletti, 1997].

If Δ satisfies the IQC defined by several multipliers $\Pi_1, \ldots, \Pi_k$, then Δ satisfies the IQC defined by any conic combination $\Pi = \sum_{i=1}^{k} \alpha_i \Pi_i$, with $\alpha_i \geq 0$. Such conic combinations are therefore useful to describe Δ as accurately as possible, leading to a better (less conservative) stability test.

The strength of the IQC framework lies in the possibility to address simultaneously uncertainties of different nature, for instance parametric uncertainties and deadzone nonlinearities. To see this, consider the interconnection of Figure 4.12, which involves an operator $\Delta = \mathrm{diag}(\Delta_1, \ldots, \Delta_N)$. Suppose also that the individual blocks Δ_i satisfy the IQCs defined respectively by some multipliers $\Pi_1, \ldots, \Pi_N$:

$$\forall i \in \{1, \ldots, N\},\ \forall y_i \in \mathcal{L}_2^{n_{y_i}},\ I(\Pi_i, y_i, \Delta_i(y_i)) \geq 0 \tag{4.47}$$

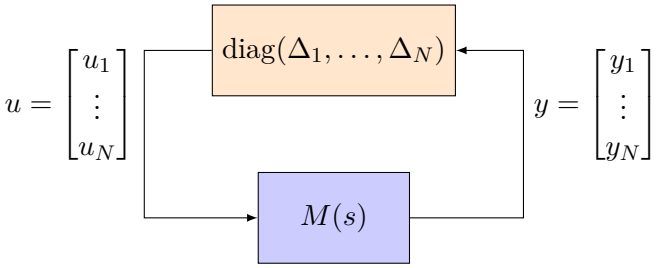

Figure 4.12: LFR with uncertainties and nonlinearities collected in $\Delta = \mathrm{diag}(\Delta_1, \ldots, \Delta_N)$

Then Δ satisfies the IQC defined by the composite multiplier Π given as:

$$\Pi = \begin{bmatrix} \mathrm{diag}(\Pi_{1,11}, \ldots, \Pi_{N,11}) & \mathrm{diag}(\Pi_{1,12}, \ldots, \Pi_{N,12}) \\ \mathrm{diag}(\Pi_{1,12}^*, \ldots, \Pi_{N,12}^*) & \mathrm{diag}(\Pi_{1,22}, \ldots, \Pi_{N,22}) \end{bmatrix} \tag{4.48}$$

As emphasised in [Veenman et al., 2016; Fetzer et al., 2018], it is particularly convenient to work with multipliers parametrised as $\Pi = \Psi^* P \Psi$ with some fixed $\Psi \in \mathcal{RH}_\infty^{n_\Psi \times (n_y + n_u)}$ and $P = P^T \in \boldsymbol{P} \subset \mathbb{R}^{n_\Psi \times n_\Psi}$, where $\boldsymbol{P}$ is described by LMI constraints capturing features of the uncertainty block. Indeed, application of the Kalman-Yakubovich-Popov (KYP) lemma then allows to replace (4.46) by the equivalent condition:

- there exists $X = X^T$ of suitable dimension and $P \in \boldsymbol{P}$ such that:

$$\begin{bmatrix} I & 0 \\ A & B \\ C & D \end{bmatrix}^T \begin{bmatrix} 0 & X & 0 \\ X & 0 & 0 \\ 0 & 0 & P \end{bmatrix} \begin{bmatrix} I & 0 \\ A & B \\ C & D \end{bmatrix} < 0 \tag{4.49}$$

where (A, B, C, D) is a minimal realisation of the system $\Psi(s)\begin{bmatrix} M(s) \\ I \end{bmatrix}$ shown in Figure 4.13a, which can obtained in Matlab by using the function `minreal`.

Thus, verifying stability of the interconnection boils down to solving an LMI problem.

The IQC framework extends seamlessly to performance analysis, by taking into account the performance channel from w to z. In particular, when evaluating performance through the $\mathcal{L}_2$-gain, (4.49) is adapted into:

$$\begin{bmatrix} I & 0 \\ \mathcal{A} & \mathcal{B} \\ \mathcal{C} & \mathcal{D} \end{bmatrix}^T \begin{bmatrix} 0 & X & 0 \\ X & 0 & 0 \\ 0 & 0 & \mathcal{P} \end{bmatrix} \begin{bmatrix} I & 0 \\ \mathcal{A} & \mathcal{B} \\ \mathcal{C} & \mathcal{D} \end{bmatrix} < 0 \tag{4.50}$$

where $\mathcal{P} = \text{diag}(P, I_{n_z}, -\gamma^2 I_{n_w})$, and $(\mathcal{A}, \mathcal{B}, \mathcal{C}, \mathcal{D})$ is a minimal realisation of the system in Figure 4.13b, from input $[u\ w]^T$ to output $[z_\Psi\ z\ w]^T$. We then seek matrices $X = X^T$ and $\mathcal{P}$ that minimise γ under the LMI constraints (4.50) and $P \in \boldsymbol{P}$. This guarantees that the interconnection is robustly stable and provides an upper bound on the worst-case $\mathcal{L}_2$-gain from w to z.

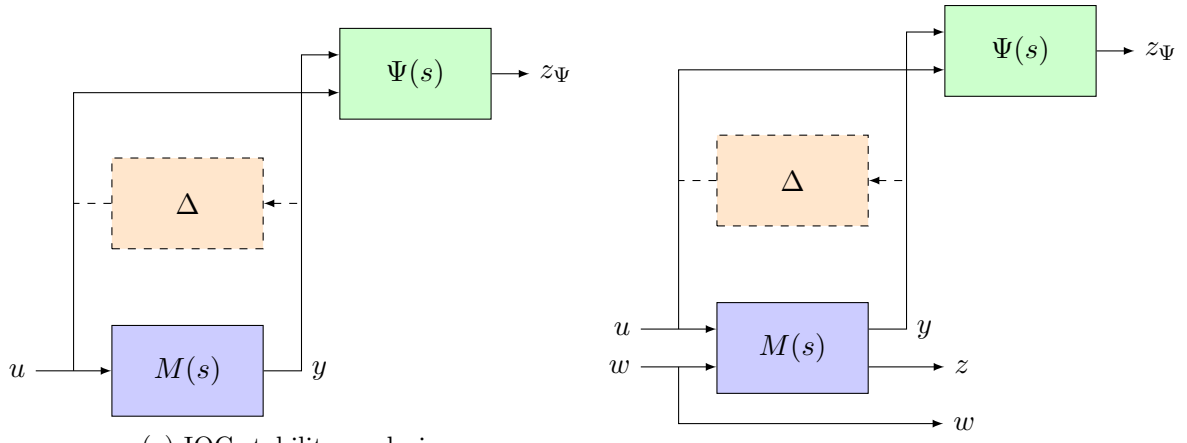

(a) IQC stability analysis

(b) IQC performance analysis

Figure 4.13: Augmented systems for IQC analysis

Finally, from an implementation point of view, the IQC analysis procedure based on the KYP lemma can be summarised as follows:

1. build the interconnection $(M(s), \Delta)$, with $M(s)$ a stable LTI system, and where $\Delta = \text{diag}(\Delta_1, \ldots, \Delta_N)$ may contain different types of uncertainties and nonlinearities,
2. select a valid class of multipliers $\Pi_i = \Psi_i^* P_i \Psi_i$ for each uncertainty Δ_i, where the Ψ_i are fixed (several choices are possible for a same class of multiplier), and each P_i belongs to a set $\boldsymbol{P}_i$ described by LMI constraints,
3. build the composite multiplier $\Psi^* P \Psi$ based on (4.48),
4. compute a minimal realisation of the system of Figure 4.13b,
5. minimise γ under the LMI constraints (4.50) and $P \in \boldsymbol{P}$.

A drawback of the reliance on the KYP lemma is that the matrix X that it introduces in the inequalities (4.49) and (4.50) can be quite large: its size grows quadratically with both the orders of the system and of the multiplier. This can lead to numerical issues for large systems. In spite of this, IQC analysis has attracted a lot of attention for its versatility. It has notably been exploited for the study of several aerospace systems, including re-entry vehicles [Marcos et al., 2010] and space launchers [Chaudenson et al., 2013] in the context of the LPVMAD study, and UAVs [Palframan et al., 2019; Fry and Farhood, 2020] in a discrete-time framework. In [Demourant, 2013], a method of resolution in the frequency domain is proposed for a specific combination of multipliers, addressing the issues raised by the use of the KYP lemma. This method is applied in [Vuillemin et al., 2016] for the study of an aeroelastic aircraft. Other works are dedicated to extending the applicability of IQC analysis in various ways. In [Fetzer et al., 2018], an additional LMI constraint is introduced, which allows to derive regional results, while [Seiler et al., 2019] investigates conditions for the robustness of uncertain LTV systems over a finite-horizon. As further illustrated by the recent release of the IQClab toolbox [Veenman et al., 2021], IQC analysis is a very active area of research.

4.3 Application to the projectile pitch/yaw channels

4.3.1 Anti-windup problem setup and synthesis method selection

We now resume the study of the pitch/yaw channels of the guided projectile, for which a gain scheduled baseline controller has been designed in Section 3.5. As with the controller synthesis, the general anti-windup strategy consists in computing local anti-windup compensators corresponding to fixed values of the scheduling variables (airspeed V, altitute h, and spin rate p_a). The anti-windup compensators are then interpolated to cover the flight envelope.

Recall that the baseline autopilot $K_{PY}(s, \boldsymbol{\lambda}_{PY})$ computed in Chapter 3 outputs signals $\boldsymbol{\delta}_{qr,c} = [\delta_{q,c}\ \delta_{r,c}]^T$ corresponding to virtual deflection angles. These signals are not adapted to design the anti-windup compensator, since the saturation level $l = 10\,\text{deg} = 10 \cdot \frac{\pi}{180}$ rad affects the real deflection angles $\boldsymbol{\delta}_{R,c} = [\delta_{1,c}\ \delta_{2,c}\ \delta_{3,c}\ \delta_{4,c}]^T$ instead. To fit into the anti-windup framework, the allocation is explicitly taken into account, with the assumption that the roll angle ϕ_f of the fuse is fixed at the desired position and that the contribution of the virtual control signal of the roll channel δ_p on the real deflection angles is negligible. The allocation is then given by:

$$\boldsymbol{\delta}_{R,c} = \begin{bmatrix} -\sin\phi_f & \cos\phi_f \\ \cos\phi_f & \sin\phi_f \\ \sin\phi_f & -\cos\phi_f \\ -\cos\phi_f & -\sin\phi_f \end{bmatrix} \boldsymbol{\delta}_{qr,c} \tag{4.51}$$

Equation (4.51) implies $\delta_{1,c} = -\delta_{3,c}$ and $\delta_{2,c} = -\delta_{4,c}$. For the purpose of anti-windup synthesis, this makes the signals $\delta_{1,c}$ and $\delta_{3,c}$ redundant, as well as the signals $\delta_{2,c}$ and $\delta_{4,c}$. Thus, with reference to the standard anti-windup architecture of Figure 4.9, we define the input y_c of the

normalised saturation as:

$$y_c = \frac{1}{l}\begin{bmatrix}\delta_{1,c}\\ \delta_{2,c}\end{bmatrix} = \frac{1}{l}\begin{bmatrix}-\sin\phi_f & \cos\phi_f\\ \cos\phi_f & \sin\phi_f\end{bmatrix}\boldsymbol{\delta}_{qr,c} = \frac{1}{l}M(\phi_f)\boldsymbol{\delta}_{qr,c} \tag{4.52}$$

which is illustrated in Figure 4.14 (note that $M^{-1}(\phi_f) = M(\phi_f)$), where $P_{PY}(s, \boldsymbol{\lambda}_{PY})$ gathers the airframe (4 states), two virtual actuators ($2 \times 2 = 4$ states), and first-order sensors (two accelerometers, two gyroscopes, two servo-sensors: 6 states) for a plant order of 14.

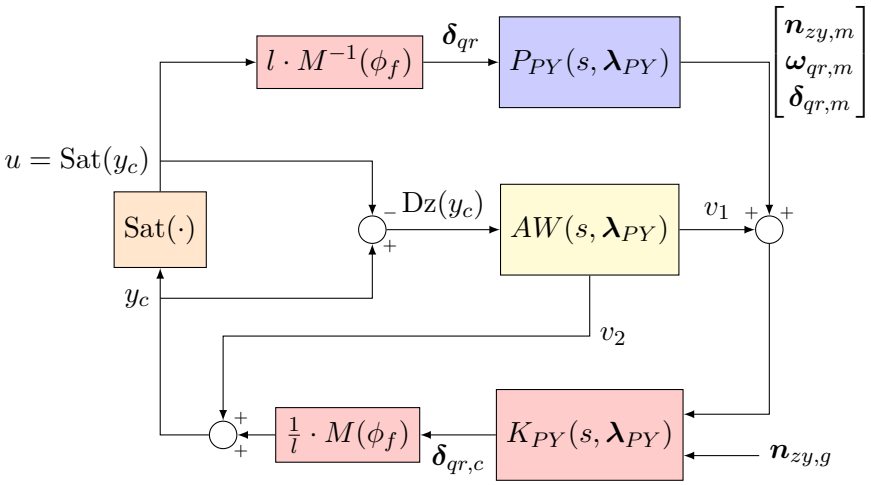

Figure 4.14: Anti-windup structure for the projectile pitch/yaw channels; the fuse roll angle ϕ_f is supposed fixed

Remark 13. *The real actuator and servo-sensor models could be used in $P_{PY}(s, \boldsymbol{\lambda}_{PY})$, increasing the plant order to 20. However, this does not modify the signals seen by the anti-windup compensator and thus has no impact on the synthesis.*

It is clear from Equation (4.52) and the relation $u = \mathrm{Sat}(y_c)$ that the fuse roll angle ϕ_f contributes to determining whether saturations occur or not. In fact, for a fixed value of ϕ_f, the set of virtual signals (δ_q, δ_r) that will not lead to saturations can be represented as a square in the (δ_q, δ_r)-plane, whose orientation depends on ϕ_f. Figure 4.15 shows this set for the two standard fuse orientations, which are the '+' ($\phi_f = 0\,\mathrm{deg}$) and '×' ($\phi_f = 45\,\mathrm{deg}$) configurations. From nonlinear simulations of realistic launch scenarios without saturations (see Chapter 5, and in particular Figures 5.12 and 5.18), the '×' configuration seems preferable to limit the occurrence of saturations. Thus the value $\phi_f = 45\,\mathrm{deg}$ is used to synthesise the pitch/yaw anti-windup compensator.

As reviewed in Sections 4.2.3 and 4.2.4, a large panel of methods are available to compute anti-windup compensators in a time-invariant framework. However, in a gain scheduling context, the theoretical guarantees regarding stability domains and performance levels are not preserved. As such, a driving criterion for selecting anti-windup synthesis methods is their simplicity. In particular, methods requiring little to no tuning are easier to implement over the whole flight envelope. Nevertheless, it still seems desirable to be able to simulate and analyse the closed-loop with anti-windup compensation in a time-invariant context. Since the airframe is known to be

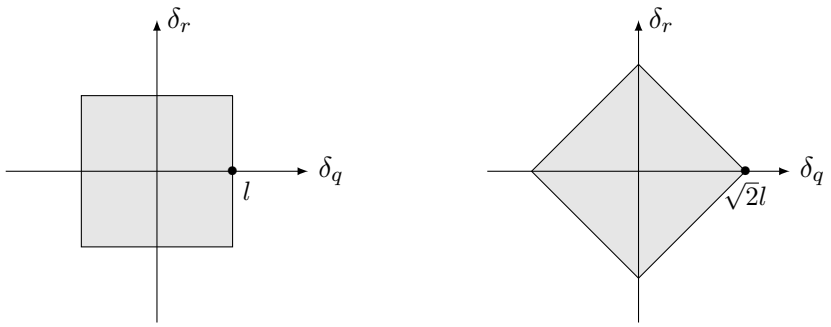

(a) '+' configuration: $\phi_f = 0\,\text{deg}$ (b) '×' configuration: $\phi_f = 45\,\text{deg}$

Figure 4.15: Set of virtual control signals leading to no saturation

unstable at some points of the flight envelope (cf. Chapter 2), this makes the MRAW methods that assume plant exponential stability irrelevant.

Based on the above discussion, three anti-windup methods are considered for local syntheses, which are done over the same $7 \times 6 \times 5$ grid of the reduced flight envelope (210 points) used for pitch/yaw autopilot synthesis in Section 3.5.

- The first method is a static DLAW synthesis method, with furthermore $v_2 = 0$ to avoid algebraic loops. The local syntheses are performed using the SAW library of the SMAC toolbox (`https://w3.onera.fr/smac/saw`) so as to maximise the amplitude of step input reference signals $\boldsymbol{n}_{zy,g}$ for which stability can be guaranteed [Biannic and Tarbouriech, 2009]. The global compensator is then obtained by linearly interpolating the coefficients of the matrix $D_{aw,1} \in \mathbb{R}^{2\times 2}$. This design was first proposed in [Thai et al., 2020].

- The second anti-windup compensator uses the LQ-based MRAW method applicable to unstable plants. The local syntheses are easily performed on Matlab with the `lqr` function [Galeani et al., 2009]. The cost function is kept the same for all the design points, enforcing a stronger penalty on the four states corresponding to the (mismatch on the) actuator states with $Q = \text{diag}(I_{10}, 50 \cdot I_4)$ and $R = I_2$. The relatively high order $n_{aw} = 14$ of the local compensators does not lend itself to the interpolation of state-space coefficients. Instead, the interpolation method chosen to obtain the global compensator is based on output blending (see Section 3.2.2). Since three scheduled variables (V, h, p_a) are considered, the interpolation is made between the outputs of $2^3 = 8$ out of the 210 local anti-windup compensators. This design was first proposed in [Thai et al., 2021].

- The third anti-windup compensator is also an LQ-based MRAW, but uses an approximated plant model where the actuator and sensor dynamics are neglected and only the airframe dynamics remain. Thus the resulting compensator has order $n_{aw} = 4$. The computation is done using $Q = I_4$ and $R = I_2$, and output blending is used as the interpolation method.

It is worth noting that computation of the local LQ-based MRAW compensators is very fast, with the synthesis over all points of the flight envelope grid taking a bit over 6 s, both for the full and reduced cases. By contrast, synthesis of the 210 static DLAW compensators takes about 180 s. The relative length of the latter computation can be attributed to the required LMI resolution, although it should be pointed out that the SAW library uses LMI Lab as an LMI

solver, and that CPU time reduction may be achieved by using faster solvers such as SeDuMi [Sturm, 1999] or MOSEK [MOSEK ApS, 2019].

4.3.2 Time-domain simulations and IQC analysis

Step responses with saturations

The baseline pitch/yaw autopilot (without anti-windup) and the three anti-windup schemes are first evaluated through step responses for fixed values of the scheduling variables. The step amplitude of the reference signal $n_{y,g}$ is chosen as $n_{y,g} = 1.05 \cdot n_{y,sat}$, where $n_{y,sat}$ is the lowest value leading to real deflection angles above 10 deg within 10 seconds. The value of $n_{y,sat}$ can easily be obtained from linear simulations. Figures 4.16 to 4.18 show the closed-loop responses for different compensation schemes at the following three realistic design points:

- Point #1 (near apogee): $(V, h, p_a) = (300 \text{ m/s}, 9000 \text{ m}, 1650 \text{ rad/s})$
- Point #2 (descent): $(V, h, p_a) = (300 \text{ m/s}, 6000 \text{ m}, 1425 \text{ rad/s})$
- Point #3 (close to impact): $(V, h, p_a) = (340 \text{ m/s}, 0 \text{ m}, 1200 \text{ rad/s})$

The load factors shown in the figures are normalised as $\hat{n}_z = n_z/n_{y,sat}$ and $\hat{n}_y = n_y/n_{y,sat}$. Without anti-windup compensation, the deflection angles eventually all reach saturating values, resulting in large errors on the load factors as well as badly damped oscillations, which become faster as we go from Point #1 to Point #3. The anti-windup schemes all greatly improve the response. A notable difference between the DLAW and MRAW responses is that the former leads to a small steady-state error on n_z (decoupling) at Points #1 and #2. The degradation on decoupling seems lessened with the MRAW compensators, but additional slow oscillations appear on both axes. Remarkably, both the MRAW ($n_{aw} = 14$) and reduced MRAW ($n_{aw} = 4$) responses are identical, despite the significant order difference.

Figure 4.19 shows the impact of the aerodynamic uncertainties on the step responses with no anti-windup compensation on Point #3. While none of the 100 samples drawn lead to instability (for better visibility, results are shown for 15 samples), the uncertainties clearly have the potential to further worsen the step response of the system. For the studied point, this degradation takes the form of oscillations of larger amplitude and a greater steady-state error. Figures 4.20 and 4.21 then show the responses with static DLAW and reduced MRAW respectively for the same samples. Responses with full MRAW are not shown since they are virtually identical to those obtained with reduced MRAW. While undesirable oscillations and steady-state errors remain, these are significantly reduced compared to the responses with no anti-windup compensation. Simulation results with static DLAW feature minimal oscillations, but slightly larger steady-state errors compared to the reduced MRAW responses, especially on the normal channel n_z, associated with decoupling for the tested scenario.

IQC analysis

The robustness of the closed-loop for fixed values of the scheduling variables is then investigated more formally using IQC analysis. The LFR model of the closed-loop pitch/yaw channels is first

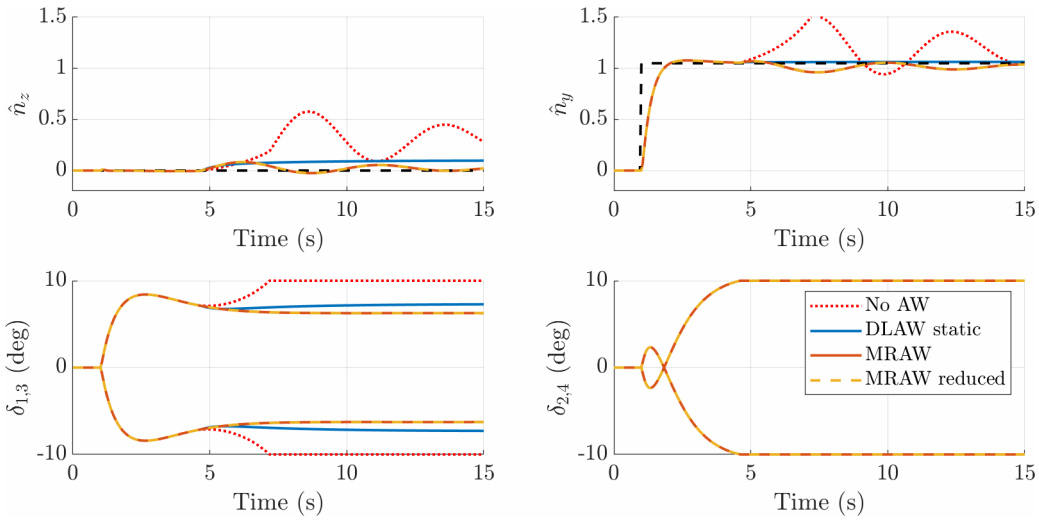

Figure 4.16: Step responses at Point #1 for different anti-windup schemes

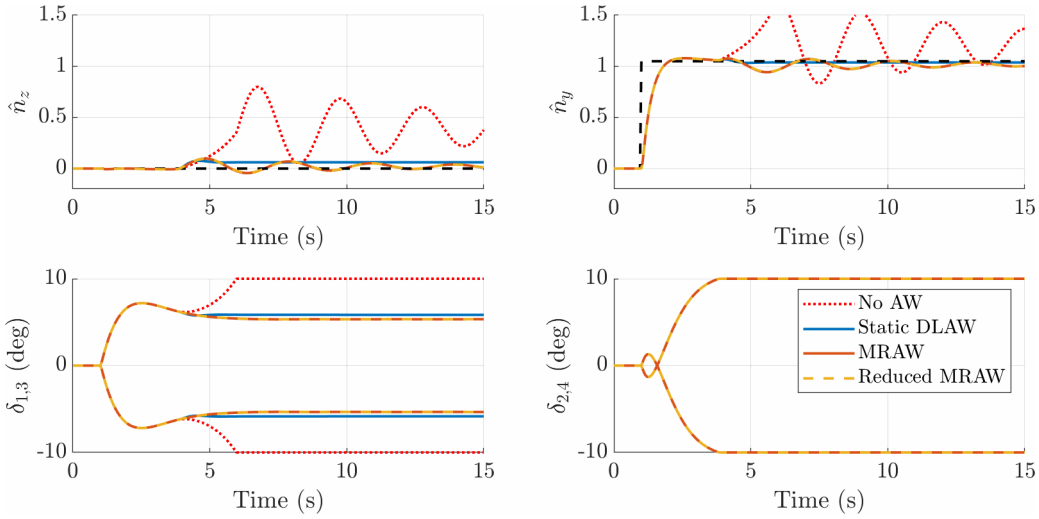

Figure 4.17: Step responses at Point #2 for different anti-windup schemes

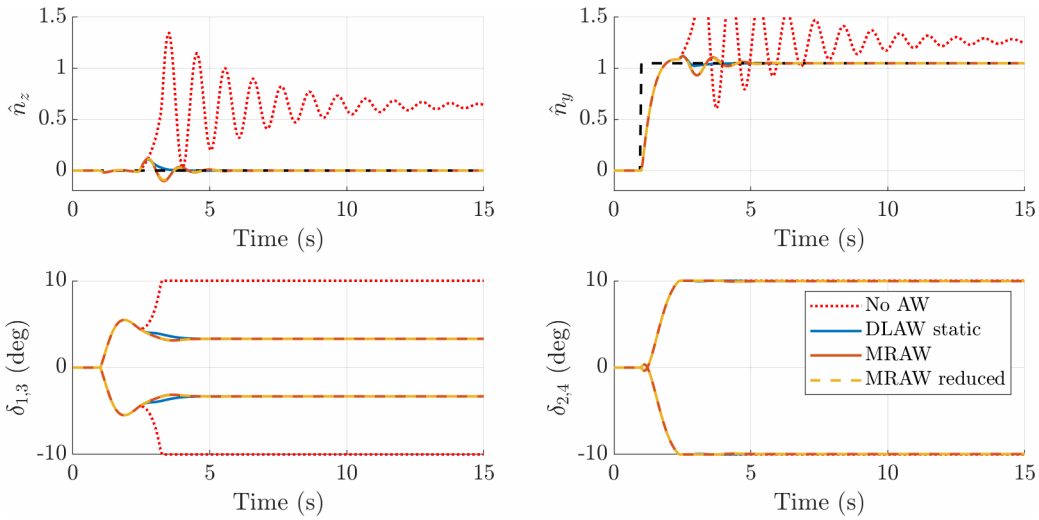

Figure 4.18: Step responses at Point #3 for different anti-windup schemes

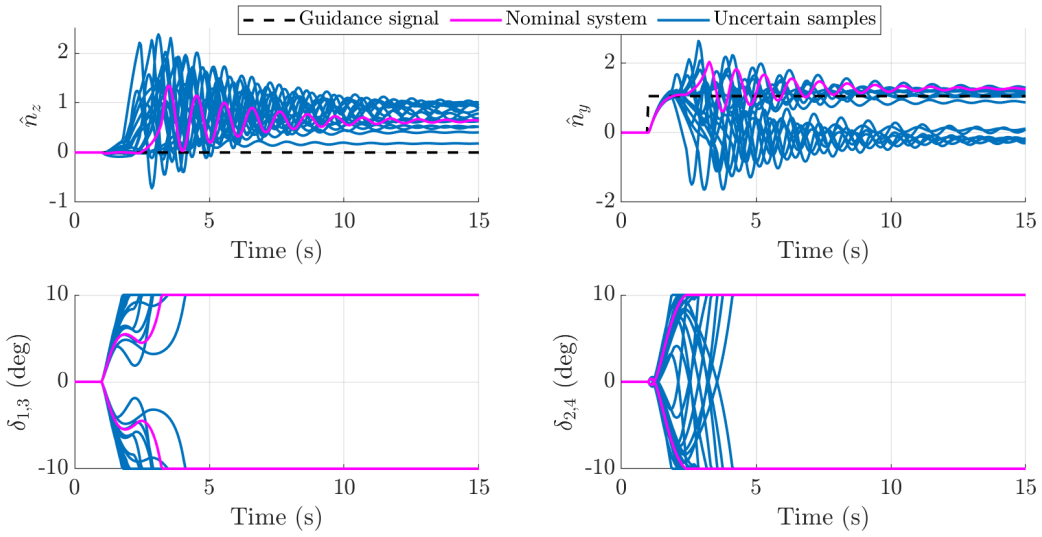

Figure 4.19: Simulation with no anti-windup and model uncertainties at Point #3

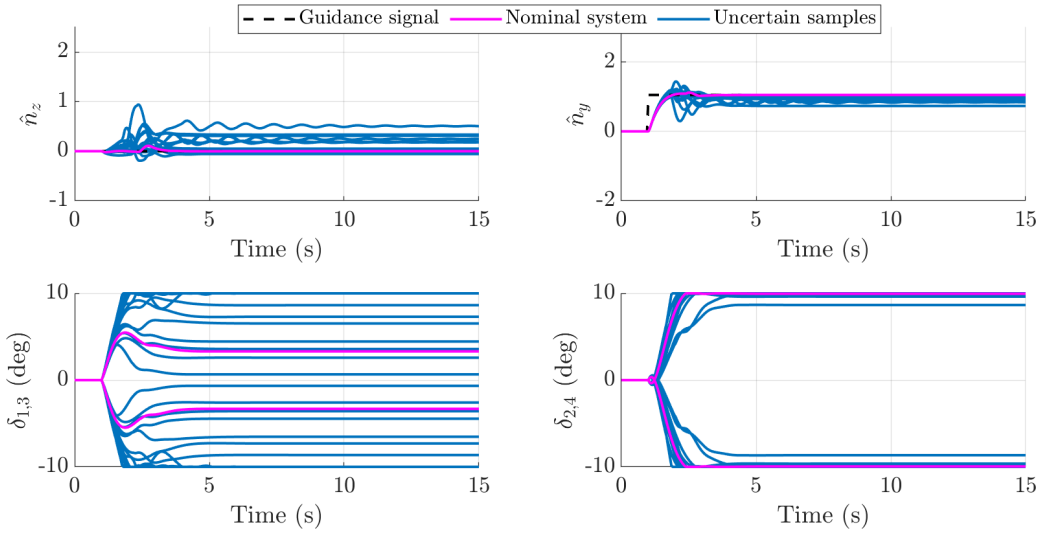

Figure 4.20: Simulation with DLAW and model uncertainties at Point #3

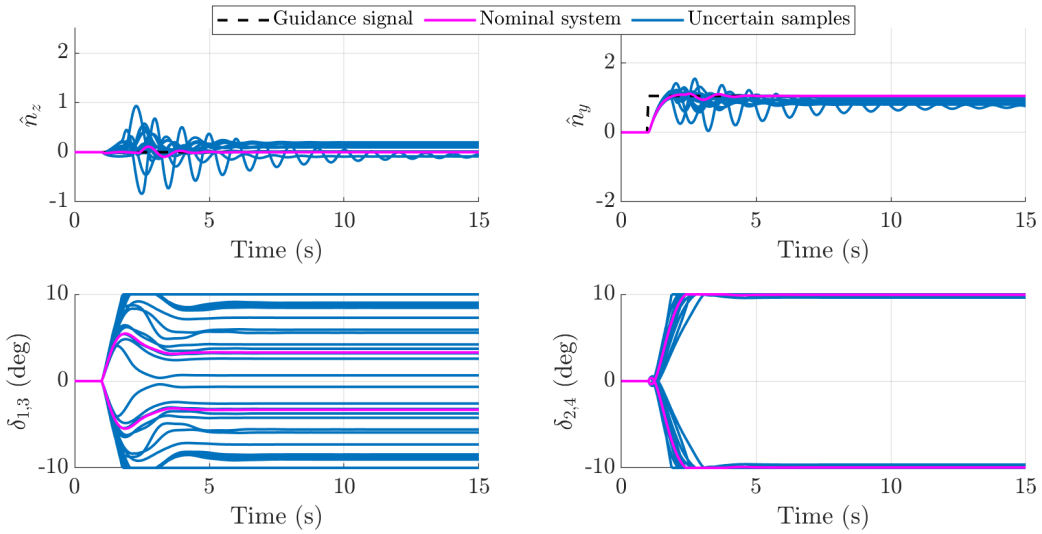

Figure 4.21: Simulation with reduced MRAW and model uncertainties at Point #3

computed for the different anti-windup configurations using the GSS library of the SMAC toolbox [Biannic and Roos, 2012-2021]. The resulting Δ block gathers both the 16×16 aerodynamic uncertainty block $\Delta_{PY} \in \mathcal{B}_{\mathbf{\Delta}PY}$ as defined in Section 2.6, and a two-dimensional deadzone nonlinearity, leading to the augmented structure:

$$\begin{aligned}\hat{\mathcal{B}}_{\mathbf{\Delta}PY} = \Big\{ & \mathrm{diag}(\delta_{C_{N\alpha}} I_2, \delta_{C_{N\delta}} I_2, \delta_{C_A} I_2, \delta_{C_{Yp\alpha}} I_2, \delta_{C_{m\alpha}} I_2, \delta_{C_{mq}} I_2, \\ & \delta_{C_{m\delta}} I_2, \delta_{C_{np\alpha}} I_2, \mathrm{Dz}(\cdot)) \colon \delta_\bullet \in [-1, 1] \Big\}\end{aligned} \tag{4.53}$$

The performance channel considered is taken as the transfer from the guidance signals $\boldsymbol{n}_{zy,g}$ to the error signals $\boldsymbol{e}_{zy,ref}$ with respect to the second-order reference model $T_{ref,PY}(s)$ (cf. Figure 3.24).

A first analysis can be done ignoring the aerodynamic uncertainties. The remaining deadzone nonlinearity can then be locally described as a sector bounded and slope-restricted nonlinearity $\Phi \in \mathrm{sec}[0, \beta]^2 \cap \mathit{slope}[0, \beta]^2$. Accordingly, we use a combination of full-block circle criterion (see e.g. Class 13 in [Veenman et al., 2016]) and full-block Zames-Falb multipliers [Fetzer and Scherer, 2017]. The parametrisation of the Zames-Falb multipliers requires the selection of real poles and their multiplicity to specify basis functions. Based on a few trials, two poles are chosen, -10 and -100, both[3] with multiplicity 1. The LMI problem stemming from the use of the KYP lemma is then solved using YALMIP [Lofberg, 2004] interfaced with the MOSEK solver [MOSEK ApS, 2019]. Table 4.1 displays the corresponding order of the augmented system (see Figure 4.13b), number of decision variables, and average computation time of the LMI resolution for one value of β. Note that the solution computed by MOSEK is checked through a feasibility test if the solver raises potential numerical issues. This additional step is included in the computation time listed.

Figure 4.22 shows bounds $\overline{\gamma}$ on the $\mathcal{L}_2$-gain plotted over the sector slope β for different compensation schemes and at the same three design points used for the time-domain simulations. It can be observed that all the anti-windup compensators are successful in increasing the maximum value of the parameter β for which stability can be guaranteed compared to the baseline. In that respect, the MRAW configuration outperforms the other configurations, as it validates stability at $\beta = 1$ (and thus also for the actual deadzone nonlinearity) for all three points, against two points for the DLAW configuration, and no point for the reduced MRAW. On the other hand, the MRAW configuration features higher gains for small values of β at Points #1 and #2 compared to the static DLAW. This degradation is possibly induced by the additional dynamics, to which the conservatism of the IQC test must be added. Indeed, the IQC test relies on a rather loose description of the deadzone nonlinearities based on the classical sector condition, although the use of Zames-Falb multipliers contributes to improving the description by taking into account the slope-restriction, thus reducing the conservatism of the test.

Next, a robustness analysis including the aerodynamic uncertainties is performed. This is done by adding a dynamic DG-scaling multiplier, with a pole -10 of multiplicity 1 for each uncertainty (cf. Class 5 in [Veenman et al., 2016]). The normalised aerodynamic uncertainties are then allowed to vary between $[-\alpha, \alpha]$, with $\alpha \leq 1$. This allows to compute upper bounds $\overline{\gamma}$ on the $\mathcal{L}_2$-gain of the uncertain system for given values of $\beta \in [0, 1]$ and $\alpha \in [0, 1]$. Taking $\alpha = 0$ corresponds to the IQC test with no aerodynamic uncertainties. Meanwhile, taking $\beta = 0$

[3] In particular, the use of these two poles greatly improves the bounds obtained for the static DLAW configuration.

Table 4.1: Computational burden of the IQC analysis with deadzone nonlinearities

Configuration	**No AW**	**Static DLAW**	**MRAW**	**Reduced MRAW**
Order of the augmented system (minimal realisation)	34	34	48	38
Number of decision variables	625	625	1207	771
Average computation time (s)	3.0	2.4	3.8	2.9

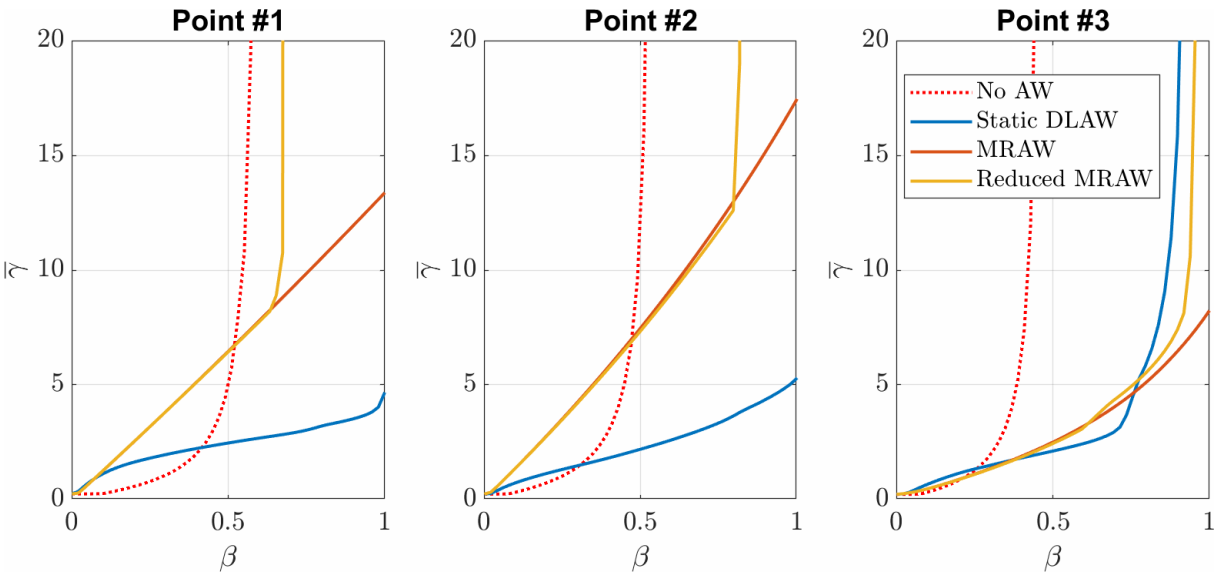

Figure 4.22: Bounds on the $\mathcal{L}_2$-gain in the presence of a sector bounded slope-restricted nonlinearity $\Phi \in sec[0,\beta]^2 \cap slope[0,\beta]^2$ at different analysis points

corresponds to computing upper bounds on the worst-case $\mathcal{H}_\infty$ performance which can also be obtained using skew-μ analysis. Table 4.2 displays the LMI problem data corresponding to the IQC test and the average resolution time for given values of α and β.

Figures 4.23 to 4.26 depict the surfaces obtained at each of the three desgin points for the different anti-windup schemes (no anti-windup, static DLAW, MRAW, and reduced MRAW respectively). For the configurations without anti-windup and with static DLAW, it can be observed that the value of β for which stability is guaranteed reduces significantly as α grows. Both MRAW configurations are comparatively more robust, as for fixed β, an increase in α still leads to finite $\mathcal{L}_2$-gains in most (but not all) cases, although the bounds on the $\mathcal{L}_2$ performance are noticeably degraded, especially for Point #3. It is also worth noting that the surfaces obtained for both the MRAW and reduced MRAW are virtually equal for small to intermediate values of β, indicating that for the corresponding set of sector nonlinearities, the MRAW and reduced MRAW have similar robust performance properties.

LTV simulation

An LTV simulation is performed next to validate the interpolation strategies of the anti-windup schemes, respectively a linear gain interpolation for the static DLAW, and output blending for both the MRAW and reduced MRAW. The evolution of the scheduling variables are given in Figure 3.35 and correspond to a ballistic trajectory. On the other hand, the guidance signals

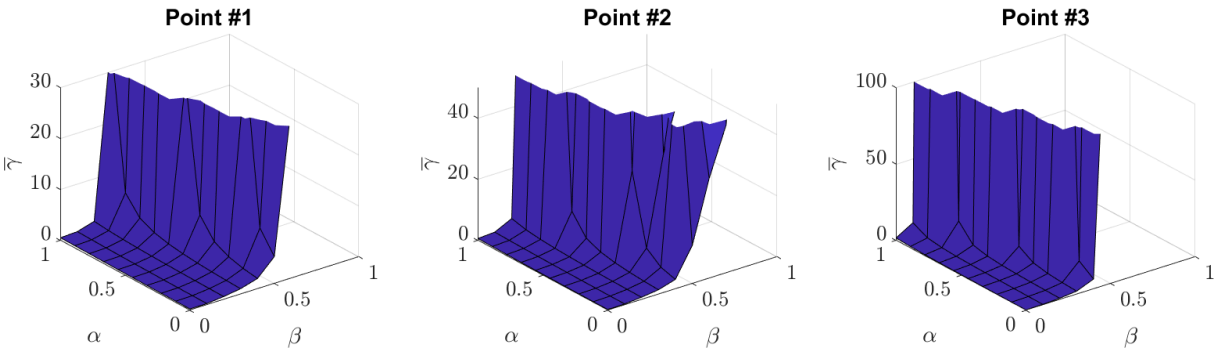

Figure 4.23: Bounds on the $\mathcal{L}_2$-gain with no anti-windup in the presence of aerodynamic uncertainties $|\delta_\bullet| \leq \alpha$ and nonlinearity $\Phi \in \text{sec}[0, \beta]^2 \cap slope[0, \beta]^2$

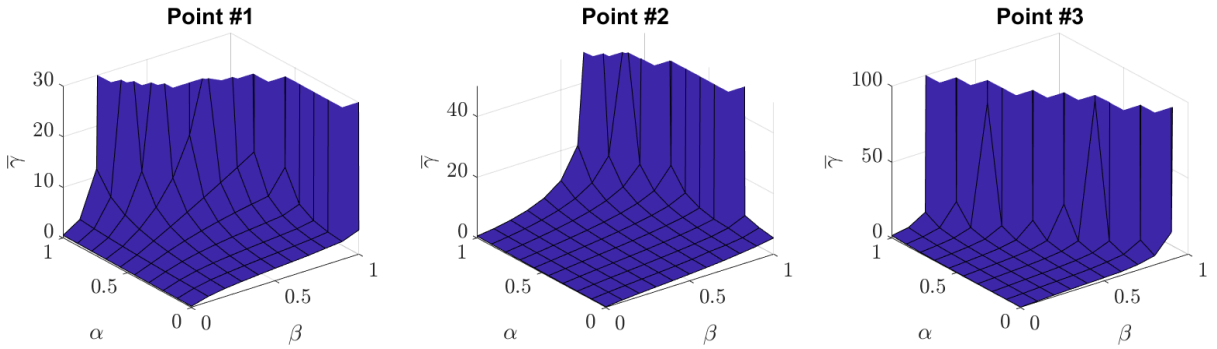

Figure 4.24: Bounds on the $\mathcal{L}_2$-gain with static DLAW in the presence of aerodynamic uncertainties $|\delta_\bullet| \leq \alpha$ and nonlinearity $\Phi \in \text{sec}[0, \beta]^2 \cap slope[0, \beta]^2$

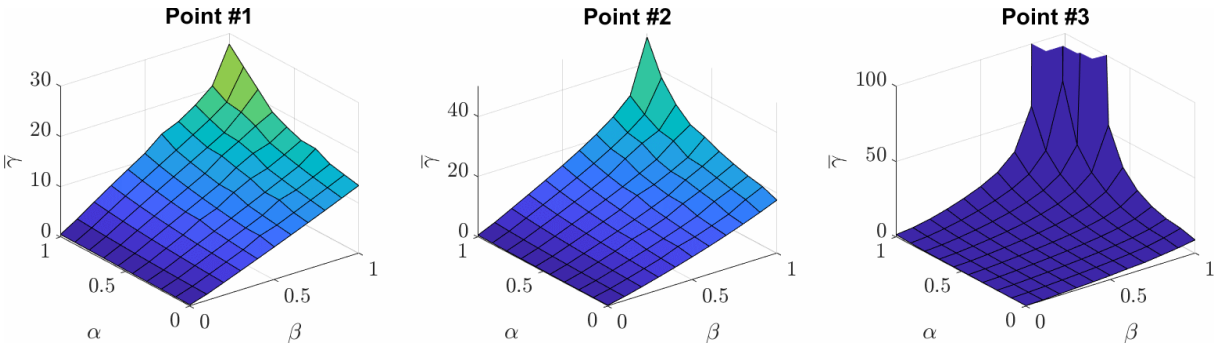

Figure 4.25: Bounds on the $\mathcal{L}_2$-gain with MRAW in the presence of aerodynamic uncertainties $|\delta_\bullet| \leq \alpha$ and nonlinearity $\Phi \in \text{sec}[0, \beta]^2 \cap slope[0, \beta]^2$

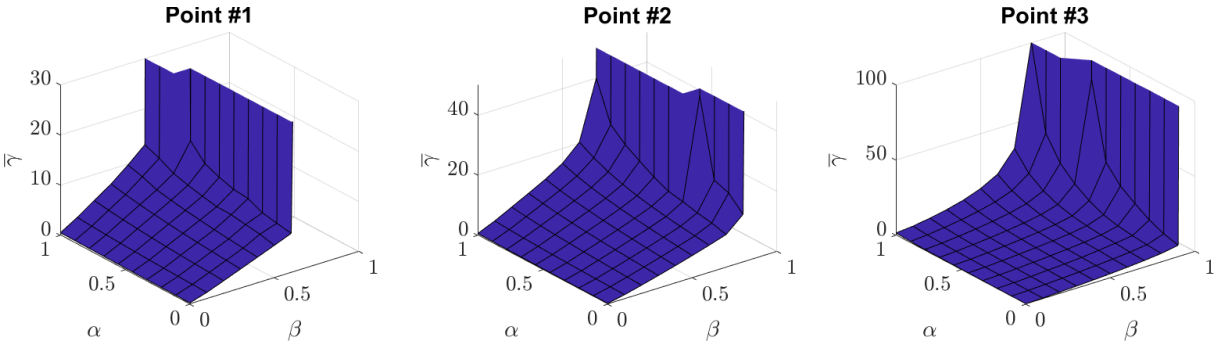

Figure 4.26: Bounds on the $\mathcal{L}_2$-gain with reduced MRAW in the presence of aerodynamic uncertainties $|\delta_\bullet| \leq \alpha$ and nonlinearity $\Phi \in \text{sec}[0, \beta]^2 \cap slope[0, \beta]^2$

Table 4.2: Computational burden of the IQC analysis with deadzone nonlinearities and aerodynamic uncertainties

Configuration	**No AW**	**Static DLAW**	**MRAW**	**Reduced MRAW**
Order of the augmented system (minimal realisation)	60	60	70	69
Number of decision variables	2012	2012	2667	2597
Average computation time (s)	11.7	9.9	17.2	17.1

correspond to the ballistic load factors scaled up by a factor 2.5 in order to provoke saturations. Figure 4.27 shows the resulting load factors and deflection angles in the absence of anti-windup compensation, where it is clear that the baseline autopilot alone is insufficient to ensure good tracking of the guidance signals. Figures 4.28 to 4.30 then show the responses for the three scheduled anti-windup compensators. They are consistent with the responses observed in the time-invariant context. Indeed, while the DLAW configuration displays a very good tracking of the lateral acceleration $n_{y,g}$, there is a noticeable error on n_z, which however reduces near the end of the trajectory. The MRAW responses are overall less smooth, with errors on both axes which however remain small. In addition, the MRAW and reduced MRAW configurations produce nearly identical responses. In the end, with respect to the LTV simulation, all three compensation schemes are clear improvements over the baseline response.

Remark 14. *Another reduced MRAW design based on a balanced truncation of the full-order MRAW was considered. While this design led to similar step responses in the time-invariant context, it produced significant tracking errors on the LTV simulation. This is possibly due to the heterogeneous state-space representations of the local truncated anti-windup compensators, combined with a lack of appropriate initialisation of the states.*

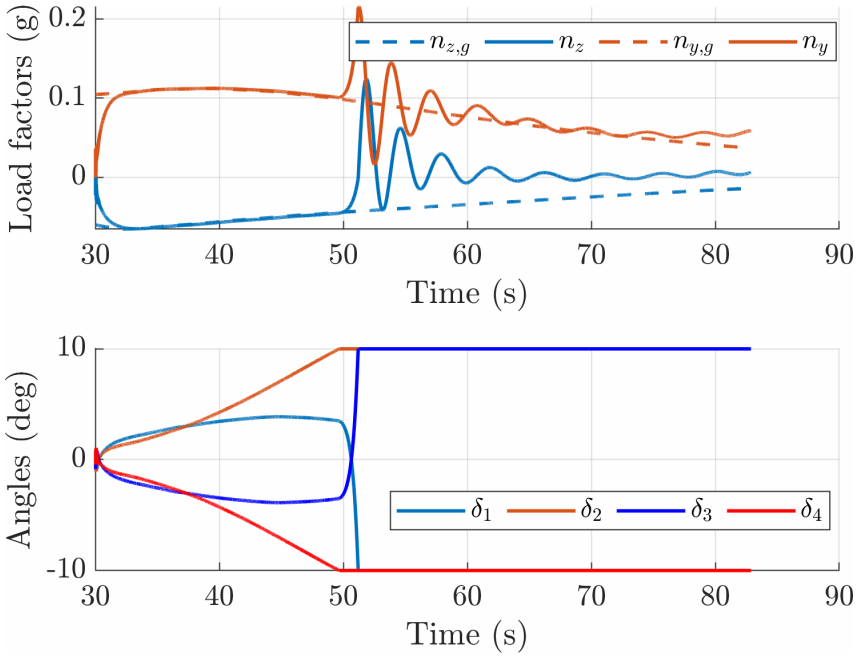

Figure 4.27: LTV simulation without anti-windup

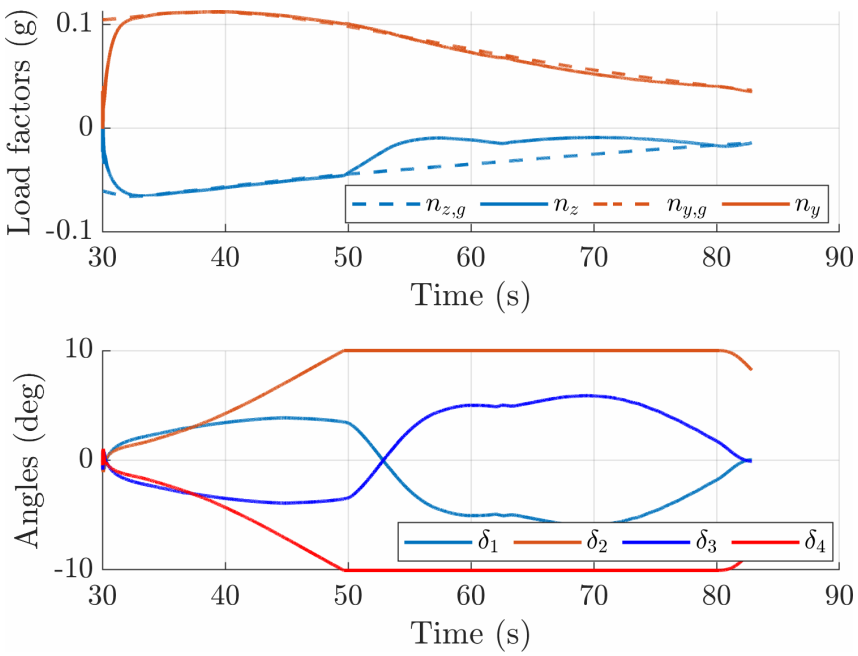

Figure 4.28: LTV simulation with linear interpolation of local static DLAW compensators

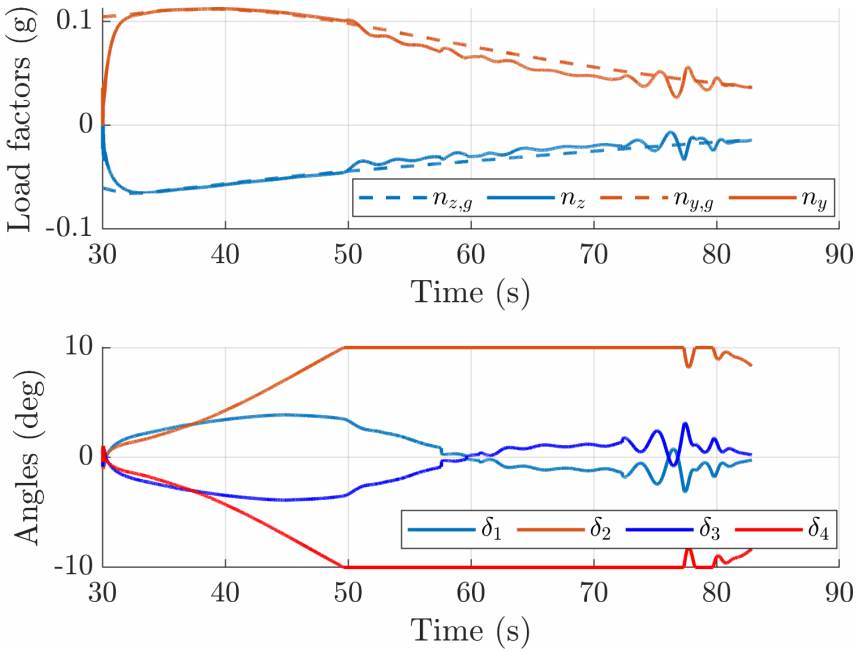

Figure 4.29: LTV simulation with output blending of local LQ-based MRAW compensators

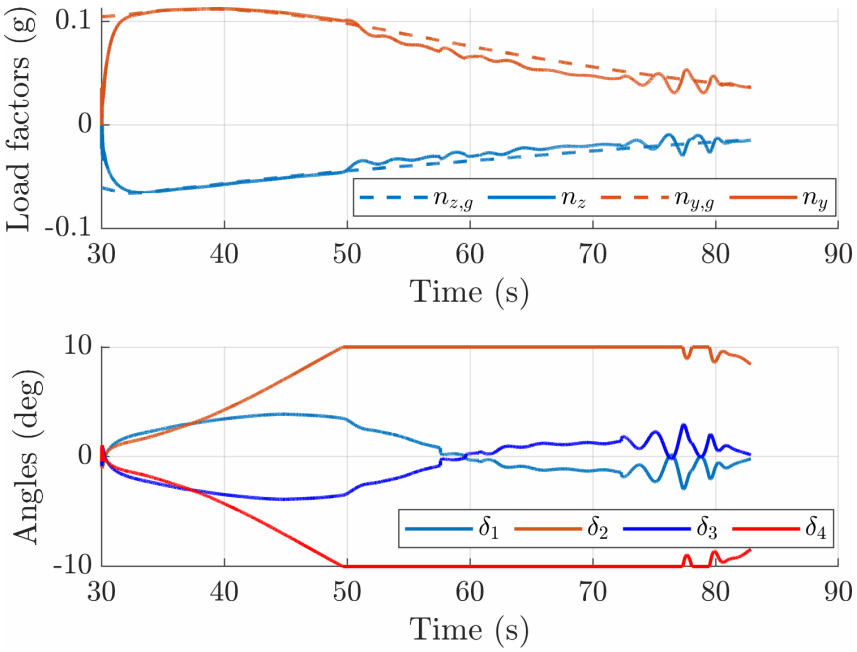

Figure 4.30: LTV simulation with output blending of local reduced LQ-based MRAW compensators

4.4 Conclusion

This chapter starts with a review of theoretical results on saturated systems, leading to a presentation of two modern anti-windup approaches, namely DLAW and MRAW, and of IQC-based robustness analysis. These elements are then applied to the pitch/yaw channels of the guided projectile to compute and evaluate anti-windup compensators. Simple methods requiring little or no tuning are preferred to make computation over the whole flight envelope easier. Three such methods are selected, which are a static stability-based DLAW, an LQ-based MRAW of order 14, and a reduced LQ-based MRAW of order 4, neglecting actuator and sensor dynamics. Despite the simplicity of the chosen schemes, time-domain simulations show that all configurations drastically improve the step response over the baseline configuration in a time-invariant context. In particular, responses with the reduced MRAW are virtually identical to those with the full MRAW. An IQC analysis is then conducted, where the deadzone nonlinearity is described using a combination of full-block circle criterion and full-block Zames-Falb multipliers, and aerodynamic uncertainties are captured using *DG*-scaling multipliers stemming from μ-analysis. Despite the conservatism of the approach, improved robust stability properties are confirmed over the baseline configuration. The gain scheduling strategies (linear interpolation for the DLAW and output blending for the MRAW compensators) are then validated through LTV simulations and show the relevance of the gain scheduled anti-windup strategies for addressing saturations on the considered application.

References

Åström, K. J. and Rundqwist, L. (1989). “Integrator windup and how to avoid it”. In: *1989 American Control Conference*. IEEE.

Bemporad, A. (1998). "Reference governor for constrained nonlinear systems". In: *IEEE Transactions on Automatic Control* 43.3, pp. 415–419.

Biannic, J.-M., Roos, C., and Tarbouriech, S. (2007). "A practical method for fixed-order anti-windup design". In: *IFAC Proceedings Volumes* 40.12, pp. 675–680.

Biannic, J.-M. and Tarbouriech, S. (2009). "Optimization and implementation of dynamic anti-windup compensators with multiple saturations in flight control systems". In: *Control Engineering Practice* 17.6, pp. 703–713.

Biannic, J.-M. and Roos, C. (2012-2021). *Generalized State Space: a new Matlab class to model uncertain and nonlinear systems as Linear Fractional Representations*. URL: `http://w3.onera.fr/smac/gss`.

Biannic, J.-M., Tarbouriech, S., and Farret, D. (2006). "A practical approach to performance analysis of saturated systems with application to fighter aircraft flight controllers". In: *IFAC Proceedings Volumes* 39.9, pp. 35–40.

Boada, J., Prieur, C., Tarbouriech, S., Pittet, C., and Charbonnel, C. (2010). "Extended Model Recovery Anti-windup for Satellite Control". In: *IFAC Proceedings Volumes* 43.15, pp. 205–210.

Boyd, S., El Ghaoui, L., Feron, E., and Balakrishnan, V. (1994). *Linear matrix inequalities in system and control theory*. SIAM.

Cao, Y.-Y., Lin, Z., and Ward, D. G. (2002). "An antiwindup approach to enlarging domain of attraction for linear systems subject to actuator saturation". In: *IEEE Transactions on Automatic Control* 47.1, pp. 140–145.

Carrasco, J., Turner, M. C., and Heath, W. P. (2016). "Zames-Falb multipliers for absolute stability: From O'Shea's contribution to convex searches". In: *European Journal of Control* 28, pp. 1–19.

Chaudenson, J., Beauvois, D., Bennani, S., Ganet-Schoeller, M., and Sandou, G. (2013). "Dynamics modeling and comparative robust stability analysis of a space launcher with constrained inputs". In: *2013 European Control Conference (ECC)*. IEEE.

Cristofaro, A., Galeani, S., Onori, S., and Zaccarian, L. (2019). "A switched and scheduled design for model recovery anti-windup of linear plants". In: *European Journal of Control* 46, pp. 23–35.

Demourant, F. (2013). "New algorithmic approach based on integral quadratic constraints for stability analysis of high order models". In: *2013 European Control Conference (ECC)*. IEEE.

Doyle, J. C., Smith, R. S., and Enns, D. F. (1987). "Control of plants with input saturation nonlinearities". In: *Proceedings of the 1987 American Control Conference*. IEEE, pp. 1034–1039.

Fertik, H. A. and Ross, C. H. (1967). *Direct digital control algorithm with anti-windup feature*. Tech. rep. ISA Transactions.

Fetzer, M. and Scherer, C. W. (2017). "Full-block multipliers for repeated, slope-restricted scalar nonlinearities". In: *International Journal of Robust and Nonlinear Control* 27.17, pp. 3376–3411.

Fetzer, M., Scherer, C. W., and Veenman, J. (2018). "Invariance with dynamic multipliers". In: *IEEE Transactions on Automatic Control* 63.7, pp. 1929–1942.

Fry, J. M. and Farhood, M. (2020). "A comprehensive analytical tool for control validation of fixed-wing unmanned aircraft". In: *IEEE Transactions on Control Systems Technology* 28.5, pp. 1785–1801.

Gahinet, P. and Apkarian, P. (1994). "A linear matrix inequality approach to H_∞ control". In: *International Journal of Robust and Nonlinear Control* 4.4, pp. 421–448.

Galeani, S., Onori, S., Teel, A. R., and Zaccarian, L. (2007a). "Regional, semiglobal, global nonlinear anti-windup via switching design". In: *2007 European Control Conference (ECC)*. IEEE.

Galeani, S., Onori, S., and Zaccarian, L. (2007b). "Nonlinear scheduled control for linear systems subject to saturation with application to anti-windup control". In: *2007 46th IEEE Conference on Decision and Control*. IEEE.

Galeani, S., Tarbouriech, S., Turner, M., and Zaccarian, L. (2009). "A Tutorial on Modern Anti-windup Design". In: *European Journal of Control* 15.3-4, pp. 418–440.

Galeani, S., Teel, A. R., and Zaccarian, L. (2007c). "Constructive nonlinear anti-windup design for exponentially unstable linear plants". In: *Systems & Control Letters* 56.5, pp. 357–365.

Garone, E., Cairano, S. D., and Kolmanovsky, I. (2017). "Reference and command governors for systems with constraints: A survey on theory and applications". In: *Automatica* 75, pp. 306–328.

Gomes da Silva, J. M. and Tarbouriech, S. (2005). "Antiwindup design with guaranteed regions of stability: an LMI-based approach". In: *IEEE Transactions on Automatic Control* 50.1, pp. 106–111.

Grimm, G., Hatfield, J., Postlethwaite, I., Teel, A. R., Turner, M. C., and Zaccarian, L. (2003). "Antiwindup for stable linear systems with input saturation: An LMI-based synthesis". In: *IEEE Transactions on Automatic Control* 48.9, pp. 1509–1525.

Hanus, R., Kinnaert, M., and Henrotte, J.-L. (1987). "Conditioning technique, a general anti-windup and bumpless transfer method". In: *Automatica* 23.6, pp. 729–739.

Hu, T. and Lin, Z. (2001). *Control systems with actuator saturation: analysis and design*. Birkhäuser.

Hu, T., Lin, Z., and Chen, B. M. (2002). "An analysis and design method for linear systems subject to actuator saturation and disturbance". In: *Automatica* 38.2, pp. 351–359.

Hu, T., Teel, A. R., and Zaccarian, L. (2005). "Regional anti-windup compensation for linear systems with input saturation". In: *Proceedings of the 2005, American Control Conference, 2005.* IEEE.

Jönnson, U. (2001). "Lecture notes on integral quadratic constraints". In:

Jun, M. and Safonov, M. G. (2001). "IQC robustness analysis for time-delay systems". In: *International Journal of Robust and Nonlinear Control* 11.15, pp. 1455–1468.

Kerr, M. L., Turner, M. C., and Postlethwaite, I. (2008). "Practical approaches to low-order anti-windup compensator design: a flight control comparison". In: *IFAC Proceedings Volumes* 41.2, pp. 14162–14167.

Khalil, H. K. (2002). *Nonlinear systems*. Second. Prentice Hall.

Köroğlu, H. and Scherer, C. W. (2007). "Robust performance analysis for structured linear time-varying perturbations with bounded rates-of-variation". In: *IEEE Transactions on Automatic Control* 52.2, pp. 197–211.

Kothare, M. V., Campo, P. J., Morari, M., and Nett, C. N. (1994). "A unified framework for the study of anti-windup designs". In: *Automatica* 30.12, pp. 1869–1883.

Li, Y. and Lin, Z. (2015). "A generalized piecewise quadratic lyapunov function approach to estimating the domain of attraction of a saturated system". In: *IFAC-PapersOnLine* 48.11, pp. 120–125.

Li, Y. and Lin, Z. (2016). "A switching anti-windup design based on partitioning of the input space". In: *Systems & Control Letters* 88, pp. 39–46.

Lofberg, J. (2004). "YALMIP : a toolbox for modeling and optimization in MATLAB". In: *2004 IEEE International Conference on Robotics and Automation (IEEE Cat. No.04CH37508)*. IEEE.

Lozier, J. (1956). "A steady state approach to the theory of saturable servo systems". In: *IRE Transactions on Automatic Control* 1.1, pp. 19–39.

Lyapunov, A. M. (1992). "The general problem of the stability of motion". In: *International Journal of Control* 55.3, pp. 531–534.

Marcos, A., Veenman, J., Scherer, C., De Zaiacomo, G., Mostaza, D., Kerr, M., Köroglu, H., and Bennani, S. (2010). "Application of LPV modeling, design and analysis methods to a re-entry vehicle". In: *AIAA Guidance, Navigation, and Control Conference*, p. 8192.

Megretski, A. and Rantzer, A. (1997). "System analysis via integral quadratic constraints". In: *IEEE Transactions on Automatic Control* 42.6, pp. 819–830.

Morari, M. and Zafiriou, E. (1989). *Robust process control*. Prentice Hall.

MOSEK ApS (2019). *The MOSEK optimization toolbox for MATLAB manual. Version 9.0*. URL: `http://docs.mosek.com/9.0/toolbox/index.html`.

Mulder, E. F., Kothare, M. V., and Morari, M. (2001). "Multivariable anti-windup controller synthesis using linear matrix inequalities". In: *Automatica* 37.9, pp. 1407–1416.

Packard, A. and Doyle, J. (1993). "The complex structured singular value". In: *Automatica* 29.1, pp. 71–109.

Palframan, M. C., Fry, J. M., and Farhood, M. (2019). "Robustness analysis of flight controllers for fixed-wing unmanned aircraft systems using integral quadratic constraints". In: *IEEE Transactions on Control Systems Technology* 27.1, pp. 86–102.

Pittet, C., Tarbouriech, S., and Burgat, C. (2007). "Stability regions for linear systems with saturating controls via circle and Popov criteria". In: *Proceedings of the 36th IEEE Conference on Decision and Control*. IEEE.

Polat, İ. and Scherer, C. W. (2012). "Stability analysis for bilateral teleoperation: an IQC formulation". In: *IEEE Transactions on Robotics* 28.6, pp. 1294–1308.

Roos, C. and Biannic, J.-M. (2008). "A convex characterization of dynamically-constrained anti-windup controllers". In: *Automatica* 44.9, pp. 2449–2452.

Saeki, M. and Wada, N. (2002). "Synthesis of a static anti-windup compensator via linear matrix inequalities". In: *International Journal of Robust and Nonlinear Control* 12.10, pp. 927–953.

Sajjadi-Kia, S. and Jabbari, F. (2011). "Modified dynamic anti-windup through deferral of activation". In: *International Journal of Robust and Nonlinear Control* 22.15, pp. 1661–1673.

Scherer, C. and Weiland, S. (2000). "Linear matrix inequalities in control". In: *Lecture Notes, Dutch Institute for Systems and Control, Delft, The Netherlands* 3.2.

Scorletti, G. (1997). "Robustness analysis with time-delays". In: *Proceedings of the 36th IEEE Conference on Decision and Control*. IEEE.

Seiler, P., Moore, R. M., Meissen, C., Arcak, M., and Packard, A. (2019). "Finite horizon robustness analysis of LTV systems using integral quadratic constraints". In: *Automatica* 100, pp. 135–143.

Sturm, J. F. (1999). "Using SeDuMi 1.02, a MATLAB toolbox for optimization over symmetric cones". In: *Optimization methods and software* 11.1-4, pp. 625–653.

Tarbouriech, S., Garcia, G., Gomes da Silva, J. M., and Queinnec, I. (2011). *Stability and stabilization of linear systems with saturating actuators*. Springer London.

Teel, A. R. and Kapoor, N. (1997a). "The L2 anti-winup problem: Its definition and solution". In: *1997 European Control Conference (ECC)*. IEEE.

Teel, A. R. and Kapoor, N. (1997b). "Uniting local and global controllers". In: *1997 European Control Conference (ECC)*. IEEE.

Thai, S., Theodoulis, S., Roos, C., and Biannic, J.-M. (2021). "An interpolated model recovery anti-windup for a canard-guided projectile subject to uncertainties". In: *2021 European Control Conference (ECC)*. IEEE.

Thai, S., Theodoulis, S., Roos, C., Biannic, J.-M., and Proff, M. (2020). "Gain-scheduled autopilot design with anti-windup compensator for a dual-spin canard-guided projectile". In: *2020 IEEE Conference on Control Technology and Applications (CCTA)*. IEEE.

Turner, M. C. (2021). *Zames-Falb multipliers: don't panic*. URL: `https://arxiv/org/abs/2106.15913`.

Turner, M. C. and Herrmann, G. (2014). "A non-square sector condition and its application in deferred-action anti-windup compensator design". In: *Automatica* 50.1, pp. 268–276.

Turner, M. C. and Kerr, M. (2018). "A nonlinear modification for improving dynamic anti-windup compensation". In: *European Journal of Control* 41, pp. 44–52.

Turner, M. C., Sofrony, J., and Herrmann, G. (2016). "An alternative approach to anti-windup in anticipation of actuator saturation". In: *International Journal of Robust and Nonlinear Control* 27.6, pp. 963–980.

Veenman, J., Scherer, C. W., Ardura, C., Bennani, S., Preda, V., and Girouart, B. (2021). "IQClab: a new IQC based toolbox for robustness analysis and control design". In:

Veenman, J., Scherer, C. W., and Köroğlu, H. (2016). "Robust stability and performance analysis based on integral quadratic constraints". In: *European Journal of Control* 31, pp. 1–32.

Vidyasagar, M. (2002). *Nonlinear systems analysis*. Third. SIAM: Society for Industrial and Applied Mathematics.

Vuillemin, P., Demourant, F., Biannic, J.-M., and Poussot-Vassal, C. (2016). "Stability analysis of a set of uncertain large-scale dynamical models with saturations: application to an aircraft system". In: *IEEE Transactions on Control Systems Technology* 25.2, pp. 661–668.

Wu, X. and Lin, Z. (2012a). “Dynamic anti-windup design in anticipation of actuator saturation”. In: *International Journal of Robust and Nonlinear Control* 24.2, pp. 295–312.

Wu, X. and Lin, Z. (2012b). “On immediate, delayed and anticipatory activation of anti-windup mechanism: static anti-windup case”. In: *IEEE Transactions on Automatic Control* 57.3, pp. 771–777.

Zaccarian, L. and Teel, A. R. (2002). “A common framework for anti-windup, bumpless transfer and reliable designs”. In: *Automatica* 38.10, pp. 1735–1744.

Zaccarian, L. and Teel, A. R. (2011). *Modern Anti-windup Synthesis: Control Augmentation for Actuator Saturation*. Princeton University Press.

Zames, G. and Falb, P. L. (1968). “Stability conditions for systems with monotone and slope-restricted nonlinearities”. In: *SIAM Journal on Control* 6.1, pp. 89–108.

Zheng, A., Kothare, M. V., and Morari, M. (1994). “Anti-windup design for internal model control”. In: *International Journal of Control* 60.5, pp. 1015–1024.

Chapter 5

Nonlinear flight simulations

Contents

5.1 Introduction

In this chapter, complete guided flight scenarios are simulated by putting together the nonlinear 7DoF model of the projectile described in Chapter 2 with the roll and pitch/yaw autopilots from Chapter 3 and the anti-windup compensators designed in Chapter 4. Performance with respect to operational requirements, and in particular the miss distance to a target, can then be evaluated in nominal conditions, but also in the presence of various uncertainties affecting initial launch conditions and aerodynamic coefficients.

This chapter is organised as follows. Section 5.2 introduces the flight simulation environment. In particular, the guidance module used to generate the reference signals is presented. Section 5.3 presents simulation results obtained for a nominal flight scenario as well as several degraded ones, which include trajectories affected by a wind disturbance, perturbed launch conditions, or aerodynamic uncertainties. In each case, simulations with deactivated saturations are first conducted, both to validate the baseline autopilot and to identify the conditions under which saturation levels are reached. Then the relevant cases are simulated again with active saturations,

and finally with the three scheduled anti-windup compensators developed in Chapter 4, allowing to observe the degradations induced by the saturations, and then the improvements brought by the augmented autopilot.

5.2 Presentation of the guided projectile flight simulator

5.2.1 Guided flight scenario and GNC architecture

The role of the guided projectile flight simulator is to simulate operational flight scenarios. The capability of the projectile to intercept a target, in nominal or degraded conditions, can then be evaluated directly through the miss distance at impact. Figure 5.1 recalls and details the standard flight scenario, which consists of a ballistic phase and a guided phase. The ballistic phase is further decomposed into three subphases:

1. During the first subphase ($0 \leq t < t_{start} = 20$ s), electronic components are switched on. This is done a few seconds after the launch to avoid possible hardware degradations due to the harsh initial conditions.

2. At $t = t_{start}$, the fuse roll rate p_f, which at this point is high due to the mechanical bearing between the body and the fuse, is decreased by sending a constant control signal $\delta_p = 8\,\text{deg}$ to the actuators. Constant deflection angles are therefore maintained until the moment t_{switch} when the roll rate reaches $p_f = 1800$ deg/s $= 10\pi$ rad/s.

3. The gain scheduled roll autopilot designed in Chapter 3 is then activated and stabilises the fuse roll angle ϕ_f at 45 deg to achieve a '×' configuration.

The guided phase starts at $t_{guid} = 30$ s, where the pitch/yaw guidance module and autopilot are activated and contribute to steering the projectile towards the target.

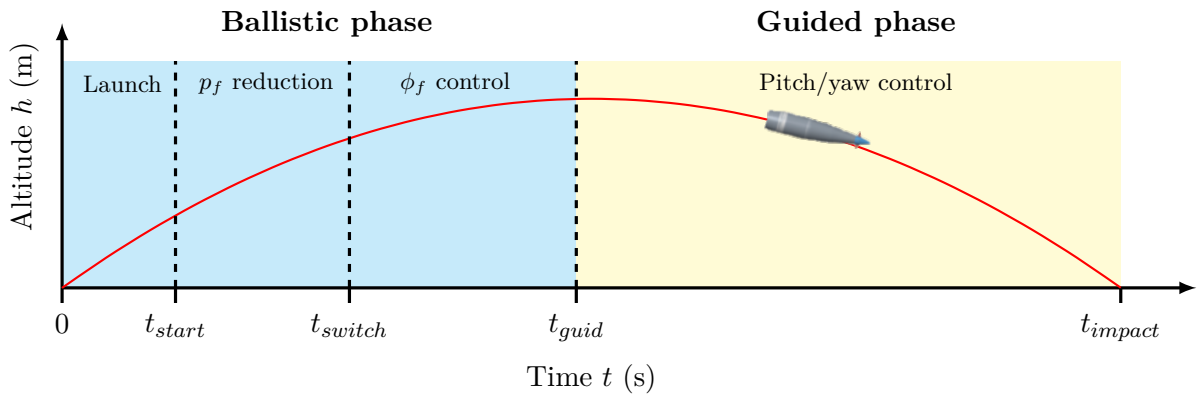

Figure 5.1: Detailed standard flight scenario of the guided projectile

To simulate the flight scenario described above, complete GNC loops corresponding to the different anti-windup schemes evaluated in Chapter 4 are implemented in Matlab/Simulink. These GNC loops all share a similar architecture depicted in Figure 5.2, and consisting of the following elements:

- the nonlinear 7DoF airframe model, for which a mathematical model is detailed in Section 2.3. The launch conditions (initial velocity V_0, elevation angle θ_0, and azimuth ψ_0) are also specified in this block.

- the four actuators associated to the canards of the projectile fuse. For testing purposes, it is useful to also consider a GNC loop model with no actuator saturations.

- the embedded sensors, consisting of accelerometers and gyroscopes measuring the load factors and angular rates of the projectile, as well as sensors from the servomotors allowing to measure the canard deflection angles.

- the *Mission* block, which sends the position of the target to the guidance module.

- the guidance system, which computes the reference signals sent to the controller, based on the position of the target and the navigation data. The guidance module is decomposed into the roll guidance module, which activates at t_{start} and sends a constant signal $\phi_{f,g} = 45\,\text{deg}$ to the roll autopilot, and the pitch/yaw guidance module, generating reference load factors $\boldsymbol{n}_{zy,g} = [n_{z,g}\ n_{y,g}]^T$ from t_{guid} to the end of the trajectory.

- the navigation system, which performs data fusion to provide, in addition to the relevant sensor measurements, estimated values of the scheduling variables V_{Nav}, h_{Nav}, and $p_{a,Nav}$ to both the guidance and controller systems. In this study, perfect navigation is assumed.

- the controller system, which combines the autopilots and anti-windup compensators designed in Chapter 3 and Chapter 4, as well as the allocation transformation described in Section 2.5. It uses the reference signals sent by the guidance along with navigation data (which gathers the relevant sensor measurements and estimations of the scheduling variables) to compute the control input signals sent to the actuators.

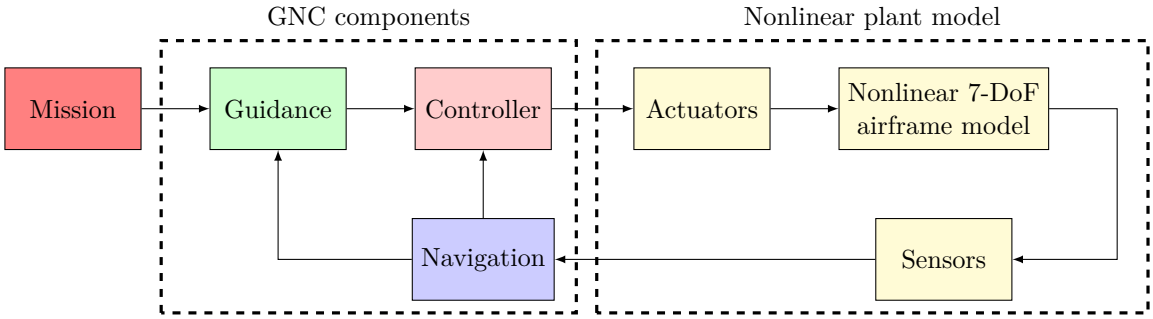

Figure 5.2: General GNC loop

5.2.2 Description of the ZEM guidance strategy for reference load factors computation

In [Sève et al., 2017], reference load factors are computed using a guidance law based on Proportional Navigation (PN). The main idea of PN is to attempt to maintain the velocity vector of the projectile in the direction of the line-of-sight, which is the straight line between the

projectile and the target [Zipfel, 2007; Zarchan, 2012]. While PN is widely used for missiles, it is ill-suited for the guided projectile concept studied here. Indeed, the resulting load factors go strongly against the naturally curved ballistic trajectory of the airframe, leading to very high deflection angles. In [Sève et al., 2017], the issue is circumvented by starting the guided phase only after the trajectory apogee, at the cost of some manoeuvrability. Another strategy, adopted here, is to use an altogether different guidance law.

The pitch/yaw guidance module implemented in the flight simulator was developed in [Proff and Theodoulis, 2019] and is based on a zero-effort-miss (ZEM) guidance technique, whose main working principles are described next. ZEM guidance relies on an impact point prediction (IPP) method to compute the lateral and longitudinal position errors between the target position and an estimated ballistic (i.e. zero-effort) impact point. These errors are regularly updated based on the current state of the projectile and on a simplified model of the airframe. The position errors, also called zero-effort misses, are then given by:

$$\begin{aligned} ZEM_x &= x(t_{go}) - x_T \\ ZEM_y &= y(t_{go}) - y_T \end{aligned} \tag{5.1}$$

with $x(t_{go})$ and $y(t_{go})$ the estimated impact longitudinal and lateral position as a function of the time to go t_{go}, and x_T and y_T the longitudinal and lateral target positions. The guidance acceleration can then computed as:

$$\boldsymbol{a}_{go} = k_g \begin{bmatrix} -ZEM_x \\ -ZEM_y \\ 0 \end{bmatrix} \tag{5.2}$$

where the guidance gain k_g is a tuning parameter of the ZEM technique. However, this guidance acceleration is not suited for a projectile with no thrust capacity, as is the case for the studied concept. The longitudinal term ZEM_x is then used to compute a normal acceleration term instead. The launch pitch angle θ_0 and flight path angle $\gamma = \theta - \alpha$ must then be taken into account, since depending on these angles, a negative force on the vertical axis can either decrease or increase the projectile longitudinal impact location. These considerations lead to the following guidance acceleration [Gagnon and Vachon, 2016]:

$$\boldsymbol{a}_{zy,go} = \begin{cases} k_g \begin{bmatrix} -ZEM_x \\ -ZEM_y \end{bmatrix} & \text{if } \theta_0 > \frac{\pi}{4} \text{ and } \gamma > 0 \\ k_g \begin{bmatrix} +ZEM_x \\ -ZEM_y \end{bmatrix} & \text{otherwise} \end{cases} \tag{5.3}$$

These accelerations represent the total effort to reduce the ZEMs to zero. In order to reduce the workload of the autopilot, the specific acceleration produced by the aerodynamic forces is also taken into account. The load factors sent to the autopilot are then computed as:

$$\boldsymbol{n}_{zy,g} = \frac{1}{g}(\boldsymbol{a}_{zy,go} + \boldsymbol{a}_{zy,eo}) \tag{5.4}$$

with $\boldsymbol{a}_{zy,eo}$ an estimation of the specific acceleration, and g the gravity constant.

The choice of the IPP method to compute the ZEM terms ZEM_x and ZEM_y and the estimated specific accelerations $\boldsymbol{a}_{zy,eo}$ is critical to handle the trade-off between accuracy and computational effort [Fresconi et al., 2011]. The ZEM algorithm developed in [Proff and Theodoulis, 2019] uses a modified point mass model, which represents the projectile as a point mass with spin rate, allowing to take into account gravity, drag, lift, and Magnus forces in the impact prediction.

5.2.3 Implementation of the autopilot in the GNC loop

With reference to Figure 5.2, the full controller combines the roll and pitch/yaw autopilots along with the allocation matrix. Figure 5.3 shows the complete scheduled baseline (no anti-windup) autopilot used from t_{guid} to t_{impact}, with $K_R(s, \boldsymbol{\lambda}_R)$ and $K_{PY}(s, \boldsymbol{\lambda}_{PY})$ respectively the roll and pitch/yaw autopilots designed in Chapter 3, and $T_{RV}(\phi_{f,m})$ the allocation matrix defined in Section 2.5, which depends on the measured fuse roll angle $\phi_{f,m}$. Figure 5.4 then depicts the autopilot augmented with a scheduled anti-windup compensator $AW(\boldsymbol{\lambda}_{PY})$, along with the necessary transformations to formulate the anti-windup synthesis problem as already detailed in Chapter 4. Note that the saturation appearing in Figure 5.4 is part of the controller, and is thus enforced by the flight software before the control signals go to the actuators. In addition, the measured fuse roll angle $\phi_{f,m}$ is used to specify the transformation $M(\phi_{f,m})$ rather than the expected value of 45 deg, ensuring that activation of the anti-windup compensator is based on the current fuse roll angle, and avoiding potential chattering effects in case it oscillates around 45 deg.

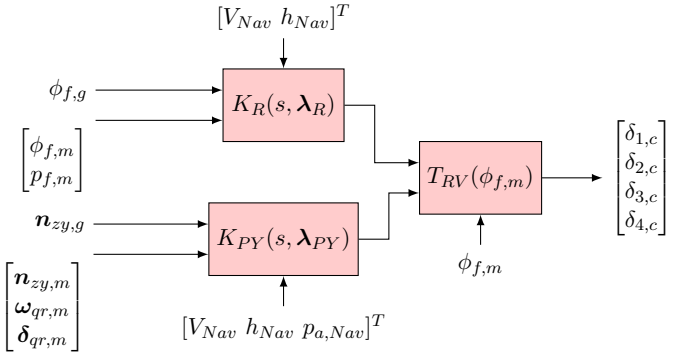

Figure 5.3: Baseline autopilot for the guided phase

5.3 Nonlinear simulations for GNC loop evaluation

5.3.1 Evaluation on a nominal flight scenario

A flight scenario representative of a standard long-range mission is considered, characterised by the following launch conditions:

$$V_0 = 939 \text{ m/s}, \quad \theta_0 = 42\,\text{deg}, \quad \psi_0 = 0\,\text{deg} \tag{5.5}$$

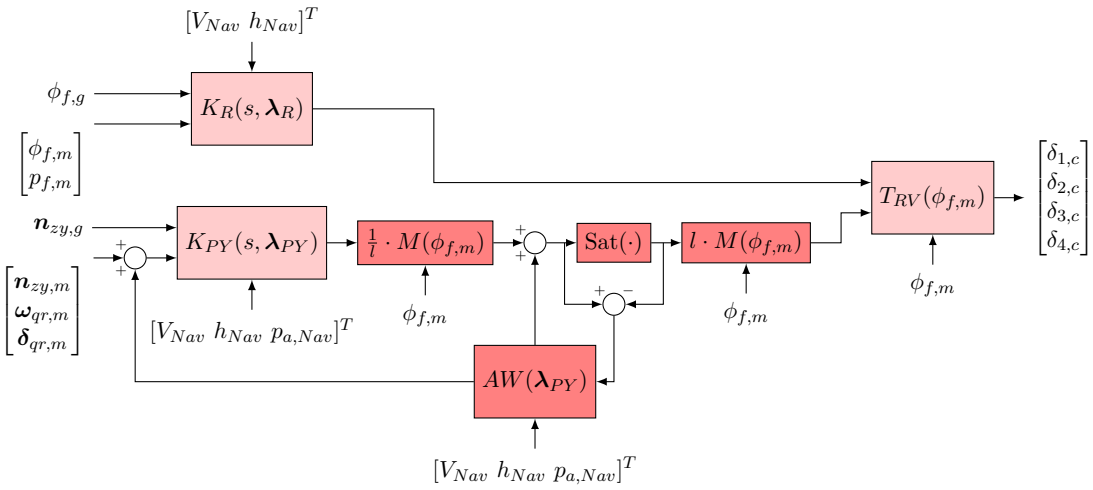

Figure 5.4: Autopilot with anti-windup augmentation for the guided phase

The mission target is set as the ballistic impact point of the projectile, located approximately 25 km downrange and 700 m crossrange from the launch point. Simulation results with the baseline autopilot are shown in Figure 5.5, where data from the ballistic trajectory are also provided for reference. Regarding the ballistic phase, it can be observed that the fuse configuration (p_f reduction and ϕ_f control) is very short, lasting about 0.5 s. Regarding the guided phase, the ZEM guidance law produces guidance load factors $n_{z,g}$ and $n_{y,g}$ that are close to the ballistic ones $n_{z,bal}$ and $n_{y,bal}$. These guidance signals are tracked accurately by the pitch/yaw autopilot, and the target is successfully reached, with a miss distance at impact of $5 \cdot 10^{-4}$ m. Since the deflection angles remain below the saturation level $l = 10\,\text{deg}$, identical trajectories are obtained regardless of the actuator model (linear or saturated) or anti-windup compensation (no anti-windup, DLAW, MRAW, or reduced MRAW) used in the GNC loop.

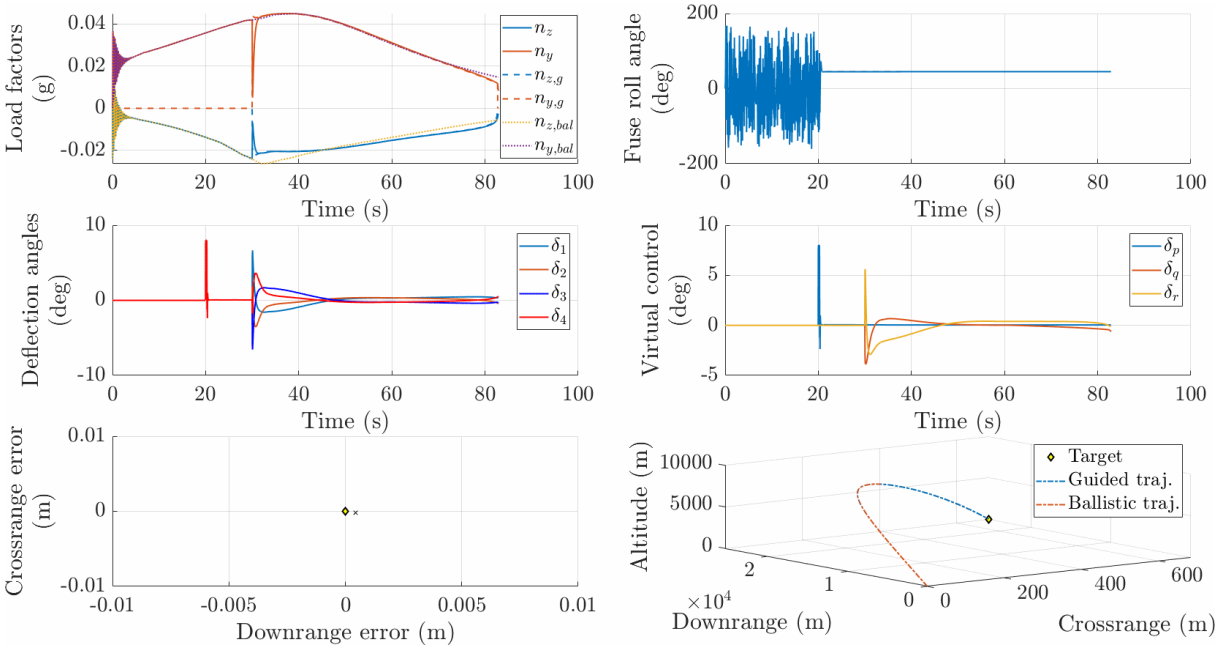

Figure 5.5: Nominal scenario with baseline autopilot: load factors, fuse roll angle, canard deflection angles, virtual control signals, miss distance, trajectory

Remark 15. *The 3D trajectories plotted in this chapter do not use equally scaled axes, since these are ill-suited to highlight the evolution along the y-axis (see Figure 2.6).*

5.3.2 Simulations with wind disturbances

The same mission with wind disturbance is considered next. A horizontal wind is assumed, and the coordinates of the wind velocity vector $[\boldsymbol{v}_A^E]^L = [u_{W,L}\ v_{W,L}\ 0]$ with respect to the Earth and expressed in the local-level frame $]^L$, i.e. the North-East-Down coordinates, are given in Figure 5.6. Since the cannon is oriented in the North direction ($\psi_0 = 0\,\text{deg}$), the significant eastward component $v_{W,L}$ of the wind contributes to increase the deviation of the ballistic projectile to the right, leading to a miss distance of 427.1 m. As seen on Figure 5.7, the guidance and the autopilot manage to successfully compensate this effect by commanding a decreased lateral load factor n_y. However, these simulation results are obtained with deactivated saturations, and require deflection angles greater than 10 deg. The same scenario with active saturations and no anti-windup compensation lead to the severely degraded results of Figure 5.8 and a miss distance of 67 m.

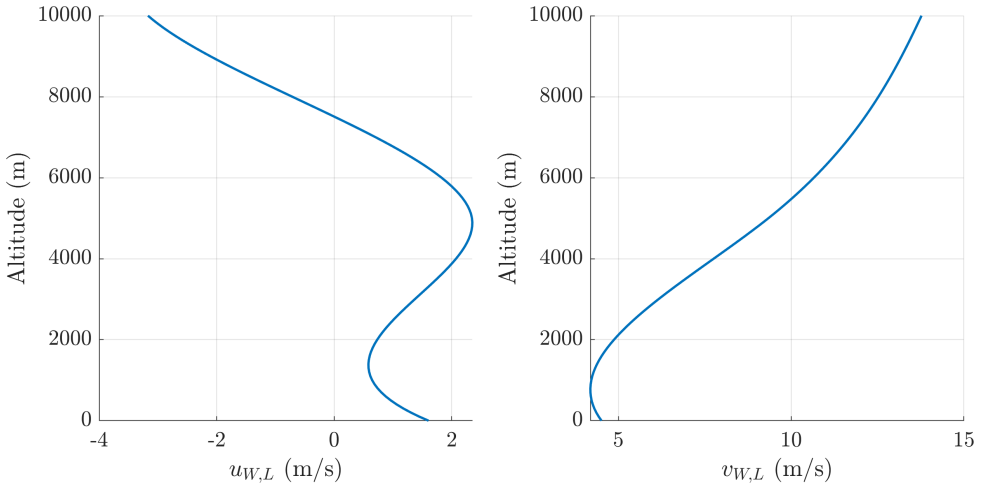

Figure 5.6: Horizontal wind profile

Figures 5.9 and 5.10 then show results for the same scenario, obtained respectively with the scheduled static DLAW and reduced MRAW (the latter are nearly identical to those obtained with full MRAW). Continuing the trend observed in Chapter 4, the static DLAW leads to a relatively noticeable error on the lateral acceleration n_y from $t = 42$ s to $t = 58$ s, while the reduced MRAW spreads the error on both axes more evenly but also adds some small oscillations. However, in the end, both anti-windup compensation schemes are able to recover a very satisfactory closed-loop behaviour, with impact points located a mere 5 mm away from the mission target.

Remark 16. *In practice, the wind vector is taken into account to define the initial yaw angle ψ_0 in order to bring the ballistic impact point closer to the target. This correction would contribute to reduce the deflection angles required by the autopilot, possibly to the point where anti-windup is not necessary. Nonetheless, the presented scenario with no adaptation of ψ_0 remains relevant to illustrate the increased manoeuvrability provided by anti-windup compensation.*

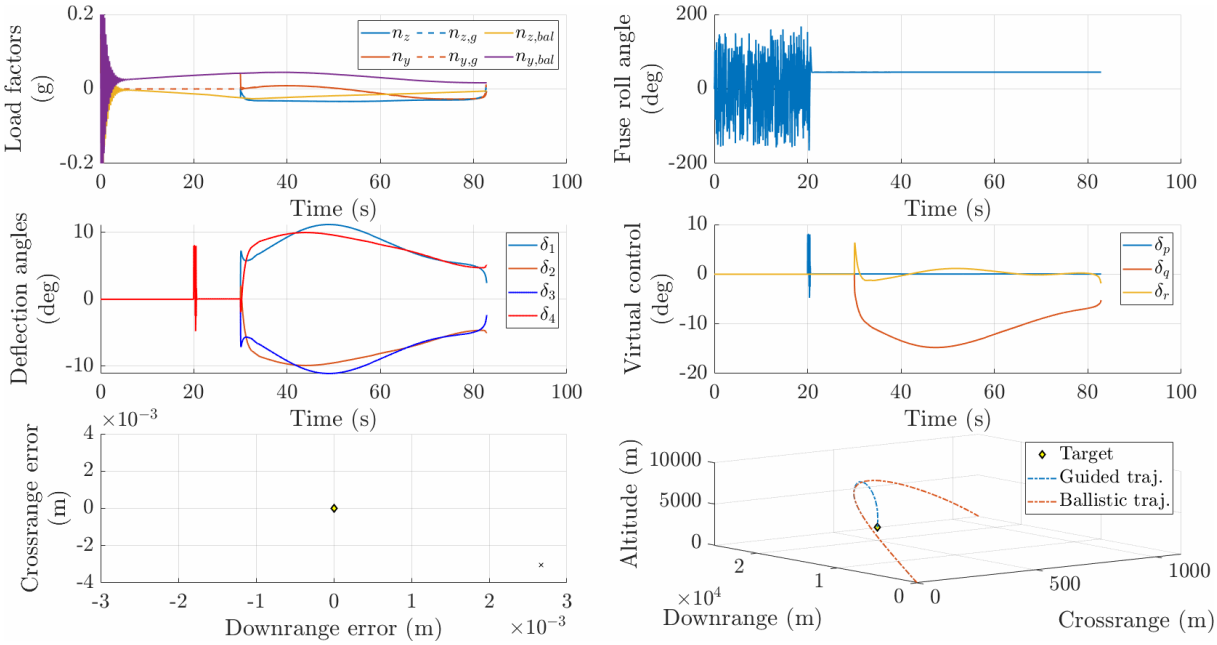

Figure 5.7: Scenario with wind disturbance and deactivated saturations: load factors, fuse roll angle, canard deflection angles, virtual control signals, miss distance, trajectory

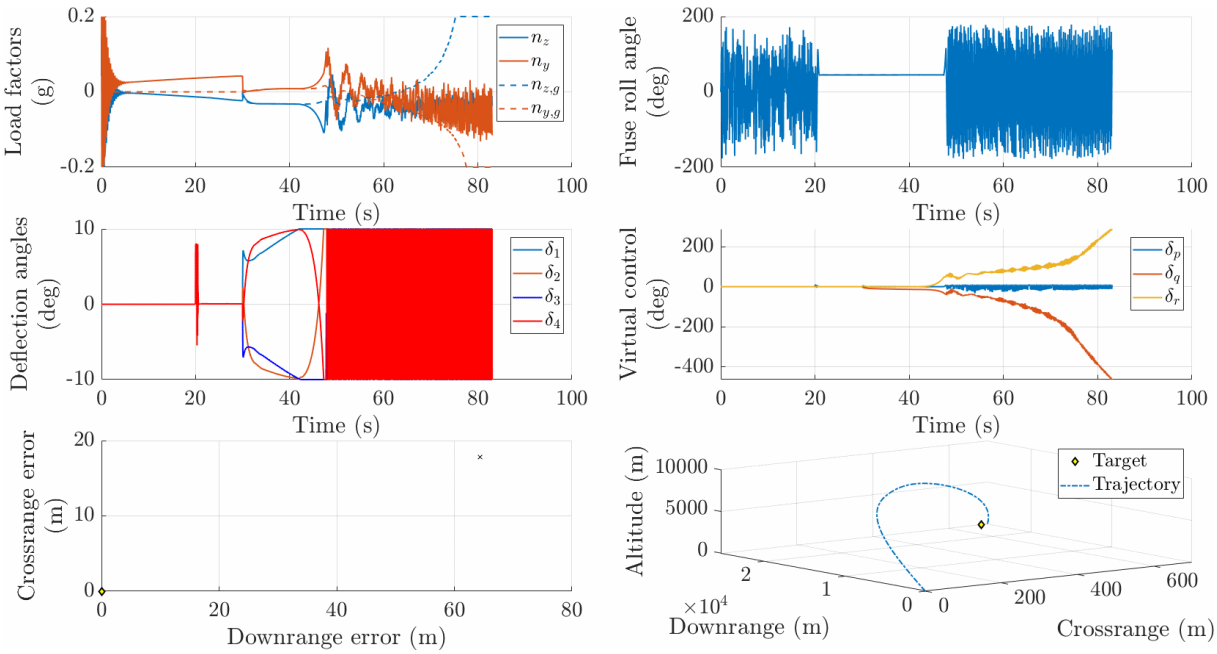

Figure 5.8: Scenario with wind disturbance and saturations: load factors, fuse roll angle, canard deflection angles, virtual control signals, miss distance, trajectory

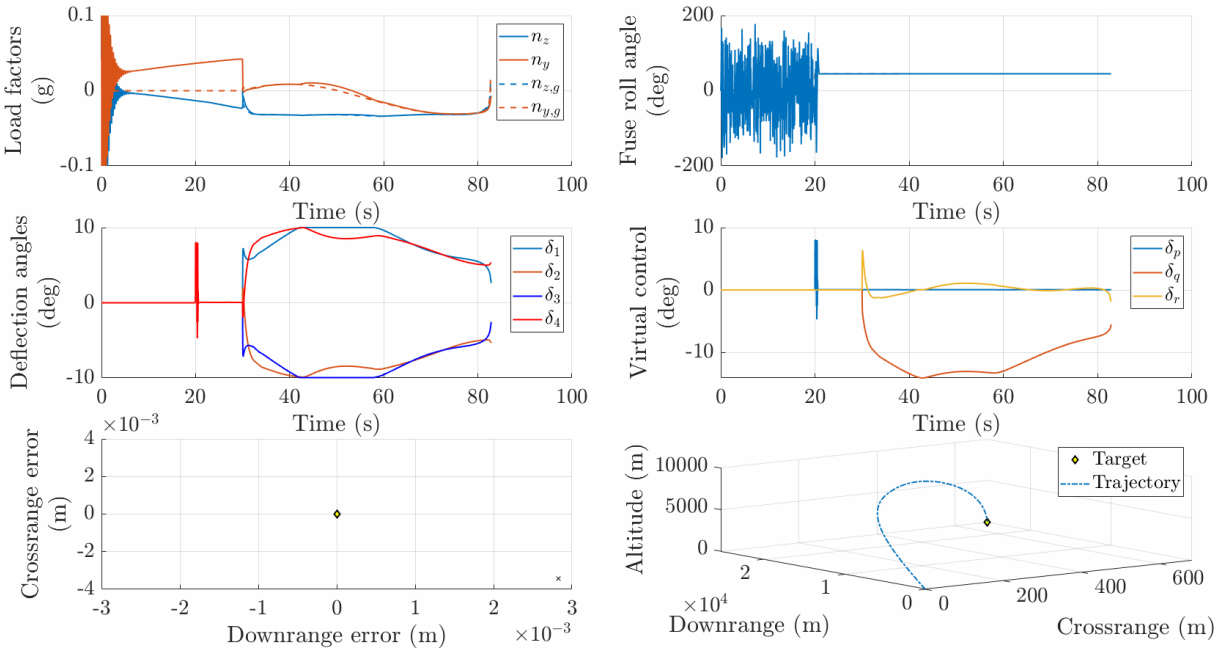

Figure 5.9: Scenario with wind disturbance and scheduled static DLAW: load factors, fuse roll angle, canard deflection angles, virtual control signals, miss distance, trajectory

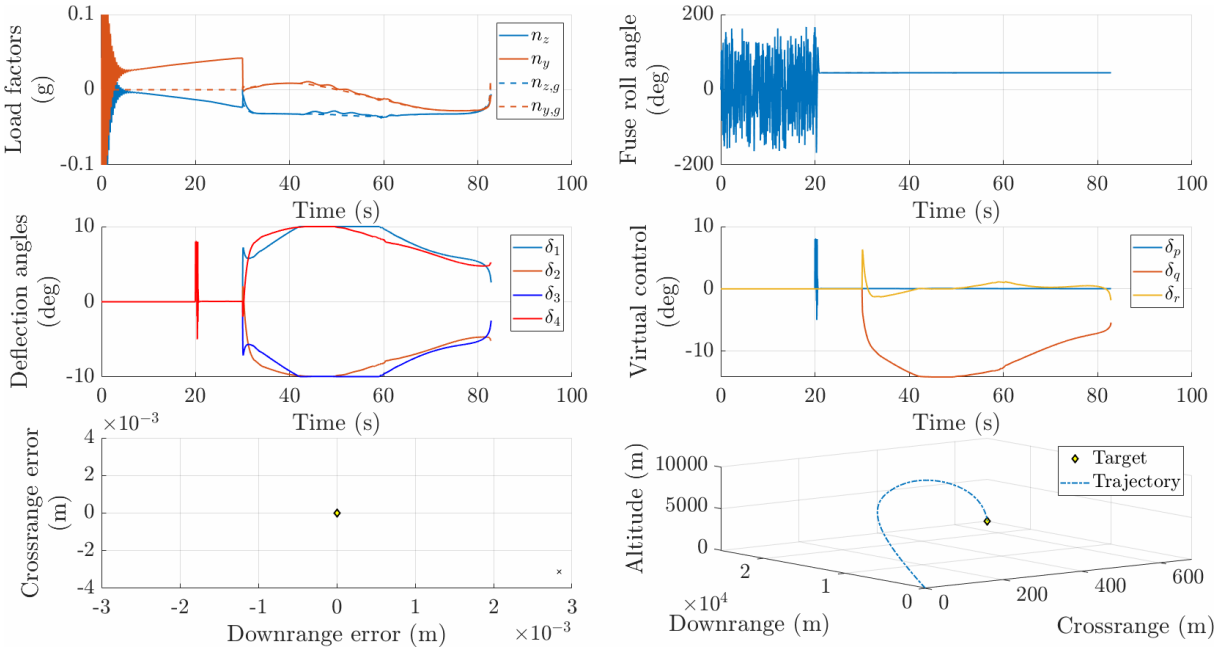

Figure 5.10: Scenario with wind disturbance and scheduled reduced MRAW: load factors, fuse roll angle, canard deflection angles, virtual control signals, miss distance, trajectory

Table 5.1: Uncertainties on the launch conditions

Parameter	Mean value	Standard deviation	Unit
V_0	939	3	m/s
θ_0	42	0.09	deg
ψ_0	0	0.12	deg

5.3.3 Monte Carlo simulations with perturbed launch conditions

Next, degraded scenarios involving uncertainties on the launch conditions are considered. Monte Carlo trajectory simulations are conducted, with 600 samples drawn following normal distributions whose characteristics are detailed in Table 5.1. Simulations are first run on the closed-loop nonlinear model with no saturations. The miss distance at impact is of the order of the millimetre for all tested trajectories, demonstrating the robustness of the baseline to launch uncertainties. However, 24 samples (4%), shown in Figure 5.11, involve deflection angles exceeding $l = 10\,\text{deg}$ and reaching up to 14 deg. Figure 5.12 depicts the trajectory of the virtual control signals in the (δ_q, δ_r)-plane for these 24 samples. The interior of the red square represents the set of virtual control signals that do not lead to canard deflection angles greater than $l = 10\,\text{deg}$ in amplitude, assuming $\phi_{f,m} = 45\,\text{deg}$ and neglecting the contribution of δ_p in the allocation. This plot illustrates that, while the '×' configuration of the fuse is not optimal for all cases, it is however more relevant than the '+' configuration in limiting the excess of control from the pitch/yaw autopilot.

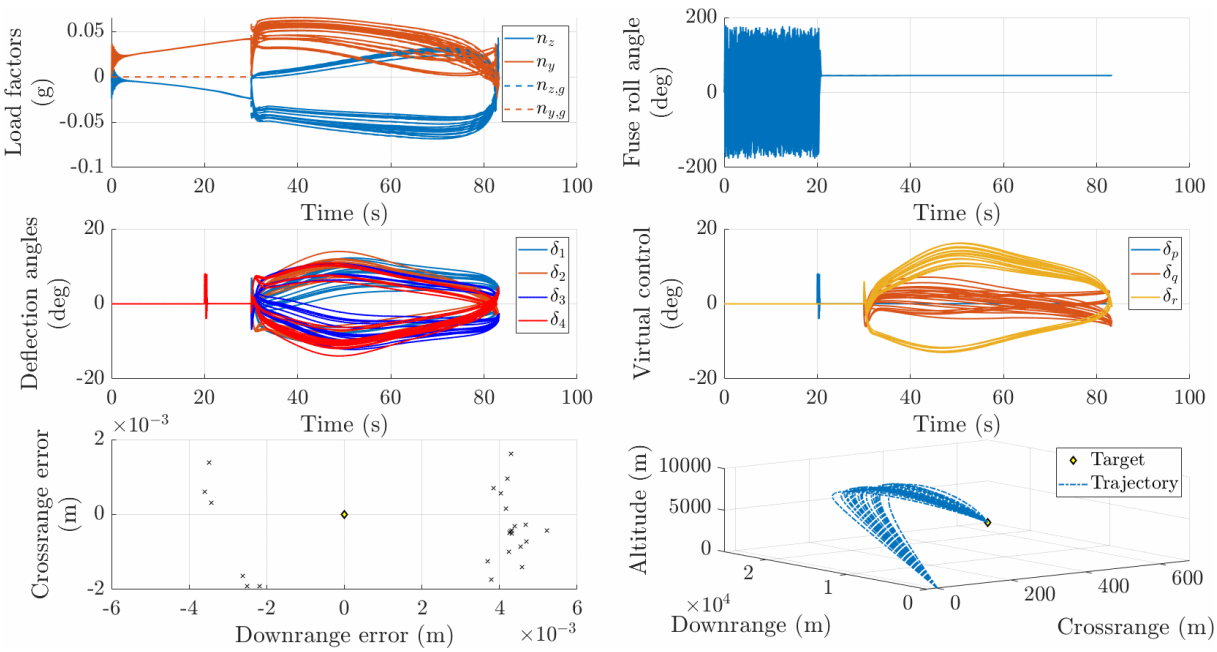

Figure 5.11: Scenarios with launch uncertainties and deactivated saturations: load factors, fuse roll angle, canard deflection angles, virtual control signals, miss distance, trajectory

The same 24 samples evaluated with actuator saturations and no anti-windup compensation can lead to a dramatic degradation of the guided phase, as shown with the trajectory featured in Figure 5.13 corresponding to one of the 24 samples, and associated to a miss distance of 84 m. Results with scheduled static DLAW and scheduled reduced MRAW for the same sample

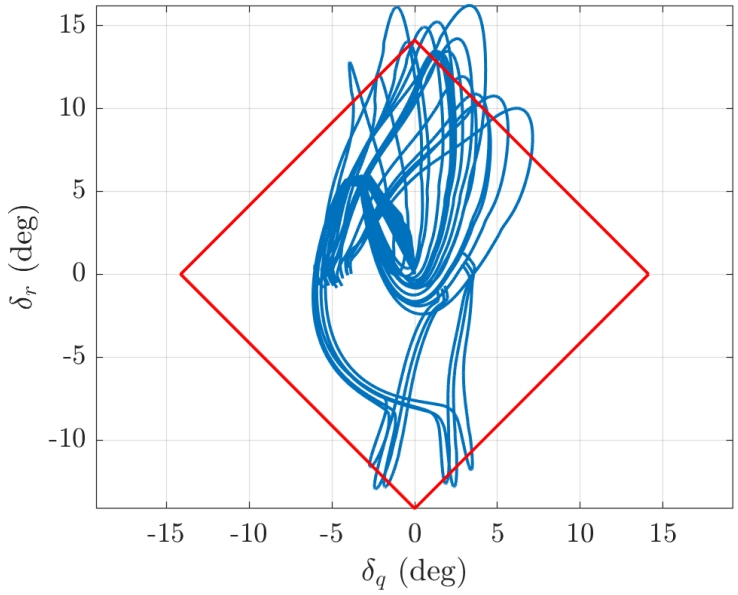

Figure 5.12: Trajectory of the virtual control signals in the (δ_q, δ_r)-plane for the 24 launch uncertainty samples leading to deflection angles greater than $l = 10\,\text{deg}$

are shown in Figures 5.14 and 5.15. Regarding the tracking of the guidance signals, similar observations as with the wind disturbance scenario can be made, except that the tracking error with static DLAW happens on n_z rather than n_y. Once again, the full MRAW produces results that are almost identical to those obtained with reduced MRAW.

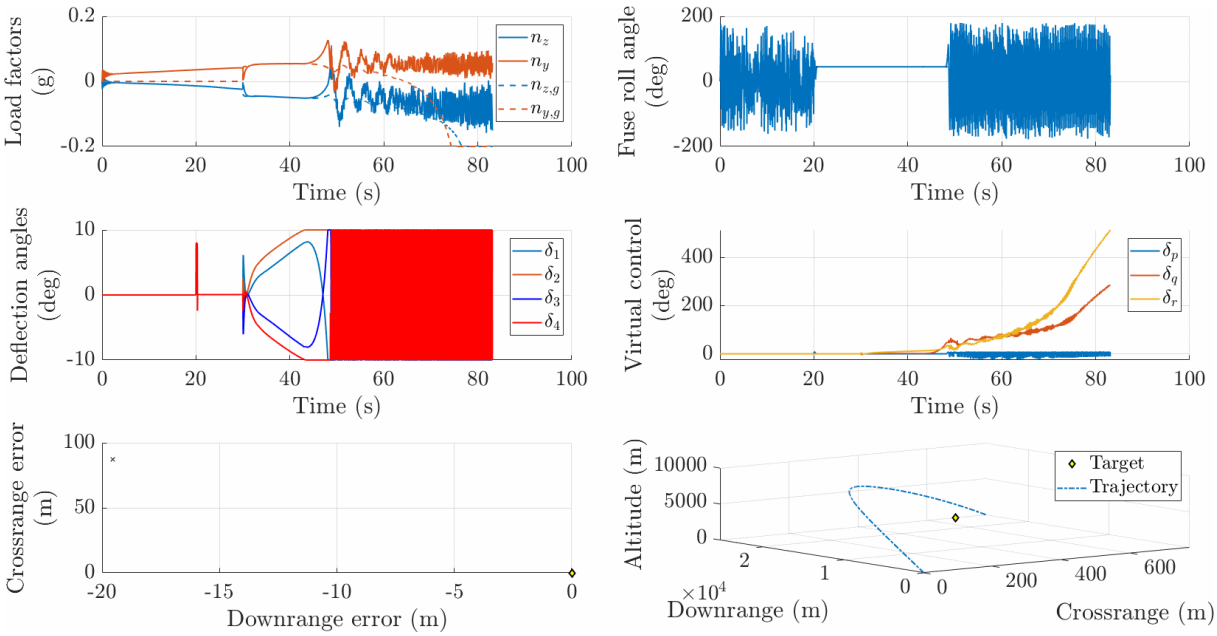

Figure 5.13: Scenario with launch uncertainties and saturations: load factors, fuse roll angle, canard deflection angles, virtual control signals, miss distance, trajectory

The left plot of Figure 5.16 shows the miss distance corresponding to the 24 identified samples leading to saturations, for different projectile configurations: ballistic, with the baseline autopilot only (i.e. with no anti-windup), and with the three scheduled anti-windup compensators (static DLAW, MRAW, and reduced MRAW). The samples are sorted by increasing order of the miss

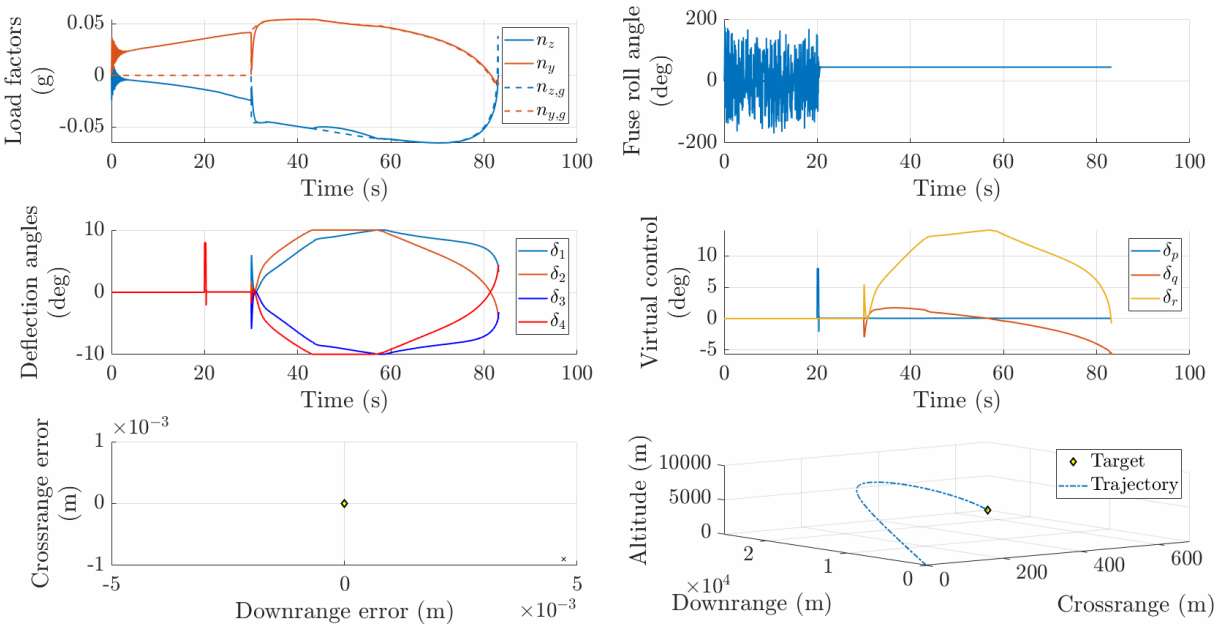

Figure 5.14: Scenario with launch uncertainties and scheduled static DLAW: load factors, fuse roll angle, canard deflection angles, virtual control signals, miss distance, trajectory

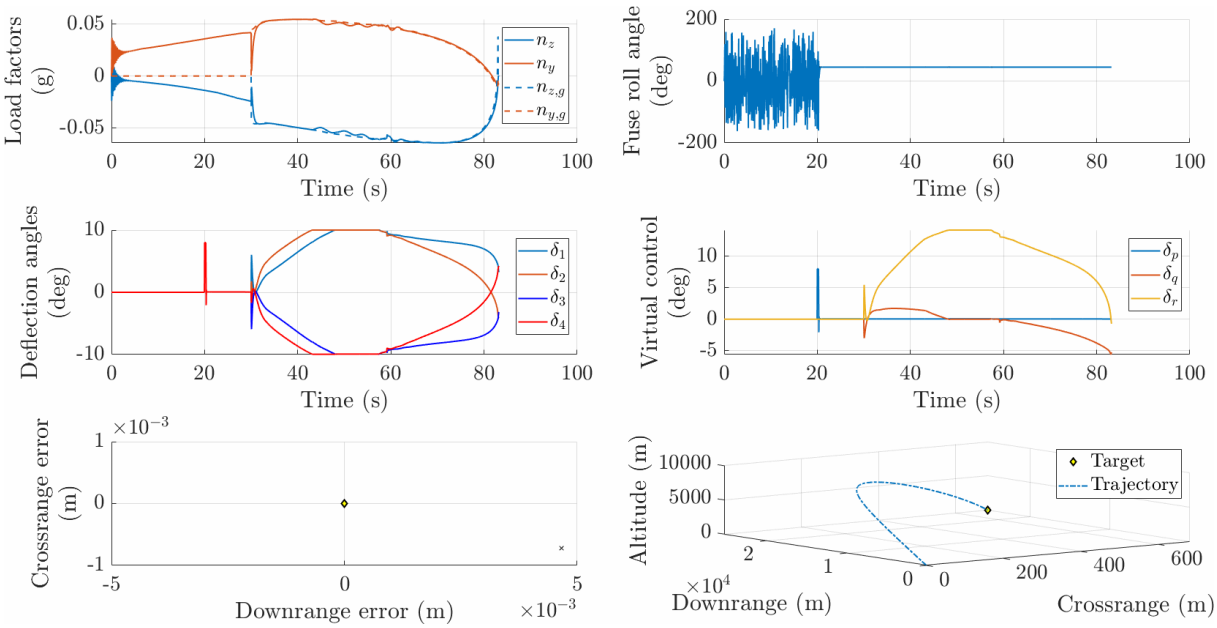

Figure 5.15: Scenario with launch uncertainties and scheduled reduced MRAW: load factors, fuse roll angle, canard deflection angles, virtual control signals, miss distance, trajectory

distance for the baseline configuration. The right plot shows the global failure rate as a function of the maximum tolerated miss distance, which may vary with the mission. Some values are reported in Table 5.2, where no distinction between the different anti-windup compensators is made since the results are very similar. Overall, it can be observed that saturations in the baseline configuration do not systematically lead to a loss of accuracy. However, in other cases, the miss distance is increased, and may exceed 100 m. With anti-windup compensators, all but two cases lead to a centimetric accuracy, but these two cases have noticeably reduced miss distances, at 15 m and 10 m respectively. Based on these 24 samples, the reduced MRAW is associated to the smallest mean and dispersion, although the difference is negligible and may not denote a genuine trend, as it hinges almost solely on Sample #23.

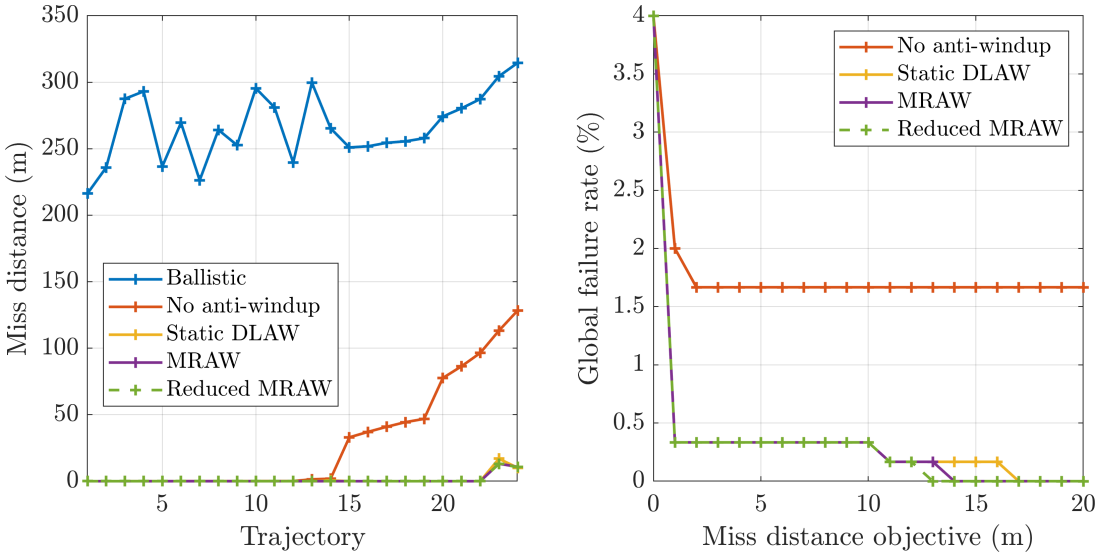

Figure 5.16: Miss distance for the 24 launch uncertainty samples leading to saturations (left), and global failure rate as a function of the maximum tolerated miss distance (right)

Objective	No AW	With AW
< 1 m	2%	0.3%
< 10 m	1.7%	0.3%
< 20 m	1.7%	0%

Table 5.2: Global failure rate for maximum tolerated miss distance of 1, 10, and 20 m with uncertainties on launch conditions

5.3.4 Monte Carlo simulations with uncertainties on the aerodynamic coefficients

The robustness of the nonlinear closed-loop to aerodynamic uncertainties is studied next. To this end, 300 Monte Carlo simulations are performed. The sampling of the aerodynamic coefficients is done assuming a normal distribution, where the standard deviation σ is such that 3σ corresponds to maximum uncertainty as reported in Table 2.2. For simplicity, the sampled uncertainty level is kept constant over the entire flight trajectory, although this may be pessimistic. Note that the aerodynamic uncertainties also impact the ZEM guidance, since the associated

IPP method relies on nominal values of the aerodynamic coefficients. Nonetheless, the terminal accuracy of the guided projectile without saturations remains of the order of the millimetre for all 300 simulations, demonstrating the robustness of the baseline autopilot. However, 47 trajectories (15.7%) feature deflection angles exceeding $l = 10\,\text{deg}$. The simulation results corresponding to these 47 scenarios are shown in Figure 5.17, and feature an overall maximum deflection angle of 24 deg. The trajectories of the virtual control signals for these samples are shown in Figure 5.18, where it is clear that aerodynamic uncertainties have more impact on the commanded deflection angles compared to launch uncertainties.

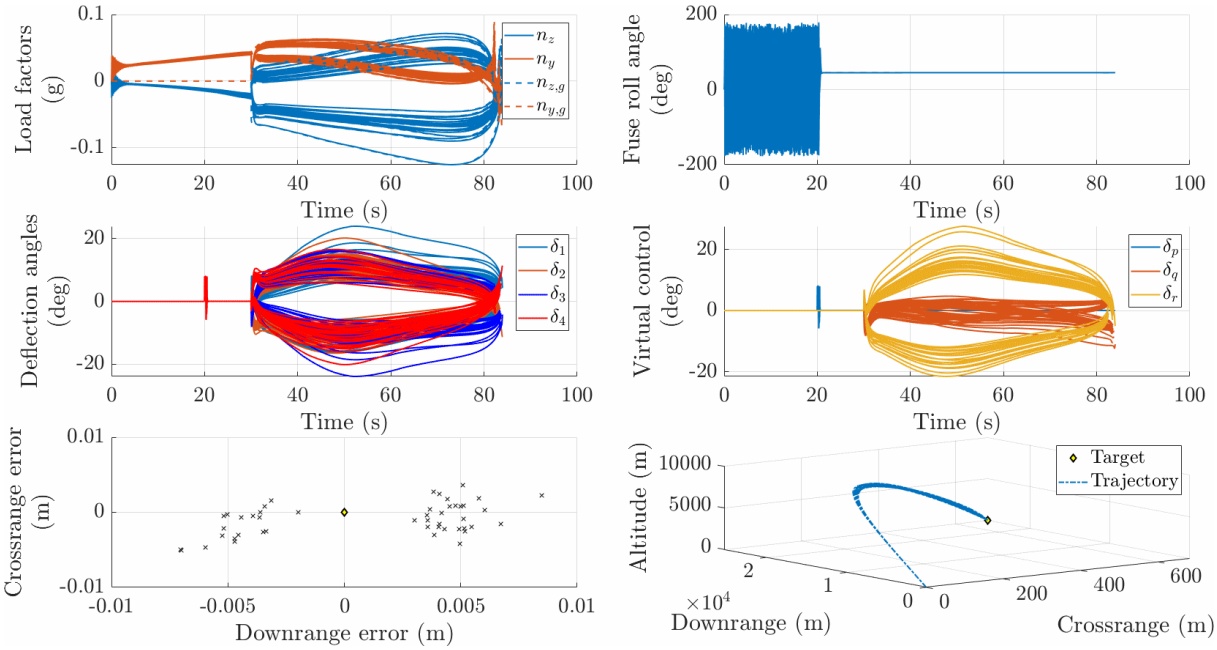

Figure 5.17: Scenarios with aerodynamic uncertainties and deactivated saturations: load factors, fuse roll angle, canard deflection angles, virtual control signals, miss distance, trajectory

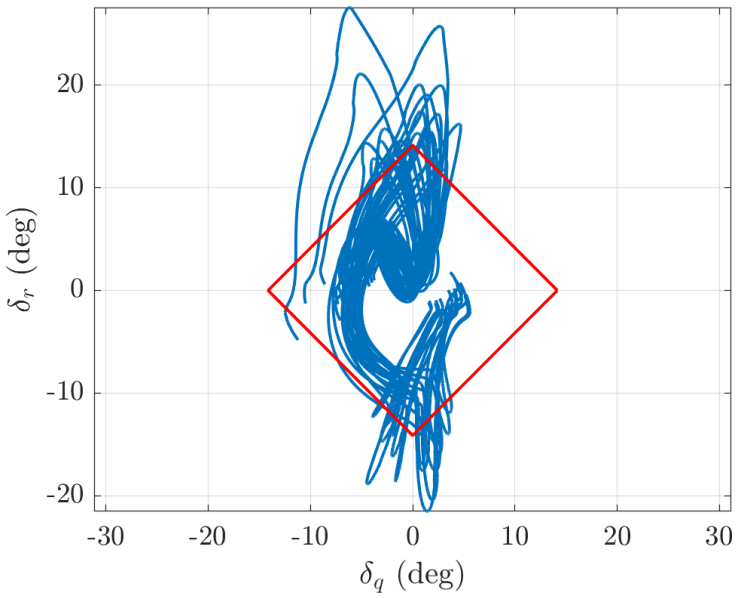

Figure 5.18: Trajectory of the virtual control signals in the (δ_q, δ_r)-plane for the 47 aerodyanmic uncertainty samples leading to deflection angles greater than $l = 10\,\text{deg}$

The miss distances for the 47 identified samples are shown in the left plot of Figure 5.19 for the different projectile configurations. The right plot of the same figure shows the global failure rate as a function of the maximum tolerated miss distance, with Table 5.3 providing some values. Performance degradations with aerodynamic uncertainties on the baseline design are noticeably more severe compared to those stemming from launch uncertainties, with a noticeable loss of accuracy for almost all scenarios. The anti-windup compensators are able to mitigate this loss, recovering a centimetric accuracy for almost half o the cases, although high miss distances are still reached in in the remaining ones. In addition, Figure 5.20 shows the miss distance difference between DLAW and reduced MRAW compensation for the 47 samples. Samples associated to positive values then correspond to cases where MRAW compensation leads to a lower miss distance compared to DLAW compensation. Thus, the reduced MRAW seems to be slightly better in general at reducing the impact point dispersion, although this does not hold for every sample. Notably, Sample #47, associated to the greatest miss distance, performs worse with MRAW than with DLAW.

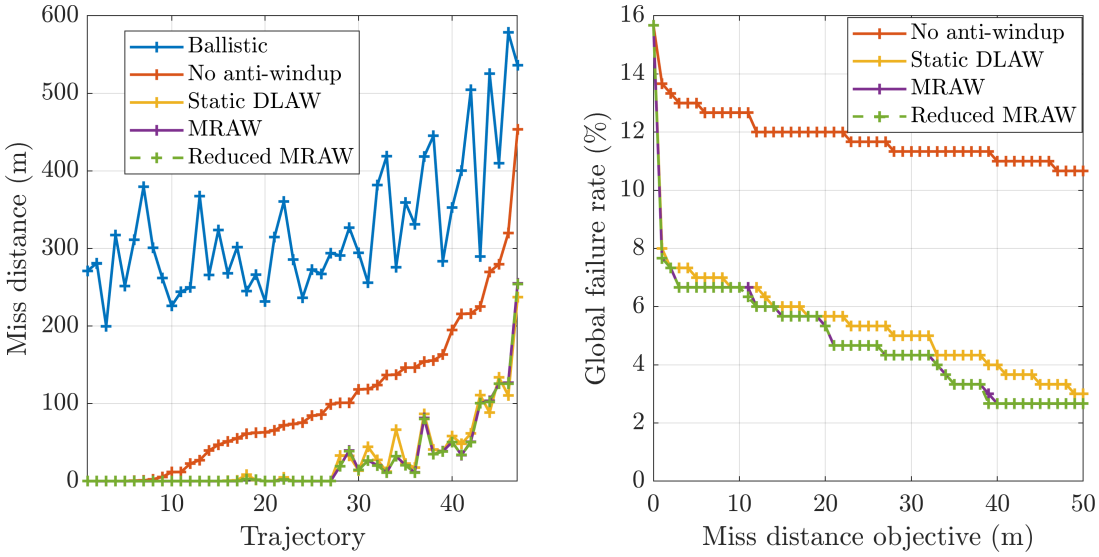

Figure 5.19: Miss distance for the 47 aerodynamic uncertainty samples leading to saturations (left), and global failure rate as a function of the maximum tolerated miss distance (right)

Objective	No AW	DLAW	MRAW
< 1 m	13.7%	8%	7.7%
< 10 m	12.7%	6.7%	6.7%
< 20 m	12%	5.7%	5.3%
< 50 m	10.7%	3%	2.7%

Table 5.3: Global failure rate for maximum tolerated miss distances set to 1, 10, 20, and 50 m with aerodynamic uncertainties

5.4 Conclusion

In this chapter, the 7DoF projectile model developed in Chapter 2 is put in closed-loop with the gain scheduled baseline autopilot and anti-windup compensators designed in Chapter 3 and

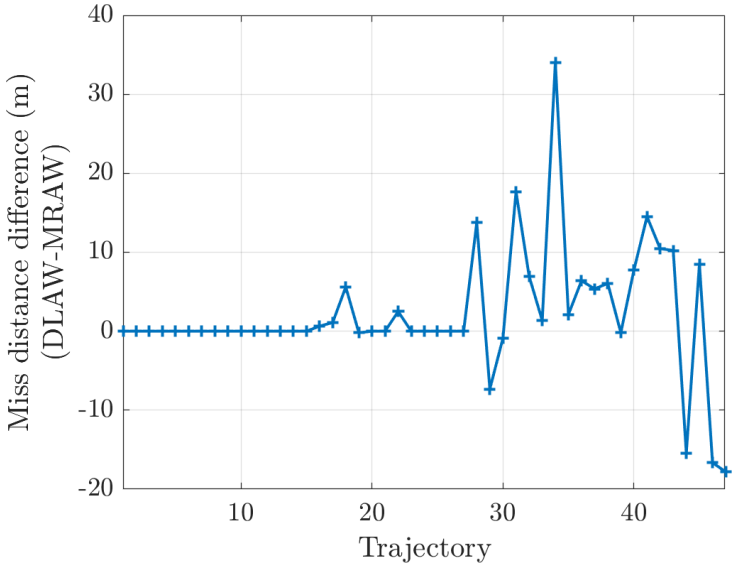

Figure 5.20: Miss distance difference between DLAW and MRAW

Chapter 4 respectively. The GNC loop is completed with a ZEM guidance law tailored for the application. Representative flight scenarios, including nominal and degraded cases, are then simulated to evaluate the performance of the baseline autopilot and anti-windup schemes through the terminal miss distance to a ballistic target. Results show that the baseline autopilot together with the ZEM guidance law ensure high terminal accuracy in nominal flight conditions, and is also able to cope with wind disturbance, perturbed law conditions, and aerodynamic uncertainties when saturations are deactivated in the flight simulator. However, several of these flight scenarios require deflection angles exceeding the saturation level, and significant degradations leading to high miss distances and mission failure are obtained when saturations are taken into account in the simulations, confirming the need for anti-windup compensation. The developed anti-windup compensators allow to recover high performance in most cases, and significantly reduce the impact point dispersion in the remaining scenarios. The scheduled MRAW and reduced MRAW produce nearly identical results, and perform slightly better than the scheduled static DLAW based on Monte Carlo simulation results, although the differences may not be significant. Overall, the results demonstrate the relevance of anti-windup compensation for the studied application, as well as the effectiveness of the proposed compensators in improving the manoeuvrability of the system.

References

Fresconi, F., Cooper, G., and Costello, M. (2011). “Practical assessment of real-time impact point estimators for smart weapons”. In: *Journal of Aerospace Engineering* 24.1, pp. 1–11.

Gagnon, E. and Vachon, A. (2016). “Efficiency analysis of canards-based course correction fuze for a 155-mm spin-stabilized projectile”. In: *Journal of Aerospace Engineering* 29.6, p. 04016055.

Proff, M. and Theodoulis, S. (2019). “Study of impact point prediction methods for zero-effort-miss guidance: application to a 155mm spin-stabilized guided projectile”. In: *5th CEAS Conference on Guidance, Navigation and Control*.

Sève, F., Theodoulis, S., Wernert, P., Zasadzinski, M., and Boutayeb, M. (2017). "Gain-scheduled H_∞ loop-shaping autopilot design for spin-stabilized canard-guided projectiles". In: *Aerospace-Lab Journal* Issue 13, December 2017, ISSN: 2107–6596.

Zarchan, P. (2012). *Tactical and strategic missile guidance*. American Institute of Aeronautics and Astronautics, Inc.

Zipfel, P. H. (2007). *Modeling and Simulation of Aerospace Vehicle Dynamics*. Second. American Institute of Aeronautics and Astronautics.

Chapter 6

Conclusion

Contents

6.1 Summary of the contributions

The objective of this thesis is to set up a generic methodology for the control design of a parameter-varying aerospace system subject to model uncertainties and actuator saturations. A novel guided dual-spin projectile concept serves as the central application to evaluate and validate the proposed process.

As a preliminary step to the study, Chapter 2 describes the 7DoF model stemming from Newton and Euler's laws of motions, which are then decomposed into the roll and pitch/yaw channels. These are subsequently linearised and written as parametrised LFRs to include model uncertainties, enabling the use of methods from robust control theory.

The general control design strategy relies on the standard two-step procedure when dealing with systems subject to actuator saturations. Namely, synthesis of a baseline autopilot based on the unconstrained system is tackled first, followed by anti-windup synthesis for saturation handling. The first step, which is the focus of Chapter 3, combines gain scheduling, robust $\mathcal{H}_\infty$ control theory, and μ-analysis. Notably, major theoretical contributions to probabilistic μ-analysis have been presented, leading to the development of enhanced branch-and-bound algorithms for stability, $\mathcal{H}_\infty$ performance, and gain, phase, and modulus margins. These methods offer a way to quantify and reduce the conservatism of standard (worst-case) μ-analysis, and, unlike Monte Carlo methods, provide hard upper and lower bounds on the evaluated probabilities.

Regarding the guided projectile application, the contributions lie in the streamlined procedure for baseline autopilot synthesis. Simple structures are used for both the roll and the pitch/yaw autopilots. Despite the parameter-varying nature of the roll channel, a study of the variations of the state-space coefficients allows to consider a single design point for controller synthesis. A scaling coefficient is then applied to cover the whole flight envelope. For the pitch/yaw autopilot, local syntheses are performed on a grid of the flight envelope. The introduction of a scaling factor based on the static gain of the pitch/yaw airframe model limits the tedious task of tuning

the weighting functions. The local robustness and performance properties of both channels are independently validated using probabilistic μ-analysis and time-domain simulations, and the scheduling strategy is also validated via an LTV simulation.

Application of anti-windup compensation in the field of guided projectiles constitutes another contribution of the thesis, and is studied in Chapter 4. While a wide array of methods are available to compute anti-windup compensators in a time-invariant framework, the theoretical guarantees regarding stability domains and performance levels are not preserved in a parameter-dependent context with ad hoc gain scheduling. Moreover, several of these methods require some assumptions on the plant that are not verified on all points of the flight envelope, or some tuning (e.g. pole selection) that is not easily parametrised. Following these considerations, three computationally simple methods requiring little or no tuning are used for the synthesis of local anti-windup compensators for the pitch/yaw channels. The first one is a static DLAW synthesis method. The second and third ones use the LQ-based MRAW method, with the former exploiting the full plant mode, and the latter using only the airframe dynamics, significantly lowering the order of the compensator.

Evaluation of the step responses on a couple of realistic flight points shows that all three anti-windup designs are able to cope with saturations. Notably, the MRAW and reduced MRAW produce virtually identical results, demonstrating the relevance of the reduced approach. The study is completed with local robustness analyses using IQCs, taking into account both deadzone nonlinearities and aerodynamic uncertainties. Despite the conservatism of the resulting performance test, some interesting trends are nevertheless identified. As expected, the obtained bounds on the $\mathcal{L}_2$-gains suggest improved robust stability properties with all three anti-windup compensators compared to the baseline configuration. The static DLAW seems more sensitive to aerodynamic uncertainties, as increasing the bounds on the parametric uncertainties in the analysis tends to make the stability test fail. Both MRAW configurations are comparatively more robust, with the full MRAW design featuring the largest guaranteed stability domain. Smaller guaranteed stability domains are obtained with the reduced MRAW, which however displays similar robust performance properties to the full MRAW on these domains.

Chapter 5 implements the designed autopilots in a complete nonlinear flight simulation environment, allowing to evaluate various closed-loop configurations through realistic flight scenarios. Simulation results demonstrate the high accuracy and robustness of the baseline autopilot when saturations are ignored, thus validating the baseline design step. However, severe degradations are observed when saturations are activated on non-nominal simulations involving wind disturbance, perturbed launch conditions, or aerodynamic uncertainties, illustrating the need for anti-windup compensation. The proposed anti-windup compensators allow for noticeably higher mission success rates, validating the chosen approach to anti-windup synthesis, and the overall control design methodology in a realistic context. With respect to the studied application, the current closed-loop flight simulator constitutes a benchmark with good performance and robustness properties, and against which to compare future developments.

6.2 Discussion and perspectives

The proposed methodology for control design combines gain scheduling, robust $\mathcal{H}_\infty$ control theory, anti-windup synthesis, and μ/IQC-analysis techniques in a way that is meant to be cohesive, applicable to aerospace systems with large operational flight envelopes, and easily accessible to control engineers.

For the baseline and anti-windup synthesis steps, care has been taken to keep the tuning effort at a reasonably low level in order to streamline the process. Nonlinear closed-loop simulation results on the guided projectile application show that good performance and robustness properties can be reached on operational flight scenarios, despite the simplicity of the anti-windup synthesis methods used. Whether these properties can be further improved with more sophisticated schemes remains to be investigated, although as already mentioned, parametrising these synthesis methods across the flight envelope comes with an additional tuning effort.

A natural follow-up to the current work would be to bring the flight simulator even closer to the physical system, by integrating a realistic navigation system, sensor noise, computational delays, and by implementing digital autopilots. The increased complexity of the system may demand further design iterations, and possibly some fine-tuning to achieve satisfactory local performance and robustness properties. To help with this task in the baseline synthesis step, methods for design point selection strategies could be implemented instead of relying on an equidistant grid, for instance by partitioning the flight envelope into clusters based on the (ν-)gap metric. This has the potential to reduce the duration of baseline design iterations. Another interesting addition to our methodology would be to integrate codesign methods, to simultaneously size the canards and actuator parameters and compute the baseline controller.

In this work, μ-analysis is applied in the time-invariant framework, providing only information on the local robustness of the uncertain closed-loop system. Thus, the contributions to probabilistic μ-analysis more directly pertain to the validation of uncertain LTI systems, on which they greatly complement Monte Carlo methods. From a theoretical point of view, extensions to time-varying parameters could be envisioned to allow more rigorous robustness analysis along a trajectory of the scheduling variables. In line with controller discretisation, extensions to hybrid systems arer also of great interest. As it is, the current developments still provide a useful and computationally affordable, albeit heuristic metric in an ad hoc gain scheduling context, and can be used for instance to compare different designs prior to time-varying simulations.

IQC analysis shares a similar status, allowing to compare anti-windup strategies. However, the analysis is computationally more expensive and cannot be reasonably applied on a dense grid of the flight envelope. In addition, results are not as easily exploited, and do not clearly correlate to the robustness observed on nonlinear closed-loop simulations. This is mainly because the conservatism of IQC analysis results remains difficult to quantify. An interesting lead to decrease the conservatism could be to consider more representative profiles of the exogenous input signals, in order to obtain a more relevant performance index than the rather conservative $\mathcal{L}_2$-gain.

All the above perspectives represent possible improvements and extensions building up on the methodology proposed in this thesis. In another direction, a very general point of interest would be to investigate altogether alternative control design methods, e.g. pure LPV or nonlinear designs, or reference governors, with the current closed-loop flight simulator serving as a basis

for comparisons.

Appendix A

Résumé de la thèse en français

Cette partie en français constitue une synthèse des travaux, structurée selon le même plan que la partie en anglais.

A.1 Introduction générale

A.1.1 Contexte de la thèse

Dans le secteur aérospatial, la conception de contrôleurs pour des systèmes évoluant sur un domaine de vol étendu constitue un défi majeur. Les difficultés liées à cette tâche proviennent de plusieurs facteurs. Tout d'abord, la plupart des systèmes aérospatiaux, tels que les avions, les missiles ou les lanceurs spatiaux, présentent une dynamique non linéaire dépendant de paramètres. En conséquence, la conception du contrôleur doit prendre en compte les variations de ces paramètres afin d'obtenir des résultats en boucle fermée satisfaisants sur l'ensemble des conditions opérationnelles. Une autre source fréquente de non-linéarité est la saturation des actionneurs. Cette contrainte sur les signaux de commande peut provenir aussi bien de limitations mécaniques que de considérations sur la validité du modèle aérodynamique. Si elles ne sont pas prises en compte, les saturations peuvent entraîner une perte de performance importante, voire une instabilité du système. Enfin, la plupart des méthodes de conception des contrôleurs reposent sur un modèle du système à contrôler. Les écarts entre le système physique réel et son modèle mathématique étant inévitables, il est nécessaire d'évaluer la robustesse aux incertitudes de modélisation et aux dynamiques négligées.

L'ingénieur automaticien est de plus confronté aux tendances industrielles, qui impliquent des applications de plus en plus complexes, soumises à des exigences strictes et des contraintes de coûts importantes. Un long processus itératif, incluant de nombreuses simulations, est alors engagé pour converger vers un réglage de contrôleur satisfaisant toutes les contraintes. Cette étape peut cependant être rendue plus efficace, par le développement et le recours à des algorithmes et des outils avancés, adaptés aux non-linéarités et aux incertitudes mentionnées plus tôt.

A.1.2 Sur la prise en compte de la variation des paramètres

Une méthode bien connue pour concevoir des autopilotes prenant en compte les paramètres variants est le séquencement de gain [Leith and Leithead, 2000; Rugh and Shamma, 2000]. Dans

sa forme la plus classique, on commence par linéariser le système autour de ses points d'équilibre. Les systèmes linéaires obtenus sont alors exploités pour calculer des contrôleurs linéaires. Enfin, ces contrôleurs sont interpolés afin de couvrir tout le domaine opérationnel. Le séquencement de gain présente l'avantage d'être conceptuellement simple, et compatible avec les méthodes de synthèse des contrôleurs linéaires. Cela inclut les méthodes plus avancées, telles que la synthèse $\mathcal{H}_\infty$ structurée basée sur l'optimisation non-lisse [Apkarian and Noll, 2006]. En revanche, le séquencement de gain est souvent lacunaire quant aux garanties théoriques de stabilité et de performance entre les points de synthèse.

En réponse à ces lacunes, et suite à l'introduction du concept de système LPV (*Linear Parameter-Varying*) par [Shamma and Athans, 1991], les techniques de synthèse LPV ont vu le jour. Le point de départ à l'application de ces méthodes est soit une modélisation polytopique [Apkarian et al., 1995], soit une modélisation LFT (*Linear Fractional Transformation*) du système LPV. Dans le premier cas, des fonctions de Lyapunov quadratiques sont utilisées pour déterminer des conditions suffisantes de stabilité ou performance du système. Dans le cas de la modélisation LFT, les conditions suffisantes sont issues de l'application du théorème du faible gain, dont le conservatisme peut être réduit grâce à l'introduction de matrices de *scaling*. Dans les deux cas, on est amené à résoudre un problème d'inégalité matricielle linéaire, ou problème LMI (*Linear Matrix Inequality*), pour lequel il existe des solveurs performants. En utilisant des fonctions de Lyapunov dépendant des paramètres, il est également possible de prendre en compte des bornes sur la vitesse de variation paramétrique [Wu, 2001; Wu and Dong, 2006]. Les méthodes LPV ont été mises en œuvre sur un grand nombre d'applications [Hoffmann and Werner, 2014], et la boîte à outils LPVTools [Hjartarson et al., 2015] leur est dédiée, attestant de leur maturité grandissante. Néanmoins, bien que ces méthodes soient capables de garantir la stabilité et la performance globale, l'étape préliminaire de modélisation peut s'avérer complexe, et les résultats conservatifs. Dans les cas où un modèle LPV ne peut être obtenu, il est possible de se placer dans le cadre plus général des systèmes quasi-LPV, au prix de difficultés supplémentaires comme l'apparition des termes de couplage cachés.

A.1.3 Sur la prise en compte des saturations des actionneurs

Les saturations sont présentes dans tous les systèmes physiques, et peuvent être à l'origine de pertes de performance importantes. Pour éviter ce scénario, une première stratégie consiste à concevoir des contrôleurs n'atteignant pas les valeurs saturantes, quitte à se satisfaire de performances amoindries. Une autre stratégie est de permettre l'occurrence de saturations, tout en mettant en place un dispositif limitant leurs effets néfastes. Cette seconde approche est le plus souvent réalisée en deux étapes. La première est la conception, sans prise en compte des saturations, d'un contrôleur linéaire, que nous appellerons contrôleur baseline. Dans un second temps, un élément de contrôle supplémentaire, appelé compensateur anti-windup, est ajouté à la boucle fermée. Celui-ci ne s'active que lorsque les saturations sont atteintes. De fait, la performance nominale est préservée pour tout scénario où les saturations n'apparaissent pas.

Les premiers travaux sur les systèmes saturés et les méthodes de compensation anti-windup se focalisent sur les contrôleurs de type PID [Lozier, 1956; Åström and Rundqwist, 1989]. Le sujet prend de l'importance suite aux travaux de [Kothare et al., 1994], qui présentent un cadre unifié

pour traiter le problème, inspiré de la forme standard utilisée dans la théorie de la commande robuste. La théorie anti-windup moderne, telle que décrite par exemple par [Galeani et al., 2009; Tarbouriech et al., 2011; Zaccarian and Teel, 2011], identifie deux familles de méthodes pour la synthèse anti-windup : l'approche DLAW (*Direct Linear Anti-Windup*) et l'approche MRAW (*Model Recovery Anti-Windup*). L'approche DLAW exploite la théorie de la stabilité de Lyapunov ainsi que la condition de secteur modifiée [Gomes da Silva and Tarbouriech, 2005] pour formuler le problème de synthèse anti-windup comme un problème de résolution d'une inégalité matricielle bilinéaire. Des hypothèses supplémentaires sur les dynamiques du compensateur anti-windup permettent de se ramener à un problème convexe, dont la résolution fournit la représentation d'état du compensateur. L'approche MRAW embarque au sein du compensateur un modèle du système à contrôler, ce qui permet un suivi de l'écart à la dynamique sans saturation. Le signal en sortie du compensateur anti-windup est alors généré de sorte à réduire cet écart, afin de se rapprocher de la réponse sans saturation.

A.1.4 Sur la prise en compte des incertitudes

L'analyse de robustesse est une étape nécessaire pour s'assurer du bon comportement du système dans un voisinage suffisamment grand autour de la configuration nominale. Dans l'industrie, l'approche classique consiste à employer des méthodes de Monte Carlo [Helton et al., 2006; Landau and Binder, 2014]. L'idée est de réaliser des simulations temporelles pour un grand nombre de configurations aléatoires du système, et d'évaluer la robustesse avec une analyse statistique des résultats. Si cette approche est relativement simple à implémenter, elle présente des inconvénients majeurs. Du fait de la nature aléatoire des tirages, l'identification de configurations pire cas n'est pas garantie, et seules des bornes probables sur la performance sont obtenues. De plus, un nombre élevé de tirages est nécessaire pour assurer un niveau de précision et de confiance suffisant en l'analyse statistique. L'étape de validation est alors coûteuse, du fait des ressources informatiques nécessaires à chaque simulation temporelle.

Les méthodes déterministes visent quant à elles à garantir la détection des pires cas. Concernant les systèmes linéaires stationnaires, ou systèmes LTI (*Linear Time Invariant*, la robustesse aux incertitudes peut être quantifiée grâce à la valeur singulière structurée μ, objet mathématique introduit par [Doyle, 1982]. La μ-analyse s'avère polyvalente ; au-delà de la stabilité robuste, elle permet d'évaluer la performance $\mathcal{H}_\infty$ ou les marges pire cas [Fan and Tits, 1992; Lescher and Roos, 2011]. Bien que le calcul de la valeur singulière structurée soit un problème NP-difficile [Braatz et al., 1994], de nombreux travaux ont permis de développer des algorithmes de calcul efficaces, capables de donner un encadrement très fin de cette valeur [Roos and Biannic, 2015; Lesprier et al., 2015], de sorte que la μ-analyse est considérée comme une approche mature par les chercheurs en automatique. Cependant, la méthode souffre de quelques lacunes qui font obstacle à son adoption dans l'industrie. En particulier, aucune mesure de la probabilité d'occurrence des configurations pire cas n'est évaluée. Le risque est alors de conclure à la non-robustesse du contrôleur sur la base de scénarios irréalistes ou excessivement pessimistes.

En présence de non-linéarités, telles que les saturations, une analyse de robustesse peut être menée en utilisant l'analyse par contraintes intégrales quadratiques, ou analyse IQC (*Integral Quadratic Constraints*). Cette approche, introduite par [Megretski and Rantzer, 1997], consiste à

rechercher un multiplicateur décrivant les non-linéarités et les incertitudes, et vérifiant une infinité d'inégalités dans le domaine fréquentiel. L'application du lemme de Kalman-Yakubovich-Popov (KYP) permet de remplacer l'infinité d'inégalités fréquentielles par une unique LMI. L'intérêt de l'analyse IQC est qu'il est possible de traiter de nombreux types d'incertitudes et de non-linéarités [Veenman et al., 2016; Fetzer and Scherer, 2017]. En revanche, le conservatisme et les difficultés sur le plan numérique sont les problèmes récurrents de cette approche.

A.1.5 Aperçu des contributions

Des paragraphes précédents, il apparaît clairement que chacun des sujets mentionnés a donné lieu à son propre axe de recherche. Cependant, l'ingénieur automaticien doit faire face à ces problèmes simultanément. Les méthodes associées doivent donc être mises ensemble de manière réfléchie pour être exploitées efficacement dans le processus de conception du contrôleur.

Les travaux de thèse s'inscrivent dans ce contexte. L'objectif est de mettre en place une méthodologie pour la conception de lois de contrôle pour des systèmes incertains à paramètres variants, et avec saturation des actionneurs. En guise d'illustration, on considèrera une application aéronautique concrète, à savoir un concept novateur de projectile guidé en configuration *dual-spin*.

Il convient de souligner que l'automatique appliquée aux projectiles guidés est un thème peu abordé dans la littérature. De nombreuses méthodes ad hoc, basées sur du suivi de trajectoire ou de la prédiction de point d'impact [Fresconi, 2011], ont été étudiées pour plusieurs types de mécanismes de guidage, mais ces approches ne permettent pas un traitement satisfaisant des incertitudes aérodynamiques. Concernant la configuration dual-spin, le premier modèle non-linéaire est publié par [Costello and Peterson, 2000] pour un projectile non guidé, et des premiers résultats de contrôle utilisant du suivi de trajectoire sont présentés par [Gagnon and Lauzon, 2007; Gagnon and Lauzon, 2008]. Les études récentes réalisées par l'ISL [Theodoulis et al., 2015; Sève et al., 2017; Sève et al., 2017] développent un algorithme de linéarisation spécifique aux projectiles dual-spin, ainsi que des autopilotes séquencés performant pour deux plans canard, obtenus par synthèses $\mathcal{H}_\infty$ locales. Les travaux de thèse présentés ici s'intéressent à une configuration alternative, où les trois axes du projectile sont contrôlés de manière aérodynamique par quatre canards indépendants, et prolongent les travaux existants sur plusieurs aspects :

- La méthodologie de séquencement de gain est revisitée afin de faciliter le réglage des gains du contrôleur.
- Des contributions théoriques à la μ-analyse probabiliste sont proposées ; elles permettent une analyse de robustesse locale plus approfondie que la μ-analyse classique, et plus pertinente dans un contexte industriel.
- La saturation des actionneurs des canards est prise en compte pour la première fois à travers le développement de compensateurs anti-windup ; la robustesse aux incertitudes aérodynamiques est évaluée grâce aux méthodes d'analyse par IQC, et à des simulations.

A.1.6 Organisation du manuscrit

Le manuscrit de thèse est organisé comme suit :

- Le Chapitre 2 a pour objectif de mettre en place le modèle du projectile en boucle ouverte qui sera utilisé pour la synthèse de contrôleurs. Le point de départ est le développement d'un modèle non-linéaire à partir des équations de la mécanique du vol. Ce modèle est ensuite linéarisé, donnant lieu à un système LPV pour la dynamique de roulis, et à un système quasi-LPV pour les axes de tangage/lacet. Ces modèles linéarisés sont ensuite complétés avec les modèles des actionneurs et des capteurs.

- Les modèles obtenus sont exploités dans le Chapitre 3 pour concevoir l'autopilote baseline, qui ne prend pas en compte les saturations. Des contrôleurs locaux sont calculés par synthèse $\mathcal{H}_\infty$ structurée en utilisant une approche par sensibilité mixte. On évalue ensuite plusieurs critères de robustesse aux points de design. En particulier, une extension probabiliste à la μ-analyse est utilisée pour évaluer la performance $\mathcal{H}_\infty$ et les marges en présence des incertitudes aérodynamiques. Cette approche permet une réduction du conservatisme par rapport à la μ-analyse classique, et présente une meilleure synergie avec les méthodes de Monte Carlo. La synthèse de l'autopilote de roulis est l'objet de [Thai et al., 2019b], tandis que les premières contributions à la μ-analyse probabiliste ont été présentées dans [Thai et al., 2019a].

- Le Chapitre 4 traite de la synthèse anti-windup. Trois méthodes issues de la théorie anti-windup moderne sont appliquées pour obtenir des compensateurs locaux. Les boucles fermées sont ensuite évaluées et comparées à l'aide de simulations temporelles et de l'analyse IQC. Ces contributions ont été présentées dans [Thai et al., 2020] et [Thai et al., 2021].

- Dans le Chapitre 5, des scénarios de tir complets sont simulés pour évaluer les autopilotes proposés dans un contexte opérationnel. Ces scénarios incluent des cas dégradés par la présence de vent, des perturbations sur les conditions initiales de tir, ou par les incertitudes aérodynamiques. Dans un premier temps, des simulations sans saturations sont menées afin de valider l'autopilote baseline et d'identifier les cas où les seuils de saturation sont dépassés. Ces scénarios sont ensuite rejoués avec les différents compensateurs anti-windup afin d'en évaluer l'efficacité.

Les sections qui suivent résument les chapitres de la thèse, en mettant l'accent sur les contributions.

A.2 Modélisation d'un projectile guidé à 7 degrés de liberté

A.2.1 Introduction

Les projectiles balistiques classiques souffrent d'un manque de précision, dû à divers facteurs tels que des conditions de lancement incorrectes ou des perturbations dues au vent. Par conséquent, plusieurs projectiles peuvent être nécessaires pour atteindre une seule cible. Cela entraîne des risques de dommages collatéraux, ainsi que des coûts de déploiement élevés et une logistique complexe. Les projectiles guidés ont pour but de pallier ces limitations. Parmi les nombreux concepts de projectiles guidés, celui d'une fusée de correction de trajectoire (FCT), découplée du corps et équipée de canards, présente de nombreux avantages par rapport à d'autres mécanismes de guidage proposés dans la littérature. Contrairement aux propulseurs à impulsion ou aux

dispositifs inertiels, les surfaces aérodynamiques fournissent une correction qui peut être modélisée en temps continu comme des effets aérodynamiques. Par rapport aux projectiles stabilisés par des ailerons, la configuration dual-spin est compatible avec une action de rénovation de munitions existantes, réduisant considérablement les coûts de développement, et permet une plus grande portée en raison de l'absence de surfaces stabilisatrices [Theodoulis and Wernert, 2017]. Cette solution conduit à un projectile guidé à sept degrés de liberté (7DDL), dont la précision et les performances dépendent alors essentiellement du matériel embarqué et des algorithmes de contrôle de vol. Le développement de ces algorithmes repose quant à lui sur un modèle mathématique du système à contrôler. Ce modèle doit décrire de manière suffisamment précise le comportement du système, tout en étant compatible avec les méthodes de conception des lois de contrôle. Ainsi, la mise en place d'un modèle adapté aux techniques de séquencement de gain constitue l'objectif du Chapitre 2.

A.2.2 Synthèse des travaux

Présentation du concept de projectile guidé

Le concept de projectile guidé étudié dans cette thèse est un projectile dual-spin, dont la partie arrière, ou corps, est issue d'une munition standard de calibre 155 mm, et équipée à l'avant d'une fusée découplée en roulis. Le corps contient la charge explosive, tandis que la fusée est munie de quatre canards, comme le montre la Figure A.1. Les canards sont actionnés indépendamment à l'aide de servomoteurs. Le concept de FCT considéré ici diffère de [Sève et al., 2017], où un moteur coaxial dédié au contrôle du roulis est intégré à la fusée. Ici, les trois axes (roulis, tangage, et lacet) sont contrôlés aérodynamiquement à l'aide des canards.

Le scénario de vol du projectile peut être décomposé en plusieurs phases, représentées sur la Figure A.2. Lors de la phase balistique ($0 \leq t < t_{start} = 20$ s), les composants électroniques sont allumés. L'allumage se fait quelques secondes après le lancement afin d'éviter d'éventuelles dégradations matérielles dues aux conditions initiales particulièrement violentes. À $t = t_{start}$, les canards sont positionnés et maintenus à des angles de déflexion constants, afin de réduire la vitesse de rotation de la fusée p_f, qui est alors élevée à cause du frottement mécanique entre le corps et la fusée. Une fois la vitesse de rotation réduite à $p_f = 1800$ deg/s $= 10\pi$ rad/s, l'autopilote de roulis est activé pour stabiliser la fusée à un angle de roulis fixe ϕ_f. Enfin, le projectile entre dans sa phase guidée à $t_{guid} = 30$ s : les canards sont alors sollicités par l'autopilote de tangage/lacet pour produire des efforts supplémentaires sur ces axes, afin de modifier la trajectoire du projectile.

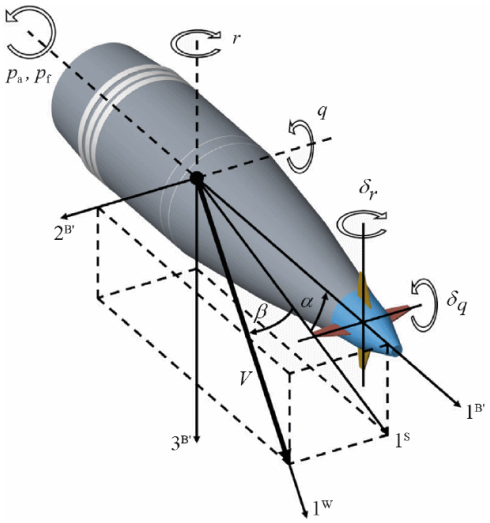

Figure A.1: Projectile de calibre 155 mm avec fusée de correction de trajectoire munie de canards

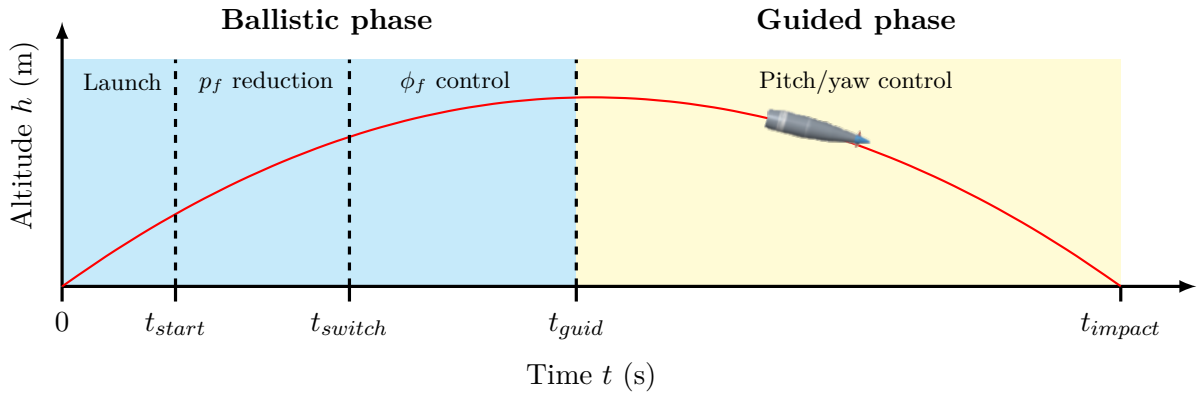

Figure A.2: Scénario de vol détaillé du projectile dual-spin

Modélisation non-linéaire issue des équations de la mécanique du vol

Le modèle à 7DDL est décrit par ses équations dynamiques en translation et en rotation. Elles s'écrivent dans un repère non tournant sous la forme :

$$\begin{bmatrix} \dot{u} \\ \dot{v} \\ \dot{w} \end{bmatrix} = \frac{1}{m} \begin{bmatrix} X \\ Y \\ Z \end{bmatrix} - \begin{bmatrix} 0 & -r & q \\ r & 0 & r\tan\theta \\ -q & -r\tan\theta & 0 \end{bmatrix} \begin{bmatrix} u \\ v \\ w \end{bmatrix} \tag{A.1}$$

$$\begin{bmatrix} \dot{p}_f \\ \dot{p}_a \\ \dot{q} \\ \dot{r} \end{bmatrix} = \begin{bmatrix} L_f/I_{xf} \\ L_a/I_{xa} \\ M/I_t \\ N/I_t \end{bmatrix} + \begin{bmatrix} 0 \\ 0 \\ -(I_{xa}{I_t}^{-1}p_a + r\tan\theta)r \\ (I_{xa}{I_t}^{-1}p_a + r\tan\theta)q \end{bmatrix} \tag{A.2}$$

avec $[u\ v\ w]^T$ les vitesses linéaires, et $[p_f\ p_a\ q\ r]^T$ les vitesses angulaires : les indices f et a correspondent respectivement aux parties avant (*forward*) et arrière (*aft*) du projectile. Les constantes qui apparaissent dans ces équations sont la masse m du projectile, et ses moments d'inertie I_{xf}, I_{xa}, et I_t. Ces équations sont complétées par les équations cinématiques, qui décrivent la position $[x_e\ y_e\ z_e]^T$ et l'attitude $[\phi_f\ \phi_a\ \theta\ \psi]^T$ du projectile par rapport au repère

terrestre supposé inertiel [Zipfel, 2007]:

$$\begin{bmatrix} \dot{x}_e \\ \dot{y}_e \\ \dot{z}_e \end{bmatrix} = \begin{bmatrix} \cos\psi\cos\theta & -\sin\psi & \cos\psi\sin\theta \\ \sin\psi\cos\theta & \cos\psi & \sin\psi\sin\theta \\ -\sin\theta & 0 & \cos\theta \end{bmatrix} \begin{bmatrix} u \\ v \\ w \end{bmatrix} \tag{A.3}$$

$$\begin{bmatrix} \dot{\phi}_f \\ \dot{\phi}_a \\ \dot{\theta} \\ \dot{\psi} \end{bmatrix} = \begin{bmatrix} 1 & 0 & 0 & \tan\theta \\ 0 & 1 & 0 & \tan\theta \\ 0 & 0 & 1 & 0 \\ 0 & 0 & 0 & 1/\cos\theta \end{bmatrix} \begin{bmatrix} p_f \\ p_a \\ q \\ r \end{bmatrix} \tag{A.4}$$

Étant donné la nature des efforts appliqués au projectile, il est commode d'introduire des variables d'état aérodynamiques, notamment pour exprimer les forces et moments extérieurs. En supposant l'absence de vent, on définit donc la vitesse propre V, l'angle d'attaque α, et l'angle de dérive β comme suit :

$$V = \sqrt{u^2+v^2+w^2}, \quad \alpha = \arctan\left(\frac{w}{u}\right), \quad \beta = \arctan\left(\frac{v}{\sqrt{u^2+w^2}}\right) \tag{A.5}$$

En dérivant ces variables, il est possible de réécrire l'équation (A.1) sous une forme plus adaptée au développement de lois de contrôle :

$$\begin{bmatrix} \dot{V} \\ \dot{\alpha} \\ \dot{\beta} \end{bmatrix} = \begin{bmatrix} 0 \\ q + r(\cos\alpha\tan\theta - \sin\alpha)\tan\beta \\ -r(\cos\alpha + \sin\alpha\tan\theta) \end{bmatrix} + \frac{1}{mV} \begin{bmatrix} V\cos\alpha\cos\beta & V\sin\beta & V\sin\alpha\cos\beta \\ -\sin\alpha/\cos\beta & 0 & \cos\alpha/\cos\beta \\ -\cos\alpha\sin\beta & \cos\beta & -\sin\alpha\sin\beta \end{bmatrix} \begin{bmatrix} X \\ Y \\ Z \end{bmatrix} \tag{A.6}$$

L'expression des forces $[X\ Y\ Z]^T$ et des moments $[L_f\ L_a\ M\ N]^T$ s'appuie sur la théorie de l'aérobalistique [McCoy, 1999]. Les forces extérieures prises en compte sont la traînée et la portance, la force de Magnus, les forces générées par les canards, et la gravité :

$$\begin{bmatrix} X \\ Y \\ Z \end{bmatrix} = \overline{q}S \left(\begin{bmatrix} -C_A(\mathcal{M},\alpha') \\ -C_{N\alpha}(\mathcal{M},\alpha')\beta \\ -C_{N\alpha}(\mathcal{M},\alpha')\alpha \end{bmatrix} + \frac{p_a d}{2V} \begin{bmatrix} 0 \\ C_{Yp\alpha}(\mathcal{M})\alpha \\ -C_{Yp\alpha}(\mathcal{M})\beta \end{bmatrix} + \begin{bmatrix} 0 \\ -C_{N\delta}(\mathcal{M})\delta_r \\ -C_{N\delta}(\mathcal{M})\delta_q \end{bmatrix} \right) + mg \begin{bmatrix} -\sin\theta \\ 0 \\ \cos\theta \end{bmatrix} \tag{A.7}$$

Les moments extérieurs comprennent les moments de tangage, le moment de Magnus, les moments d'amortissement, les moments générés par les canards, et des termes de frictions :

$$\begin{bmatrix} L_f \\ L_a \\ M \\ N \end{bmatrix} = \overline{q}Sd \left(\begin{bmatrix} 0 \\ 0 \\ C_{m\alpha}(\mathcal{M},\alpha')\alpha \\ -C_{m\alpha}(\mathcal{M},\alpha')\beta \end{bmatrix} + \frac{p_a d}{2V} \begin{bmatrix} 0 \\ 0 \\ C_{np\alpha}(\mathcal{M})\beta \\ C_{np\alpha}(\mathcal{M})\alpha \end{bmatrix} + \frac{d}{2V} \begin{bmatrix} 0 \\ C_{lp}(\mathcal{M})p_a \\ C_{mq}(\mathcal{M})q \\ C_{mq}(\mathcal{M})r \end{bmatrix} + \begin{bmatrix} 0 \\ -C_{l\delta}(\mathcal{M})\delta_p \\ C_{m\delta}(\mathcal{M})\delta_q \\ -C_{m\delta}(\mathcal{M})\delta_r \end{bmatrix} \right) + \begin{bmatrix} L_{f-a} \\ -L_{f-a} \\ 0 \\ 0 \end{bmatrix} \tag{A.8}$$

L'expression de ces efforts fait apparaître des coefficients aérodynamiques qui dépendent de

manière non-linéaire du nombre de Mach $\mathcal{M} = V/a(h)$, avec a la vitesse du son, fonction de l'altitude, et pour certains également de l'angle d'incidence totale α', défini par :

$$\alpha' = \arccos\left(\frac{u}{V}\right) = \arccos(\cos\alpha\cos\beta) \tag{A.9}$$

Du fait des limites en précision des mesures en soufflerie, les coefficients aérodynamiques prennent des valeurs incertaines autour de leurs valeurs nominales. Le Tableau A.1 reporte les niveaux d'incertitude retenus pour l'étude.

Table A.1: Incertitudes sur les coefficients aérodynamiques

Coefficient de force	Incertitude (%)	Coefficient de moment	Incertitude (%)
C_A	3	-	-
$C_{N\alpha}$	6	$C_{m\alpha}$	3
$C_{Yp\alpha}$	33	$C_{np\alpha}$	25
-	-	C_{lp}	15
-	-	C_{mq}	15
$C_{N\delta}$	15	$C_{l\delta}$	15
-	-	$C_{m\delta}$	15

Les autres paramètres qui apparaissent dans l'expression des forces et des moments sont la pression dynamique $\overline{q} = \frac{1}{2}\rho(h)V^2$, l'accélération de la pesanteur g, la surface de référence S, et le calibre du projectile d. Les variables de contrôle $[\delta_p\ \delta_q\ \delta_r]^T$ sont des signaux virtuels. Ils dépendent de l'angle de roulis de la FCT ϕ_f et des angles de déflexion réels des canards $[\delta_1\ \delta_2\ \delta_3\ \delta_4]^T$ à travers la relation [Siouris, 2004]:

$$\begin{bmatrix}\delta_p\\ \delta_q\\ \delta_r\end{bmatrix} = T_{VR}(\phi_f)\begin{bmatrix}\delta_1\\ \delta_2\\ \delta_3\\ \delta_4\end{bmatrix} = \begin{bmatrix}1 & 0 & 0\\ 0 & \cos\phi_f & -\sin\phi_f\\ 0 & \sin\phi_f & \cos\phi_f\end{bmatrix}\begin{bmatrix}\frac{1}{4} & \frac{1}{4} & \frac{1}{4} & \frac{1}{4}\\ 0 & \frac{1}{2} & 0 & -\frac{1}{2}\\ \frac{1}{2} & 0 & -\frac{1}{2} & 0\end{bmatrix}\begin{bmatrix}\delta_1\\ \delta_2\\ \delta_3\\ \delta_4\end{bmatrix} \tag{A.10}$$

Enfin, le moment L_{f-a} provoqué par le frottement entre les parties avant et arrière du projectile est donné par :

$$L_{f-a} = \overline{q}SC_A(\mathcal{M},\alpha,\beta)\,\mathrm{sign}(p_a - p_f)(K_s + K_v|p_a - p_f|) \tag{A.11}$$

avec K_s et K_v les coefficients de frottement statique et visqueux, incertains à 40%.

Modèles linéarisés des dynamiques de roulis et de tangage/lacet

Le modèle non-linéaire du projectile peut être décomposé selon l'axe de roulis d'une part, et les axes de tangage/lacet d'autre part. Cette décomposition correspond aux deux autopilotes mentionnés dans la description du scénario de vol.

Les variables d'état pertinentes pour décrire la dynamique selon l'axe de roulis sont l'angle de roulis ϕ_f de la FCT et sa vitesse angulaire p_f. Les équations dynamiques sont extraites des

équations complètes du mouvement (A.1) et (A.3), et réécrites sous forme d'un système LPV :

$$\begin{bmatrix}\dot{\phi}_f\\ \dot{p}_f\end{bmatrix} = \begin{bmatrix}0 & 1\\ 0 & a_{22}(\boldsymbol{\sigma}_R)\end{bmatrix}\begin{bmatrix}\phi_f\\ p_f\end{bmatrix} + \begin{bmatrix}0\\ b_2(\boldsymbol{\sigma}_R)\end{bmatrix}\delta_p + \begin{bmatrix}d_\phi\\ d_p\end{bmatrix} \tag{A.12}$$

avec :

$$a_{22}(\boldsymbol{\sigma}_R) = -\left(\frac{\overline{q}Sd}{I_{xf}}\right)C_A(\mathcal{M},\alpha')K_v \quad b_2(\boldsymbol{\sigma}_R) = -\left(\frac{\overline{q}Sd}{I_{xf}}\right)C_{l\delta}(\mathcal{M}) \tag{A.13}$$

et $\boldsymbol{\sigma}_R = [\alpha'\ V\ h]^T$ un vecteur de paramètres. Les termes de perturbation d_ϕ et d_p sont donnés par :

$$d_\phi = r\tan\theta \qquad d_p = \left(\frac{\overline{q}Sd}{I_{xf}}\right)C_A(\mathcal{M},\alpha')[\text{sign}(p_a - p_f)K_s + K_v p_a] \tag{A.14}$$

Sur la base de simulations de trajectoires balistiques, on montre qu'en pratique, l'angle d'incidence totale α' évolue dans l'intervalle $[0\text{ deg}, 15\text{ deg}]$. Dans cet intervalle, la valeur du coefficient de traînée $C_A(\mathcal{M},\alpha')$ dépend principalement du nombre de Mach, c'est-à-dire des paramètres V et h. Il est donc légitime de considérer un vecteur de paramètres réduit $\boldsymbol{\lambda}_R = [V\ h]^T$.

Les dynamiques de tangage/lacet peuvent se mettre sous la forme générique :

$$\begin{cases}\dot{\boldsymbol{x}} = f(\boldsymbol{x},\boldsymbol{u},\boldsymbol{\sigma}_{PY})\\ \boldsymbol{y} = g(\boldsymbol{x},\boldsymbol{u},\boldsymbol{\sigma}_{PY})\end{cases} \tag{A.15}$$

avec $\boldsymbol{x} = [\alpha\ q\ \beta\ r]^T$ le vecteur d'état, $\boldsymbol{u} = [\delta_q\ \delta_r]^T$ le vecteur d'entrée, $\boldsymbol{y} = [n_z\ n_y\ q\ r]^T$ le vecteur de sortie, et $\boldsymbol{\sigma}_{PY} = [V\ h\ p_a\ \theta]^T$ le vecteur de paramètres. Les sorties n_z et n_y sont respectivement les facteurs de charge normal et latéral. Ils se définissent comme la résultante des forces extérieures autres que la gravité, divisée par le poids mg du projectile, et exprimés en nombre de g.

Dans la perspective de concevoir un autopilote par séquencement de gain, le système non-linéaire est linéarisé autour de ses points d'équilibre [Rugh and Shamma, 2000; Leith and Leithead, 2000]. Le point de départ à cette procédure est le calcul des points d'équilibre pour des valeurs fixées $\overline{\boldsymbol{\sigma}}_{PY} = [\overline{V}\ \overline{h}\ \overline{p_a}\ \overline{\theta}]^T$ du vecteur de paramètres. En d'autres termes, on cherche les solutions $(\overline{\boldsymbol{x}},\overline{\boldsymbol{u}})$ de l'équation :

$$f(\overline{\boldsymbol{x}},\overline{\boldsymbol{u}},\overline{\boldsymbol{\sigma}}_{PY}) = 0 \tag{A.16}$$

Il s'agit d'un système de quatre équations à six inconnues, qui est donc sous-déterminé. Afin de pouvoir poursuivre la résolution, on définit un vecteur d'équilibrage étendu $\overline{\boldsymbol{\rho}} = [\overline{V}\ \overline{h}\ \overline{p_a}\ \overline{\theta}\ \overline{\alpha}\ \overline{\beta}]^T$, dans lequel on fixe également les valeurs des angles d'attaque et de dérive. Les solutions $(\overline{\boldsymbol{x}},\overline{\boldsymbol{u}})$ peuvent alors être obtenues analytiquement, et servent de plus à calculer les sorties à l'équilibre $\overline{\boldsymbol{y}}$ (voir [Theodoulis et al., 2013] pour les détails de la résolution). Notant $\boldsymbol{x}_\varepsilon = \boldsymbol{x} - \overline{\boldsymbol{x}}$, $\boldsymbol{u}_\varepsilon = \boldsymbol{u} - \overline{\boldsymbol{u}}$, et $\boldsymbol{y}_\varepsilon = \boldsymbol{y} - \overline{\boldsymbol{y}}$, le système non-linéaire est approximé par un développement de Taylor au premier

ordre, qui a pour représentation d'état :

$$\begin{cases} \dot{\boldsymbol{x}}_\varepsilon = \boldsymbol{A}(\overline{\boldsymbol{\rho}})\boldsymbol{x}_\varepsilon + \boldsymbol{B}(\overline{\boldsymbol{\rho}})\boldsymbol{u}_\varepsilon \\ \boldsymbol{y}_\varepsilon = \boldsymbol{C}(\overline{\boldsymbol{\rho}})\tilde{\boldsymbol{x}}_\varepsilon + \boldsymbol{D}(\overline{\boldsymbol{\rho}})\boldsymbol{u}_\varepsilon \end{cases} \tag{A.17}$$

Comme le vecteur d'équilibrage utilisé a pour composante des variables d'état, et en s'autorisant un abus de langage qui reste courant, on qualifiera de quasi-LPV ce continuum de systèmes LTI paramétrés par $\boldsymbol{\rho}$. Afin de réduire la quantité de calcul pour l'étape de synthèse de contrôleur, seuls les paramètres les plus influents sont considérés pour le séquencement. Les analyses de sensibilité réalisées par [Sève et al., 2017] montrent qu'un vecteur de paramètres réduit pertinent est donné par $\boldsymbol{\lambda}_{PY} = [V\ h\ p_a]^T$. L'enveloppe de vol réduite est décrite par les intervalles $V \in [140\text{ m/s}, 380\text{ m/s}]$, $h = [0\text{ m}, 15000\text{ m}]$, et $p_a \in [750\text{ rad/s}, 1650\text{ rad/s}]$, et les autres paramètres sont fixés à $\theta = -17.5\,\text{deg}$, $\alpha = 0\,\text{deg}$, et $\beta = 0\,\text{deg}$.

Définition des modèles des actionneurs et des capteurs

Les quatre servomoteurs qui actionnent les canards sont modélisés par des systèmes linéaires du second ordre, de pulsation $\omega_{act} = 2\pi \cdot 20$ rad/s et avec un facteur d'amortissement $\xi_{act} = 0.781$. Une saturation en amplitude $\delta_{sat} = \pm 10\,\text{deg}$ est introduite à l'entrée de chaque actionneur. En revanche, on ne considèrera pas de saturation en vitesse. En effet, les saturations modélisées ici ne reflètent pas des contraintes mécaniques, mais sont introduites pour rester dans le domaine de validité du modèle des efforts générés par les canards, qui utilise l'hypothèse des petits angles. L'équation (A.10) est utilisée pour passer des sorties des actionneurs aux signaux virtuels.

Pour refléter la séparation des dynamiques de roulis et de tangage/lacet, il est naturel de considérer $\delta_{p,c}$ comme sortie de l'autopilote de roulis, et $(\delta_{q,c}, \delta_{r,c})$ comme sortie de l'autopilote de tangage/lacet. Pour obtenir les signaux à envoyer aux quatre actionneurs, on considère une matrice d'allocation basée sur la pseudo-inverse $T_{VR}(\phi_f)^\dagger$ de $T_{VR}(\phi_f)$.

La FCT est équipée d'accéléromètres et de gyroscopes, fournissant des mesures $(n_{z,m}, n_{y,m})$ et $(p_{f,m}, q_m, r_m)$ des facteurs de charge et des vitesses angulaires. De plus, les capteurs des servomoteurs donnent en sortie les mesures $(\delta_{1,m}, \delta_{2,m}, \delta_{3,m}, \delta_{4,m})$ des angles de déflexion des canards. Pour simplifier le problème, tous les capteurs sont modélisés par des systèmes du premier ordre, de même pulsation $\omega_s = 2\pi \cdot 133$ rad/s.

A.2.3 Conclusion

Ce chapitre traite de la modélisation en boucle ouverte d'un projectile guidé dual-spin en vue de la conception d'un contrôleur séquencé. Dans un premier temps, les équations du mouvement sont établies à partir de la mécanique du vol et de la théorie de l'aérobalistique, et exprimées dans un repère non tournant, mieux adapté à l'application.

L'introduction de signaux de contrôle virtuels permet de séparer les dynamiques de l'axe de roulis d'une part, et des axes de tangage/lacet d'autre part. Cette séparation correspond à deux problèmes de contrôle distincts survenant au cours du vol. Le premier problème concerne la stabilisation de l'angle de roulis de la fusée. Le second est lié à la phase guidée. La linéarisation de ces dynamiques conduit à un modèle LPV pour l'axe de roulis, et à un modèle quasi-LPV

pour les axes de tangage/lacet. Afin de limiter le nombre de variables de séquencement, une enveloppe de vol de dimension réduite, ne préservant que les paramètres les plus influents, est considérée. Enfin, les modèles en boucle ouverte des axes de roulis et de tangage/lacet sont complétés avec les modèles des actionneurs et des capteurs.

A.3 Développement d'un autopilote baseline séquencé

A.3.1 Introduction

La dynamique de l'application étudiée se décompose en un système LPV pour l'axe de roulis et un système quasi-LPV pour les axes de tangage/lacet. Conformément au scénario de vol envisagé, deux autopilotes doivent être conçus. L'autopilote de roulis est chargé de stabiliser la FCT tout le long de la trajectoire, et notamment de contrecarrer les effets de frottement entre le corps du projectile et la FCT. L'autopilote de tangage/lacet est dédié à la modification de la trajectoire en vol. Pour chacun de ces problèmes de contrôle, des variations paramétriques, des incertitudes, et potentiellement de saturations, entrent en jeu. Le traitement simultané de ces aspects étant particulièrement délicat, on choisit dans ce chapitre de ne pas prendre en compte les saturations, dont le traitement est relégué au Chapitre 4. La présence de paramètres variants est prise en compte à travers des stratégies de séquencement de gain, plus simples et moins conservatives que les méthodes LPV, ce qui les rend adaptées à un design préliminaire. Concernant la prise en compte des incertitudes, des contributions théoriques et algorithmiques à la μ-analyse sont présentées, et appliquées à l'analyse de robustesse du projectile guidé.

A.3.2 Synthèse des travaux

Contributions à la μ-analyse probabiliste

La μ-analyse, introduite par [Doyle, 1982], est l'outil privilégié pour l'étude de la robustesse des systèmes linéaires incertains. Elle repose sur la la modélisation du système à étudier sous forme LFR (*Linear Fractional Representation*, voir Figure A.3), où $M(s)$ correspond à la configuration nominale, et le bloc $\Delta(s) \in \mathcal{B}_{\mathbf{\Delta}}$ regroupe et isole les paramètres incertains et dynamiques négligées. Une quantité associée à la LFR, appelée la valeur singulière structurée et notée μ, est alors calculée pour obtenir la marge de stabilité robuste $k_r = 1/\mu$. Dans le cas d'incertitudes bornées et normalisées, la stabilité robuste équivaut à $k_r > 1$. En pratique, le calcul de exact de k_r est impossible. On cherche donc à calculer des bornes supérieure $\overline{k_r}$ et inférieure $\underline{k_r}$ aussi précises que possible. Des algorithmes efficaces pour obtenir de telles bornes sont implémentées dans la bibliothèque SMART de la toolbox SMAC [Roos et al., 2011; Roos, 2013].

Malgré sa maturité théorique et algorithmique, la μ-analyse souffre de l'absence d'évaluation de la probabilité des configurations pires cas, ce qui peut la rendre excessivement pessimiste et donc peu adaptée dans des phases de certification. Dans la pratique, il est préférable d'évaluer le risque d'occurrence d'événements rares, ce qui explique le recours fréquent aux méthodes de Monte Carlo. Ces dernières peuvent cependant s'avérer coûteuse, car nécessitant un grand nombre de simulations pour obtenir des résultats statistiques fiables. Ces lacunes ont incité les chercheurs à étudier d'autres méthodes probabilistes d'analyse de robustesse, parmi lesquelles

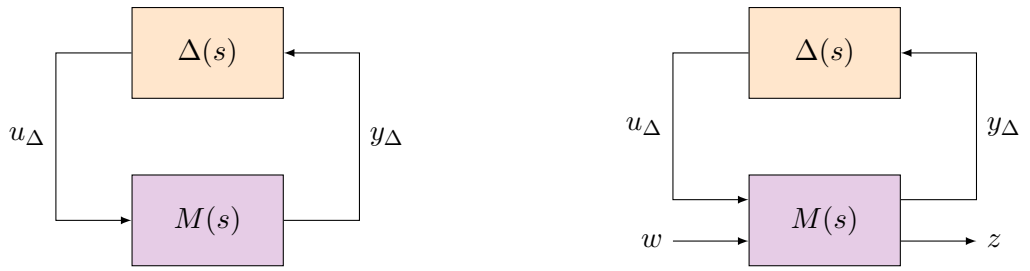

(a) Interconnexion pour la stabilité robuste (b) Interconnexion pour la performance robuste

Figure A.3: LFR pour l'analyse de robustesse

la μ-analyse probabiliste [Zhu et al., 1996; Khatri and Parrilo, 1998]. Le but de celle-ci est d'évaluer la distribution de probabilité de μ, pour une distribution donnée des incertitudes. Contrairement aux méthodes de Monte Carlo, l'exploration du domaine des paramètres incertains est déterministe et exhaustif.

Plus précisément, soit l'interconnexion de la Figure A.3a, où l'on supposera pour simplifier que $\Delta(s)$ ne contient que des incertitudes paramétriques réelles $\boldsymbol{\delta} = (\delta_1, \ldots, \delta_N) \in \mathcal{B}_{\boldsymbol{\delta}}$. Ces dernières sont modélisées par des variables aléatoires indépendantes, décrites par les densités de probabilité $\boldsymbol{f} = (f_1, \ldots, f_N)$. L'analyse de stabilité robuste peut alors être formulée comme la résolution du problème suivant :

Problem A.1 (Stabilité robuste probabiliste)**.** *Calculer la probabilité* $\overline{P}_{\boldsymbol{\Delta},f}(M(s))$ *que l'interconnexion* $(M(s), \Delta)$ *soit instable, pour* $\Delta \in \mathcal{B}_{\boldsymbol{\Delta}}$.

Le calcul exact de cette probabilité est évidemment impossible de manière générale. Cependant, par un algorithme de type branch-and-bound, on est capable de calculer un domaine de stabilité garantie $D_s \subset \mathcal{B}_{\boldsymbol{\delta}}$, exploitable pour le calcul d'une borne supérieure de la probabilité cherchée. Cette approche est notamment proposée par [Falcoz et al., 2017].

Il y a également un grand intérêt à calculer une borne inférieure de $\overline{P}_{\boldsymbol{\Delta},f}(M(s))$. Cela permet non seulement d'obtenir une caractérisation plus précise du domaine de stabilité, mais aussi de potentiellement invalider très rapidement un design vis-à-vis d'un seuil de tolérance ε. Pour ce faire, le calcul d'un domaine d'instabilité garantie $D_{\overline{s}}$ est souhaitable, afin d'obtenir l'encadrement suivant :

$$p(D_{\overline{s}}) \leq \overline{P}_{\boldsymbol{\Delta},f}(M(s)) \leq 1 - p(D_s) \tag{A.18}$$

Le calcul de $D_{\overline{s}}$ peut être fait en s'appuyant sur les mêmes principes que la μ-analyse classique. En effet, les algorithmes de calcul de μ repose essentiellement sur la détection du passage des pôles du système incertain sur l'axe imaginaire lorsque l'on fait grandir Δ. L'application du même principe au cas d'un système $M(s)$ nominalement instable mène à la notion de "marge d'instabilité robuste". L'Algorithme 6, également décrit dans [Thai et al., 2019a], améliore la stratégie de branch-and-bound en y intégrant l'utilisation des données probabilistes et de la marge d'instabilité robuste. Le résultat de l'algorithme est un partitionnement de $\mathcal{B}_{\boldsymbol{\delta}}$ de la forme :

$$\mathcal{B}_{\boldsymbol{\delta}} = D_s \cup D_{\overline{s}} \cup D_{s_u} \tag{A.19}$$

ainsi que la mesure de probabilité de ces trois ensembles. Ceux-ci correspondent respectivement aux domaines de stabilité garantie, d'instabilité garantie, et de stabilité non déterminée. La présence de ce troisième ensemble D_{s_u} traduit le fait qu'en pratique, le calcul exact des domaines de stabilité et d'instabilité n'est pas possible. Idéalement, D_{s_u} doit être aussi petit que possible, bien que selon les besoins de la validation, des résultats relativement peu précis peuvent suffire.

Algorithm 6 μ-analyse probabiliste pour l'analyse de stabilité

Inputs: $M(s)$, $\mathbf{\Delta}$, $f_i(\delta_i)$ for $i = 1, \ldots, N$, p_{min}
Outputs: D_s, $D_{\bar{s}}$, D_{s_u}, $p(D_s), p(D_{\bar{s}}), p(D_{s_u})$
$\mathcal{L} \leftarrow \{\mathcal{B}_{\boldsymbol{\delta}}\}$ ▷ $\mathcal{L}$ constitutes the list of all boxes left to investigate
$D_s, D_{\bar{s}}, D_{s_u} \leftarrow \emptyset$
$p(D_s), p(D_{\bar{s}}), p(D_{s_u}) \leftarrow 0$
while $\mathcal{L} \neq \emptyset$ **do**
    select and remove the box $\tilde{D}$ from $\mathcal{L}$ with highest probability measure
    compute the interconnection $\left(\tilde{M}(s), \tilde{\Delta}\right)$ normalised wrt $\tilde{D}$
    compute a guaranteed robust stability margin $\underline{k_r}$ for $\left(\tilde{M}(s), \tilde{\Delta}\right)$
    if $\underline{k_r} \geq 1$ **then**
        if $\mathcal{F}_u(\tilde{M}(s), \tilde{\Delta})$ is nominally stable **then**
            add $\tilde{D}$ to D_s
            $p(D_s) \leftarrow p(D_s) + p(\tilde{D})$
        else
            add $\tilde{D}$ to $D_{\bar{s}}$
            $p(D_{\bar{s}}) \leftarrow p(D_{\bar{s}}) + p(\tilde{D})$
        end if
    else ▷ analysis was inconclusive on the current box
        if $p(\tilde{D}) > p_{min}$ **then**
            select a direction for cutting $\tilde{D}$
            partition $\tilde{D}$
            add the boxes obtained by partitioning $\tilde{D}$ into $\mathcal{L}$
        else
            add $\tilde{D}$ to D_{s_u}
            $p(D_{s_u}) \leftarrow p(D_{s_u}) + p(\tilde{D})$
        end if
    end if
end while

La μ-analyse probabiliste peut être étendue à l'évaluation de la performance $\mathcal{H}_\infty$. Soit l'interconnexion de la Figure A.3b. On cherche alors à résoudre le problème suivant :

Problem A.2 (Performance $\mathcal{H}_\infty$ robuste)**.** *Pour un niveau de performance $\gamma > 0$ fixé, calculer la probabilité $\overline{P}^{\gamma}_{\mathbf{\Delta},f}(M(s))$ que $\|\mathcal{T}_{w\to z}(s)\|_\infty > \gamma$ pour $\Delta \in \mathcal{B}_{\mathbf{\Delta}}$.*

Comme pour le cas de la stabilité robuste, l'idée est de combiner un algorithme de branch-and-bound à la μ-analyse pour calculer des domaines de performance et de non-performance garanties et leurs mesures de probabilité. Si la vérification de la performance peut s'effectuer en utilisant la μ-analyse asymétrique, une difficulté apparaît dans la vérification de non-performance

sur $\mathcal{B}_{\mathbf{\Delta}}$, qui s'exprime formellement comme :

$$\min_{\Delta \in \mathcal{B}_{\mathbf{\Delta}}} \|\mathcal{F}_u(M(s), \Delta)\|_\infty > \gamma \tag{A.20}$$

Un résultat clé, présenté et démontré dans [Thai et al., 2019a], est la condition suffisante de non-performance suivante, applicable au cas d'un canal de performance scalaire :

Proposition A.3. *Soit $\mathcal{I} = \{\omega \in \mathbb{R}_+ : |M_{22}(j\omega)| > \gamma\}$, et pour chaque $\omega \in \mathcal{I}$, soit $N(j\omega)$ tel que $(\mathcal{F}_u(M(j\omega), \Delta))^{-1} = \mathcal{F}_u(N(j\omega), \Delta)$. S'il existe $\omega_0 \in \mathcal{I}$ tel que*

$$\nu_{\mathbf{\Delta}_a}(N(j\omega_0)) < \frac{1}{\gamma} \tag{A.21}$$

avec $\mathbf{\Delta}_a = \mathrm{diag}(\mathcal{B}_{\mathbf{\Delta}}, \mathbb{C})$, alors la non-performance est garantie pour tout $\Delta \in \mathcal{B}_{\mathbf{\Delta}}$.

Ce résultat est intégré dans un algorithme de branch-and-bound dédié à l'étude de la performance $\mathcal{H}_\infty$ et analogue à l'Algorithme 6.

Supposons maintenant que l'interconnexion de la Figure A.3b représente une boucle qui a été ouverte à un point d'analyse des marges de stabilité classiques (marges de gain ou de phase). On se placera dans le cas scalaire. La boucle fermée correspond alors au cas $G = 1$ dans la Figure A.4.

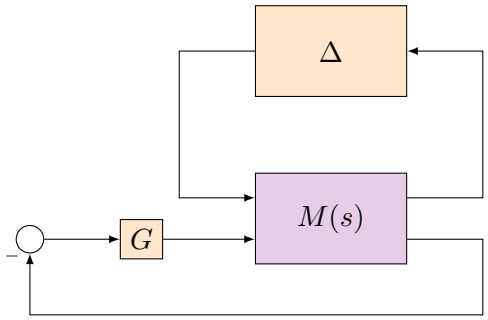

Figure A.4: Interconnexion pour l'analyse de robustesse des marges de gain et de phase

Remarque : *Le cas de la marge de module peut se ramener au cas d'une analyse de performance $\mathcal{H}_\infty$ sur la fonction de sensibilité $S(s) = (1 + \mathcal{F}_u(M(s), \Delta))^{-1}$.*

L'expression de G dépend du type de marge (gain ou phase) étudié, mais il est possible dans les deux cas, par une normalisation et des manipulations matricielles élémentaires, de se ramener à l'interconnexion de la Figure A.5, avec $\delta_m \in [-1,\ 1]$ une incertitude paramétrique réelle supplémentaire associée à une quantité de marge (de gain ou de phase) voulue ϕ.

Vérifier qu'une valeur de marge de gain ou de phase est respectée sur un hypercube $D \subset \mathcal{B}_{\boldsymbol{\delta}}$ est alors un problème de μ-analyse classique. Dans le cas de la marge de phase, les fréquences négatives doivent cependant être considérées, car la fonction de transfert $N(s)$ possède alors des coefficients complexes. Les valeurs propres de l'interconnexion de la Figure A.5 ne sont donc plus nécessairement symétriques par rapport à l'axe réel. Quant au dépassement de marge sur $D \subset \mathcal{B}_{\boldsymbol{\delta}}$, il peut être vérifié à l'aide de la condition suffisante suivante :

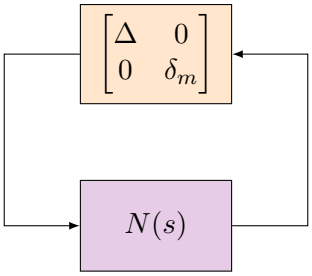

Figure A.5: Interconnexion standard pour l'analyse de robustesse des marges de gain et de phase

Proposition A.4. *S'il existe* $\hat{\delta}_m \in [-1, 1]$ *tel que :*

$$\forall \Delta \in D, \ \textit{l'interconnexion} \left(N(s), \mathrm{diag}(\Delta, \hat{\delta}_m)\right) \textit{ est instable}$$

alors la marge de gain ou de phase est inférieure à ϕ *sur tout l'hypercube* $D \subset \mathcal{B}_{\boldsymbol{\delta}}$

Le point le plus critique dans l'utilisation de cette condition suffisante est le choix de $\hat{\delta}_m$. Une stratégie efficace mais empirique consiste à tester un nombre fini de valeurs $(\delta_m^k)_k$ dans l'intervalle $[-1, 1]$ puis de choisir $\hat{\delta}_m$ comme le δ_m^k de plus grande amplitude qui rend l'interconnexion $(N(s), \mathrm{diag}(0_{p\times p}, \delta_m^k))$ instable. À partir des éléments qui précèdent, on met alors en place un algorithme de branch-and-bound analogue à l'Algorithme 6.

Développement de l'autopilote de roulis

La conception de l'autopilote de roulis s'appuie sur le système LPV donné par l'équation (A.12). Celui-ci est simplifié en considérant le vecteur de paramètres réduit $\boldsymbol{\lambda}_R = [V \ h]^T$ au lieu de $\boldsymbol{\sigma}_R$, et les perturbations $[d_\phi \ d_{p_f}]^T$ sont négligées. Le système a un pôle en 0, et un autre pôle à la valeur $a_{22}(\boldsymbol{\lambda}_R)$. Les variations des coefficients $a_{22}(\boldsymbol{\lambda}_R)$ et $b_2(\boldsymbol{\lambda}_R)$ sont données par la Figure A.6. On remarque notamment que le second pôle ne varie que sur un petit intervalle de l'axe des réels strictement négatifs. On peut donc raisonnablement l'approximer par un coefficient constant $\overline{a_{22}}$. La fonction de transfert de δ_p vers $[\phi_f \ p_f]^T$ prend alors la forme :

$$G_R(s, \boldsymbol{\lambda}_R) = b_2(\boldsymbol{\lambda}_R) \begin{bmatrix} \dfrac{1}{s(s - \overline{a_{22}})} \\ \dfrac{1}{s - \overline{a_{22}}} \end{bmatrix} = b_2(\boldsymbol{\lambda}_R) \hat{G}_R(s) \tag{A.22}$$

La stratégie de conception de l'autopilote de roulis consiste alors à synthétiser un contrôleur $\hat{K}_R(s)$ pour le système LTI $\hat{G}_R(s)$. Le contrôleur séquencé, adapté au système LPV $G_R(s, \boldsymbol{\lambda}_R)$, s'obtient directement comme :

$$K_R(s, \boldsymbol{\lambda}_R) = \frac{1}{b_2(\boldsymbol{\lambda}_R)} \hat{K}_R(s) \tag{A.23}$$

Un seul point de vol est nécessaire pour réaliser le design, ce qui simplifie considérablement la tâche. La validité de l'approximation peut être validée a posteriori grâce à des analyses et des simulations.

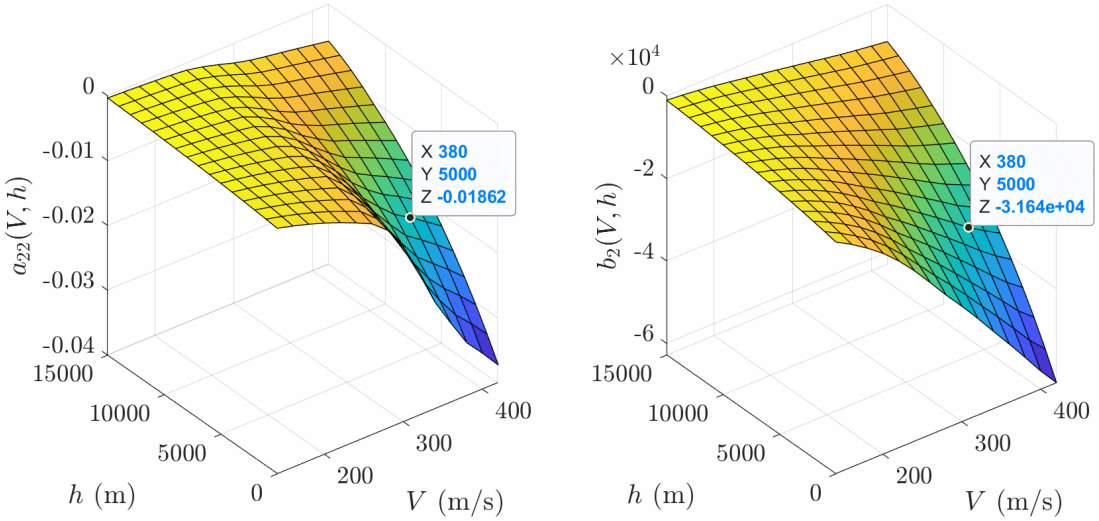

Figure A.6: Variation des coefficients de la représentation d'état sur l'enveloppe de vol, et point de vol $\boldsymbol{\lambda}_{R0}$ sélectionné pour le design

La structure du contrôleur est donnée par la Figure A.7. Il s'agit d'un contrôleur de type PI-P (gains $K_{p,e}$, $K_{i,e}$, et K_{p,p_f}), auquel s'ajoute un gain *feedforward* K_{ff} qui permet d'améliorer le suivi de consigne en phase transitoire. Les valeurs des gains du contrôleur sont calculées en résolvant un problème de synthèse $\mathcal{H}_\infty$ structurée [Skogestad and Postlethwaite, 2005; Apkarian and Noll, 2006], illustré par le schéma-bloc de la Figure A.8. La boucle fermée de la dynamique de roulis est augmentée à l'aide de fonctions de pondération $W_S(s)$, $W_{KS}(s)$, et $W_M(s)$. Celles-ci correspondent respectivement à des contraintes de rejet de perturbation à basse fréquence, d'atténuation du signal de commande en haute fréquence, et de suivi de modèle aux fréquences intermédiaires. La contrainte de suivi de modèle s'applique au transfert de l'angle de roulis commandé $\phi_{f,g}$ à l'angle de roulis réalisé ϕ_f, avec un modèle de référence $T_{ref,R}(s)$ du second ordre ayant pour pulsation $\omega_{ref,R} = 14.3$ rad/s et pour facteur d'amortissement $\xi_{ref,R} = 0.781$. Le suivi de modèle n'étant pas un impératif du design, la contrainte associée est utilisée comme fonction objectif du problème d'optimisation $\mathcal{H}_\infty$, qui s'écrit donc :

$$\begin{aligned} \underset{\boldsymbol{\kappa}_R}{\text{minimise}} \quad & \left\| W_M(s)\mathcal{T}_{\phi_{f,g}\to e_{ref}}(s) \right\|_\infty \\ \text{subject to} \quad & \left\| W_S(s)\mathcal{T}_{d_o\to\phi_f}(s) \right\|_\infty < 1 \\ & \left\| W_{KS}(s)\mathcal{T}_{d_o\to\delta_p}(s) \right\|_\infty < 1 \end{aligned} \tag{A.24}$$

avec $\boldsymbol{\kappa}_R = \begin{bmatrix} K_{i,e} & K_{p,e} & K_{p,p_f} & K_{ff} \end{bmatrix}^T$. Les fonctions de pondération sont données par :

$$W_M(s) = \frac{s+30}{0.15s + 30\cdot 10^{-4}} \qquad W_S(s) = \frac{s+10}{1.6s + 10\cdot 10^{-4}} \qquad W_{KS}(s) = \frac{s+40}{10^{-4}s + 40\cdot 0.5} \tag{A.25}$$

Le problème d'optimisation est résolu en utilisant la fonction `systune` de la *Control System Toolbox* de Matlab. On aboutit alors à un indice de performance (valeur de la fonction objectif) $\gamma = 0.62$. Les fonctions de transfert façonnées sont présentées en Figure A.9, et valident le respect des contraintes fréquentielles ainsi que le bon suivi de modèle.

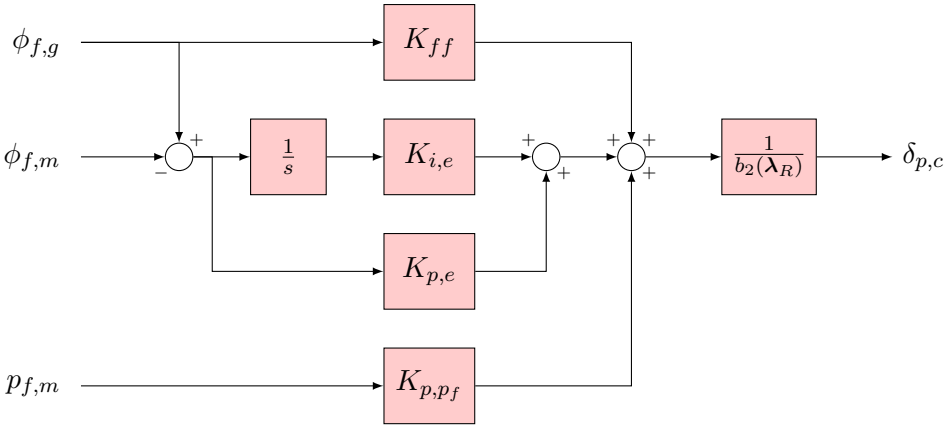

Figure A.7: Structure de l'autopilote de roulis

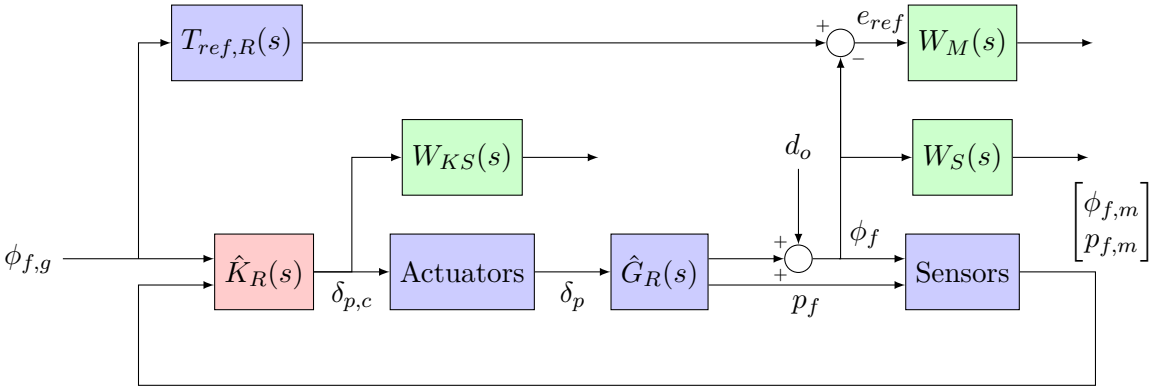

Figure A.8: Problème de synthèse $\mathcal{H}_\infty$ structurée pour l'autopilote de roulis

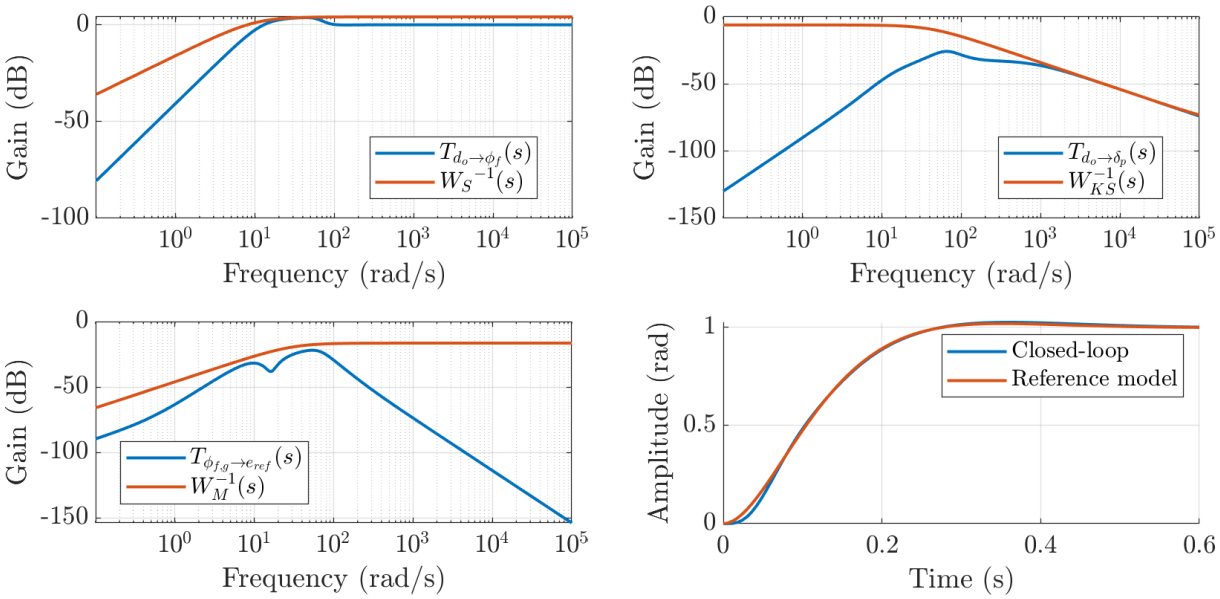

Figure A.9: Fonctions de transfert en boucle fermée: rejet de perturbation (en haut à gauche), atténuation du signal de commande (en haut à droite), suivi de modèle (en bas à gauche), et réponse à un échelon (en bas à droite)

La robustesse aux incertitudes est évaluée avec la μ-analyse. La bibliothèque GSS de la toolbox SMAC [Biannic and Roos, 2012-2021] est utilisée pour obtenir une LFR de la boucle

fermée au point de design $\boldsymbol{\lambda}_{R0}$. Le système LTI $M_R(s)$ obtenu est d'ordre 13, bouclé avec un bloc Δ_R appartenant à l'ensemble :

$$\mathcal{B}_{\boldsymbol{\Delta}R} = \{\text{diag}(\delta_{C_A}, \delta_{C_{l\delta}}, \delta_{K_v}) \colon \delta_\bullet \in [-1, 1]\} \tag{A.26}$$

La bibliothèque SMART de la toolbox SMAC [Roos, 2013] permet de calculer une borne $\overline{\mu} = 0.19 < 1$ ($\underline{k_r} = 1/0.19 \approx 5.26 > 1$) qui valide la stabilité robuste au point de design. La performance robuste est également satisfaisante, avec une valeur pire cas $\max_{\Delta \in \mathcal{B}_{\boldsymbol{\Delta}R}} \left\| \mathcal{T}_{\phi_{f,g} \to e_{ref}} \right\|_\infty < 0.094$ qui reste proche de la valeur nominale de 0.087. La μ-analyse probabiliste permet une étude plus fine. La Figure A.10 trace ainsi des bornes sur la probabilité de satisfaction du niveau de performance $\mathcal{H}_\infty$. Les résultats sont montrés pour une distribution uniforme et une distribution normale des incertitudes. Les meilleurs niveaux de satisfaction obtenus avec la distribution normale illustrent l'intérêt de prendre en compte les données probabilistes du problème. Le faible écart entre les bornes indique que les probabilités sont évaluées avec précision, démontrant l'efficacité des algorithmes de branch-and-bound développés. De la même manière, la μ-analyse probabiliste peut être appliquée aux marges de gain, de phase, et de module, qui restent cependant satisfaisantes même dans le pire cas, à respectivement 7.4 dB, 30.3 deg, et 0.40.

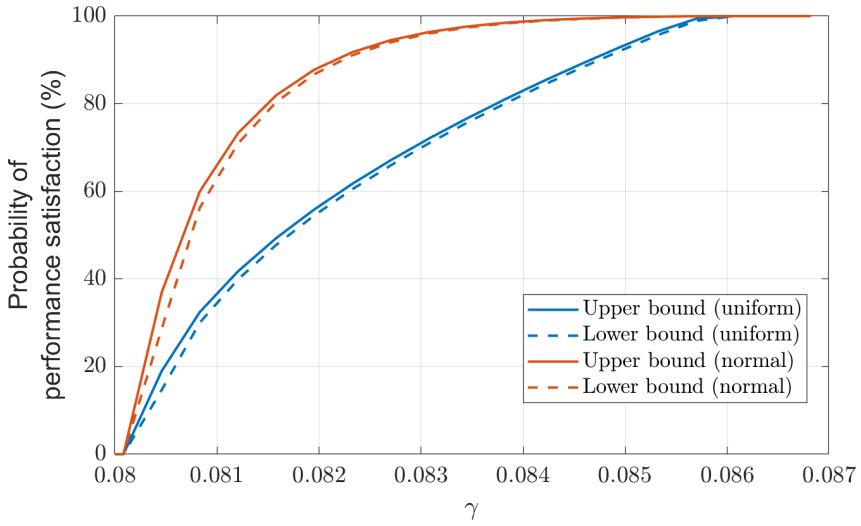

Figure A.10: Bornes sur la probabilité de satisfaction d'un niveau de performance $\mathcal{H}_\infty$ en supposant une distribution uniforme (bleu) ou normal (orange) des incertitudes

Développement de l'autopilote de tangage/lacet

La conception de l'autopilote de tangage/lacet s'appuie sur le continuum de modèles LTI défini sur l'enveloppe de vol réduite $\boldsymbol{\lambda}_{PY} = [V \ h \ p_a]^T$ (voir l'équation (A.17)). Le temps de réponse doit être suffisamment élevé par rapport à celui de la dynamique de roulis (0.43 s), puisqu'on fait l'hypothèse que l'angle de roulis est stabilisé, mais aussi suffisamment petit pour assurer un bon suivi des signaux de guidage et, à terme, une bonne précision à l'impact. Du fait du fort couplage entre les dynamiques de tangage et de lacet, il n'est pas envisageable de réaliser un traitement axe par axe. On est donc confronté à un problème de contrôle multivariable. Une structure d'ordre faible et comportant un nombre limité de gains est favorisée, pour faciliter un

séquencement de gains basé sur une interpolation linéaire.

Remarque : *Pour alléger les notations, les indices ε dénotant l'écart aux valeurs à l'équilibre sont omis dans cette section.*

La structure proposée est présentée par la Figure A.11. Des symétries sont imposées sur les matrices de gains du contrôleur, reflétant les symétries du système, et simplifiant davantage l'étape d'interpolation, et l'implémentation de manière générale :

$$\begin{aligned} \mathbf{K}_{i,e} &= \begin{bmatrix} K_{i,e}^{(11)} & K_{i,e}^{(12)} \\ K_{i,e}^{(12)} & -K_{i,e}^{(11)} \end{bmatrix} \quad \mathbf{K}_{p,n} = \begin{bmatrix} K_{p,n}^{(11)} & K_{p,n}^{(12)} \\ K_{p,n}^{(12)} & -K_{p,n}^{(11)} \end{bmatrix} \\ \mathbf{K}_{p,\omega} &= \begin{bmatrix} K_{p,\omega}^{(11)} & K_{p,\omega}^{(12)} \\ -K_{p,\omega}^{(12)} & K_{p,\omega}^{(11)} \end{bmatrix} \quad \mathbf{K}_{p,\delta} = \begin{bmatrix} K_{p,\delta}^{(11)} & K_{p,\delta}^{(12)} \\ K_{p,\delta}^{(12)} & -K_{p,\delta}^{(11)} \end{bmatrix} \end{aligned} \tag{A.27}$$

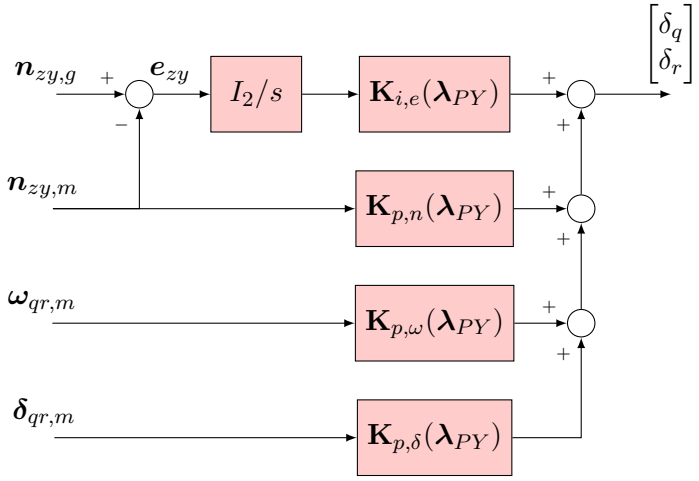

Figure A.11: Structure de l'autopilote de tangage/lacet

Les huit gains du contrôleur sont calculés en résolvant un problème de synthèse mixte $\mathcal{H}_2/\mathcal{H}_\infty$ à l'aide de `systune`. Comme pour l'autopilote de roulis, on introduit des fonctions de pondération $W_S(s)$ et $W_{KS}(s)$, et un modèle du second ordre est encore une fois utilisé pour exprimer une contrainte de suivi de modèle, de pulsation $\omega_{ref,PY} = 5$ rad/s et facteur d'amortissement $\xi_{ref,PY} = 0.781$. La fonction objectif associée est exprimée dans le domaine temporelle (la formulation classique dans le domaine fréquentiel conduit à des marges de robustesse moins élevées, et à des surfaces de gain moins lisses sur l'enveloppe de vol). La fonction `systune` minimise ainsi la quantité donnée par :

$$f(\boldsymbol{\kappa}_{PY}) = \frac{\left\| \frac{1}{s} \mathcal{T}_{\boldsymbol{n}_{zy,g} \to \boldsymbol{e}_{zy,ref}}(s) \right\|_2}{\eta \left\| \frac{1}{s} [T_{ref,PY}(s) - I] \right\|_2} \tag{A.28}$$

avec $\boldsymbol{\kappa}_{PY}$ contenant les huit gains du contrôleur, et η un paramètre à fixer, représentant l'écart relatif maximal toléré par rapport au modèle de référence (des valeurs élevées de η réduisent l'indice de performance, relaxant la contrainte). Cette valeur est fixée ici à 0.05. Le problème de

synthèse pour un point de design $\boldsymbol{\lambda}_{PY}$ de l'enveloppe de vol réduite s'écrit donc :

$$\begin{aligned} \underset{\boldsymbol{\kappa}_{PY}}{\text{minimise}} \quad & f(\boldsymbol{\kappa}_{PY}) \\ \text{subject to} \quad & \left\| W_S(s)\mathcal{T}_{d_z \to n_z}(s) \right\|_\infty < 1 \\ & \left\| W_S(s)\mathcal{T}_{d_y \to n_y}(s) \right\|_\infty < 1 \\ & \left\| W_{KS}(s, \boldsymbol{\lambda}_{PY})\mathcal{T}_{\boldsymbol{d}_{zy} \to bm\delta_{qr}}(s) \right\|_\infty < 1 \end{aligned} \tag{A.29}$$

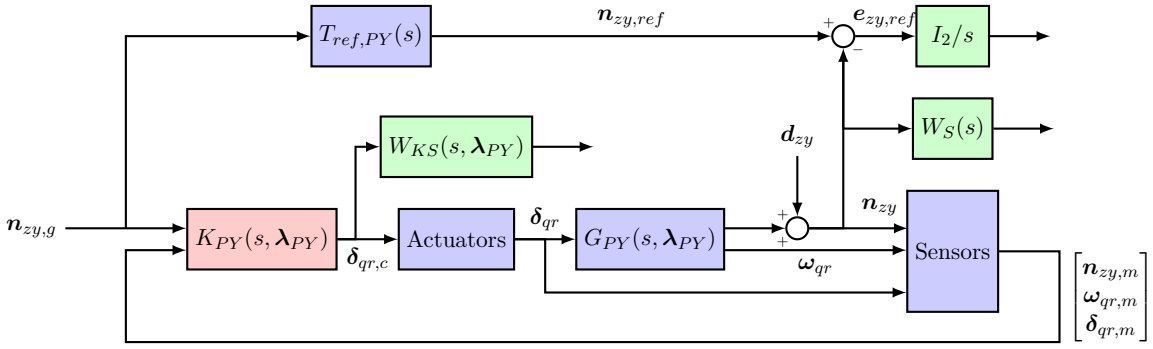

Figure A.12: Problème de synthèse $\mathcal{H}_2/\mathcal{H}_\infty$ structurée pour l'autopilote de tangage/lacet

La variation de l'autorité de contrôle sur l'enveloppe de vol est prise en compte à travers une paramétrisation adaptée de la fonction de pondération $W_{KS}(s, \boldsymbol{\lambda}_{PY})$. Cette paramétrisation repose sur l'introduction d'un facteur multiplicatif $k(\boldsymbol{\lambda}_{PY})$, dont la valeur est donnée par le gain statique de l'entrée δ_q à la sortie n_z. La fonction de pondération $W_{KS}(s, \boldsymbol{\lambda}_{PY})$ est alors donnée par :

$$W_{KS}(s, \boldsymbol{\lambda}_{PY}) = k(\boldsymbol{\lambda}_{PY}) \cdot \hat{W}_{KS}(s) \tag{A.30}$$

avec $\hat{W}_{KS}(s)$ à paramétrer.

Un point de design $\boldsymbol{\lambda}_{PY0}$ correspondant à une vitesse propre $V = 340$ m/s, à altitude $h = 0$ m, et pour une vitesse de rotation du projectile $p_a = 1200$ rad/s, est choisi pour réaliser une première synthèse locale. Ce point est typique d'une fin de trajectoire, moment où la performance est critique pour garantir la précision à l'impact. Les fonctions de pondération sont paramétrées comme suit :

$$W_S(s) = \frac{s+5}{2s + 5 \cdot 10^{-4}} \qquad \hat{W}_{KS}(s) = \frac{s+110}{10^{-2}s + 110 \cdot 3} \tag{A.31}$$

La réponse à un échelon en boucle fermée est donnée par la Figure A.13. L'indice de performance associé est à 2.52. La Figure A.14 montre les fonctions de transfert façonnées, illustrant la satisfaction des contraintes définies par les fonctions de pondération.

Ce même problème de synthèse est résolu sur un maillage de l'enveloppe de vol réduite. Le maillage considéré est de dimension $7 \times 6 \times 5$, pour un total de 210 points de vol. Les contraintes sont respectées pour tous les points, tandis que l'indice de performance atteint une valeur pire cas de 4.86, au point $(V, h, p_a) = (380 \text{ m/s}, 9000 \text{ m}, 750 \text{ rad/s})$. La réponse à un échelon demeure néanmoins satisfaisante, comme le montre la Figure A.13. Les Figures A.15 et A.16 montrent les valeurs prises par les gains du contrôleur, sous la forme de surfaces paramétrées par V et h, pour les valeurs extrémales de p_a. Les surfaces sont relativement lisses, à l'exception de celles

des gains $K_{p,\delta}^{(11)}$ et $K_{p,\delta}^{(12)}$, dont les variations restent néanmoins cantonnées à de petits intervalles.

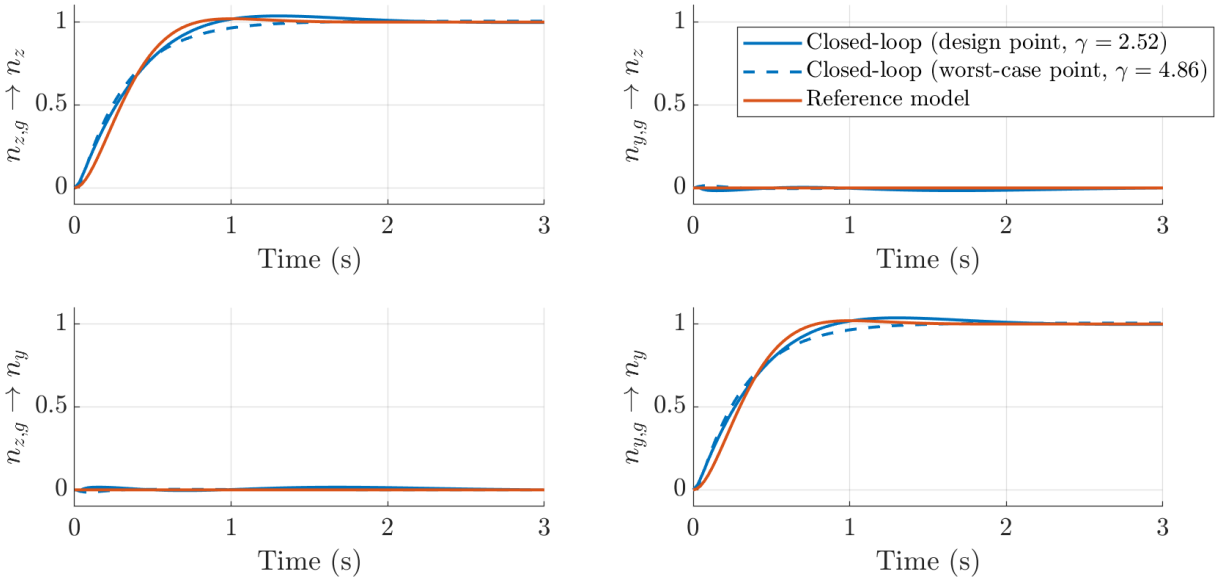

Figure A.13: Réponse à un échelon de la boucle fermée au point de design (en trait plein), et réponse pire-cas (en pointillé)

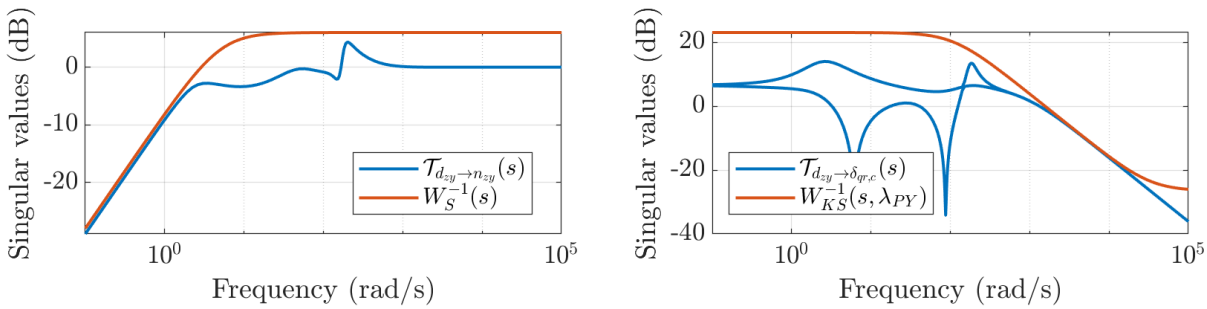

Figure A.14: Fonctions de transfert façonnées pour le rejet de perturbation (gauche) et l'atténuation du signal de commande (droite)

La robustesse aux incertitudes est vérifiée en chaque point du maillage avec la μ-analyse. Les modèles LFR sont paramétrés par $\boldsymbol{\lambda}_{PY} = [V \ h \ p_a]^T$, et constitués d'un système LTI $M_{PY}(s, \boldsymbol{\lambda}_{PY})$ à 16 états et d'un bloc Δ_{PY} élément de l'ensemble :

$$\mathcal{B}_{\boldsymbol{\Delta}PY} = \left\{ \text{diag}(\delta_{C_{N\alpha}} I_2, \delta_{C_{N\delta}} I_2, \delta_{C_A} I_2, \delta_{C_{Yp\alpha}} I_2, \delta_{C_{m\alpha}} I_2, \delta_{C_{mq}} I_2, \delta_{C_{m\delta}} I_2, \delta_{C_{np\alpha}} I_2) : \delta_\bullet \in [-1, 1] \right\} \tag{A.32}$$

Seul le point $(V, h, p_a) = (300 \text{ m/s}, \ 3000 \text{ m}, \ 750 \text{ rad/s})$ du maillage ne valide pas la stabilité robuste, avec $\mu \in [1.009, \ 1.02]$ ($k_r \in [0.980, 0.991]$). Ce point correspond à une vitesse propre légèrement inférieure à Mach 1, qui correspond à des extrema ou des fortes variations de la plupart des coefficients aérodynamiques, ainsi qu'à une valeur de p_a peu élevée, c'est-à-dire à une plus faible contribution gyroscopique à la stabilité. Cependant, la μ-analyse probabiliste est ici utile pour établir que la probabilité d'instabilité est en fait très faible, à moins de 0.013% dans le cas d'une distribution uniforme des incertitudes, et à environ $9 \cdot 10^{-7}$% pour une distribution normale (pour laquelle le 3σ correspond à des niveaux d'incertitude maximaux).

L'application des algorithmes de μ-analyse probabiliste pour l'évaluation de la performance

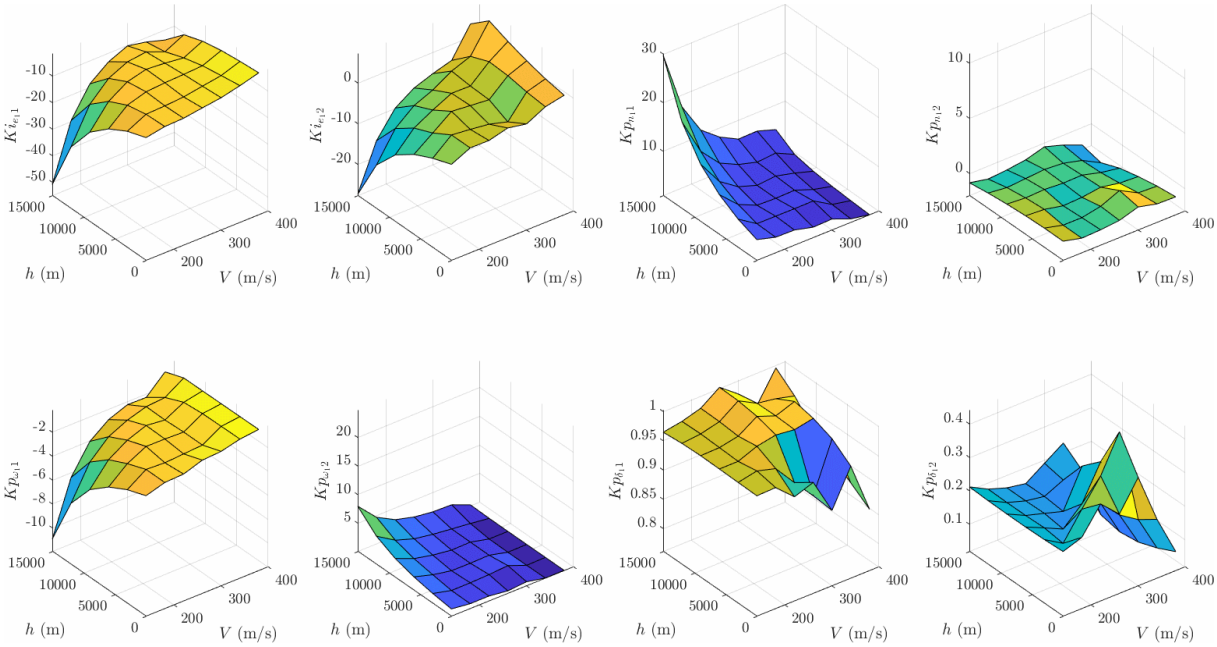

Figure A.15: Surface de gains à $p_a = 750$ rad/s

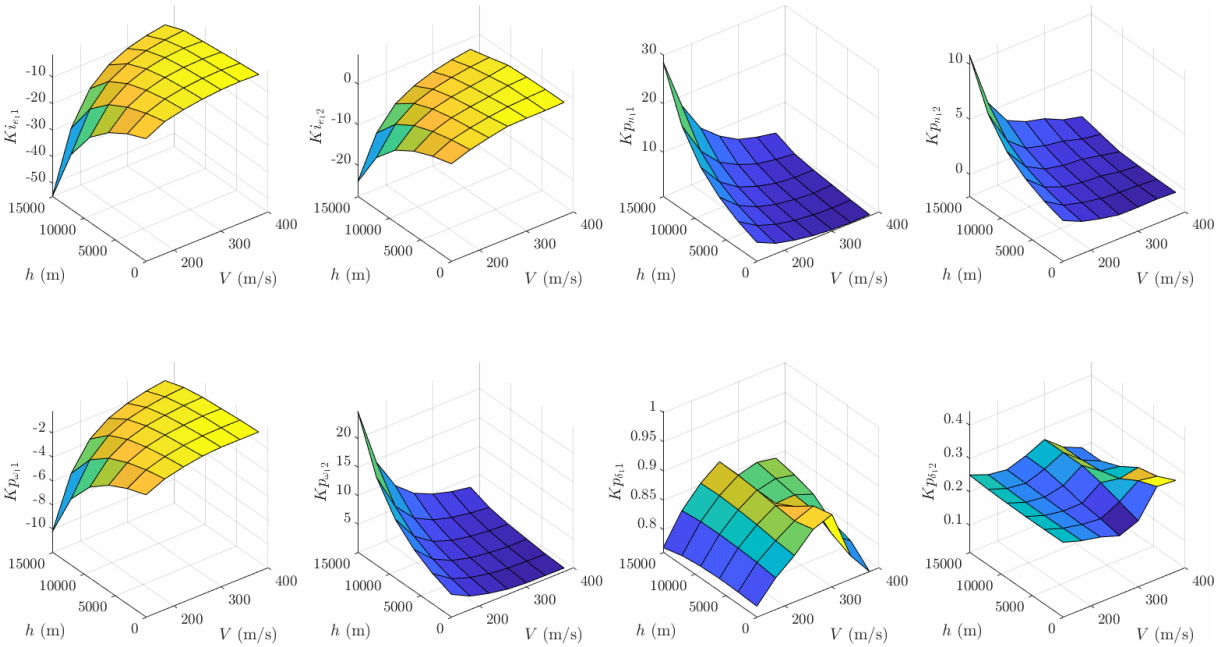

Figure A.16: Surface de gains à $p_a = 1650$ rad/s

$\mathcal{H}_\infty$ et des marges donne ici lieu à des écarts importants entre bornes supérieures et inférieures, indiquant qu'une partie importante du domaine des paramètres incertains n'est pas catégorisée. Toutefois, il est possible de conclure sur certaines propriétés de robustesse sans recourir à une exploration exhaustive du domaine. Ainsi, en modifiant le critère d'arrêt de l'algorithme de branch-and-bound, et en priorisant les domaines proches de la configuration pire cas, il est très rapide d'invalider les niveaux de marge de 6 dB et de 30 deg en des points de vol représentatifs d'une trajectoire balistique. Dans un second temps, on peut vérifier que des marges moins exigeantes, à 3 dB et 25 deg, sont robustement validées au sens probabiliste. Ces marges sont jugées suffisantes pour poursuivre avec la synthèse anti-windup, traitée au chapitre suivant.

A.3.3 Conclusion

Ce chapitre présente des contributions théoriques majeures en μ-analyse probabiliste, qui ont mené au développement de nouveaux algorithmes de type branch-and-bound pour étudier la stabilité, la performance $\mathcal{H}_\infty$, et les marges de gain/phase/module d'un système incertain. Grâce à ces méthodes, il est désormais possible de quantifier le conservatisme de la μ-analyse standard, et de calculer des bornes sur les probabilités recherchées, ce que ne permettent pas les méthodes de Monte Carlo. Une idée clé, commune à tous les algorithmes développés, consiste à formuler des conditions suffisantes pour garantir la non-satisfaction du critère testé sur un sous-domaine de l'espace des paramètres incertains.

Concernant l'application du projectile guidé, des autopilotes séquencés ont été calculés pour l'axe de roulis d'une part, et les axes de tangage/lacet d'autre part. Les gains des contrôleurs sont obtenus par synthèse $\mathcal{H}_\infty$ structurée. Dans le cas de l'autopilote de roulis, une seule synthèse est effectuée, et l'adaptation des gains au point de vol est réalisée par introduction d'un facteur d'échelle. La boucle fermée présente de bonnes propriétés de robustesse, et la μ-analyse probabiliste permet notamment de calculer de très bonnes approximations des distributions de performance $\mathcal{H}_\infty$ et des marges. Concernant l'autopilote de tangage/lacet, plusieurs synthèses locales sont dans un premier temps réalisées sur un maillage de l'enveloppe de vol réduite. L'autopilote global est ensuite obtenu en interpolant linéairement les gains. Un unique point de vol ne valide pas la stabilité robuste, mais l'application de la μ-analyse probabiliste permet de montrer que la probabilité de se trouver dans une configuration instable est en fait négligeable.

A.4 Développement de compensateurs anti-windup

A.4.1 Introduction

L'objectif de ce chapitre est de traiter les saturations, qui n'ont pas été prises en compte dans la conception de l'autopilote baseline des axes de tangage/lacet. Les saturations peuvent provoquer un grand nombre de phénomènes non linéaires indésirables, tels que des cycles limites, une perte de performance, voire l'instabilité. Dans la procédure en deux étapes adoptée ici, l'ajout d'un compensateur anti-windup à la baseline a pour but d'atténuer les effets des saturations. Ce composant supplémentaire devient actif et modifie le comportement en boucle fermée lorsque les saturations sont atteintes. En revanche, les propriétés de la boucle fermée initiale sont préservées dès lors qu'aucune saturation n'a lieu.

Trois architectures anti-windup sont considérées pour la boucle fermée des axes de tangage/lacet du projectile guidé. La première consiste en un compensateur statique DLAW maximisant un domaine de stabilité. La deuxième et la troisième sont toutes deux des compensateurs MRAW basés LQ, respectivement d'ordre plein et d'ordre réduit. Les trois approches nécessitent peu de réglage, ce qui rend la synthèse sur un maillage de l'enveloppe de vol très simple. Les boucles fermées augmentées qui en résultent sont ensuite évaluées et comparées via des simulations temporelles et une analyse IQC.

A.4.2 Synthèse des travaux

Mise en place du problème anti-windup et synthèse de compensateurs

Le principe de la compensation anti-windup est illustré par la Figure A.17. Le compensateur anti-windup $AW(s)$ prend en entrée la différence $\mathrm{Dz}(y_c) = y_c - \mathrm{Sat}(y_c)$ entre le signal de contrôle souhaité y_c et celui réalisé en sortie de la saturation $u = \mathrm{Sat}(y_c)$, et génère un signal $v = [v_1\ v_2]^T$ utilisé pour modifier la dynamique du contrôleur.

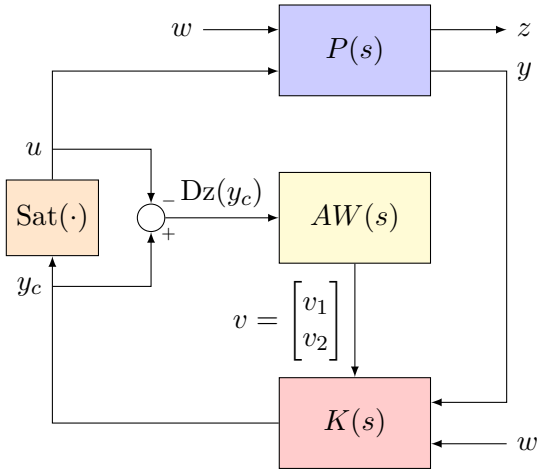

Figure A.17: Principe de la compensation anti-windup

Dans l'application étudiée, les signaux en sortie de l'autopilote baseline $\boldsymbol{\delta}_{qr,c} = [\delta_{q,c}\ \delta_{r,c}]^T$ sont les signaux virtuels. La saturation en amplitude à $l = 10\,\mathrm{deg}$ ne s'applique cependant pas à ces signaux, mais bien aux angles de déflexion des canards $\boldsymbol{\delta}_{R,c} = [\delta_{1,c}\ \delta_{2,c}\ \delta_{3,c}\ \delta_{4,c}]^T$. Afin de se placer dans le cadre du problème anti-windup, on fait apparaître les angles de déflexion réels en utilisant la matrice d'allocation. On suppose que l'angle de roulis ϕ_f de la FCT est stabilisé à la valeur souhaitée, et que la contribution du signal de contrôle virtuel δ_p de l'axe de roulis sur les angles de déflexion réels est négligeable. L'allocation s'exprime alors ainsi :

$$\boldsymbol{\delta}_{R,c} = \begin{bmatrix} -\sin\phi_f & \cos\phi_f \\ \cos\phi_f & \sin\phi_f \\ \sin\phi_f & -\cos\phi_f \\ -\cos\phi_f & -\sin\phi_f \end{bmatrix} \boldsymbol{\delta}_{qr,c} \tag{A.33}$$

L'équation (A.33) implique $\delta_{1,c} = -\delta_{3,c}$ et $\delta_{2,c} = -\delta_{4,c}$. Dans le cadre de la synthèse anti-windup, les signaux $\delta_{1,c}$ et $\delta_{3,c}$ sont donc redondants, et il en est de même pour les signaux $\delta_{2,c}$ et $\delta_{4,c}$. Ainsi, suivant les notations du schéma de la Figure A.17, on définit l'entrée y_c de la saturation normalisée par :

$$y_c = \frac{1}{l}\begin{bmatrix}\delta_{1,c}\\ \delta_{2,c}\end{bmatrix} = \frac{1}{l}\begin{bmatrix}-\sin\phi_f & \cos\phi_f \\ \cos\phi_f & \sin\phi_f\end{bmatrix}\boldsymbol{\delta}_{qr,c} = \frac{1}{l}M(\phi_f)\boldsymbol{\delta}_{qr,c} \tag{A.34}$$

Ces transformations préliminaires sont illustrées par la Figure A.18 (notons que $M^{-1}(\phi_f) = M(\phi_f)$), avec $P_{PY}(s, \boldsymbol{\lambda}_{PY})$ réunissant les dynamiques de tangage/lacet (4 états), deux actionneurs virtuels ($2 \times 2 = 4$ états), et les capteurs (6 états), pour un total de 14 états.

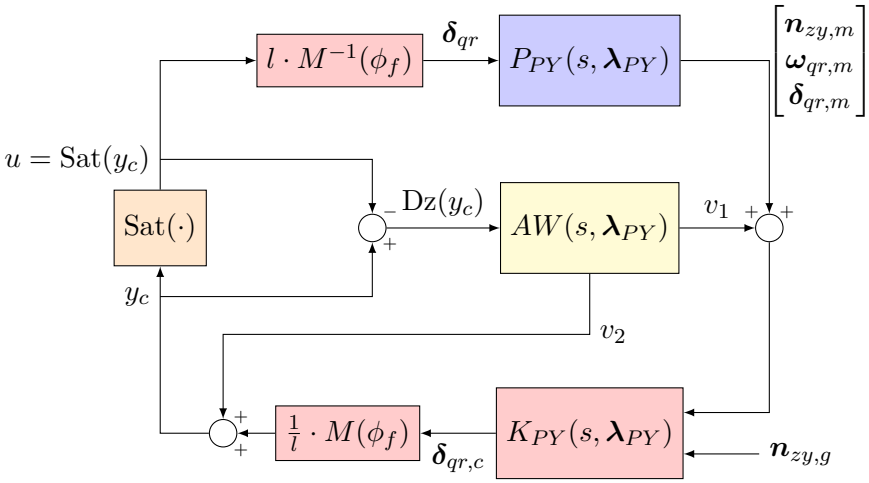

Figure A.18: Système en boucle fermée avec compensation anti-windup

Remarque : *Les actionneurs et capteurs réels peuvent également être utilisés dans* $P_{PY}(s, \boldsymbol{\lambda}_{PY})$*, augmentant le nombre d'états à 20. Cependant, cela n'impacte pas l'entrée du compensateur anti-windup, et ne présente donc pas d'intérêt pour la synthèse.*

De l'équation (A.34) et la relation $u = \mathrm{Sat}(y_c)$, il apparaît clairement que l'angle de roulis ϕ_f de la FCT joue un rôle dans l'occurrence ou non de saturations. Plus précisément, pour une valeur donnée de ϕ_f, l'ensemble des signaux virtuels (δ_q, δ_r) qui ne conduisent pas à des saturations est donné par l'intérieur d'un carré dans le plan (δ_q, δ_r), dont l'orientation dépend de ϕ_f. La Figure A.19 montre cet ensemble pour les deux orientations standards de la FCT, à savoir la configuration '+' ($\phi_f = 0\,\mathrm{deg}$) et la configuration '×' ($\phi_f = 45\,\mathrm{deg}$). Sur la base de simulations non-linéaires pour des scénarios de tir réalistes, il apparaît que la configuration '×' est préférable pour limiter le risque de saturations. C'est donc la valeur $\phi_f = 45\,\mathrm{deg}$ que l'on retiendra comme hypothèse pour la synthèse du compensateur anti-windup pour les axes de tangage/lacet.

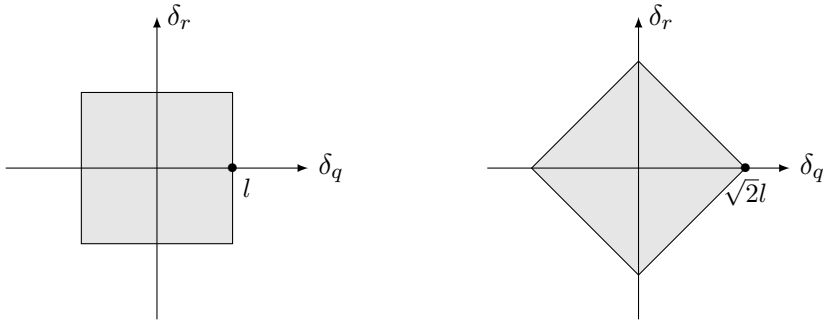

(a) Configuration '+' : $\phi_f = 0\,\mathrm{deg}$ (b) Configuration '×' : $\phi_f = 45\,\mathrm{deg}$

Figure A.19: Ensemble des signaux virtuels ne menant pas à des saturations

De nombreuses méthodes permettent de calculer des compensateurs anti-windup dans un contexte stationnaire. La théorie anti-windup moderne, telle que décrite par exemple par [Galeani et al., 2009], identifie deux familles de méthodes pour la synthèse anti-windup : l'approche DLAW (*Direct Linear Anti-Windup*) et l'approche MRAW (*Model Recovery Anti-Windup*). Ces approches sont formulées dans un contexte stationnaire. Les garanties théoriques sur les domaines de stabilité ou les niveaux de performance ne sont donc pas préservées quand des variations

paramétriques entrent en jeu. Néanmoins, ces méthodes demeurent intéressantes pour le calcul de compensateurs locaux, qui peuvent être ensuite interpolés pour couvrir l'enveloppe de vol. Dans ce contexte, les méthodes ne nécessitant que peu de réglages sont préférables car plus faciles à implémenter. Selon ce critère de simplicité, on retiendra trois méthodes de synthèse anti-windup, mises en œuvre sur le même maillage de dimension $7 \times 6 \times 5$ de l'enveloppe de vol réduite que pour l'autopilote de tangage/lacet.

La première méthode est issue de l'approche DLAW. On y impose de plus $v_2 = 0$ afin d'éviter de créer une boucle algébrique. Les synthèses locales sont réalisées à l'aide de la bibliothèque SAW de la toolbox SMAC (`https://w3.onera.fr/smac/saw`), de sorte à maximiser l'amplitude des échelons sur les signaux d'entrée $\boldsymbol{n}_{zy,g}$ pour laquelles la stabilité est garantie [Biannic and Tarbouriech, 2009]. Le compensateur global est alors obtenu par interpolation linéaire des coefficients de la matrice $D_{aw,1} \in \mathbb{R}^{2\times 2}$. Ce compensateur est également décrit dans [Thai et al., 2020].

Le second compensateur anti-windup considéré est issu de la méthode MRAW basée LQ applicable aux systèmes instables [Galeani et al., 2009]. Suivant les notations de la Figure A.20, le signal anti-windup $\tilde{v}_2$ est donné par $\tilde{v}_2 = K_{lqr} x_{aw}$, et minimise l'indice de performance LQ :

$$J = \int_0^\infty \left(x_{aw}^T Q x_{aw} + \tilde{v}_2^T R \tilde{v}_2 \right) dt \tag{A.35}$$

Une même fonction coût J est utilisée pour chaque point du maillage. On contraint davantage les états liés aux actionneurs en choisissant $Q = \mathrm{diag}(I_{10}, 50 \cdot I_4)$ et $R = I_2$. Les compensateurs locaux étant d'ordre élevé $n_{aw} = 14$, une interpolation des coefficients de la représentation d'état est difficilement envisageable. On choisira donc d'interpoler les signaux de sortie [Kelly et al., 1997]. Ce compensateur est décrit dans [Thai et al., 2021].

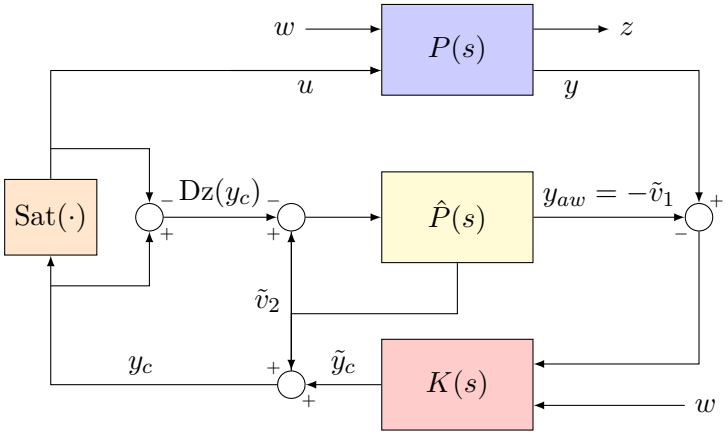

Figure A.20: Architecture MRAW

Le troisième compensateur anti-windup proposé exploite la même méthode que le second, mais utilise un modèle réduit du système à contrôler, dans lequel on retire les dynamiques des actionneurs et des capteurs. Le compensateur qui en résulte est donc un système d'ordre $n_{aw} = 4$. Le calcul est effectué avec $Q = I_4$ et $R = I_2$, et le séquencement est encore une fois réalisé par interpolation des sorties.

La Figure A.21 montre les réponses en boucle fermée à des échelons au point de design

$\boldsymbol{\lambda}_{PY0}$, pour différentes configurations anti-windup. L'amplitude de l'échelon $n_{y,g}$ est donnée par $n_{y,g} = 1.05 \cdot n_{y,sat}$, avec $n_{y,sat}$ la plus petite valeur conduisant à des angles de déflexion dépassant les 10 deg en amplitude en moins de dix secondes. Les facteurs de charge tracés sur les figures sont normalisés, avec $\hat{n}_z = n_z/n_{y,sat}$ et $\hat{n}_y = n_y/n_{y,sat}$. En l'absence de compensation anti-windup, les angles de déflexion finissent tous par atteindre la saturation, ce qui conduit à des erreurs importantes sur les facteurs de charge, ainsi qu'à des oscillations mal amorties. Tous les compensateurs proposés permettent d'améliorer la réponse de manière significative. De façon remarquable, les compensateurs MRAW d'ordre plein et MRAW réduit donnent lieu à des réponses quasiment identiques, malgré la différence d'ordre importante entre les deux.

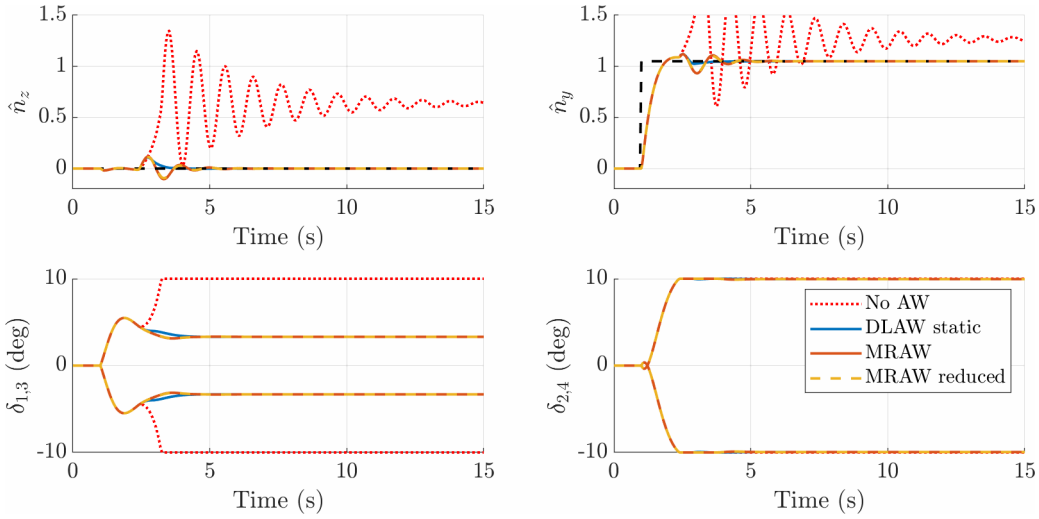

Figure A.21: Réponses à des échelons pour différentes configurations anti-windup

Analyse IQC

La robustesse de la boucle fermée pour des valeurs fixes des paramètres de séquencement est étudiée grâce aux méthodes d'analyse IQC, décrite en détail dans [Megretski and Rantzer, 1997; Veenman et al., 2016]. D'un point de vue pratique, la procédure d'analyse IQC basée sur l'application du lemme de Kalman-Yakubovich-Popov (KYP) peut se résumer en ces quelques étapes :

1. construire la LFR $(M(s), \Delta)$, avec $M(s)$ un système LTI stable, et où $\Delta = \text{diag}(\Delta_1, \ldots, \Delta_N)$ contient les incertitudes et non-linéarités du système,

2. pour chaque bloc Δ_i, choisir une classe appropriée de multiplicateurs $\Pi_i = \Psi_i^* P_i \Psi_i$, avec Ψ_i fixé (plusieurs choix sont possibles pour une même classe de multiplicateur), et où chaque P_i appartient à un ensemble $\boldsymbol{P}_i$ défini par des contraintes LMI,

3. construire le multiplicateur composite $\Psi^* P \Psi$ [**VeenmanEtA2016**],

4. calculer une réalisation minimale du système de la Figure A.22,

5. minimiser γ sous les contraintes LMI issues de l'application du lemme de KYP et $P \in \boldsymbol{P}$.

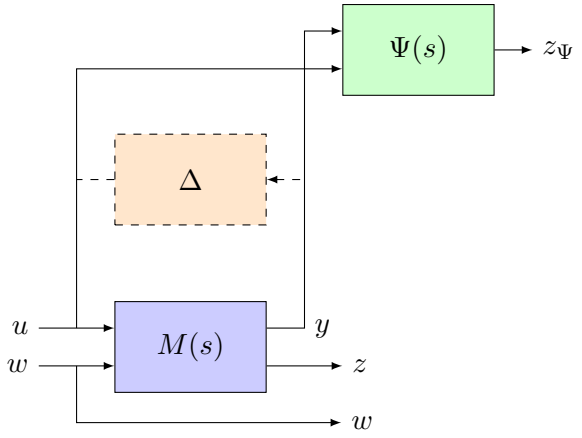

Figure A.22: Analyse IQC pour la performance

L'étape préliminaire de mise sous forme LFR des axes de tangage/lacet du projectile est réalisée à l'aide de la bibliothèque GSS. Le bloc Δ qui en résulte contient le bloc $\Delta_{PY} \in \mathcal{B}_{\boldsymbol{\Delta}PY}$ des incertitudes aérodynamiques, de taille 16×16, mais également une non-linéarité de type zone morte de dimension 2 :

$$\begin{aligned}\hat{\mathcal{B}}_{\boldsymbol{\Delta}PY} = \Big\{ &\mathrm{diag}(\delta_{C_{N\alpha}} I_2, \delta_{C_{N\delta}} I_2, \delta_{C_A} I_2, \delta_{C_{Yp\alpha}} I_2, \delta_{C_{m\alpha}} I_2, \delta_{C_{mq}} I_2, \\ &\delta_{C_{m\delta}} I_2, \delta_{C_{np\alpha}} I_2, \mathrm{Dz}(\cdot)) \colon \delta_\bullet \in [-1, 1] \big\}\end{aligned} \tag{A.36}$$

Le canal de performance considéré a pour entrée les signaux de guidage $\boldsymbol{n}_{zy,g}$, et pour sortie les erreurs $\boldsymbol{e}_{zy,ref}$ par rapport au modèle de référence d'ordre 2 $T_{ref,PY}(s)$ (voir Figure A.12).

La robustesse aux zones mortes et aux incertitudes aérodynamiques est ensuite évaluée. On décrit localement les zones mortes comme des non-linéarités de secteur, et de pente bornée $\Phi \in \mathrm{sec}[0, b]^2 \cap \mathit{slope}[0, b]^2$. On associe à cette description un multiplicateur combinant le critère du cercle (voir la Classe 13 dans [Veenman et al., 2016]) et les multiplicateurs de Zames-Falb [Fetzer and Scherer, 2017]. Ces derniers requièrent de choisir les pôles réels et leur multiplicité afin de construire une base de fonctions dans le domaine fréquentiel. On choisira les pôles -10 et -100, tous deux de multiplicité 1, qui donnent de bons résultats, mais sans garantie d'optimalité. Les incertitudes aérodynamiques sont décrites à l'aide de multiplicateurs de "*DG*-scaling", avec un pôle à -10 de multiplicité 1 pour chaque incertitude (voir la Classe 5 dans [Veenman et al., 2016]). Les incertitudes aérodynamiques normalisées peuvent alors varier dans l'intervalle $[-a, a]$, pour $a \leq 1$. On peut ensuite calculer une borne supérieure $\overline{\gamma}$ du gain $\mathcal{L}_2$ pour des valeurs données de $b \in [0, 1]$ et $a \in [0, 1]$. Le cas $a = 0$ correspond au test IQC sans incertitudes aérodynamiques. Le cas $b = 0$ correspond au calcul de la performance $\mathcal{H}_\infty$ pire cas, que l'on peut aussi obtenir en utilisant la μ-analyse asymétrique. Le Tableau A.2 montre quelques propriétés des problèmes LMI associés à l'analyse IQC, ainsi que le temps de résolution moyen pour a et b fixés.

La Figure A.23 montre les surfaces obtenues pour différentes configurations anti-windup. Pour les configurations sans anti-windup et avec anti-windup statique DLAW, la valeur de b pour laquelle la stabilité est garantie diminue fortement quand on fait grandir a. Les deux configurations MRAW sont relativement plus robustes, puisqu'à b fixé, des valeurs plus élevées de a mènent dans la plupart des cas à un gain $\mathcal{L}_2$ fini, bien que la borne sur ce gain soit dégradée.

Table A.2: Charge de calcul de l'analyse IQC avec zones mortes et incertitudes aérodynamiques

Configuration	**Pas d'AW**	**DLAW statique**	**MRAW**	**MRAW réduit**
Ordre du système augmenté (réalisation minimale)	60	60	70	69
Nombre de variables de décision	2012	2012	2667	2597
Temps de calcul moyen (s)	11.7	9.9	17.2	17.1

On note également que les surfaces obtenues pour le MRAW et le MRAW réduit coïncident quasiment pour des petites valeurs et des valeurs intermédiaires de b. Cela signifie que pour l'ensemble des non-linéarités de secteur correspondant, les propriétés de performance robuste des configurations MRAW et MRAW réduit sont similaires.

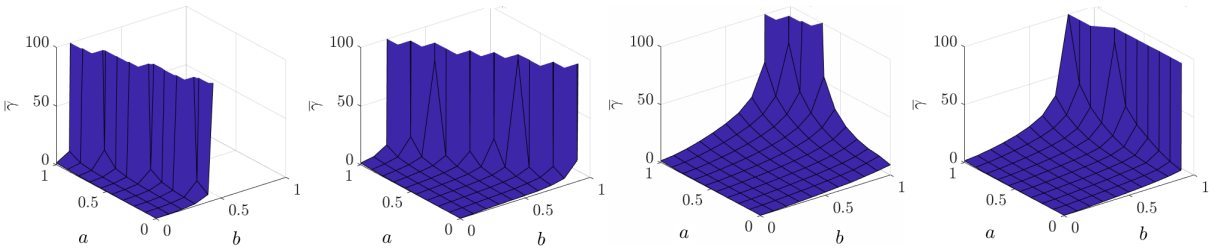

Figure A.23: Bornes sur le gain $\mathcal{L}_2$ en présence d'incertitudes aérodynamiques $|\delta_\bullet| \leq a$ et de non-linéarités de secteur $\Phi \in \text{sec}[0, b]^2 \cap \mathit{slope}[0, b]^2$; de gauche à droite : sans anti-windup, avec anti-windup statique DLAW, avec anti-windup MRAW, avec anti-windup MRAW réduit

A.4.3 Conclusion

Dans ce chapitre, la théorie moderne de l'anti-windup et l'analyse IQC sont appliquées aux axes de tangage et de lacet du projectile guidé afin de calculer et d'évaluer les propriétés de performance et de robustesse de différents compensateurs anti-windup. Des méthodes de synthèse simples, nécessitant peu ou pas de réglage, sont préférées pour faciliter le calcul sur l'ensemble de l'enveloppe de vol. Trois méthodes de ce type sont sélectionnées, à savoir un compensateur DLAW statique, un compensateur MRAW basé LQ d'ordre 14, et un compensateur MRAW réduit d'ordre 4, dans lequel on néglige les dynamiques des actionneurs et des capteurs. Malgré la simplicité des schémas choisis, les simulations temporelles montrent une amélioration considérable de la réponse à un échelon par rapport à la configuration baseline dans un contexte stationnaire. En particulier, les réponses avec le compensateur MRAW réduit sont pratiquement identiques à celles avec le compensateur MRAW complet. Une analyse IQC est ensuite réalisée. Malgré le conservatisme de l'approche, l'amélioration des propriétés de stabilité robuste est confirmée par rapport à la configuration baseline.

A.5 Simulations non-linéaires

A.5.1 Introduction

Dans ce chapitre, on simule des tirs guidés en connectant le modèle non-linéaire du projectile 7DDL du Chapitre 2 aux autopilotes de roulis et de tangage/lacet du Chapitre 3 et aux compensateurs anti-windup du Chapitre 4. On peut alors évaluer la performance selon des critères opérationnels, et l'on se servira notamment de l'écart entre le point d'impact du projectile et la position de la cible. Après analyse d'un scénario de tir nominal, plusieurs cas dégradés sont étudiés. Ceux-ci incluent des perturbations dues au vent, aux incertitudes sur les conditions de tir, ou aux incertitudes sur les coefficients aérodynamiques. Dans chaque cas, on regarde tout d'abord les trajectoires obtenues en désactivant les saturations dans le simulateur de vol. Ceci permet d'une part de valider l'autopilote baseline, et d'autre part d'identifier les cas où les seuils de saturation sont dépassés. Ces derniers sont ensuite rejoués avec saturations activées, afin de constater les dégradations qu'elles induisent. Dans un dernier temps, les compensateurs anti-windup sont implémentés pour vérifier qu'ils entraînent une amélioration des performances.

A.5.2 Synthèse des travaux

Description et simulation d'un scénario de vol nominal

On considère un scénario de vol représentatif d'une mission longue portée, caractérisé par les conditions de lancement suivantes :

$$V_0 = 939 \text{ m/s}, \quad \theta_0 = 42\,\text{deg}, \quad \psi_0 = 0\,\text{deg} \tag{A.37}$$

La cible est située au point d'impact balistique du projectile, à environ 25 km du site de tir. La position de la cible est prise en compte dans la boucle fermée grâce à un module de guidage implémentant une loi de type *zero-effort-miss* (ZEM), décrite par [Proff and Theodoulis, 2019]. En quelques mots, le guidage ZEM utilise une méthode de prédiction du point d'impact pour calculer les erreurs latérales et longitudinales entre la cible et le point d'impact balistique estimé. Ces erreurs sont régulièrement mises à jour en fonction de l'état actuel du projectile, obtenu à partir d'un modèle simplifié, et servent à calculer les facteurs de charge correcteurs $\boldsymbol{n}_{zy,g}$.

La Figure A.24 montre les résultats de simulation avec autopilote baseline. Les données de la trajectoire balistique sont également fournies à titre informatif. Concernant la phase balistique, on observe que l'étape de configuration de la FCT (réduction de la vitesse angulaire p_f et stabilisation de l'angle ϕ_f) est très court, ne durant qu'environ 0.5 s. Pendant la phase guidée, le guidage ZEM génère des consignes en accélération $n_{z,g}$ et $n_{y,g}$ qui restent proches des accélérations balistiques $n_{z,bal}$ et $n_{y,bal}$. Ces signaux de guidage sont suivis avec précision par l'autopilote de tangage/lacet, et la cible est atteinte avec grande précision, puisque l'écart à la cible lors de l'impact est de $5 \cdot 10^{-4}$ m. Comme les angles de déflexion restent inférieurs à $l = 10\,\text{deg}$, la trajectoire ne dépend pas de la présence ou non d'un compensateur anti-windup.

Remarque : *Les axes utilisés pour tracer les trajectoires en 3D n'utilisent pas la même échelle, afin de mettre en évidence la déviation latérale (selon l'axe y).*

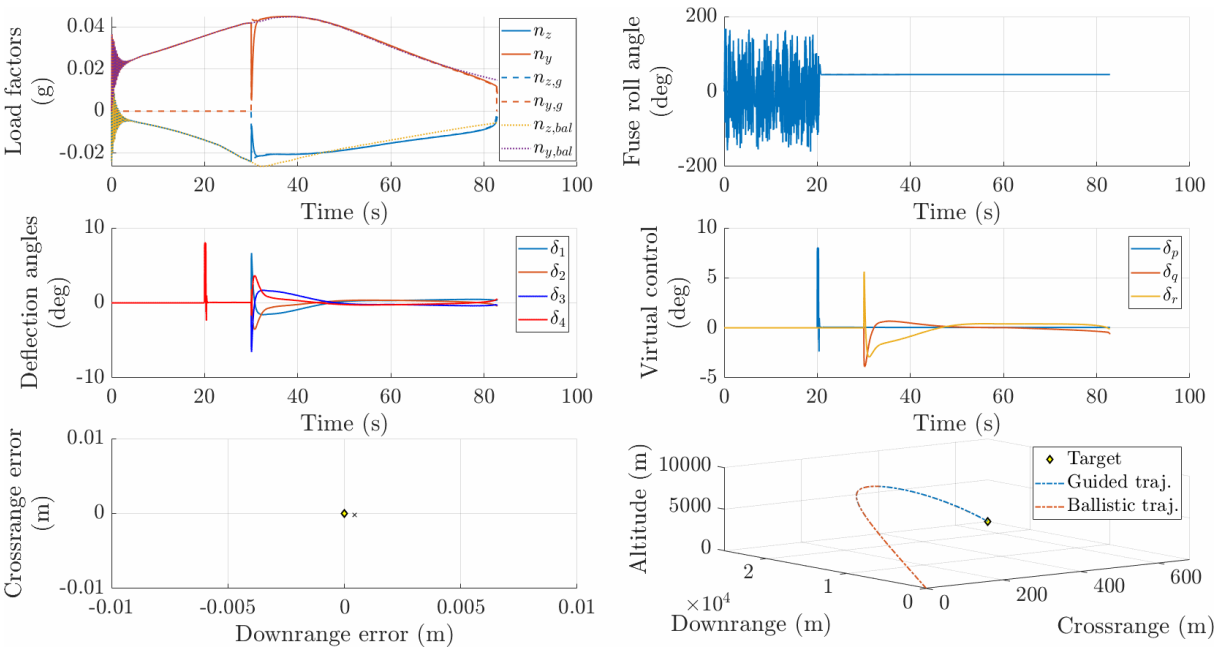

Figure A.24: Scénario nominal avec autopilote baseline : facteurs de charge, angle de roulis de la FCT, angles de déflexion des canards, signaux de contrôle virtuels, écart à la cible, trajectoire

Simulations de scénarios dégradés

La même mission est considérée, cette-fois ci en présence d'un vent horizontal qui contribue à dévier le projectile vers sa droite. Le point d'impact balistique se situe alors à 427.1 m de la cible. La Figure A.25 montre les résultats avec autopilote baseline. L'autopilote requiert des angles de déflexion supérieurs en valeur absolue à 10 deg. Cela conduit à des saturations, et finalement à l'échec de la mission, puisque l'impact a lieu à 67 m de la cible. Les Figures A.26 et A.27 montrent les résultats pour le même scénario, mais cette fois-ci avec compensation anti-windup, respectivement avec les compensateurs DLAW et MRAW réduit (le compensateur MRAW plein donne des résultats identiques au compensateur réduit). Dans ces configurations, le projectile guidé retrouve un comportement satisfaisant, ainsi qu'une précision millimétrique.

Remarque : *En pratique, la perturbation due au vent peut être prise en compte en adaptant l'orientation initiale du canon, afin de rapprocher le point d'impact balistique de la cible. Cette correction contribuerait à réduire les angles de déflexion requis par l'autopilote, potentiellement sous le seuil de saturation. Néanmoins, le scénario présenté ici, sans adaptation de l'orientation du canon, reste pertinent pour illustrer la manœuvrabilité accrue du projectile guidé avec compensation anti-windup.*

On considère ensuite des scénarios dégradés par des incertitudes. On génère un premier lot de 600 trajectoires de Monte Carlo, avec incertitudes sur les conditions de tir (ou conditions initiales). Le tirage des échantillons se base sur une distribution normale autour des valeurs nominales données par l'équation(A.37), avec pour écarts-type 3 m/s, 0.09 deg, et 0.12 deg respectivement pour V_0, θ_0, et ψ_0. En désactivant les saturations dans le simulateur, l'écart à la cible est de l'ordre du millimètre pour toutes les trajectoires. Cependant, 24 cas (4%) mettent en jeu des angles de déflexion dépassant le seuil des 10 deg, et allant jusqu'à 14 deg. La Figure A.28 montre la trajectoire suivi par les signaux de contrôle virtuels dans le plan (δ_q, δ_r) pour ces 24 scénarios.

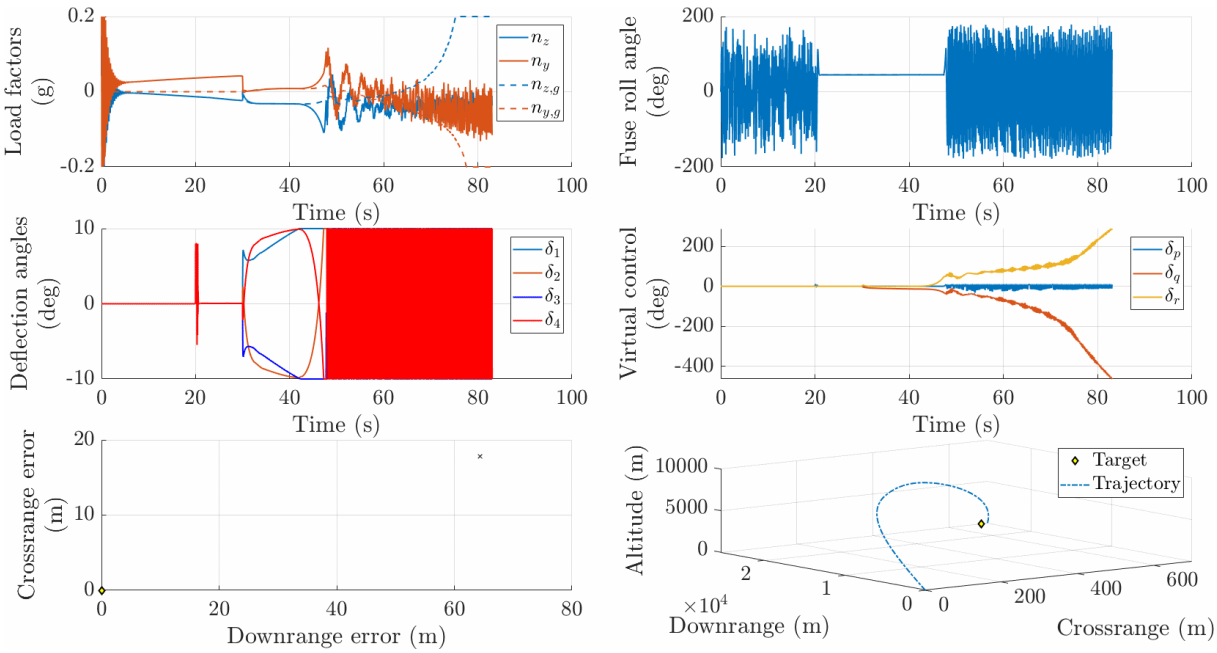

Figure A.25: Scénario avec vent et saturations : facteurs de charge, angle de roulis de la FCT, angles de déflexion des canards, signaux de contrôle virtuels, écart à la cible, trajectoire

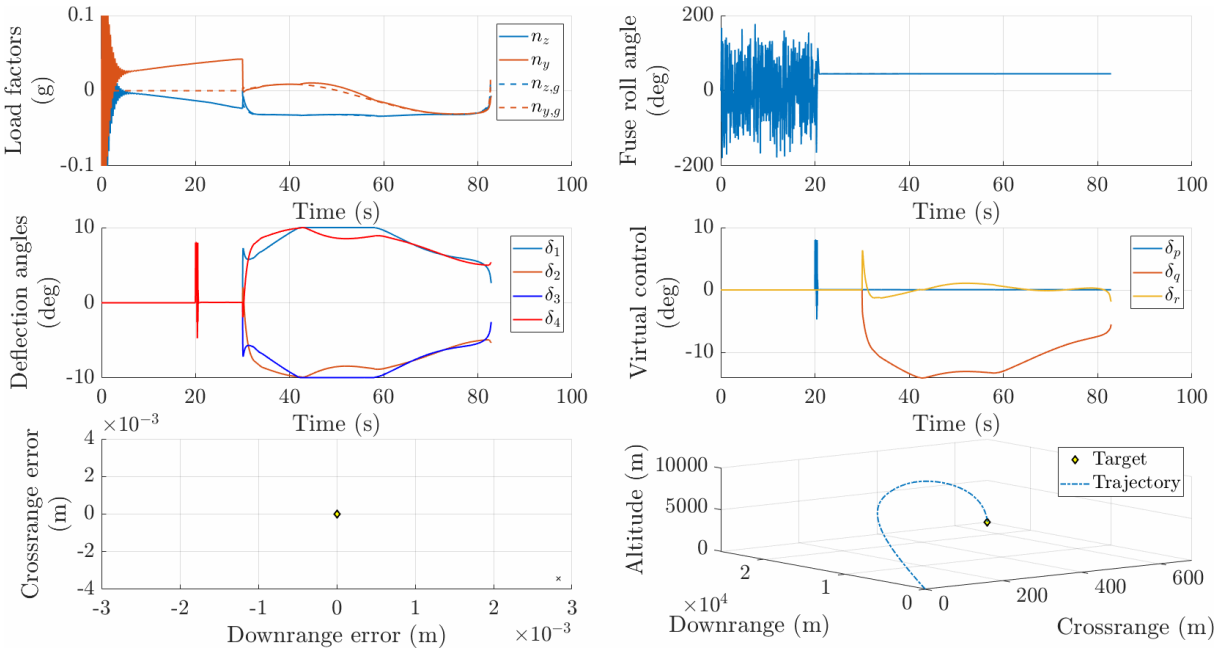

Figure A.26: Scénario avec vent et compensateur DLAW statique séquencé : facteurs de charge, angle de roulis de la FCT, angles de déflexion des canards, signaux de contrôle virtuels, écart à la cible, trajectoire

L'intérieur du carré rouge représente l'ensemble des signaux virtuels qui ne conduisent pas à des saturations, en supposant $\phi_{f,m} = 45\,\text{deg}$ et en négligeant la contribution de δ_p dans l'allocation. Il apparaît clairement que la configuration '×' de la FCT est plus intéressante que la configuration '+' pour limiter le dépassement des signaux de contrôle générés par l'autopilote de tangage/lacet.

La Figure A.29 montre la distance à la cible pour les 24 scénarios avec saturations, pour les différentes configurations du projectile : balistique, avec autopilote baseline seul (c'est-à-dire

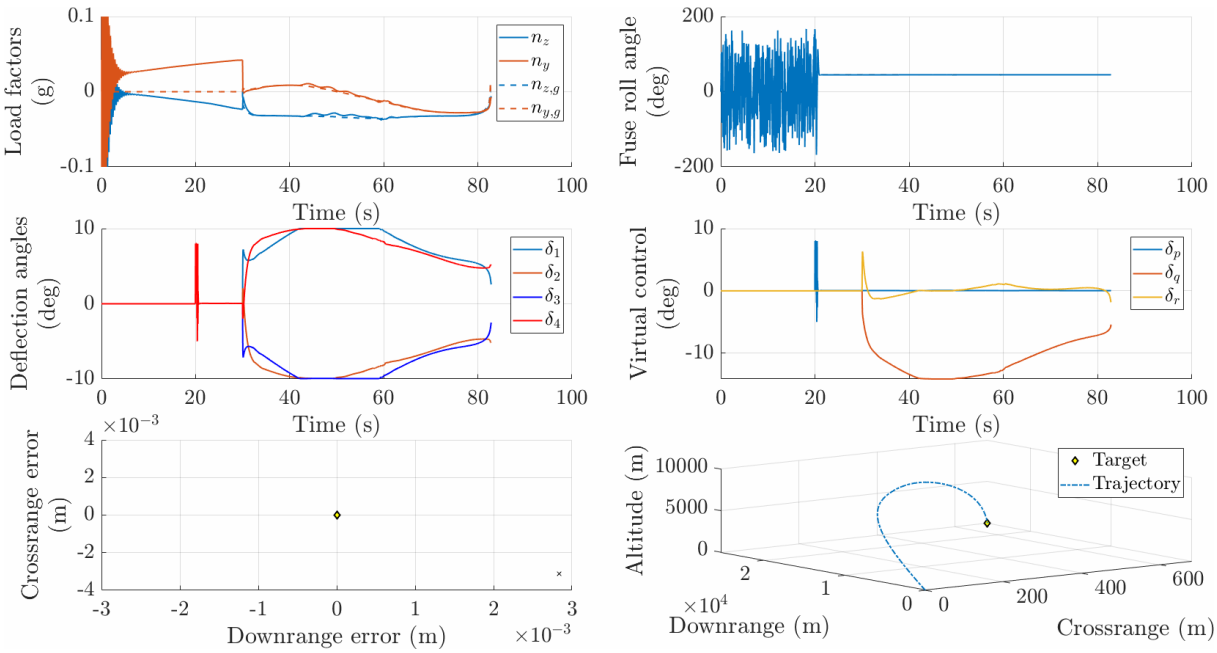

Figure A.27: Scénario avec vent et compensateur MRAW réduit séquencé : facteurs de charge, angle de roulis de la FCT, angles de déflexion des canards, signaux de contrôle virtuels, écart à la cible, trajectoire

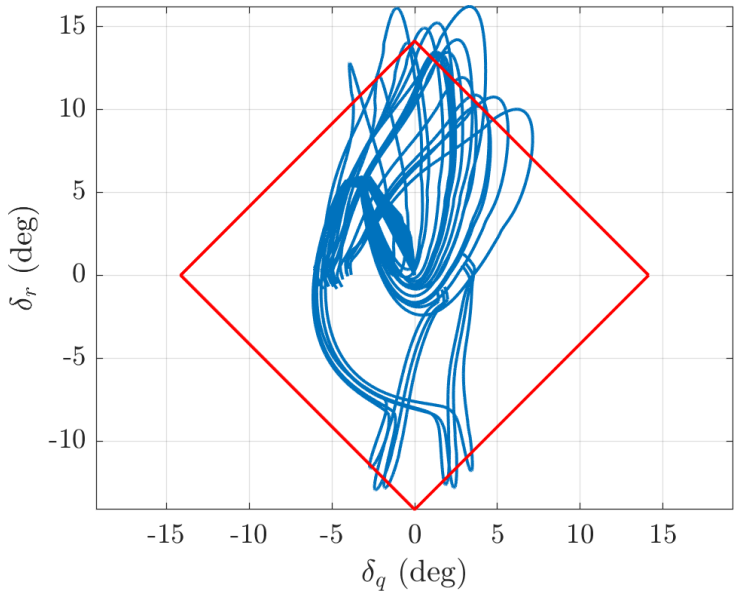

Figure A.28: Trajectoire des signaux de contrôle virtuels dans le plan (δ_q, δ_r) avec incertitudes sur les conditions initiales

sans compensation anti-windup), et avec chacun des trois compensateurs séquencés (DLAW statique, MRAW, et MRAW réduit). Les cas sont ordonnés selon la distance à la cible pour la configuration baseline. On observe que dans certains cas, les saturations ne remettent pas en cause la précision de l'autopilote baseline. Mais l'absence de compensation anti-windup conduit aussi à des cas où la distance à la cible dépasse les 100 m. Les compensateurs anti-windup permettent d'améliorer la performance, puisque presque tous les cas aboutissent à une précision centimétrique. Seuls deux cas font exception, mais la distance à la cible demeure fortement

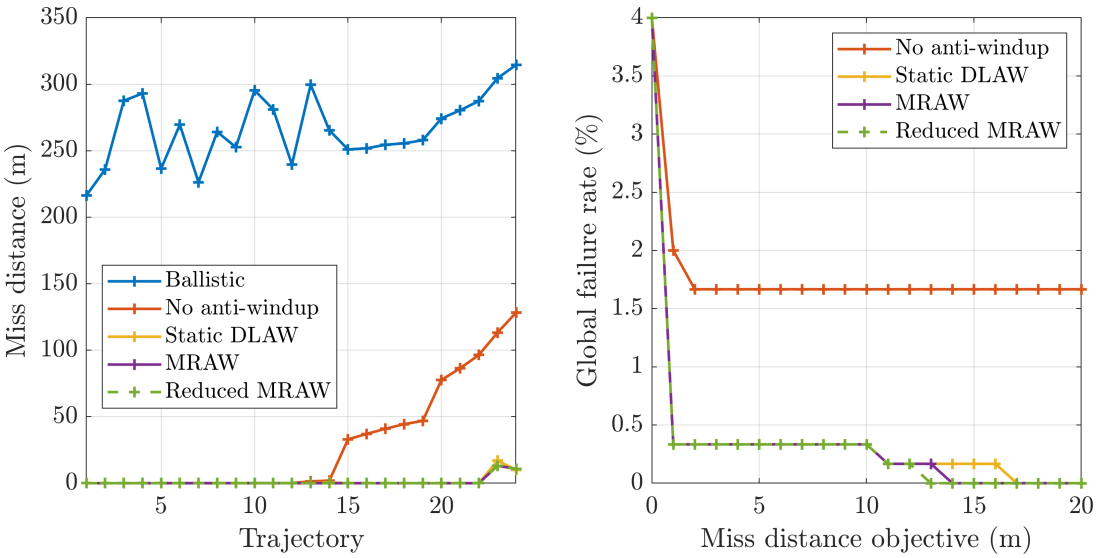

Figure A.29: Écart à la cible pour les 24 scénarios conduisant à des saturations (gauche), et taux d'échec global en fonction de l'écart maximal toléré (droite)

réduite, respectivement à 15 m et 10 m. L'écart à la cible qui peut être toléré étant dépendant de la mission, on trace également sur la Figure A.29 le taux d'échec global en fonction de l'écart maximal toléré. Le Tableau A.3 donne les taux d'échec associés à des seuils de 1 m, 10 m, et 20 m. Aucune distinction n'est faite entre les trois compensateurs anti-windup, car ceux-ci donnent des résultats très similaires.

Objectif	Sans anti-windup	Avec anti-windup
< 1 m	2%	0.3%
< 10 m	1.7%	0.3%
< 20 m	1.7%	0%

Table A.3: Taux d'échec global à 1, 10, et 20 m avec incertitudes sur les conditions initiales

On étudie ensuite la robustesse de la boucle fermée non-linéaire aux incertitudes aérodynamiques. Pour cela, on réalise 300 simulations de Monte Carlo. Le tirage des coefficients aérodynamiques suit une loi normale, dont l'écart-type σ est pris tel que 3σ corresponde au niveau d'incertitude maximal, renseigné dans le Tableau A.1. Les incertitudes aérodynamiques impactent également la loi de guidage ZEM, puisque celle-ci exploite les valeurs nominales des coefficients aérodynamiques. La précision du projectile, évaluée dans un premier temps en n'incluant pas les saturations dans le simulateur, reste de l'ordre du millimètre pour toutes les trajectoires simulées. Cependant, 47 de ces trajectoires (15.7% des cas) donnent lieu à des angles de déflexion dépassant les 10 deg. La Figure A.31 montre la trajectoire des signaux virtuels correspondant à ces scénarios, et illustre l'impact plus important des incertitudes aérodynamiques par rapport aux incertitudes sur les conditions initiales.

La Figure A.31 montre l'écart à la cible pour les 47 scénarios identifiés, ainsi que le taux d'échec global en fonction de l'écart maximal toléré. Les valeurs aux seuils de 1, 10, 20, et 50 m sont renseignés dans le Tableau A.4. Les dégradations sont dans l'ensemble plus sévères que dans le cas des incertitudes sur les conditions initiales, et l'écart à la cible demeure élevé pour

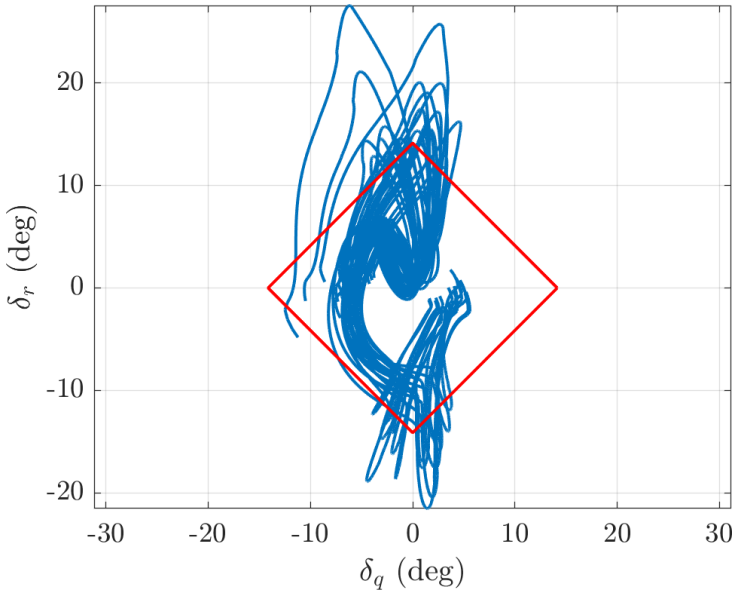

Figure A.30: Trajectoire des signaux de contrôle virtuels dans le plan (δ_q, δ_r) avec incertitudes aérodynamiques

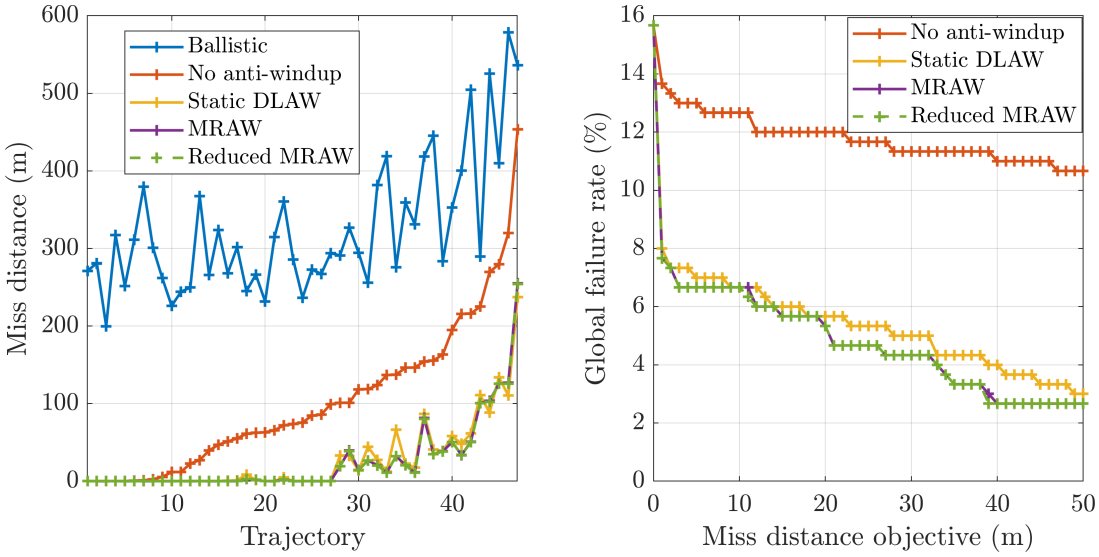

Figure A.31: Écart à la cible pour les 47 scénarios conduisant à des saturations (gauche), et taux d'échec global en fonction de l'écart maximal toléré (droite)

Objectif	Sans anti-windup	DLAW	MRAW
< 1 m	13.7%	8%	7.7%
< 10 m	12.7%	6.7%	6.7%
< 20 m	12%	5.7%	5.3%
< 50 m	10.7%	3%	2.7%

Table A.4: Taux d'échec global à 1, 10, 20, et 50 m avec incertitudes aérodynamiques

plusieurs cas même en présence de compensateurs anti-windup. Cependant, ces compensateurs n'en restent pas moins intéressants, car ils diminuent significativement la dispersion.

A.5.3 Conclusion

Dans ce chapitre, le modèle du projectile à 7DDL développé au Chapitre 2 est connecté à l'autopilote séquencé du Chapitre 3 et aux compensateurs anti-windup du Chapitre 4. Une loi de guidage de type ZEM, mieux adaptée à l'application, complète la boucle GNC. Des scénarios de tirs sont ensuite simulés pour évaluer la performance de l'autopilote baseline et des compensateurs anti-windup, en utilisant comme critère la distance entre le point d'impact et la cible balistique. Les résultats montrent que la combinaison de l'autopilote baseline et de la loi de guidage ZEM permet d'atteindre une précision très élevée dans des conditions de tir nominales, mais également en présence de perturbations (vent, incertitudes sur les conditions initiales, incertitudes aérodynamiques) lorsque les saturations sont désactivées dans le simulateur de vol. En revanche, certains de ces cas dégradés requièrent des angles de déflexion de canards supérieurs à la valeur de saturation. Ces mêmes cas, simulés cette fois avec saturations, conduisent à une dégradation importante de la distance à la cible, ce qui justifie l'ajout de compensateurs anti-windup. Les compensateurs développés permettent ainsi de retrouver une performance élevée dans la plupart des cas, et de réduire de façon drastique la dispersion à l'impact sur les scénarios restant.

A.6 Conclusion générale

A.6.1 Résumé des contributions

L'objectif de cette thèse est de mettre en place une méthodologie pour la conception de lois de contrôle de systèmes aérospatiaux à paramètres variants en présence d'incertitudes de modélisation et de saturations des actionneurs. Un cas concret, à savoir un concept novateur de projectile guidé dual-spin, est étudié pour évaluer et valider la procédure proposée.

En préliminaire, le Chapitre 2 met en place un modèle non-linéaire issu des équations générales du mouvement. Les dynamiques selon l'axe de roulis d'une part, et les axes de tangage/lacet d'autre part, sont ensuite séparées, puis linéarisées, afin de permettre l'application des méthodes issues de la théorie de la commande robuste.

La méthode générale de conception de l'autopilote s'appuie sur un procédé en deux étapes classiquement utilisé pour traiter des saturations. Dans un premier temps, on synthétise un contrôleur baseline en ne tenant pas compte des saturation. Cette baseline est ensuite enrichie avec un compensateur anti-windup dont le but est de limiter l'impact des saturations. La première étape est traitée dans le Chapitre 3. Elle combine des éléments de séquencement de gain, de la commande robuste $\mathcal{H}_\infty$, et de la μ-analyse. En particulier, des contributions théoriques à la μ-analyse sont présentées, associées à de nouveaux algorithmes de branch-and-bound, qui permettent d'évaluer la stabilité, la performance $\mathcal{H}_\infty$, et les marges de gain, de phase, et de module. Par rapport à l'approche pire cas de la μ-analyse standard, la μ-analyse probabiliste permet une quantification et une réduction du conservatisme. Elle fournit aussi des bornes garanties sur les probabilités évaluées, comblant une lacune des méthodes de Monte Carlo.

La simplification de l'étape de synthèse de l'autopilote baseline constitue une contribution applicative. Les autopilotes de roulis et de tangage/lacet envisagés gardent une structure basique. Malgré les variations paramétriques qui affectent la dynamique de roulis, une étude de ces

variations permet de ne considérer qu'un seul point de design. Un facteur multiplicatif est alors appliqué pour couvrir toute l'enveloppe de vol. Pour l'autopilote de tangage/lacet, des synthèses locales sont réalisées sur un maillage de l'enveloppe de vol. L'introduction d'un facteur multiplicatif basé sur le gain statique de la dynamique en boucle ouverte simplifie le réglage usuellement fastidieux des fonctions de pondération. Les propriétés de robustesse locales sont ensuite évaluées à l'aide de la μ-analyse probabiliste et de simulations temporelles.

L'application de la théorie anti-windup au domaine des projectiles guidés, traitée au Chapitre 4, constitue une autre contribution majeure de la thèse. La littérature propose en grand nombre de méthodes pour la synthèse anti-windup dans un contexte stationnaire. En revanche, ces méthodes n'offrent pas de garantie de stabilité ou de performance dès lors que des variations paramétriques entrent en jeu. De plus, certaines de ces méthodes reposent sur des hypothèses sur la dynamique qui ne sont pas vérifiées sur toute l'enveloppe de vol, ou sur des réglages délicats et fastidieux. Suite à ces réflexions, trois méthodes de synthèse anti-windup ont été retenues, caractérisées par leur simplicité de mise en place sur un maillage de l'enveloppe de vol. La première est issue de l'approche DLAW, et fournit un anti-windup statique. Les seconde et troisième méthodes sont issues de l'approche MRAW basée LQ. Elles se distinguent par le modèle de la dynamique utilisé, qui peut être plein ou réduit.

L'évaluation des réponses à des échelons montrent que la compensation anti-windup permet de contrecarrer les effets néfastes des saturations. En particulier, les compensateurs MRAW et MRAW réduit donnent des résultats quasiment identiques, ce qui démontre la pertinence de la réduction d'ordre. L'étude est complétée d'une analyse IQC, qui prend en compte simultanément les non-linéarités de type zone morte et les incertitudes aérodynamiques. En dépit du conservatisme de l'approche, on peut identifier des tendances intéressantes. Conformément aux attentes, la présence de compensateurs anti-windup permet d'élargir le domaine de stabilité garantie, et suggère de meilleures propriétés de robustesse. Le compensateur DLAW statique semble plus sensible aux incertitudes aérodynamiques, tandis que le compensateur MRAW d'ordre plein présente le plus grand domaine de stabilité garantie.

Dans le Chapitre 5, les autopilotes développés sont intégrés à un simulateur de vol non-linéaire. La performance en boucle fermée est alors évaluée à partir de scénarios de vol complets. Les résultats de simulations démontrent une excellente précision à l'impact, et de bonnes propriétés de robustesse lorsque les saturations sont retirées du simulateur, ce qui valide l'étape de conception de l'autopilote baseline. En revanche, des dégradations importantes sont observées sur des scénarios dégradés quand les saturations sont activées, témoignant du besoin en compensation anti-windup. Les compensateurs anti-windup sont capables de fortement améliorer le taux de réussite sur des campagnes de Monte Carlo, validant les méthodes de synthèse retenues, et la méthodologie générale, dans un contexte opérationnel. Le simulateur de vol en boucle fermé obtenu constitue donc un modèle avec de bonnes propriétés de performance et de robustesse, qui peut servir de référence pour les développements futurs.

A.6.2 Discussion et perspectives

La méthodologie proposée pour la conception de contrôleurs combine des éléments issus du séquencement de gain, de la commande robuste $\mathcal{H}_\infty$, de la synthèse anti-windup, ,de la μ-analyse,

et de l'analyse par IQC. Ces éléments sont interfacés afin d'obtenir une procédure cohérente, applicable aux systèmes aérospatiaux évoluant sur une enveloppe de vol étendue, et accessible aux ingénieurs automaticiens.

Les choix effectués dans les étapes de synthèse de la baseline et des compensateurs anti-windup visent explicitement à alléger la tâche de réglage des contrôleurs, qui peut généralement être fastidieuse. Les simulations non-linéaires en boucle fermée montrent que de très bonnes propriétés de performance et de robustesse peuvent être atteintes, en dépit de structures anti-windup simples. Pour autant, il serait intéressant de déterminer si, au prix d'une étape de réglage plus poussée, des structures plus sophistiquées permettraient d'améliorer davantage ces propriétés.

Une suite naturelle aux travaux présentés serait de rendre le simulateur de vol plus représentatif du système réel, en y intégrant un algorithme de navigation, des bruits capteurs, des retards liés aux temps de calcul, et en discrétisant l'autopilote. Des itérations de design supplémentaires et des réglages plus fins peuvent alors être nécessaires pour répondre à la complexité accrue du système. L'utilisation d'un maillage plus adapté qu'un simple maillage équidistant, par exemple basé sur un partitionnement de l'enveloppe de vol issu de la (ν)-*gap metric*, peut permettre une réduction du temps consacré à chaque itération. Il peut aussi être intéressant d'intégrer à la procédure des méthodes de *co-design*, afin de dimensionner les canards et les actionneurs en même temps que les gains du contrôleur.

Dans ces travaux, la μ-analyse est utilisée dans un contexte stationnaire, et ne fournit donc que des résultats de robustesse locaux. Il serait intéressant d'étendre les contributions à la μ-analyse probabiliste au cas non-stationnaire, pour permettre une analyse de robustesse plus rigoureuse le long d'une trajectoire de vol. Une extension aux systèmes hybrides serait également utile en vue d'une modélisation de l'autopilote par un système discret. En l'état, les contributions présentées fournissent en temps raisonnable une métrique qui devient empirique dans un contexte avec paramètres variants, mais qui reste utile pour une comparaison préliminaire entre différents autopilotes.

Le statut de l'analyse IQC dans ces travaux est similaire, et permet de comparer différents compensateurs anti-windup. La charge de calcul plus importante empêche cependant d'envisager son application sur un maillage fin de l'enveloppe de vol. De plus, les résultats, au-delà d'une comparaison qualitative, ne sont pas facilement exploitables, et ne sont pas bien corrélés aux résultats des simulations non-linéaires. Cet écart s'explique par le conservatisme difficilement quantifiable de l'analyse IQC. Une piste intéressante pour réduire ce conservatisme serait de considérer des profils d'entrée plus représentatifs, afin de calculer un indice de performance plus pertinent que le gain $\mathcal{L}_2$.

Toutes les pistes énoncées constituent des améliorations et des extensions possibles à la méthodologie proposée dans cette thèse. De manière plus générale, l'étude de méthodes alternatives, comme les contrôleurs LPV ou adaptatifs, ou l'utilisation de *reference governors*, constitue un point d'intérêt. La méthodologie et le simulateur en boucle fermée actuels serviraient alors de référence pour comparer les approches.

References

Apkarian, P. and Noll, D. (2006). "Nonsmooth H_∞ Synthesis". In: *IEEE Transactions on Automatic Control* 51.1, pp. 71–86.

Apkarian, P., Gahinet, P., and Becker, G. (1995). "Self-scheduled H_∞ control of linear parameter-varying systems: a design example". In: *Automatica* 31.9, pp. 1251–1261.

Åström, K. J. and Rundqwist, L. (1989). "Integrator windup and how to avoid it". In: *1989 American Control Conference*. IEEE.

Biannic, J.-M. and Tarbouriech, S. (2009). "Optimization and implementation of dynamic anti-windup compensators with multiple saturations in flight control systems". In: *Control Engineering Practice* 17.6, pp. 703–713.

Biannic, J.-M. and Roos, C. (2012-2021). *Generalized State Space: a new Matlab class to model uncertain and nonlinear systems as Linear Fractional Representations*. URL: `http://w3.onera.fr/smac/gss`.

Braatz, R. P., Young, P. M., Doyle, J. C., and Morari, M. (1994). "Computational complexity of μ calculation". In: *IEEE Transactions on Automatic Control* 39.5, pp. 1000–1002.

Costello, M. and Peterson, A. (2000). "Linear theory of a dual-spin projectile in atmospheric flight". In: *Journal of Guidance, Control, and Dynamics* 23.5, pp. 789–797.

Doyle, J. (1982). "Analysis of feedback systems with structured uncertainties". In: *IEE Proceedings D Control Theory and Applications* 129.6, p. 242.

Falcoz, A., Alazard, D., and Pittet, C. (2017). "Probabilistic μ-analysis for system performances assessment". In: *IFAC-PapersOnLine* 50.1, pp. 399–404.

Fan, M. K. H. and Tits, A. L. (1992). "A measure of worst-case H_∞ performance and of largest acceptable uncertainty". In: *Systems & Control Letters* 18.6, pp. 409–421.

Fetzer, M. and Scherer, C. W. (2017). "Full-block multipliers for repeated, slope-restricted scalar nonlinearities". In: *International Journal of Robust and Nonlinear Control* 27.17, pp. 3376–3411.

Fresconi, F. (2011). "Guidance and control of a projectile with reduced sensor and actuator requirements". In: *Journal of Guidance, Control, and Dynamics* 34.6, pp. 1757–1766.

Gagnon, E. and Lauzon, M. (2007). "Maneuverability analysis of the conventional 155 mm gunnery projectile". In: *AIAA Guidance, Navigation and Control Conference and Exhibit*. American Institute of Aeronautics and Astronautics.

Gagnon, E. and Lauzon, M. (2008). "Course correction fuze concept analysis for in-service 155 mm spin-stabilized gunnery projectiles". In: *AIAA Guidance, Navigation and Control Conference and Exhibit*. American Institute of Aeronautics and Astronautics.

Galeani, S., Tarbouriech, S., Turner, M., and Zaccarian, L. (2009). "A Tutorial on Modern Anti-windup Design". In: *European Journal of Control* 15.3-4, pp. 418–440.

Gomes da Silva, J. M. and Tarbouriech, S. (2005). "Antiwindup design with guaranteed regions of stability: an LMI-based approach". In: *IEEE Transactions on Automatic Control* 50.1, pp. 106–111.

Helton, J. C., Johnson, J. D., Sallaberry, C. J., and Storlie, C. B. (2006). "Survey of sampling-based methods for uncertainty and sensitivity analysis". In: *Reliability Engineering & System Safety* 91.10-11, pp. 1175–1209.

Hjartarson, A., Seiler, P., and Packard, A. (2015). "LPVTools: A Toolbox for Modeling, Analysis, and Synthesis of Parameter Varying Control Systems". In: *IFAC-PapersOnLine* 48.26, pp. 139–145.

Hoffmann, C. and Werner, H. (2014). "A survey of linear parameter-varying control applications validated by experiments or high-fidelity simulations". In: *IEEE Transactions on Control Systems Technology* 23.2, pp. 416–433.

Kelly, J., Evers, J., Kelly, J., and Evers, J. (1997). "An interpolation strategy for scheduling dynamic compensators". In: *Guidance, Navigation, and Control Conference*. American Institute of Aeronautics and Astronautics.

Khatri, S. and Parrilo, P. A. (1998). "Guaranteed bounds for probabilistic μ". In: *37th IEEE Conference on Decision and Control)*. IEEE.

Kothare, M. V., Campo, P. J., Morari, M., and Nett, C. N. (1994). "A unified framework for the study of anti-windup designs". In: *Automatica* 30.12, pp. 1869–1883.

Landau, D. P. and Binder, K. (2014). *A guide to Monte Carlo simulations in statistical physics*. Cambridge university press.

Leith, D. J. and Leithead, W. E. (2000). "Survey of gain-scheduling analysis and design". In: *International Journal of Control* 73.11, pp. 1001–1025.

Lescher, F. and Roos, C. (2011). "Robust stability of time-delay systems with structured uncertainties: a μ-analysis based algorithm". In: *50th IEEE Conference on Decision and Control and European Control Conference*. IEEE.

Lesprier, J., Roos, C., and Biannic, J.-M. (2015). "Improved μ upper bound computation using the μ-sensitivities". In: *IFAC-PapersOnLine* 48.14, pp. 215–220.

Lozier, J. (1956). "A steady state approach to the theory of saturable servo systems". In: *IRE Transactions on Automatic Control* 1.1, pp. 19–39.

McCoy, R. L. (1999). *Modern Exterior Ballistics: The Launch and Flight Dynamics of Symmetric Projectiles*. Schiffer Publishing.

Megretski, A. and Rantzer, A. (1997). "System analysis via integral quadratic constraints". In: *IEEE Transactions on Automatic Control* 42.6, pp. 819–830.

Proff, M. and Theodoulis, S. (2019). "Study of impact point prediction methods for zero-effort-miss guidance: application to a 155mm spin-stabilized guided projectile". In: *5th CEAS Conference on Guidance, Navigation and Control*.

Roos, C. and Biannic, J.-M. (2015). "A detailed comparative analysis of all practical algorithms to compute lower bounds on the structured singular value". In: *Control Engineering Practice* 44, pp. 219–230.

Roos, C. (2013). "Systems modeling, analysis and control (SMAC) toolbox: an insight into the robustness analysis library". In: *2013 Conference on Computer Aided Control System Design (CACSD)*. IEEE.

Roos, C., Lescher, F., Biannic, J.-M., Döll, C., and Ferreres, G. (2011). "A set of μ-analysis based tools to evaluate the robustness properties of high-dimensional uncertain systems". In: *2011 International Symposium on Computer-Aided Control System Design (CACSD)*. IEEE.

Rugh, W. J. and Shamma, J. S. (2000). "Research on gain scheduling". In: *Automatica* 36.10, pp. 1401–1425.

Sève, F., Theodoulis, S., Wernert, P., Zasadzinski, M., and Boutayeb, M. (2017). "Flight dynamics modeling of dual-spin guided projectiles". In: *IEEE Transactions on Aerospace and Electronic Systems* 53.4, pp. 1625–1641.

Shamma, J. S. and Athans, M. (1991). "Guaranteed properties of gain scheduled control for linear parameter-varying plants". In: *Automatica* 27.3, pp. 559–564.

Siouris, G. M. (2004). *Missile Guidance and Control Systems*. Springer.

Skogestad, S. and Postlethwaite, I. (2005). *Multivariable feedback control: analysis and design*. Wiley-Interscience.

Tarbouriech, S., Garcia, G., Gomes da Silva, J. M., and Queinnec, I. (2011). *Stability and stabilization of linear systems with saturating actuators*. Springer London.

Thai, S., Roos, C., and Biannic, J.-M. (2019a). "Probabilistic μ-analysis for stability and H_∞ performance verification". In: *2019 American Control Conference (ACC)*. IEEE.

Thai, S., Theodoulis, S., Roos, C., and Biannic, J.-M. (2019b). "Robust design for the roll-channel autopilot of a canard-guided dual-spin projectile". In: *IFAC-PapersOnLine* 52.12, pp. 232–237.

Thai, S., Theodoulis, S., Roos, C., and Biannic, J.-M. (2021). "An interpolated model recovery anti-windup for a canard-guided projectile subject to uncertainties". In: *2021 European Control Conference (ECC)*. IEEE.

Thai, S., Theodoulis, S., Roos, C., Biannic, J.-M., and Proff, M. (2020). "Gain-scheduled autopilot design with anti-windup compensator for a dual-spin canard-guided projectile". In: *2020 IEEE Conference on Control Technology and Applications (CCTA)*. IEEE.

Theodoulis, S., Gassmann, V., Brunner, T., and Wernert, P. (2013). "Fixed structure robust control design for the 155mm canard-guided projectile roll-channel autopilot". In: *21st Mediterranean Conference on Control and Automation*. IEEE.

Theodoulis, S., Sève, F., and Wernert, P. (2015). "Robust gain-scheduled autopilot design for spin-stabilized projectiles with a course-correction fuze". In: *Aerospace Science and Technology* 42, pp. 477–489.

Theodoulis, S. and Wernert, P. (2017). "Flight dynamics & control for smart munition: the ISL contribution". In: *IFAC-PapersOnLine* 50.1, pp. 15512–15517.

Veenman, J., Scherer, C. W., and Köroğlu, H. (2016). "Robust stability and performance analysis based on integral quadratic constraints". In: *European Journal of Control* 31, pp. 1–32.

Wu, F. (2001). "A generalized LPV system analysis and control synthesis framework". In: *International Journal of Control* 74.7, pp. 745–759.

Wu, F. and Dong, K. (2006). "Gain-scheduling control of LFT systems using parameter-dependent Lyapunov functions". In: *Automatica* 42.1, pp. 39–50.

Zaccarian, L. and Teel, A. R. (2011). *Modern Anti-windup Synthesis: Control Augmentation for Actuator Saturation*. Princeton University Press.

Zhu, X., Huang, Y., and Doyle, J. (1996). "Soft vs. hard bounds in probabilistic robustness analysis". In: *35th Conference on Decision and Control*. IEEE.

Zipfel, P. H. (2007). *Modeling and Simulation of Aerospace Vehicle Dynamics*. Second. American Institute of Aeronautics and Astronautics.